The APEX submillimeter imaging survey of distant galaxies in the COSMOS field

Dissertation
zur
Erlangung des Doktorgrades (Dr. rer. nat.)
der
Mathematisch-Naturwissenschaftlichen Fakultät
der
Rheinischen Friedrich-Wilhelms-Universität Bonn

vorgelegt von
Felipe Pedro Navarrete Avendaño
aus
Santiago, Chile

Bonn, Dezember 2014

Angefertigt mit Genehmigung der Mathematisch-Naturwissenschaftlichen Fakultät
der Rheinischen Friedrich-Wilhelms-Universität Bonn

1. Referent: Prof. Dr. Frank Bertoldi
2. Referent: Prof. Dr. Karl Menten

Tag der Promotion: 04.Mai 2015
Erscheinungsjahr: 2015

Diese Dissertation ist auf dem Hochschulschriftenserver der ULB Bonn unter
http://hss.ulb.uni-bonn.de/diss_online elektronisch publiziert.

To Germán Rojas

Abstract

Submillimeter galaxies (SMGs) are far-infrared luminous, vigorously star forming galaxies in the early universe. They are major contributors to the extragalactic far-infrared background emission, and they trace the most intense phase of stellar mass build up in cosmic history. The star formation rates in SMGs is higher by a factor hundred to thousand compared to that of "normal" galaxies such as our Milky Way galaxy.

In order to understand the nature of SMGs, numerous (sub)millimeter surveys have been carried out to collect large statistical samples of these galaxies. In particular, surveys at wavelengths in the range 800–2000 μm have the unique advantage that, at a fixed wavelength, a galaxy with a given infrared luminosity is observed with the same flux density in the redshift range $z \sim 1$–8.

The Cosmic Evolution Survey (COSMOS) is an equatorial 2 deg^2 field designed to probe the formation and evolution of galaxies as a function of cosmic time and large scale structure environment. To date the field has been observed with most major space and ground-based telescopes over a large fraction of the electromagnetic spectrum. However, at 850–870 μm the largest survey covers only $\sim$ 0.11 deg^2.

In this work, we carried out the yet largest, 0.75 deg^2, 870 μm survey of the COSMOS field, using the Large Apex BOlometer CAmera (LABOCA) at the APEX telescope. We provide a catalog with reliably detected sources and compare it with other (sub)millimeter studies in the same field. We derive the number counts and redshift distribution of the sources, which are useful to constrain models that try to follow the evolution of galaxies throughout cosmic history.

We present high-resolution interferometric observations at 1.3 mm wavelength of a subsample of SMGs that we previously detected in our LABOCA imaging of the COSMOS field. The high resolution allows to unambiguously identify the location of the most likely counterparts at other wavelenghts. The conclusions from our study are: (i) 15% to 40% of SMGs observed with single-dish telescopes break up into multiple (sub)mm galaxies, (ii) identifications through statistical arguments, of counterparts to single-dish submillimeter sources could be wrong up to 30% , and (iii) the redshift distribution of SMGs shows a higher mean and broader width than what was found in previous studies.

We study the average (sub)millimeter properties of large samples of galaxies that have more moderate SFRs than SMGs. They are not individually detected in (sub)millimeter maps. However, they can be studied through stacking. We implement a recently developed stacking algorithm that we test on simulations with a wide range of source densities and source clustering properties. The algorithm is applied in the COSMOS field, where the large area and a deep 2.2 μm source catalog allow us to stack samples more than an order of magnitude larger than those of previous studies for similar types of galaxies. We detect the average submillimeter emission from high redshift star-forming galaxies, while high-redshift passive galaxies remain undetected, mainly due to their low number statistics. We find that at redshift 1.4 to 2.5, star-forming galaxies are four times brighter than those at lower redshifts. We study the redshift evolution of these populations, and combine this information with the stacking at radio wavelengths of the same populations, confirming that the well-known tight correlation between radio and far-infrared luminosities is also seen for these galaxy populations up to $z \sim 2$.

Publications

Chapter 2 will be submitted to A&A as:

“The LABOCA Submillimeter Survey of the COSMOS field”, **Navarrete, F.**, Smolčić V., Albrecht, M., Aravena, M., Bertoldi, F., Vaduvescu, O.

Chapter 3 was published as:

“Millimeter imaging of submillimeter galaxies in the COSMOS field: redshift distribution”, Smolčić, V., Aravena, M., **Navarrete, F.**, Schinnerer, E., Riechers, D. A.,Bertoldi, F., Feruglio, C., Finoguenov, A., Salvato, M., Sargent, M., McCracken, H. J., Albrecht, M., Karim, A., Capak, P., Carilli, C. L., Cappelluti, N., Elvis, M., Ilbert, O., Kartaltepe, J., Lilly, S., Sanders, D., Sheth, K., Scoville, N. Z., Taniguchi, Y. 2012, A&A, 548A, 4

Additional publications that were not incorporated into this thesis:

“Quest for COSMOS Submillimeter Galaxy Counterparts using CARMA and VLA: Identifying Three High-redshift Starburst Galaxies”, Smolčić, V., **Navarrete, F.**, Aravena, M. et. al. 2012, ApJS, 200, 10

“Properties of submillimetre galaxies in a semi-analytic model using the ‘Count Matching’ approach: application to the ECDF-S”, Muñoz Arancibia, A. M., **Navarrete, F.**, Padilla, N. D., Cora, S. A., Gawiser, E., Kurczynski, P., Ruiz, A. N. 2015, MNRAS, 446, 2291

“New insights from deep VLA data on the potentially recoiling black hole CID-42 in the COSMOS field”, Novak, M., ..., **Navarrete, F.** et. al., accepted for publication in MNRAS

“Evolution of the dust emission of massive galaxies up to z=4 and constraints on their dominant mode of star formation”, Béthermin, M., ..., **Navarrete, F.** et al. accepted for publication in A&A

“Confirming the Quiescent Galaxy Population out to $z = 3$: A Stacking Analysis of Mid-, Far-Infrared and Radio Data”, Man, A. W. S., ..., **Navarrete, F.** et. al. submitted to ApJL

Contents

1

Introduction

The origin of our Universe is known as the Big Bang, when all of space was confined to a single point. Ever since that moment the Universe has been expanding and cooling down. From about one second to few minutes after the Big Bang, the temperature fell sufficiently to allow the combination of protons and neutrons and form certain species of atomic nuclei, i.e., hydrogen, helium, deuterium, and traces of lithium and beryllium. This is known as "Big Bang nucleosynthesis". The prevalence of free electrons obstructed the photons until the Universe was 300,000 years old, when electrons combined with the nuclei to form neutral atoms. The radiation from this epoch is known as cosmic microwave background(CMB), microwaves that we detect arriving from all directions in the sky, and is extremely uniform. The process of how all the structures in the Universe (i.e., galaxy clusters, galaxies, stars, etc) are formed from that uniform gas is one of the main goals of modern physical cosmology. A serie of well understood physical processes, i.e., gas dynamics, cooling physics, nuclear reactions, and radiative transfer, are involved in the fomation of the Universe as we know it nowadays. However, the numerous possible initial conditions and the non-linearity of the events that conducted to the formation of the gravitationally bounded structures that we see, and also live on, makes plausible a wide range of possible outcomes.

In order to reproduce the Universe in its actual state, semi-analytical models and numerical simulations that attempt to model the evolution of the Universe need constraints from observational data. With this aim, astronomers and astrophysicists have to collect and understand the data in a multiwavelength framework. However, the atmospheric opacity kept us for a long time restricted to the optical and radio windows of the electromagnetic spectrum (see Fig. 1.1). Fortunately, technological development of the receivers, and also the launch of telescopes into the space, ultimately opened up the full electromagnetic spectrum. In this multiwavelength view of the Universe the far infrared/(sub)mm regime,i.e. 40–1000μm, where this thesis is mainly focused, has proven to be a critical component for the understanding of the galaxy formation process, unveiling a Universe that for long

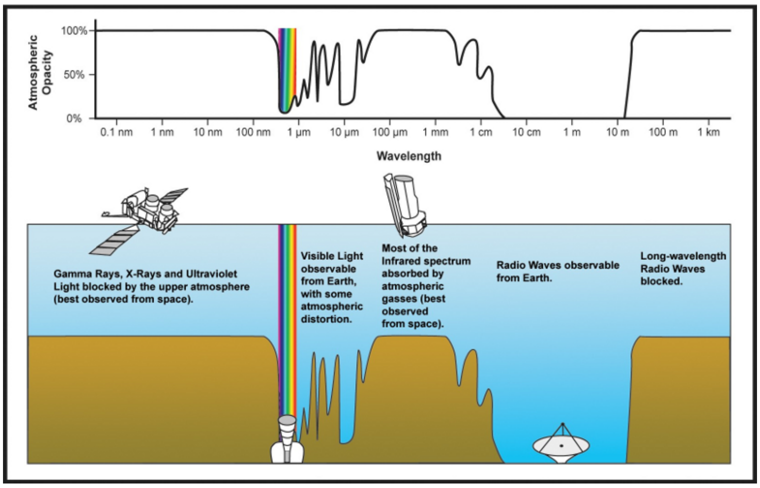

Figure 1.1: A representative schema of the opacity of the atmosphere as a function of wavelength. It is clear that the optical, the region represented with rainbow colors, and radio regimes are transparent to the atmosphere, while other regimes are difficult to observe given the large opacity, e.g., the far infrared regime. Credits: $http://www.eso.org/public/images/atm_opacity/$

time was invisible to us. The first extragalactic observations at this wavelength regime came from early efforts in the sixties, where, for instance, Low (1965) carried out observations of two quasi stellar objects (QSOs), i.e., 3C 273 and 3C 279, at 1 mm. Johnson (1966) defines as far infrared regime the wavelength range between 4 to 22 μm (nowadays the far infrared term is used for the wavelength range from about 40–200μm). In these early studies, already interesting conclusions were drawn at these wavelengths, for example Rees et al. (1969) pointed out that the infrared radiation from Seyfert galaxies in the wavelengths 2.2 to 22 μm could be emitted by dust grains that absorb energy from an intense optical or ultraviolet source at the galactic nucleus. Later on at the end of the seventies, Telesco & Harper (1977) reported the far infrared observations ($\lambda \gtrsim 30$ μm) of extragalactic sources, i.e., NGC 253, NGC 1068, M82, and QSO 3C 273. Rieke & Lebofsky (1979) reviews the status of the far-infrared/(sub)millimeter extragalactic astronomy at the time reporting that among the thousands of galactic nuclei and QSOs studied in the optical and radio, barely 10 were observed at 100 μm. In summary, this shows that the knowledge of the far-infrared regime was still very limited. Early in the eighties (1983) the Infrared Astronomical Satellite (IRAS) provided the first all sky area survey of the infrared and far-infrared sky at 12, 25, 60, and 100 μm wavelengths. The most impressive galaxies observed by IRAS were a population of galaxies with infrared luminosities in excess of 10^{12} $L_\odot$, which were named Ultraluminous Infrared Galaxies (ULIRGs). In spite of IRAS limited sensitivity and low angular resolution , which is the reason that most of the discoveries were related to the local Universe, the data was able to determine that there has been very strong number evolution in the ULIRG population (compared to the local Universe) out to $z \sim 0.5$. The Infrared Space Observatory (ISO), probed that this evolution extended out to $z \sim 1$. The Cosmic Background Explorer (COBE), which main mission was to study the cosmic microwave background radiation, also taught us that there was an extragalactic infrared background (FIRB; Puget et al. 1996; Fixsen et al. 1998). Studying the cosmological implications of this discovery, Dwek et al. (1998) strongly favored an extragalactic origin of the FIRB light over a galactic origin. These findings led to revisions of the star formation history of the Universe derived until then, implying that ultraviolet (UV) and optical derivations of the star-formation rate have had missed a significant fraction of the star formation activity that takes place in dust-enshrouded galaxies or star-forming regions. In particular, at z ∼1.5, predictions from UV and optical would be off by at least a factor of 2.

In a perfect timing with this discovery, SCUBA and MAMBO bolometers resolved for the first time, at (sub)millimeter wavelengths, the diffuse extragalactic background observed by COBE. Hughes et al. (1998) observed an area of 9 arcmin^2 of the *Hubble* Deep Field down to a depth of 0.5 mJy at 850 μm. These first observations already had profound implications: at this depth, a non-evolution of the dusty starburst population, i.e., the source density is similar to what is observed in the local Universe, would translate into only 0.1 sources with $S_{850} > 2$ mJy; if there was strong evolution up to $z \sim 2$ two sources would have been observed . However, Hughes et al. (1998) detected five sources, implying that likely the evolution would continue even to higher redshifts.

1.1 Submillimeter extragalactic surveys

1.1.1 Summary of (sub)mm surveys: 800–2000 μm

One of the great contributions from the first imaging surveys with bolometer array cameras, e.g., SCUBA and MAMBO, was that the extragalactic background began to be resolved to individual galaxies. Since then, many surveys have greatly enhanced the number of galaxies in order to study them in an statistical sense. In Table 1.1 we list all the surveys that we are aware of in the range 800–2000 μm. We focus on this wavelength range since most of the thesis is focused on observations at 870 μm, and also because it has been shown that while observations at 24 μm resolve 55-95% of the cosmic infrared background at 70-500 μm (Devlin et al. 2009; Chary & Pope 2010), they only are able to resolve ∼ 30 % of the Cosmic Infrared Background (CIRB) at $\lambda = 1$ mm (Scott et al. 2010; Penner et al. 2011), hence it is of main importance to study the extragalactic universe at $\lambda > 800$ μm, where this thesis is focused.

A key advantage of surveys at these wavelengths is its essentially flat selection function over the redshift range $1 \lesssim z \lesssim 8$, which is due to the negative K-correction at this wavelength range. The K-correction is a factor that is applied to convert an observed-frame flux density to the rest-frame flux density of the galaxy. The value of the factor depends on the Spectral Energy Distribution (SED) of the galaxy. A negative K-correction implies that the flux density increases with increasing redshift. This is the case of the submillimeter wavelength range, where the SED can be well approximated by a modified blackbody, i.e., $B_\nu \nu^\beta$, where B_ν is the Planck function, and β is the dust emissivity spectral index. Using the Rayleigh Jeans approximation for the Planck function the flux density behave as $S_\nu \propto \nu^{2+\beta}$, where S_ν is the observed flux density, and common values for β range from 1.5 to 2. If we move a galaxy of fixed luminosity L_ν towards higher redshift the observed flux density decreases $\propto (1+z)^4$ since $S_\nu = L_\nu/(4\pi D_L^2)$ and D_L is $\propto (1+z)^2$. However, the SED also shifts towards higher frequencies, $\nu \propto \nu_{rest}(1+z)$ therefore the redshift dependence of the observed flux density behaves like $S_\nu(z) \propto \nu^{2+\beta}/(4\pi D_L^2) \propto \nu_{rest}^{2+\beta}(1+z)^{2+\beta}/(1+z)^4$ $\propto (1+z)^{\beta-2}$, hence the observed flux density remains constant. This can be seen in Fig.

1.2, at 850μm the flux of a galaxy with fixed luminosity L will be constant in the range $z \approx$ 1–8, furthermore, going to longer wavelengths, e.g., 2 mm, galaxies will be even easier to detect at high redshift than at low redshift.

Table 1.1: Summary of the submillimeter galaxy surveys carried out since 1997

Author	year	λ [μm]	Number of galaxies	Area arcmin^2	Field	rms$_{best}$ [mJy/beam]	rms$_{worst}$ [mJy/beam]	Instrument
Smail	1997	850	6	10	Clusters	2.00	2.00	SCUBA
Hughes	1998	850	5	9	HDF−N	0.50	0.50	SCUBA
Barger	1998	850	2	9	LH+SSA13	0.80	0.80	SCUBA
Eales	1999	850	12	22	CFRS	1.00	1.00	SCUBA
Eales	2000	850	19	50	SLUGS	1.20	1.20	SCUBA
Cowie	2002	850	14	20	Clusters	0.60	0.60	SCUBA
Scott	2002	850	38	260	ELAISN2+LHE	2.50	2.50	SCUBA
Serjeant	2003	850	3	9	HDFN	0.40	0.40	SCUBA
Webb	2003	850	15	60	CUDSS	1.00	1.00	SCUBA
Greve	2004	1200	27	357	ELAISN2+LHE	2.65	2.65	MAMBO
Wang	2004	850	45	110	HDFN+GOODS	0.40	4.00	SCUBA
Pope	2005	850	40	200	HDFN+GOODSN	3.40	3.40	SCUBA
Laurent	2005	1100	17	324	LH	3.44	3.44	BOLOCAM
Coppin	2006	850	120	720	SXDF+LH	2.00	2.00	SCUBA
Bertoldi	2007	1200	15	400	COSMOS	3.31	3.31	MAMBO
Scott	2008	1100	50	540	COSMOS	3.20	3.20	AzTEC
Greve	2008	1200	30	287	GOODSN	2.32	2.32	MAMBO
Perera	2008	1100	28	245	GOODS	2.46	2.46	AzTEC
Weiss	2009	870	126	1260	ECDFS	1.20	1.20	LABOCA
Scott	2010	1100	41	270	GOODSS	1.48	1.48	AzTEC
Austermann	2010	1100	114	2520	SHADES	2.21	4.18	AzTEC
Aretxaga	2011	1100	129	2592	COSMOS	3.10	3.10	AzTEC
Lindner	2011	1200	41	566	LH	1.49	4.97	MAMBO
Casey	2013	850	99	394	COSMOS	0.80	0.80	SCUBA-2
Navarrete	2014	870	39	2698	COSMOS	1.70	4.70	LABOCA

Another key contribution of these surveys is related to the evolution of the Universe, for which is important to study the different components that contribute to the FIRB at different redshifts. In Fig. 1.3 it is shown that the slope of the long wavelength part of the FIRB, $I_\nu \propto \nu^{1.4}$, is much less steep than the long-wavelength spectrum of galaxies. This is evidence that the millimeter portion of the FIRB is not due to the millimeter emission of the galaxies that account for the peak of the FIRB ($\simeq$ 170 μm). Moreover, in the lower panel of the same Fig. it is shown that the (sub)millimeter contains information of the total FIRB intensity contributed by high-redshift galaxies ($z > 2$).

1.1.2 The cosmic evolution survey

The design of sky surveys is always a compromise between area size and sensitivity. Small fields are usually the deepest and allow the observations of the faintest sources out to the greatest distances. However, in these surveys the likelihood to observe rare objects is low, e.g., the most massive haloes in the Universe. The "cosmic variance" is another difficulty in these surveys, hence global conclusions can vary from field to field, depending on the targeted environment. On the other hand, large area surveys are shallower but allow to study the large scale structure (LSS) and the detection of the most massive sources in the Universe. The Cosmic Evolution Survey (COSMOS; Scoville et al. 2007), where the

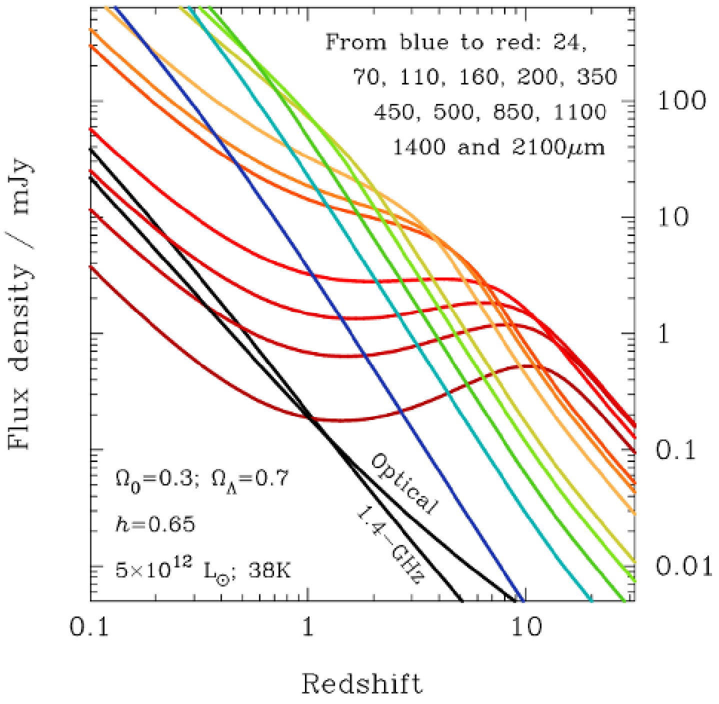

Figure 1.2: The flux density of a galaxy of fixed luminosity, L_{IR}=5×10^{12} $L_{\odot}$, as a function of redshift for different observed wavelengths. The negative K correction at submm wavelengths yields, at λ > 500μm a flux density almost independent of redshift. Credits: Blain (2002).

work presented in this thesis is focused, is the first survey encompassing a sufficiently large area, i.e., 2 deg^2 that allow the study of the coupled evolution of the Large Scale Structure (LSS), galaxies, star formation, and AGNs. The size has been determined following the results from a LSS Λ-CDM simulation for $z = 1$ and 2 (Virgo Consortium; Frenk et al. 2000), where it is shown that structure occurs on mass scales up to $\geq 10^{14} M_{\odot}$. In COSMOS, the probability to observe at least one structure with M = $10^{14} M_{\odot}$ at $z \sim 1$ is almost 100 %, while in other fields like HDF-N or GOODS this probability is negligible.

Furthermore, COSMOS is the largest HST survey ever undertaken, with I-band exposures to a point source depth of I_{AB} = 26.0 mag. Its equatorial position on the sky allows the observation of this field with a large range of astronomical facilities, both space and ground-based, e.g., *Spitzer*, *Herschel*, Subaru, $XMM - Newton$, etc. This is a comparative advantage compared to other high declination fields such as the Hubble Deep Field North (HDF-N), Chandra Deep Field North (CDF-N), Chandra Deep Field South(CDF-S), etc.

In particular different areas of the field have been mapped at (sub)mm wavelengths. At 2 mm it has been observed with GISMO (Karim et al., in preparation); at 1.2 mm it has been observed with MAMBO (Bertoldi et al. 2007); at 1.1 mm it has been observed with BOLOCAM (Aguirre et al., in preparation), and AzTEC (Scott et al. 2008; Aretxaga et al. 2011); at 850 μm an area of 400 arcmin^2 has been observed with SCUBA-2 (Casey et al. 2013).

The COSMOS field is ideal to characterize these galaxies given the wealth of panchromatic data, with more than 30 observed photometric bands, which allows the computation of high precision photometric redshifts (Smolčić et al. 2012b). Also is ideal to study the full SED of SMGs, as data is available from X-ray to radio wavelengths.

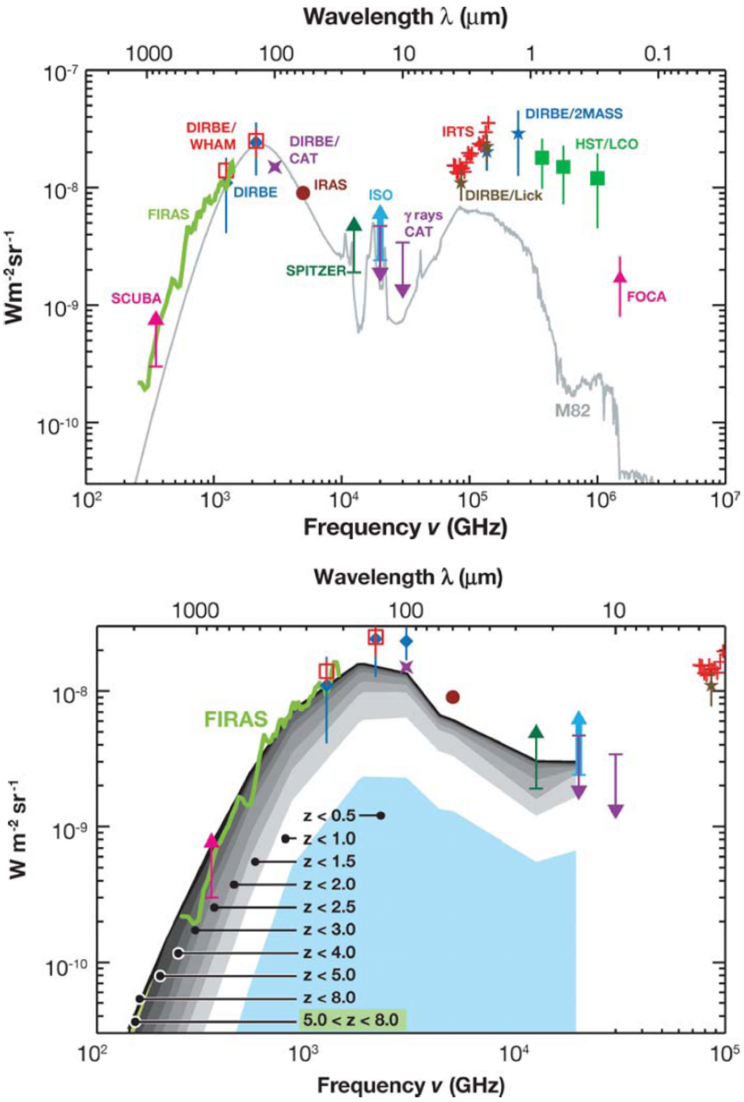

Figure 1.3: Top: Measurements of the extragalactic background at different wavelengths, covering from the near UV to millimeter wavelengths. For comparison, the spectral energy distribution (SED) of M82 (gray solid line) normalized to the peak of the FIRB at 140 μm is shown. Note that the slope of the long wavelength part of the FIRB, $I_\nu \propto \nu^{1.4}$, is much less steep than the long-wavelength spectrum of galaxies. This is evidence that the millimeter portion of the FIRB is not due to the millimeter emission of the galaxies that account for the peak of the FIRB ($\simeq 170$ μm). Bottom: Cumulative contribution to the FIRB of galaxies, at various redshifts from 0.5 to 8, from the model of Lagache et al. (2005). Symbols are the same as in the top panel.

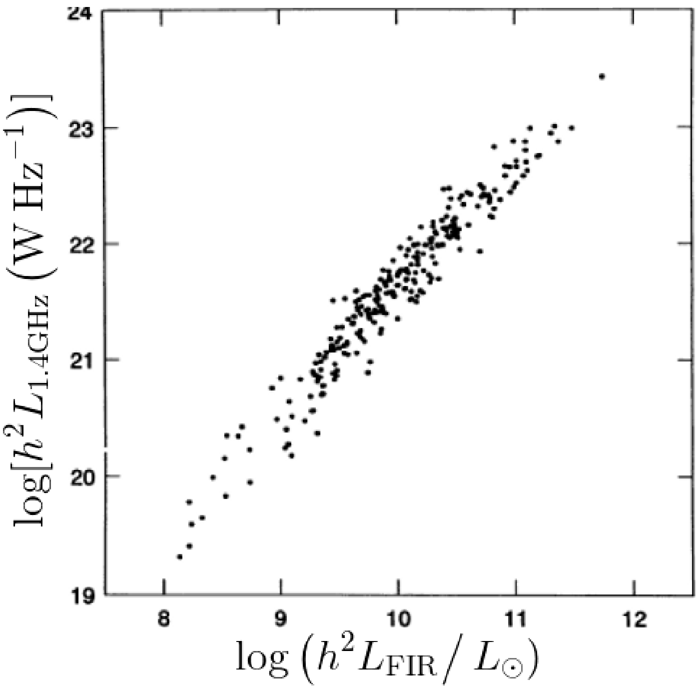

Figure 1.4: The 1.4 GHz luminosity as a function of the far infrared luminosity. The data points are strong selected sources at 60 μm, which do not contain a detected AGN. It can be seen that both luminosities are strongly correlated spanning about 5 orders of magnitude in far infrared luminosity Credits: Condon (1992).

In this thesis, we present the results of the largest contiguous survey at 870 μm, i.e. 0.75 deg^2, which reach a depth of 1.68 mJy/beam at the center. We report of 39 detected sources with a signal-to-nose ratio (S/N) $>$ 3.8. Using simulated maps, we test the reliability of our extracted sources and also compute quantities such as the positional uncertainty, and completeness. The source number counts and the redshift distribution are also reported.

1.2 Redshift distribution

As the number of sources from the blank surveys started to increase, it was of primordial interest to have knowledge of the redshift distribution of submillimeter galaxies (SMGs) in order to shed light on their role in the evolution of the Universe. However, the large beam of single-dish surveys, i.e., 10 to 30 arcsec, make difficult the process of assigning optical counterparts in order to observe them spectroscopically or to at least calculate photometric redshifts. Luckily, and this is a nice example of multiwavelength astronomy, the observations in the radio regime played a crucial role in building up redshift distributions for submillimeter galaxies. The correlation between radio and far infrared emission is one of the tightest extragalactic correlations (Condon 1992, and Sect. 1.7 of this Chapter), spanning about five orders of magnitude in luminosity (see Fig. 1.4). With the aim of determining the redshift of SMGs, Carilli & Yun (1999) took advantage of the far infrared radio correlation (FIRRC) and studied the flux ratio between 1.4 GHz and 850μm (352GHz) as a function of redshift for starburst galaxies, concluding that submillimeter sources likely had a typical redshift $z > 1.5$. Moreover, given that the high resolution of interferometric radio observations match the resolution of optical surveys and that also the source density in radio surveys is much smaller, radio identifications of submillimeter sources became the standard method to pinpoint the true counterparts. Chapman et al. (2005) exploited this technique and reported spectroscopic redshifts obtained with the Keck I Telescope for a sample of 73 submillimeter sources, finding a median redshift of 2.2. This was robust evidence, which showed that submillimeter sources were indeed high-redshift ULIRGs. Moreover, as shown in Fig. 1.5 SMGs are an important contributor to the star formation rate density (SFRD) of the Universe, being comparable to estimates inferred from rest-frame UV observations (Steidel et al. 1999; Adelberger & Steidel 2000). Since then several studies have further investigated the redshift distribution (Wardlow et al. 2011). Just recently, given the higher sensitivities and higher resolutions achieved with submillimeter interferometers, i.e., SMA, PdBI, and especially ALMA, optical counterparts of submillimeter sources can be unambiguously identified. In Smolčić et al. (2012b) (see also Chapter 3) we used the PdBI interferometer in order to identify the counterparts of submillimeter sources detected with the LABOCA bolometer camera in the COSMOS field. We also quantified that up to 50% of sources identified through radio are likely to be false matches. Regarding the redshift distribution of SMGs in the COSMOS field, in Smolčić et al. (2012b), we calculate it for two statistical samples. The first is a 1.1 mm-selected sample, where we obtain an average redshift of 3.1 ± 0.4, and the second is a 870 μm sample , where we obtain an average redshift of 2.6 ± 0.4. Weiß et al. (2013) present redshift distributions for a subsample of 26 lensed galaxies, originally observed at 1.4 mm with the *South Pole Telescope* (SPT) and followed up at 3 mm with ALMA in order to obtain spectroscopic redshifts using molecular emission lines, e.g., ^{12}CO, ^{13}CO, H_2O. 23 of these sources are detected in one or more emission lines, obtaining a mean redshift for the distribution of 3.5, which is significantly higher than the mean redshift obtained for submillimeter sources with radio detected counterparts. The most up to date unbiased redshift distribution is given by Simpson et al. (2014) who use the ALMA observations at 344 GHz of the submillimeter sources originally observed with LABOCA. They compute photometric redshifts for 77 of 96 submillimeter galaxies, which have enough photometric information, i.e., 4 to 17 photometric bands. The mean redshift for this sample is 2.5, which is similar to what is observed in radio selected samples. This seems to add evidence for a higher redshift distribution for millimeter selected galaxies compared to submillimeter sources.

In this thesis, we show redshift distributions obtained by statistically matching radio/mid-infrared/infrared galaxies to submillimeter sources observed with the Large APEX Bolometer CAmera, LABOCA, and in this way pinpointing the most likely optical counterpart (see Chapter 2). We also compute photometric redshifts to the unbiased follow up observations with the PdBI interferometer (see Chapter 3 and Smolčić et al. (2012b)).

1.3 Physical characteristics

Although the main driver of this thesis is not the physical characterization of the (sub)mm galaxies we consider important to give a brief outlook of the current knowledge on this topic.

From (sub)mm surveys, such as the one we present in Chapter 2, follow-ups of selected

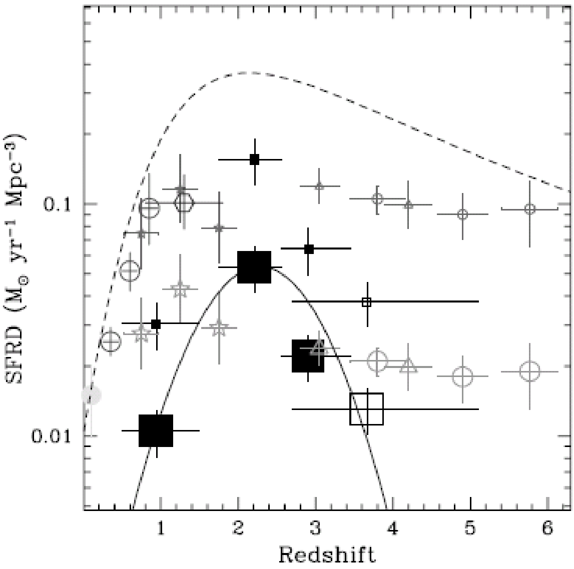

Figure 1.5: Evolution of the star formation rate density (SFRD) as a function of redshift. The SMGs are represented by large square symbols and are compared with estimates from optical/UV surveys and radio/IR tracers of the star formation rate density. The smaller square symbols indicates that they have been corrected by incompleteness estimates, while other smaller symbols indicate dust-corrected estimates. At $z \sim 2$–3 the contribution of SMGs to the SFRD of the Universe is similar to what is expected only for UV/optical galaxies.

subsamples of submillimeter sources have been studied in greater detail in order to understand their physical nature, i.e., physical size, if they are mergers or discs, dust mass, depletion time, SFR, stellar mass, etc.

Molecular Content & Dust Mass. We start describing the molecular content and dust mass of SMGs given that a significant fraction of the physical knowledge of the SMGs that we have nowadays comes from the observation of molecules in the interstellar medium such as CO or HCN. These observations have proven to be time consuming, and as a proof of that, 6 years after the first extragalactic submillimeter surveys with SCUBA, only two galaxies have had been observed in CO. Then in the framework of a CO programme with the IRAM Plateau de Bure interferometer (PdBI), Neri et al. (2003) added three SMGs to the list. Bothwell et al. (2013) reported the final results of the program, where previous galaxies observed in the same framework (Neri et al. 2003; Greve et al. 2005; Tacconi et al. 2006, 2008; Bothwell et al. 2010) are included. The final sample consisted of 40 galaxies, where 32 of them were detected in CO. Some of the main conclusions drawn from these studies are that in general, the gas reservoirs of SMGs are quite large, with a mean value of (5.3 ± 1.0)×10^{10} $M_{\odot}$. From the average linewidths, i.e., 510 ± 80 km s^{-1}, dynamical masses were estimated to be (7.1 ± 1.0) × 10^{10} $R_{\rm kpc}$ $M_{\odot}$ in case the morphology of SMGs is spheroid-like or (1.6 ± 0.3) × 10^{10} $R_{\rm kpc}$ $M_{\odot}$ in case the morphology is disk-like.

Morphology. The morphology study of (sub)mm galaxies requires high resolution observations, i.e., << 1 arcsec. At z∼ 0.3, 1 arcsec translates into a physical scale of ∼ 4 kpc, while at $z > 1$ scales smaller than ∼ 8 kpc are unresolved. For this reason, high optical resolution imaging or interferometric observations in the millimeter or radio are required. Tacconi et al. (2008); Bothwell et al. (2010); Engel et al. (2010) carried out high angular resolution CO observations of SMGs at submillimeter wavelengths and find relatively large and extended gas reservoirs, i.e., ∼ 2 kpc, when compared to local ULIRGs. However, these size measurements should be considered as lower limits. At a typical redshift $z \sim 2$ of a SMG, the rest-frequencies of the observed lines are in the frequency range 300-900 GHz, where only high CO transition lines can be found. These high transitions need a more excited medium than the ground transition CO(1-0) at a rest-frequency of 150 GHz [1]. Instead of using (sub)mm interferometric observations, Swinbank et al. (2010) carried out morphological studies of SMGs at optical and near infrared wavelengths with the *Hubble* Space Telescope (HST), using ACS and NICMOS cameras. They targeted a subsample of 25 galaxies from the Chapman et al. (2005) spectroscopically confirmed sample of SMGs. They measure characteristic sizes of $\mathrm{r_i} = 2.3 \pm 0.3$ kpc and $\mathrm{r_H} = 2.8 \pm 0.4$ kpc, at the i and H bands, respectively. Moreover, the calculation of the Sersic index indicated that the morphology of these galaxies was in better agreement with spheroidal or elliptical light distributions than exponential distributions (typical of disc galaxies).

The discussion of morphology and size of SMGs is still an open debate. This can be seen from a more recent study of Targett et al. (2013), where they targeted with the WFC3/IR on the HST a subsample of 24 SMGs drawn from the Extended Chandra Deep Field South (ECDFS; Weiß et al. 2009). They report sizes of ~ 4 kpc and disk-like morphologies, concluding that only a fraction < 0.25 of submillimeter sources in the GOODS-South Field could be regarded as involved in a merger event. This is an opposite view to several studies which argue that SMGs are spheroid systems that are experimenting a merger event.

Halo Mass. CO observations have suggested that SMGs have large dynamical masses, $> 10^{11}\ M_{\odot}$, although not nearly as large as the halo masses where they reside based on their clustering properties (Blain et al. 2004)[2]
Recently, Hickox et al. (2012) have re-analyzed the clustering properties of 50 SMGs observed with LABOCA in the ECDFS, where spectroscopic (if available) and photometric redshift information is added to the projected position of the galaxies in the sky. They obtain the tightest constraint to date on the clustering amplitude of SMGs and calculate typical dark matter halo masses for this sample of $10^{12.8^{+0.3}_{-0.5}}\ h^{-1}\ M_{\odot}$. Based on evolutionary models of dark matter mass haloes (Fakhouri et al. 2010), an halo mass of this magnitude implies that a typical SMG at $z = 2$ would end up at $z = 0$ as a massive elliptical galaxy ($\sim 2 - 3L^{*}$) residing in moderate- to high- mass groups, i.e., $10^{13.3^{+0.3}_{-0.5}}$ $h^{-1}\ M_{\odot}$ Other studies have focused at single systems and have calculated their individual dark matter haloes, arriving at different conclusions though. Daddi et al. (2009b) in a serendipitous discovery detected molecular gas CO emission lines towards GN20, one of the brightest unlensed galaxies detected to date in the GOODS-N Field (Pope et al. 2006). Around GN20 a significant $z = 4.05$ redshift spike is detected with a strong spatial overdensity of B-band dropouts and IRAC selected $z > 3.5$ selected galaxies. With the assumption of a luminosity-mass ratio of 50 (Lin et al. 2003) and also considering incompleteness, the halo mass of this proto-cluster is $\sim 10^{14}\ M_{\odot}$. However, Chapman et al. (2009) studying an overdensity of SMGs at $z = 1.99$ concludes that SMGs are not necessarily tracing the most massive dark matter haloes. This does not exclude the possibility that some of SMGs are the progenitors of rich clusters, however if all of the SMGs are associated to rich clusters, there is a factor of 10 less rich clusters than expected from the observed density of SMGs.

---

[1] Typically, CO observations are carried out in the wavelength range 1 to 3 mm (100 to 300 GHz), although lower transitions can be observed with radio astronomical facilities, e.g., JVLA.

[2] For a better understanding on how dark matter halo masses can be inferred from clustering measurements the reader is referred to Hickox et al. (2011)

Stellar Mass. It is accepted that SMGs are very massive with stellar masses in the range few$\times 10^{10}$ to few$\times$ $10^{11} M_{\odot}$, however, the measurements have probed to be uncertain. For the same sample of 76 SMGs Michałowski et al. (2010) and Hainline et al. (2011) obtain $3.5 \times 10^{11} M_{\odot}$ and $7 \pm 3 \times 10^{10} M_{\odot}$, respectively. Both studies use SED fitting in order to derive the stellar masses. The underlying explanation for these discrepancies are the different assumptions for some key components in the build up of stars in galaxies such as the initial stellar mass function (IMF); star formation history, i.e., quiescent, burst mode; single stellar population models (SSP), etc. More recent results are presented by Wiklind et al. (2014), who studied a subsample of 10 SMGs drawn from a sample originally observed with the LABOCA bolometer in the GOODS-South field and subsequently targeted for 870 μm continuum observations with ALMA. They get a median stellar mass of $M_{\star} \approx 9 \times 10^{10}$ $M_{\odot}$. However, in their sample two of the galaxies have stellar masses 2 or 3 order of magnitude smaller than the rest of the sample. Excluding these galaxies implies a median stellar mass of $\sim 1 \times 10^{11}$ $M_{\odot}$

Depletion time. The ratio of gas mass over star formation rate defines the depletion time, which is the timescale of the burst, i.e., the time in which the galaxy will consume the available gas to produce stars. Given the monstrous star formation rates of SMGs, in the range of 100 to 1000 $M_{\odot}$/yr, the depletions times are typically very short $\sim$ 40–200 Myr. In order to calculate this value, on one hand the infrared luminosity (8–1000 μm), $L_{\rm IR}$, is assessed. This quantity can be directly related to a star formation rate (Kennicutt, Jr. 1998). On the other hand, gas masses can be computed from direct observations of CO (Greve et al. 2005; Bothwell et al. 2013).

1.4 Evolution of submillimeter sources

Since ULIRGS were the only objects in the local Universe with infrared luminosities comparable to SMGs, i.e., $L_{\rm IR} > 10^{12}$ $M_{\odot}$, it was natural to propose the hypothesis that SMGs were the high-z cousins of ULIRGS. One of the main characteristics of ULIRGS is that nearly all of them are interacting merger systems (Sanders et al. 1988; Sanders & Mirabel 1996). There are strong indications, that this is also the case for SMGs. Greve et al. (2005) found that most of the CO observations of SMGs galaxies had double peak profiles which is an indication, that SMGs, are either merger systems or disk rotating disks. Later on, sub-arcsec resolution observations for a sample of 12 SMGs presented by Engel et al. (2010) showed that most of submillimeter galaxies are indeed major mergers. This view has been confirmed for other SMG samples by Bothwell et al. (2010) and Alaghband-Zadeh et al. (2012). Another characteristic that has been found in ULIRGs is that there is evidence that AGN contribution increases as the galaxies become more luminous in the far-infrared, i.e. $\log(L_{\rm IR} > 12.5)$ $M_{\odot}$ year^{-1} (Sanders 1999). However, in the specific case of SMGs, Johnson et al. (2013) and Wang et al. (2013) found evidence for AGN activity in only $\sim$ 15% of their samples. Alexander et al. (2005) using a radio-selected SMG sample, identify that $\sim$ 75% of their SMGs hosted AGN activity, however they conclude that the bolometric luminosity is still dominated by the star formation activity. A popular explanation for the relation between SMGs and AGNs is an evolutionary sequence, where SMGs evolve into QSOs. (Chapman et al. 2005), shows further evidence that supports this scenario finding a similar redshift distribution for SMGs and QSOs. In this evolution-

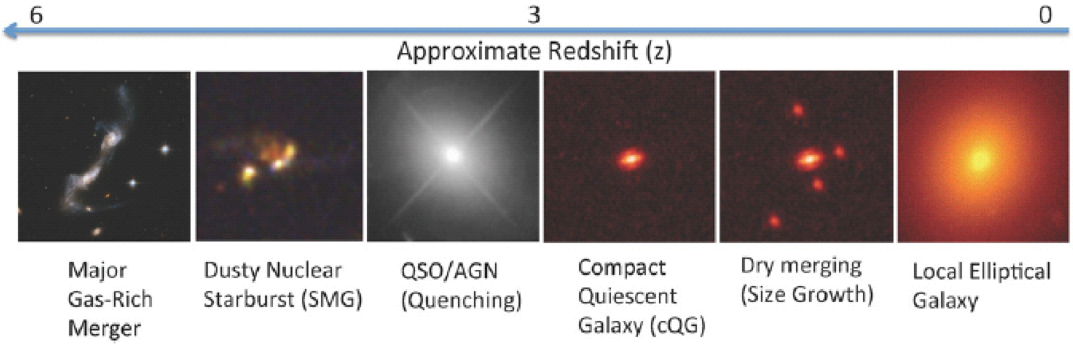

Figure 1.6: Illustration of the evolution of a SMG galaxy from Toft et al. (2014). First, gas rich major mergers in the early Universe, i.e., z >3, trigger a starburst (SMG stage) which last a short time ($\sim$ 50 Myr), followed by a quenching of the star formation due to the ignition of an AGN. The next 1 Gyr, it evolves passively into a compact quiescent galaxy at z ~2. The growth of the galaxy continues gradually, mainly through minor mergers, and becomes one of the local elliptical galaxies.

ary scenario, a SMG would end its life as a massive elliptical galaxy. These galaxies are very massive with stellar masses $M_\star > 10^{11}$ $M_\odot$. Unlike SMGs, elliptical galaxies have no star formation, their morphology is spheroidal, and have red color as a consequence of the old stellar population content. Before the discovery of SMGs, astronomers were puzzled about how these red dead galaxies became so massive. At that time, the most famous high-z population were the LBGs, but given its "modest" star formation rates ,i.e., <50 $M_\odot$year^{-1}, which fell an order of magnitude short of the ~1000 $M_\odot$ year^{-1} required to form the stars in the most massive elliptical on a timescale of < 1 Gyr. For this reason, since the discovery of SMGs, they were suspected to be the progenitors of massive elliptical galaxies, at low and high redshift. In fact, a recent study by Fu et al. (2013) present observations of a submillimeter source at $z = 2.3$ which has been followed up at high resolution at wavelengths ranging from optical to radio. The original submillimeter source is resolved in an interacting pair of galaxies which are about to merge. The involved masses in the merging and the high star formation rates ($\sim$ 2000 $M_\odot$ year^{-1}) are large enough for the formation of one of the most massive elliptical galaxies at $z \approx 1.5$. Putting all these pieces of information together, the most popular scenario for the connection between all these components is an evolutionary sequence where at first two galaxies merger and trigger a massive cool starburst (Sanders et al. 1988; Fabian 1999; Lipari et al. 2003; Fu et al. 2013; Toft et al. 2014). The new galaxy starts to warm as a QSO turns on inside, which is also responsible of removing the gas and dust from the galaxy, hence quenching all star-formation processes and the QSO becoming optically bright. Finally, the galaxy reach it ultimate state as a final massive elliptical galaxy (see Fig. 1.6).

1.5 Implications for galaxy formation models

A full understanding of the Universe and its evolution requires the capacity to model it. With this aim, cosmological N-body simulations describe the evolution of dark matter through gravitational interactions. As an output from these simulations we have the so-called merger trees, which can be traced from redshift 0 up to $z \sim 50$. Semi-analytical simulations (SAM) use this information to trace the behavior of baryonic particles ap-

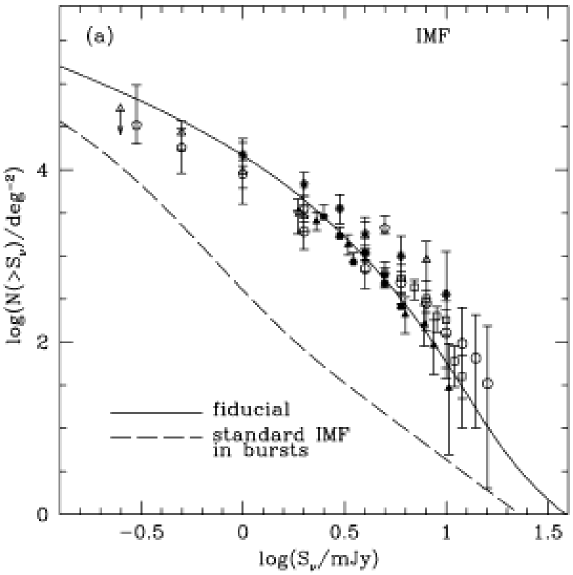

Figure 1.7: The source counts at 850 μm as obtained from a semi-analytical model. The dashed line show the prediction from a fiducial model with a standard initial mass function (IMF) for all the galaxies. This demonstrate the difficulty that semi-analytical models have in order to reproduce the (sub)millimeter source counts. The solid line assumes a flat IMF for straburst galaxies, which is in a good agreement with the observations. Credits: Baugh et al. (2005)

plying simple physical formalism which describe processes like gas cooling, feedback, star formation, etc. The information of the merger trees is crucial, as analytic descriptions of the physical processes are dependent on galaxy environment.

It turns out that the submillimeter (submm) sources, whose contribution to the total bolometric luminosity of the local Universe is rather small, at high redshift have a contribution which is similar to what is estimated for Lyman Break galaxies. The brightest submm sources, besides their spectacular star formation rates, large gas and stellar masses, became a real problem for semi-analytical models (see Fig. 1.7), which struggle to reproduce the number of submm sources, especially at the bright end. Baugh et al. (2005) coupled a spectrophotometric code, GRASIL (Silva et al. 1998), to a semi-analytical model. The output of the model, i.e., cold gas mass, hot gas mass, star formation rate, age, etc., was given as an input to GRASIL, which made a self-consistent treatment of the radiative transfer process including dust, hence obtaining SEDs for simulated galaxies covering the electromagnetic spectrum from ultraviolet to radio wavelengths. With this procedure, the source counts at 850 μm underpredicted the observed number of galaxies at the bright end. To solve the discrepancy between the models and the observed submillimeter counts, Baugh et al. (2005) adopted a flat initial mass function (IMF) for starburst galaxies. This means that the submillimeter flux could be produced without the need of huge star formation rates. In this way not only the submillimeter galaxy luminosity function was fitted but also the luminosity of Lyman Break galaxies was reproduced. An enigma with this scenario is that only a small fraction of the stellar mass in evolved elliptical galaxies in the local Universe would be made up of stars formed during these burst episodes. However, the need of a flat IMF to reproduce the SMG luminosity function has been challenged by Hayward et al. (2012), who combining high-resolution 3D hydrodynamic simulations of isolated and merging massive, gas-rich galaxies with a radiative transfer code,i.e., SUNRISE (Jonsson 2006), produce the SED of simulated galaxies. In order to predict the SMG number counts from their model, they combine the submm lightcurves obtained from the simulations, with a semi-empirical merger rate model (Hopkins et al. 2010). Using a standard IMF (Kroupa 2001) they are able to reproduce the observed submm counts, without the need of modifying the IMF. They conclude that the difficulty of semi-analytical models to reproduce the observed submm counts is not an intrinsic problem related to SMGs but rather is indicative of problems related to the underprediction of abundance of massive galaxies or a star formation rate and stellar mass relation normalization lower than that observed.

Given that there is still controversy about how high submillimeter fluxes can be achieved in these models some authors have preferred to ignore, for the moment, the mechanisms which lead to high submillimeter fluxes and instead study the properties of the galaxies that are likely to be submillimeter galaxies. This is the case of Davé et al. (2010), they use a cosmological hydrodynamic simulation and sort the simulated galaxies according to their star formation rate. From this sorted list they set a threshold in star formation rate such that the number of galaxies match the observed density of submillimeter galaxies. The SMGs identified in this way have stellar masses of $M_\star \sim 10^{11-11.7}$ $M_\odot$, and SFRs of $\sim$ 180–500 $M_\odot \mathrm{yr}^{-1}$. At z=2, they live in $\sim 10^{13}$ $M_\odot$ haloes, and by z=0 they mostly end up as brightest group galaxies in $\sim 10^{14}$ $M_\odot$ haloes. However, associating SMGs to galaxies with the highest star formation rates in the model might not be correct. More recent studies like the one from Hayward et al. (2012) found that actually the submm flux is better described by a combination of star formation and dust mass. **In Muñoz Arancibia et al. (2015), using a semi-analytical model (Cora 2006; Lagos et al. 2008; Tecce et al. 2010) we follow a similar approach as Davé et al. (2010), however, instead of sorting galaxies only by star formation rate, we also sort the galaxies according to other suitable proxies, i.e., stellar mass, dust mass, depletion time, etc. The conclusion from this study is that the proxy which match best the observed properties of submillimeter galaxies is a linear combination of star formation rate and dust mass, which is in line with what is found by Hayward et al. (2012).**

1.6 Bulk of the population dominating the cosmic star formation rate density

Star formation tracers are available at different wavelengths, and among them, (sub)millimeter wavelengths have the advantage that they do not suffer from dust obscuration, and that also they have a flat selection function over a large redshift range. The most important assumption here corresponds to accept the FIR luminosity as powered from star formation. As we already discussed, studies investigating whether the AGNs or rather starbursts (show references in Lonsdale 2006) are the origin of the FIR emission of submillimeter galaxies, tend to favor an scenario where a coeval of AGNs and starbursts is present, being the starburst the main contributor to the FIR emission.

SMGs are galaxies with enormous SFRs and very massive, i.e., $M_\odot \gtrsim 10^{10}$, however they trace only the bright end of the IR luminosity function. Star forming galaxies that dominate the star formation rate density of the Universe (SFRD) have much lower star formation rates, i.e. SFR $\lesssim 10 M_\odot$/year. Unfortunately, these galaxies are undetectable with current submillimeter surveys, where the access is mainly restricted to galaxies brighter than 4 mJy at 850 μm. The only exception being surveys targeted towards galaxy clusters, which take advantage of the lensing effect (Knudsen et al. 2008; Johansson et al. 2011).

In order to detect an average submillimeter signal from these galaxies, sensitivities as low as 0.1 mJy/beam at 850 μm have to be reached. With submillimeter single dish telescopes this sensitivity is not possible as the confusion noise is greater than this level. Submillimeter interferometers, e.g., ALMA, PdBI, are the natural answer to reach deeper sensitivities, however they are not suitable for large area surveys. In fact, with ALMA to cover a field of 100 arcmin^2 would take $\sim$ 500 hours to reach a sensitivity of $\sim$ 0.1 mJy. A suitable technique that helps to alleviate this problem is the stacking technique (see Chapter 4 for a detailed explanation of this technique.), which at the expense of individual information for each galaxy, push down the sensitivity of the original image by doing cutouts centered on the galaxies of interest and subsequently averaging those cutouts. In this way the average properties of specific galaxy populations can be studied.

In this thesis we stack different color selected populations, which are more representative of the bulk of the galaxy population at different redshifts. We do this in the framework of the LABOCA-COSMOS data one of the largest contiguous field observed to date at 850 μm, i.e., $\sim$ 0.75 deg^2. Covering such a large field implies that we stack $\sim$ 50000 sources, compared to $\sim$ 1000 or less from similar studies (Greve et al. 2010; Decarli et al. 2014).

1.7 Far-infrared radio correlation

The Far-Infrared radio correlation (FIRRC) is one of the tightest correlations known to date. It holds over many order of magnitudes in flux and is found in many different environments as well (see Fig. 1.4).

It has been largely known that the Far Infrared (FIR) and radio signals of star-forming galaxies are correlated (van der Kruit 1973; Helou et al. 1985). This correlation usually is attributed to the UV radiation emitted from massive short-lived stars (OB type), which is reprocessed by dust grains and finally re-emitted in the FIR regime. These same stars will end their lives as Type II supernovae remnants, where relativistic charged particles will move in a spiral trajectory on the present magnetic field, producing synchrotron radiation observed in the radio regime. The connection between these two processes is reflected in the FIRRC. Although the explanation given above is reasonable, detailed calculations of the correlation face many problems and the mechanisms driving it are not fully understood yet. The current problems in the FIRRC can be separated into two branches. i) *Mechanisms.* In the literature different physical mechanisms are discussed in order to explain the FIRRC. One of the first theories developed to explain the FIRRC was the calorimeter theory proposed by Voelk (1989) and since then many other theories have been proposed (Helou & Bicay 1993; Niklas & Beck 1997). ii) *Evolution.* Besides the responsible mechanism of the FIRRC it is necessary to check a possible evolution of it as we observe the universe back in time. In Murphy (2009), it is predicted that given the different environmental conditions of the Universe at high redshift, especially the rapid increase of the CMB energy density, i.e., $\sim (1+z)^4$, which suppresses the energy losses to synchrotron radiation (radio regime) , the FIRRC would be expected to increase with redshift. However, Lacki et al. (2010) by using one-zone steady-state models of cosmic ray (CR) injection, cooling, and escape over the redshift interval $0 \leq z \leq 10$ show that the strength of inverse Compton (IC) losses off the cosmic microwave background (CMB), which suppresses the nonthermal radio emission of galaxies depends strongly on the gas surface density (Σ_g^a) and scale height(h) of the galaxies. Thus, compact starbursts (h ∼ 100 pc) show little evolution out to very high redshift, i.e., $z \sim 5{-}{-}10$, because IC losses of the CMB must compete against other losses process, e.g., bremsstrahlung, ionization, and IC off starlight. In normal galaxies these other processes are not significant and the CMB becomes effective in diminishing the radio emission, so the net effect in the FIRRC is an increase with redshift. As an example, the radio emission of Milky Way−like galaxies should be severely diminished by $z \sim 2$. The special case of submillimeter galaxies (SMGs) corresponding to starburst galaxies but with a larger scale height than compact starbursts (h ∼ 1 kpc) show that they are radio bright galaxies in comparison to galaxies that lie on the FIRRC (Kovacs et al. 2006; Murphy 2009). This could be explained in the case that the magnetic field scales as $B \propto \Sigma_g^a$ (Lacki et al. 2010).

From the observational point of view, the FIRRC has been mainly analyzed in two different ways: i) *Individual detections.* The most extended studies using individual detections have been carried out are either IR or radio selected samples. As shown by Sargent et al. (2010), differently selected samples could lead to biased conclusions. Sargent et al. (2010) investigate the largest sample of individual detections to date by using data from the COSMOS field. The study has been done on IR, radio, and a joint radio−−IR selected samples in order to study the selection biases inherent to each sample. The main conclusions are: a) discrepant results found in the literature can be explained by properly accounting for the selection band of the respective studied sample. b) No evolution of the FIRRC up to high redshift. ii)*Stacking analysis.* Analyzing the FIRRC at high redshift by using individual detections give us insight into only the most extreme galaxies at high redshifts, the stacking analysis allows us to investigate the underlying population, i.e., sources which cannot be detected given the limited sensitivity of the astronomical instruments. It could perfectly be that we have been missing any evolution of the FIRRC because we have not had access to normal galaxies in the high redshift universe. Four studies (Boyle et al. 2007; Beswick et al. 2008; Garn & Alexander 2009; Ivison et al. 2010) have analyzed the stacking of 24 μm detected sources in 1.4 GHz maps and one study (Bourne et al. 2011) has analyzed the stacking of 3.6 μm and 4.5 μm detected sources on MIPS (24 μm, 70 μm, 160 μm), 610 MHz, and 1.4 GHz maps. The main conclusion of all these studies is that the FIRRC extends to μJy radio flux levels and that does not evolve with redshift (however see also Ivison et al. (2010)).

In this thesis, we stack the LABOCA 870 μm data and the VLA 1.4 GHz data available in the COSMOS field, in order to analyze the FIRRC of different color selected populations as a function of redshift.

1.8 Outline of the thesis

The Cosmic Evolution Survey is an equatorial 2 deg^2 field and it has been observed over most of the electromagnetic spectrum, from gamma rays to radio. It is an ideal field to carry out the observations of large samples of galaxies at submillimeter wavelengths and study their relation with the counterparts found at other wavelengths. The large area reduces the cosmic variance that could be introduced by observing smaller areas and also allows to study the relation of submillimeter galaxies to the cosmic large scale structure. This was the initial motivation of this thesis, whose structure is presented in the following.

The LABOCA COSMOS Survey (COSLA) is presented in Chapter 2, where the observations, data reduction, and the source catalog are discussed. The submillimeter source counts derived with the so-called P(D) analysis and the redshift distribution are also shown.

In Chapter 3 an interferometric, high-resolution follow-up of a sub-sample of sources from the COSLA survey is carried out with the Plateau de Bure Interferometer. The aim of this study is to unambiguously determine the position of the submillimeter sources. Precise positions and the wealth of multiwavelength information available in the COSMOS field allow us to determine accurate photometric redshifts, and compare the resulting redshift distribution with previous studies.

In Chapters 4 we present the stacking method which allow us to study in the submillimeter galaxies with star formation rates more moderate than those of the actual detected sources. In specific for submillimeter single dish maps, a recent stacking algorithm presented by Kurczynski & Gawiser (2010) is implemented in IDL. We extensively tested it in different environments and also study its behavior in non-uniform maps.

In Chapter 5 we apply the stacking technique to the COSLA survey data. Different known optical color selected populations are stacked. We study their submillimeter flux density as a function of magnitude, stellar mass, and also redshift. The results are compared with previous stacking studies which have been carried out in smaller areas. The VLA 1.4 GHz available in the field is also stacked in order to study the far infrared radio correlation of the different color selected populations as a function of redshift.

The multiwavelength cutouts for the submillimeter sources presented in the catalog in Chapter 2 are shown in Appendix A.
Appendix B discusses the point spread function of the LABOCA map and how to optimize the simulations presented in Chapter 2.

Some studies where the author of this thesis was deeply involved are not presented in this work, but sometimes are referenced when contextually appropriate. This is the case for the study at high resolution of 3 submillimeter galaxies studied with the Combined Array for Research (CARMA) presented in Smolčić et al. (2012b). The paper Muñoz Arancibia et al. (2015) study the properties of submillimeter galaxies in a semi-analytical model, where all the simulation machinery developed in Chapter 2 is used to turn the model catalogs in realistic submillimeter maps.

2

The COSLA source catalog

In this chapter we introduce the LABOCA-COSMOS survey, which is the main driver of this thesis. This is the largest contiguous survey at 870 μm, i.e., 0.75 deg^2, which reach a depth of 1.68 mJy/beam at the center. 39 detected sources with a signal-to-nose ratio (S/N) > 3.8 are detected. Using simulated maps, we test the reliability of our extracted sources and also compute quantities such as the positional uncertainty, and completeness. The source counts and the redshift distribution are also reported.

2.1 Multi-wavelength surveys in the Cosmic Evolution Survey

The Cosmic Evolution Survey (COSMOS; Scoville et al. 2007) is a panchromatic imaging and spectroscopic survey of an equatorial 2 square degree field designed to probe the formation and evolution of galaxies and supermassive black holes as a function of cosmic time and large scale structure environment. To date the field has been observed with the most major space- and ground-based telescopes over nearly the full electromagnetic spectrum reaching high sensitivities. It includes very deep broad-band (u*BVgrizYJHK) and medium/narrow-band photometry in more than 30 bands, GALEX, deep Spitzer IRAC/MIPS, Herschel PACS/SPIRE and HST/ACS high-resolution imaging, XMM-Newton and Chandra X-ray observations, 200, 320, 600, and 1400 MHz VLA, and GMRT radio observations, as well as more than 25,000 optical spectra (Capak et al. 2007; Sanders et al. 2007; Scoville et al. 2007; Leauthaud et al. 2007; Hasinger et al. 2007; Zamojski et al. 2007; Taniguchi et al. 2007; Trump et al. 2007; Lillly et al. 2007; Lilly et al. 2009; Frayer et al. 2009; Le Floc'h et al. 2009; Elvis et al. 2009; McCracken et al. 2010; Schinnerer et al. 2004, 2007, 2010; Smolčić et al. 2012a). Various parts of the field, from 0.11 to 0.72 square degrees in area, were mapped at millimeter wavelengths (using MAMBO, BOLOCAM and AzTEC bolometers; Bertoldi et al. 2007; Aguirre et al. in prep; Scott et al. 2008; Aretxaga et al. 2011).

In the wavelength range $800 \leq \lambda \leq 1000$ μm, up to now ~ 400 arcmin^2 have been mapped with the SCUBA-2 bolometer on the James Clerk Maxwell Telescope (JCMT) at 850 μm (Casey et al. 2013). Here we present an 870 μm survey of the inner 0.75 deg^2 (2698 arcmin^2) of the COSMOS field with LABOCA at the APEX Telescope (COSLA). The mapped area matches that of the AzTEC/ASTE COSMOS 1.1 mm survey, forming to date the largest contiguous field observed at both millimeter and submillimeter wavelengths. Although the millimeter (1.1-1.2 mm) and submillimeter (870 μm) bands are very close in wavelength-space, they may trace different populations of galaxies (Greve et al. 2004; Younger et al. 2007; Greve et al. 2008; Younger et al. 2009; Smolčić et al. 2012a). This raises the need for independent (sub)millimeter wavelength observations.

At shorter wavelengths, the field has been extensively covered at 100, 160, 250, 300, and 500 μm with *Herschel*. Most of these observations cover an area larger than what has been observed so far at $\lambda > 800$ μm. However, it has been shown that while observations at 24 μm resolve 55-95% of the Cosmic Infrared Background (CIRB) at 70-500 μm (Devlin et al. 2009; Chary & Pope 2010), they only are able to resolve ~ 30 % CIRB at $\lambda = 1$ mm (Scott et al. 2010; Penner et al. 2011). This stress the importance of studying the extragalactic universe at $\lambda > 800$ μm.

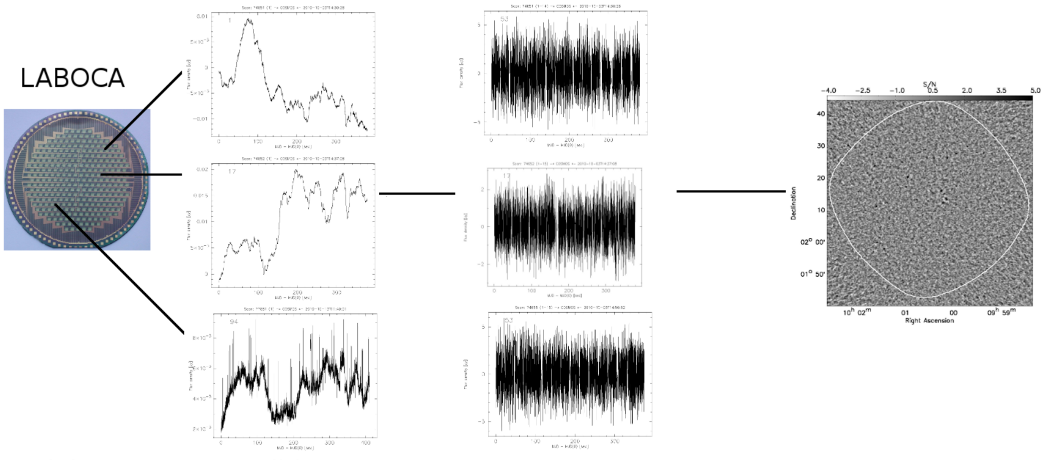

(a) (b) (c) (d)

Figure 2.1: General description of the data reduction with the BoA software. **(a):** The Large Apex BOlometer CAmera. Each light-green square is a bolometer (channel). **(b):** Three examples of raw time series from three different bolometers. **(c):** Same raw time series after being reduced with BoA (see text for more details) **(d):** From the reduced raw time series a map is finally computed.

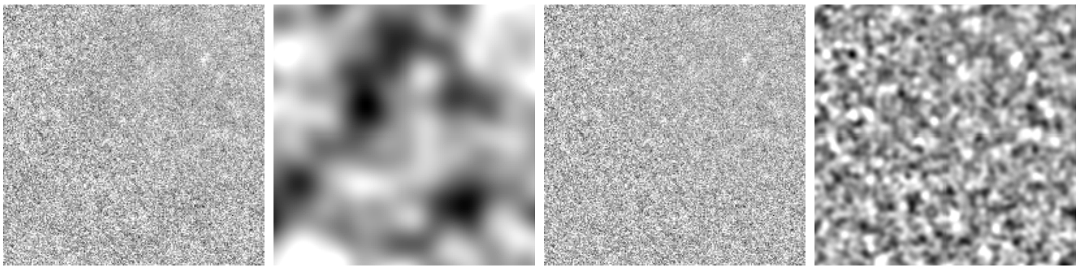
(a) (b) (c) (d)

Figure 2.2: **(a):** The image obtained after the reduction with the BoA software. **(b):** The same image smoothed to 92″. **(c):** Image (b) is subtracted from image (a) in order to remove the large scale structure present in the image. **(d):** image (c) is optimally filtered with the LABOCA beam. The final resolution of this image is 27.″6.

2.2 Description of the observations of the COSMOS field with LABOCA

The observations were carried out with the Large APEX Bolometer Camera (LABOCA; Siringo et al. 2009) at the Atacama Pathfinder Experiment (APEX; Güsten et al. 2006) on Cerro Chajnantor in Chile in November 2007, May and September to December 2008, May 2009, and October 2010. A total of 81.3 hours integration time was acquired, shared between ESO (53 %), MPIfR (35 %) and Chilean (12 %) allocations, resulting in 520 individual maps (scans).
LABOCA is composed of 295 bolometers (channels) with an average noise-equivalent flux density (NEFD) of 55 mJy $s^{1/2}$, a field of view of 11.′4 and a bandwidth of ∼60 GHz (∼150 μm) around the central frequency of 345 GHz (870 μm). The beam shape is close to a circular Gaussian with a full width at half maximum (FWHM) of $19.''5 \pm 0.''4$ and an effective beam area of 521 arcsec^2 as determined from observations of Uranus.

Mapping was performed in spiral raster mode as well as on-the-fly mode. The observing strategy was such that first the region of the preceding MAMBO2 map (Bertoldi et al. 2007) was observed and then data was subsequently added to increase the covered field size, resulting in a rms distribution which reaches 1.68 mJy in the center of the map and increases toward the outskirts (see Sec. 2.4).

Focus settings were determined from observations of planets during sunset, sunrise and at least twice per night. The pointing was checked on strong continuum sources (mainly the quasar J090910.09+012135.6) close to the COSMOS field about every hour and was found to be stable within 3″ rms. Correction for atmospheric attenuation was enabled through determinations of the zenith opacity via skydips about every two hours and more frequently in unstable weather conditions. Absolute flux calibration was achieved through observations of Mars, Uranus and Neptune as well as a set of secondary calibrators and was found to be accurate within 10% rms, which is in accordance with the value given by Siringo et al. (2009). Albrecht et al. (in prep.) compared the flux calibration methods for LABOCA and Herschel/SPIRE to ensure a correct cross-calibration and the usage of LABOCA data in multi-wavelength studies. They obtain on average 2% lower flux densities from the LABOCA calibration compared to the SPIRE method.

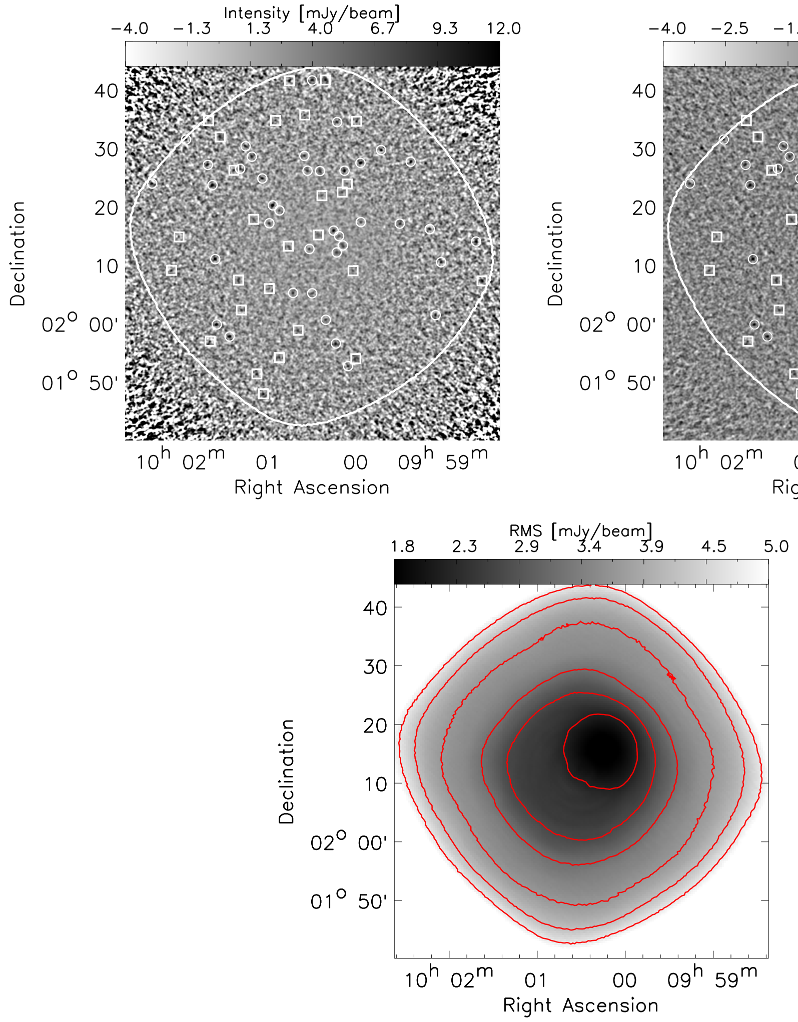

Figure 2.3: Intensity, signal-to-noise, and RMS maps of the COSMOS field at a resolution of 27″. **Upper left panel:** LABOCA intensity map of the COSMOS field. The white circles mark sources detected above a signal-to-noise threshold of 3.8 at a resolution of 27″6, while the white squares correspond to sources detected above the same threshold but at other resolutions. The white contour indicates the 4.68 mJy/beam noise level. **Upper right panel:** The same as in the left panel, but this time the intensity image is replaced by the signal-to-noise image. **Lower panel:** RMS map, which has been scaled in order to take into account the confusion noise as described in the text. Overlaid are the contour levels starting from 1.68 mJy/beam and increasing in steps of 0.5 mJy/beam. The outermost contour level depicts the 4.68 mJy/beam level, which confines the region where we applied source extraction.

2.3 Data reduction

The data were reduced using the BoA[1] software package (Schuller 2012). A simple scheme of the reduction is shown in Fig. 2.1. The processing of the raw time series, i.e. the time-ordered data stream (down-sampled to 25 Hz) of each channel and scan, consists of the following steps: calibration correction by applying a linearly interpolated calibration factor; opacity correction by applying the linearly interpolated opacity at the elevation of

---

[1] http://www.astro.uni-bonn.de/boawiki/Boa

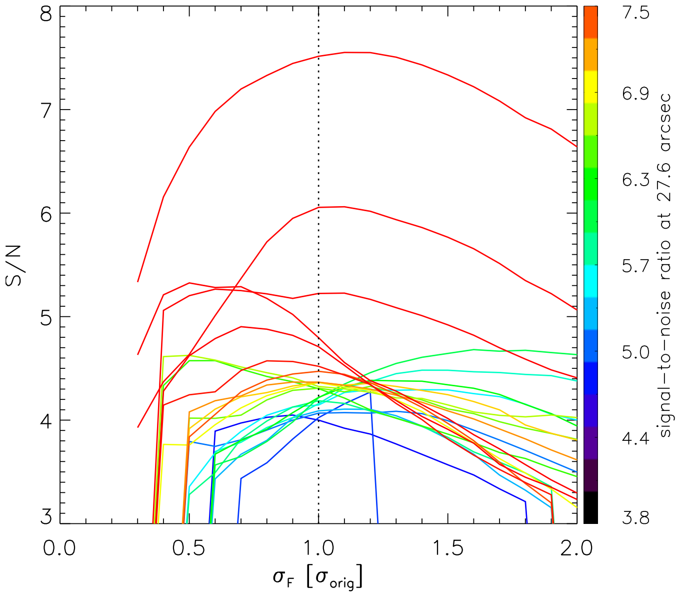

Figure 2.4: Empirical S/N for all the sources that are detected in the beam-smoothed map at a level of S/N $\geq$4, as a function of the width of the Gaussian with which the image is smoothed, i.e., σ_F. The color code indicates the S/N corresponding to each curve. A vertical line at $\sigma_F = \sigma_{orig}$, where the theoretical maximum S/N should be reached, is shown for reference.

the scan; correction for temperature drifts due to the cryosystem using two bolometers that have been sealed to block the sky signal for this purpose; flat fielding by applying the relative bolometer gains (determined from beam maps of planets); conversion from counts to Jansky; flagging of bad channels. In addition to the known dead or noisy channels, bad channels are identified as those having an rms of their time series a given ratio r higher or $1/r$ lower than the median rms of all channels. Additional bad channels, which escaped the automated detection, were identified by surveying the time streams of all scans of the remaining channels.

The data reduction applies (in part repeatedly) the following tasks: correlated noise removal on the full array; correlated noise removal on groups sharing (a) the same amplifier box and (b) the same wiring; baseline subtraction; despiking; low-frequency filtering in the Fourier domain applied to frequencies below 0.5 Hz; flagging of data outside suitable telescope scanning velocity and/or acceleration limits; flagging of bad channels. Each reduced scan (i.e. raster pattern or rectangular map) is then gridded into a weighted intensity map with a pixel size of $4'' \times 4''$ and a corresponding weight map. The weights of the data points contributing to a certain pixel of the intensity map were determined as $1/\sigma_{\mathrm{ts}}^2$, where σ_{ts} denotes the rms of the reduced time series of the corresponding channel and subscan. Individual maps were then co-added, again noise-weighted, to build the final intensity map and the corresponding weight map, which in turn allows to retrieve the rms for each pixel and to construct a signal-to-noise ratio (S/N) map.

In a first step a map is produced by a "blind" execution of the reduction as described above. The resulting signal-to-noise ratio map is then used to mask the areas of apparent source emission in the second iteration. For this we extract from the signal-to-noise ratio map at a resolution of $27.''6$ (i.e. beam-smoothed, see below) all pixels with a signal-to-noise ratio $\geq 3\sigma$, where σ is the rms of the map. This mask is then converted into a time series for each bolometer channel and the corresponding data points are excluded from the determination of the correlated sky noise and of the baselines.

To remove the large-scale structures originating from low-frequency noise artifacts we

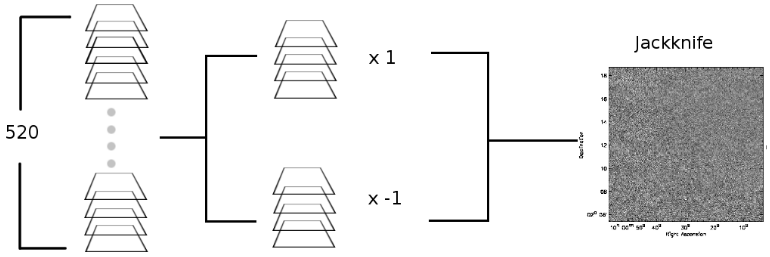

Figure 2.5: Schematic diagram of the construction of a noise map. The 520 individual scans obtained with LABOCA are randomly split in two halves. One half remains unchanged, while the other half is inverted, i.e., multiplied by -1. They are co-added in order to get the so-called jackknife map, which is a pure noise map as all signal information has been removed in the process.

have convolved the map resulting from the second iteration with a Gaussian kernel of $90''$ (FWHM) and subtracted it from the original map. The convolution is integral normalized, i.e. preserving the total signal of the map by using a kernel with integrated volume equal to one. This process leads to a decrease of the source fluxes by a factor of 0.92, which we determined by applying the same process to a simulated point source of FWHM=$19\farcs5$ (see Appendix A).

Finally, to optimally filter the high frequencies for point sources, the map is beam smoothed, i.e. convolved with its own PSF of $\sigma_{\rm orig} = 19\farcs5$ (FWHM). The convolution is peak normalized, i.e. preserving the peak signal of point sources by using a kernel with a peak value of one. This approach is derived by Ivison et al. (2007) to maximize the peak signal-to-noise ratio of point sources in the presence of white noise that is not independent from pixel to pixel due to smoothing. This process is illustrated in Fig. 2.2.

The final map, for the LABOCA COSMOS field, obtained after the reduction is presented in Fig. 2.3.

To investigate whether the approach of the optimal filtering is applicable to our data, we determined the signal-to-noise ratio of the sources having signal-to-noise ratios ≥ 4 in the beam-smoothed map, for different widths (FWHM) of the Gaussian smoothing kernel, i.e., $\sigma_{\rm F}$, varying between 0.1 $\sigma_{\rm orig}$ and 2 $\sigma_{\rm orig}$. This method is valid as the LABOCA beam is close to a Gaussian. The results are shown in Fig. 2.4. For the two sources with the highest signal-to-noise ratio we find a close agreement with the shape of the theoretical curve. However, for the remaining sources the optimal smoothing, i.e. the resolution at which the signal-to-noise ratio adopts its maximum, varies. Sources showing an increasing signal-to-noise ratio with increasing $\sigma_{\rm F}$ can be explained by galaxy pairs or multiple systems (either interacting or through projection). Nevertheless, we found no systematic trend for the deviations of the position of the maximum from $\sigma_{\rm F} = \sigma_{\rm orig}$, and when averaging over the different curves the maximum is again found close to $\sigma_{\rm F} = \sigma_{\rm orig}$. Accordingly, we conducted all the following analysis using the beam-smoothed maps. For the purpose of completeness we also list in the catalog (see Table 2.1) those sources which are detected above a signal-to-noise ratio threshold of 3.8 in maps at different resolutions.

2.4 Noise properties

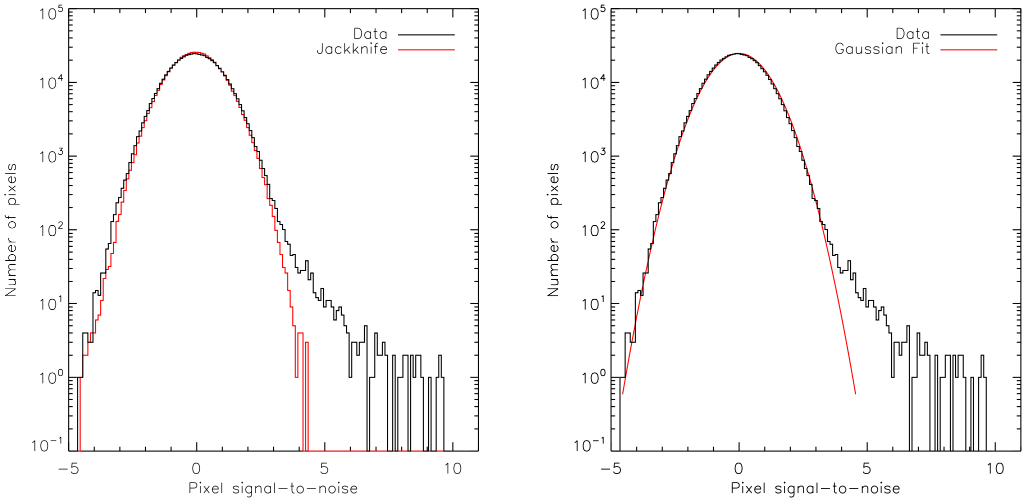

Figure 2.6: Upper Panel: Comparison of the S/N pixel histograms, for the jackknife map (red solid line) and the LABOCA map (black solid line), after scaling the rms map in order to take into account the confusion noise (as described in the text). The broadening at the negative and positive sides of the LABOCA map histogram are caused by sources. Bottom Panel: Signal-to-noise pixel histogram of the LABOCA map. This time instead of the jackknife map, we overlay a Gaussian fit to the negative part of the S/N map, which has a standard deviation of σ. Since, the overlayed Gaussian has to have a S/N = 1 (by definition of noise), we properly scale the RMS map by σ.

To study the noise properties of the LABOCA map we randomly inverted half of the individual maps. They were co-added with the other half of the maps (which remain untouched) to produce a so-called jackknife map, which provides a representation of the pure noise properties with all astronomical signals removed. This ensures that the noise behavior is kept, while emission from any astronomical source is essentially removed (see Fig. 2.5). The jackknife maps were treated the same way as the original map, i.e., each map was smoothed (integral normalized) with a Gaussian kernel of 90", which was then subtracted from the unsmoothed map ($19\overset{\prime\prime}{.}5$) to remove the large-scale structures. Finally, the maps were beam-smoothed (peak normalized).

The S/N ratio distribution of the jackknife maps was compared to the signal-to-noise ratio distribution of the real map in Fig. 2.6 . The distribution of the real map contains a broad positive tail due to the presence of sources in the map, however it is also broader than the jackknife distribution in the negative part. The latter effect arises because the rms in the real map is affected by source confusion. Namely, the inclusion of sources into a pure noise map shifts the flux density distribution towards positive values and also broadens it. However, given that the zero point of the map is determined via baseline subtraction some contribution from sources is also present on the negative side of the distribution. Moreover, the map making process adds a negative ring to the point source profile (see Appendix A), which is also reflected on the negative part of the distribution. For thist reason, it is important to account for the confusion noise prior to source extraction, as underestimated noise would lead to an artificial overestimate of the signal-to-noise ratio of the sources. We have done this by scaling the rms-weighted noise map to match the

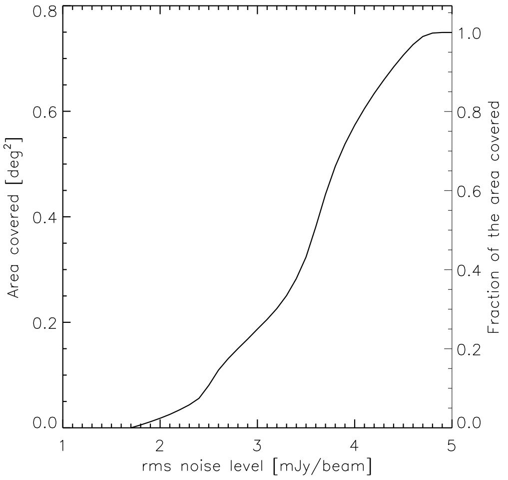

Figure 2.7: Cumulative plot of the rms noise level as a function of the area (left y axis) and fraction of the area (right y axis).

negative part of the S/N distribution in the real map (i.e. to reach a standard deviation of unity in the negative part of the Gaussian S/N distribution).

The resulting noise map is shown in Fig. 2.3, and the corresponding visibility function in Fig. 2.7, where the lowest noise is reached in the central parts of the map, i.e., 1.68 mJy/beam, and it rises towards the outskirts.The total area covered down to 4.68 mJy/beam is 0.75 deg^2 (2698 arcmin^2).

2.5 The COSLA source catalog

2.5.1 Source extraction

The sources were extracted using SExtractor[2] version 2.8.6. (Bertin & Arnouts 1996), which is a software that identifies sources from astronomical images, retrieving several parameters for each source, e.g., position, flux density. We have used it in order to search for peaks in the beamsmoothed map (see Fig. 2.3), i.e., at a resolution of 27″.6, down to a signal-to-noise ratio of 3.8 (see Sec. 2.5.2.1). As an extra requirement for each source at least five pixels had to have a signal-to-noise ratio greater than 3 in order to avoid spurious detections. To account for the different rms levels of the map, we provided SExtractor with the scaled rms map discussed in the previous section (Fig. 2.3). From the obtained fluxes a local background value was subtracted, which was derived as the mean flux of the 64 pixels in the square surrounding the source position. The most deviant pixel values were discarded for a new iteration of the process. This was repeated until all the remaining pixels within the box were within ± 3σ from the mean value. Finally, as already discussed in Sec. 2.2, we divided the retrieved fluxes by a factor of 0.92, which is the factor a point source in the original nominal resolution map, i.e. 19″.5, is decreased on average due to our imaging process (see Fig.2.2).

Given that not all sources reach their maximum S/N when smoothed with a 19″.5 kernel,

---

[2] http://www.astromatic.net/software/sextractor

as theory would predict, we also conducted the source extraction to maps smoothed to different resolutions, applying the same SExtractor settings. For this reason, sources detected in the beam smoothed map and also sources that have been detected at different resolutions are shown in Table 2.1.

In Table 2.1 we list the sources detected in the beam-smoothed map as well as in versions of the map smoothed to different resolutions. Typically, sources whose maximum is detected at a resolution greater than 27″.6 are the result of sources that are blended into one (see Appendix A).

The catalog, hereafter the COSLA source catalog, is presented in Table 2.1 and includes 39 sources detected at a resolution of 27″.6, where 7 sources are predicted to be spurious detections (see Section 2.5.2). Additionally, we present 27 sources which are detected at different resolutions.

Multiwavelength cutouts for all the COSLA sources are presented in Appendix B.

2.5.2 Testing the reliability of the COSLA catalog with Monte Carlo simulations: positional accuracy, completeness, deboosting

Based on simulations we determine quantitatively the reliability of various characteristics of our signal map, i.e., positional accuracy, completeness, false detections, and signal boosting.

2.5.2.1 Positional accuracy

To derive the positional accuracy, and also the completeness (see Sec. 2.5.2.2), we injected artificial sources in the real map at a 19″.5 resolution and then we applied the same image processing as explained in Sec. 2.2. (see Fig. 2.2). In each simulation we injected into the real map only sources in a specific flux range. The first time we injected sources between 3 and 4 mJy, the second time, sources from 4 to 5 mJy and so on up to a flux of 23 mJy. Each time we injected 300 sources (to avoid overlapping) and for each flux range we produce 100 maps, in order to provide solid statistics, especially in the case of faint sources. As we injected sources on the real map, before doing statistics, we removed any coincidence between real sources and artificial sources.

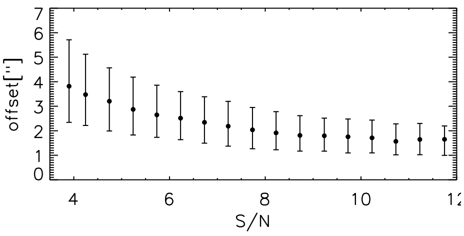

Figure 2.8: Positional accuracy of artificial sources as a function of signal-to-noise ratio. The erros bars show the interquartile range of the offsets between the injected and extracted positions in each signal-to-noise bin.

Once the simulations are produced, we run SExtractor on each map, using the same settings as for the real map, hence the retrieved information allowed us to compute the distance between the injected and extracted positions and also compute errors as the in-

Table 2.1: Source Catalog of the LABOCA-COSMOS survey at 870 μm. For the flux density two values are given: (a): S_ν, the flux density as measured in the map. (b): $S_{\nu,\mathrm{deb}}$, the deboosted flux density, which depends on the underlying source counts (see Sect. 2.5.2.3)

COSLA	R.A. J2000 [deg]	Dec J2000 [deg]	S_ν [mJy]	rms [mJy]	S/N	$S_{\nu,\mathrm{deb}}$ [mJy]	$\mathrm{rms}_{\mathrm{deb}}$ [mJy]	resolution [arcsec]
COSLA-1	150.0641	2.2651	19.40	1.68	10.53	18.12	1.59	27.60
COSLA-2	150.2383	2.3369	25.15	2.50	9.20	20.97	2.02	27.60
COSLA-3	149.9873	2.4580	24.32	3.23	6.88	18.80	2.59	27.60
COSLA-4	150.4021	2.1841	23.19	3.12	6.79	18.31	2.58	27.60
COSLA-5	150.4102	2.3944	22.79	3.44	6.06	17.25	2.95	27.60
COSLA-6	150.0334	2.4360	18.98	2.89	5.99	15.50	2.78	27.60
COSLA-7	150.3981	1.9974	22.50	3.48	5.92	16.93	3.04	27.60
COSLA-8	150.0553	2.2023	11.03	1.83	5.50	9.35	2.02	27.60
COSLA-9	150.3608	1.9631	20.70	3.44	5.50	15.53	3.31	27.60
COSLA-10	150.1334	2.2125	11.87	1.98	5.47	10.00	2.19	27.60
COSLA-11	149.9282	2.4947	20.36	3.48	5.34	15.05	3.48	27.60
COSLA-12	150.2679	2.4141	17.30	3.04	5.20	13.35	3.29	27.60
COSLA-13	150.0381	2.2229	9.95	1.77	5.15	8.18	2.00	27.60
COSLA-14	149.8438	2.4615	20.72	3.69	5.13	14.59	3.86	27.60
COSLA-15	150.2477	2.2858	13.20	2.47	4.88	10.18	2.92	27.60
COSLA-16	150.1798	2.0872	12.91	2.46	4.80	9.83	2.94	27.60
COSLA-17	150.4863	2.5254	23.18	4.44	4.77	13.25	5.20	27.60
COSLA-18	150.0582	1.9422	15.82	3.17	4.56	10.68	4.01	27.60
COSLA-19	149.9863	2.2893	9.93	2.05	4.43	7.17	2.49	27.60
COSLA-20	149.7575	2.1754	16.85	3.60	4.28	9.53	4.79	27.60
COSLA-21	150.1251	2.6943	19.31	4.12	4.28	9.65	5.44	27.60
COSLA-22	150.1478	2.4788	13.92	3.03	4.20	8.39	4.01	27.60
COSLA-23	150.4240	2.4531	16.64	3.66	4.16	8.70	4.90	27.60
COSLA-24	150.0865	2.0108	11.67	2.61	4.09	7.10	3.38	27.60
COSLA-25	150.1392	2.4357	11.91	2.70	4.03	6.98	3.51	27.60
COSLA-26	150.1250	2.0857	10.57	2.43	3.98	6.32	3.08	27.60
COSLA-27	150.0545	2.5749	15.04	3.50	3.93	7.07	4.60	27.60
COSLA-28	150.3161	2.5064	15.31	3.59	3.89	6.81	4.68	27.60
COSLA-29	150.2190	2.3223	10.38	2.45	3.88	5.91	3.08	27.60
COSLA-30	149.6573	2.2335	17.37	4.11	3.86	6.46	5.13	27.60
COSLA-31	150.2975	2.4765	14.57	3.45	3.86	6.58	4.47	27.60
COSLA-32	150.0488	2.2498	7.20	1.71	3.85	4.63	1.98	27.60
COSLA-33	149.8748	2.2844	12.96	3.08	3.85	6.37	3.99	27.60
COSLA-34	149.7733	2.0243	15.85	3.77	3.84	6.47	4.80	27.60
COSLA-35	150.0229	1.8784	14.80	3.54	3.83	6.37	4.54	27.60
COSLA-36	150.3313	2.4414	14.30	3.42	3.82	6.33	4.40	27.60
COSLA-37	149.7901	2.2695	14.75	3.54	3.81	6.29	4.52	27.60
COSLA-38	150.5822	2.3992	18.39	4.41	3.81	5.88	5.22	27.60
COSLA-39	150.1027	2.4346	11.28	2.71	3.80	5.85	3.44	27.60
Sources detected at higher resolution								
COSLA-40	149.9985	2.5768	21.82	4.20	4.75	13.06	4.98	21.80
COSLA-41	150.2301	2.5794	19.72	4.23	4.26	9.44	5.57	21.80
COSLA-42	150.4168	1.9490	20.50	4.43	4.23	9.08	5.77	21.80
COSLA-43	150.5264	2.1516	19.87	4.35	4.17	8.69	5.68	21.80
COSLA-44	150.5054	2.2474	20.97	4.68	4.10	7.75	5.87	21.00
COSLA-45	150.4210	2.5793	23.07	5.17	4.08	6.97	6.04	21.80
COSLA-46	150.1471	2.5947	18.54	4.17	4.06	7.92	5.44	21.80
COSLA-47	150.2186	1.9032	15.90	3.59	4.04	7.87	4.79	22.74
COSLA-48	150.0977	2.3655	10.47	2.37	4.03	6.46	3.00	22.74
COSLA-49	150.1933	2.2208	11.05	2.52	4.00	6.59	3.23	22.74
COSLA-50	150.2919	2.2970	12.14	2.84	3.91	6.51	3.69	22.74
COSLA-51	150.0252	2.3987	13.23	3.09	3.91	6.75	4.05	21.80
COSLA-52	150.2474	2.0996	12.75	2.99	3.89	6.58	3.90	21.80
COSLA-53	150.2834	1.8555	16.13	3.80	3.88	6.70	4.88	23.80
COSLA-54	150.0399	2.3744	9.91	2.35	3.85	5.68	2.93	24.97
COSLA-55	150.3279	2.0388	14.54	3.46	3.85	6.46	4.47	22.74
COSLA-56	150.2643	1.7992	17.35	4.15	3.82	6.15	5.09	23.80
COSLA-57	150.1898	2.6925	19.12	4.59	3.81	5.70	5.29	22.74
COSLA-58	150.3490	2.4372	14.85	3.56	3.81	6.28	4.54	23.80
COSLA-59	150.0089	2.1504	9.51	2.28	3.80	5.42	2.81	23.80
Sources detected at lower resolution (likely mergers)								
COSLA-60	150.1078	2.2528	9.90	2.09	4.32	6.94	2.57	43.60
COSLA-61	150.3874	2.5322	18.46	4.38	3.85	6.19	5.29	40.15
COSLA-62	150.1661	1.9802	12.22	2.91	3.84	6.20	3.75	31.98
COSLA-63	150.0878	2.6953	19.95	4.77	3.82	5.61	5.38	41.87
COSLA-64	150.0009	1.8999	16.98	4.07	3.81	6.14	5.02	43.60
COSLA-65	149.6410	2.1216	19.29	4.63	3.81	5.66	5.30	33.55
COSLA-66	150.3352	2.1234	13.09	3.14	3.81	6.18	4.04	38.46

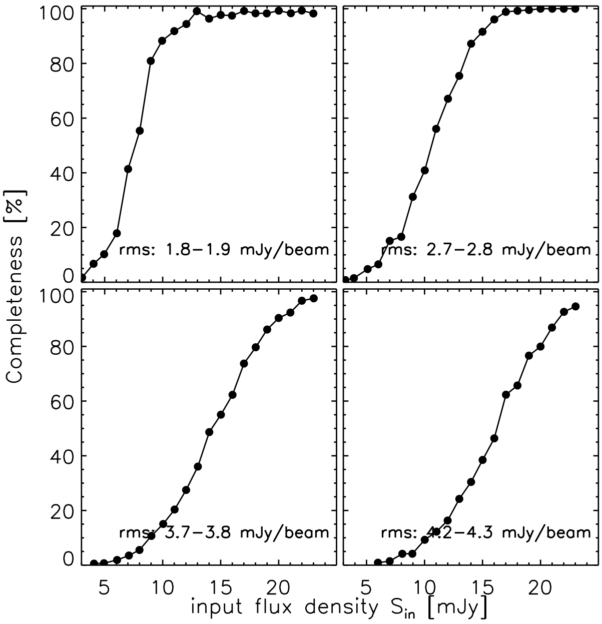

Figure 2.9: The completeness of the COSLA survey for four different noise levels. The ratio of the number of detected sources, which have a counterpart in the injected catalog, and the number of injected sources defines the completeness.

terquartile range of the offsets in each signal-to-noise bin. This is shown in Fig. 2.8. As expected the positional uncertainty decreases as the signal-to-noise increases. The lowest S/N bin in Fig. 2.8 (S/N ∼ 3.9) has a median offset of 3″.8 with an interquartile range from 2″.34 to 5″.70, while at a S/N ∼ 14, the median offset is 1″.25 with an interquartile range from 0″.77 to 1″.96. Sometimes high S/N sources show large positional uncertainties. The reason for this is that in the simulations some of the brightest sources are the overlap of two bright injected sources, which are identified as one by the extraction algorithm. As a result, the assigned position is placed between the two bright sources. Overall, the position uncertainties make possible to target the COSLA sources with the most advanced (sub)mm interferometers up-to-date, e.g., ALMA, PdBI, CARMA, which have typical field of views of ∼20″ (Smolčić et al. 2012a).

2.5.2.2 Completeness

The simulations also allow us to estimate the completeness level of the detections. From the sources retrieved by SExtractor we computed the completeness as the ratio of the number of detected sources, which had a counterpart in the injected catalog, and the number of injected sources. Given that the noise level is variable across the map, we computed the completeness separately for regions with different noise levels (see Fig. 2.3), in rms steps of 0.1 mJy/beam. In Fig. 2.9 we show the results for four different levels. At the lowest noise level of 1.68 − 1.78 mJy/beam our catalog is >95% complete down to an input flux of ∼ 10.44 mJy and the 50% completeness level is reached at ∼ 7.01 mJy. On the other hand, in the region that spans an rms from 4.3 to 4.4 mJy our catalog is >95% complete down to an input source flux of ∼ 23.02 mJy and the 50% completeness level is reached at ∼ 16.24 mJy. As only a handful of sources were observed at such high flux levels, it is most likely that anything observed on the outer areas are either lensed sources or strongly boosted sources.

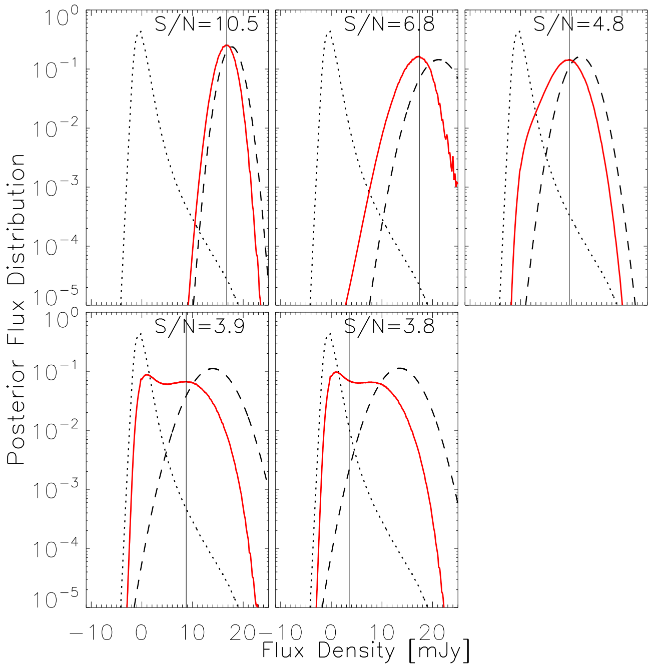

Figure 2.10: Posterior probability distribution for five sources, from high to low S/N. The dashed lines represent the Gaussian probability distribution for each of the five measurements, where the width of the Gaussian varies depending on the position of the source in the map. The dotted lines represent the prior flux distribution obtained from simulated maps, where the sources were injected following a power law with the best fit parameters obtained from the P(D) analysis. The red solid line represent the normalized posterior probability distributions, from which the deboosted fluxes are computed according to Eq. 2.3

2.5.2.3 Deboosting

The fluxes obtained from a submillimeter survey have the effect of the Eddington bias, which artificially boosts the flux of the sources, given the steep underlying number counts (Hogg & Turner 1998; Scott & Fox 2002; Coppin et al. 2006). This means that given that the flux distribution of the sources is asymmetric, as shown below by the dotted line distribution in Fig. 2.10, it is more likely that a source flux is boosted up than boosted down.

To correct for this effect, and recover the deboosted (intrinsic) fluxes we use a Bayesian approach, which has already been successfully applied in other (sub)millimeter surveys (Coppin et al. 2006; Scott et al. 2008; Lindner et al. 2011)

In the Bayesian approach, the aim is to obtain the intrinsic flux (S_i) of a source given its measured flux (S_m) and its respective uncertainty (σ_m). Writing down it in a Bayesian formalism, we have:

$$p\left(\mathrm{S}_i|\mathrm{S}_m,\sigma_m\right) = \frac{p\left(\mathrm{S}_i\right)p\left(\mathrm{S}_m,\sigma_m|\mathrm{S}_i\right)}{p\left(\mathrm{S}_m,\sigma_m\right)}. \tag{2.1}$$

In order to assess the intrinsic flux of each source we need: p(S_i), the prior distribution of flux densities; p(S_m,σ_m|S_i), the likelihood of observing a flux density of $\mathrm{S_m}$ when the intrinsic flux density is $\mathrm{S_i}$; and p(S_m,σ_m) which is a normalizing constant.

The likelihood of observing the data is assumed to be represented by a Gaussian distribution

$$p(S_m,\sigma_m|S_i) = \frac{1}{\sqrt{2\pi\sigma_m^2}}e^{\frac{-(S_m-S_i)^2}{2\sigma_m^2}}. \tag{2.2}$$

This approach is justified by the fact that the pixel distribution of the jackknife maps is indeed well described by a Gaussian distribution.

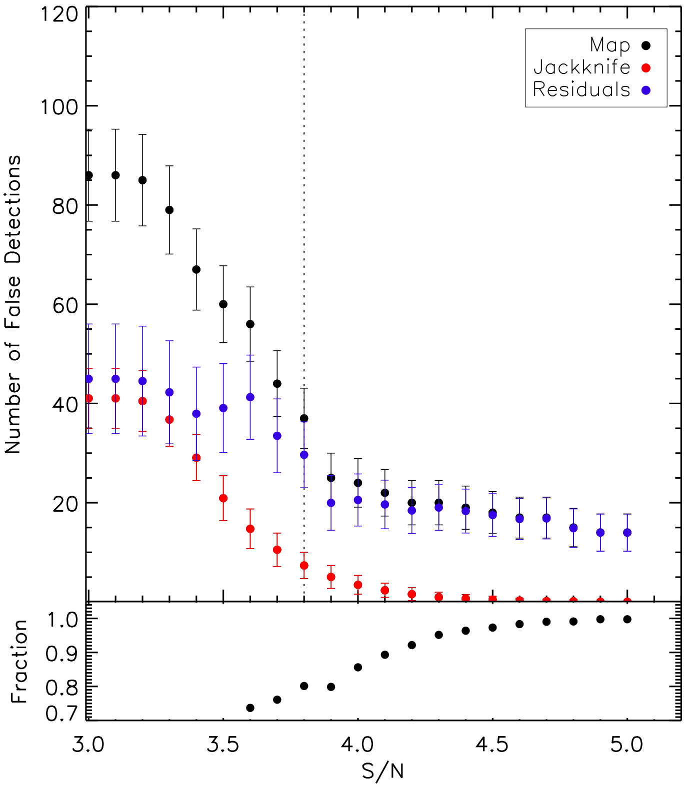

Figure 2.11: **Upper panel:** The cumulative expected number of false detections as function of the S/N are shown as red dots. The number of detections in the real map are shown as black dots, while the difference between detections in the real map and expected false detections are shown as blue dots. The vertical dashed line indicates the threshold of the catalog shown in Table 2.1. **Lower panel:** The expected fraction of real sources as the detection threshold is increased.

The other component we need to compute in Eq. 2.1 is the prior distribution of flux densities. This means that we need a function that accurately describes the source counts of the submm galaxies in the COSMOS field. For this purpose we use the result obtained with the P(D) analysis, which is explained in Sec. 2.6. The distribution, for each source, described by Eq. 2.1 is shown in red in Fig. 2.10.

The deboosted fluxes and the respective uncertainties listed in Table 2.1 are calculated using

$$< S_i >= \int \frac{S_i p(S_m, \sigma_m | S_i) p\,(\mathrm{S}_i)\, dS_i}{p(S_m, \sigma_m | S_i) p\,(\mathrm{S}_i)\, dS_i} \tag{2.3}$$

$$\sigma_i^2 = \int \frac{(S_i - < S_i >)^2\, p(S_m, \sigma_m | S_i) p\,(\mathrm{S}_i)\, dS_i}{p(S_m, \sigma_m | S_i) p\,(\mathrm{S}_i)\, dS_i}. \tag{2.4}$$

2.5.3 False detections

In order to quantify the expected amount of false detections of the catalog shown in Table 2.1 we run the extraction algorithm on the jackknife maps with exactly the same set up that was used for the real data. Given that in the jackknife maps we know beforehand that there are not real sources present, the sources detected with the extraction algorithm become automatically false detections. We run the extraction algorithm in 10 different jackknife maps, obtaining an average and its respective error for the expected false detections down to specific signal-to-noise thresholds. In Fig. 2.11 we show the number of expected false detections, as the signal-to-noise ratio threshold is decreased. We expect ∼ 0.03 false detections down to a S/N of 5, while if we set the threshold down to a S/N of 3.8 we expect $\sim$ 7 false detections, which we found to be a reasonable compromise between the number of detections and false detections.

From Fig. 2.11 it is clear that if we set an even lower threshold, e.g., signal-to-noise ratio of 2, we will have more detections but at the same time the amount of false detections increase considerably. In fact, down to a S/N of 2 one would have a catalog where half of the sources are false detections.

In next section we will see that although pixels at S/N of 2 are not useful or better said *reliable* in order to detect sources, they still provide a good source of information to determine the source counts.

2.6 Source counts

2.6.1 Fluctuation analysis (P(D) analysis)

The fluctuation analysis or "P(D)" analysis (Maloney et al. 2005; Weiß et al. 2009; Scott et al. 2010; Lindner et al. 2011) provides us with a powerful tool to derive the source counts. This technique uses the information from the pixel flux histogram of the map rather than the more intuitive approach of counting the number of detected sources in each flux bin. Determining the source counts directly from the pixel flux histogram has the advantage of using all the available information of the data. This is illustrated in the top panel of Fig. 2.6, where we show the difference between the flux pixel distribution of the map and the distribution obtained from averaging 10 jackknife maps. It can be seen that the presence of sources produce a redistribution of the flux density pixels towards the negative and positive parts of the histogram. Using the standard approach of counting sources per flux several uncertainties are included, related to completeness correction, deboosting correction, and also neglecting sources below the detection limit of our catalog, i.e., a S/N of 3.8.

The P(D) analysis does not suffer from these drawbacks as it is based on analytical modeling of the flux pixel distribution of the image, which is simulated by randomly injecting sources into a noise map, whose fluxes are modeled according to a parametrized model of the number counts.

2.6.2 Random number generator

As we have to inject sources into a noise map, we have to decide which source count model we will use, down to which flux limit we will inject the sources, and how many sources have to be injected given the area of the map.

For this reason we define F(S), a function that describes the flux distribution of the sources, where S stands for flux and it spans the range [S_{min},S_{max}]. The problem we will often find, in any programming language, is that random number generators are available only for a couple of well-known distributions, e.g., Uniform, Gaussian, Exponential. However, in general, we will need to draw random numbers from specific distributions that suit the requirements of our problem. To do so, we discuss two methods which allow to draw numbers from any kind of distribution starting from the uniform distribution.

2.6.2.1 Transformation method

We aim to draw random numbers, S, that follow the distribution F(S). The transformation method does this by relating a random number, u, drawn from a uniform distribution to a random number, S, from any probability distribution.

We define p(u) as the uniform distribution

$$p(u) = \begin{cases} 1, & \text{for } 0 \leq \text{u} < 1. \\ 0, & \text{otherwise.} \end{cases} \tag{2.5}$$

From conservation of probability, we have that intervals δu and δS are related by

$$|p(u)\Delta u| = |F(S)\Delta s|, \tag{2.6}$$

integrating we have

$$\int_{u=0}^{u} 1du' = \int_{S=-\infty}^{S} F(S')dS', \tag{2.7}$$

where in the left-hand side we have used the definition for a uniform distribution (Eq. 2.5). Solving the equation we obtain the relation

$$u = \int_{S=-\infty}^{S} F(S')dS'. \tag{2.8}$$

In order to find a random number S which follows the distribution F(S) we generate a random number u, and solve Eq. 2.8 for S. Notice that F(S) has to be normalized as the integral of the uniform distribution, i.e., $\int_{u=0}^{1} 1du'$, is 1.

In this way, whenever a number is drawn we have a one-to-one relation between a number drawn from a uniform distribution and a number drawn from an arbitrary distribution. However, this is only true in the most favorable case, where the integral on the right-hand side of Eq. 2.8 can be solved analytically, which result in a direct relation of the form,

$$u = T(S), \tag{2.9}$$

where T is the expression after integrating the right-hand side.

However, frequently we will have expressions that do not have an analytical solution. In this case we have to integrate the right-hand side of the expression numerically, and we have to integrate it several times, as we have to change the upper limit value of the integral in Eq. 2.8. Each time we solve the integral we will obtain a number between 0 and 1 (given that the F(S) function is normalized), hence we build a table with S values and their corresponding u values.

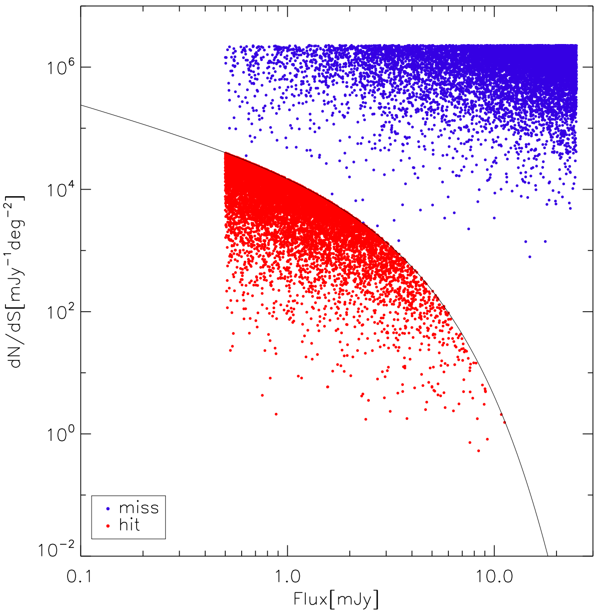

Figure 2.12: An illustration of how the Rejection Method works. If F(S') is greater than F', the corresponding (S',F') point is rejected (blue points), otherwise the (S',F') point is accepted (red points).

Finally, we draw numbers from a uniform distribution and search for the corresponding S in the table. In case the random number , i.e., u, is not found in the table, interpolation is required.

2.6.2.2 Rejection method

This is the easiest method. We use the same function F(S) of the transformation method. We choose a range in S, i.e, [S$_{min}$,S$_{max}$], where our function is not zero, and in case that our function never becomes zero and ranges from $-\infty$ to ∞ we truncate the function accordingly to the requirements of our problem. Correspondingly, the function F(S) will range from 0 to F$_{max}$. The next step is to choose the right values that belong to the distribution. To this purpose we choose randomly many pairs of numbers S' and F' as follows

$$S' = (S_{max} - S_{min})\, u_i + S_{min} \tag{2.10}$$

$$F' = F_{max} u_{i+1}, \tag{2.11}$$

where u$_i$ and u$_{i+1}$ are consecutive generated random numbers. Once we have all of these numbers, we try each pair of (S',F') and compare to F(S'). If F' $\leq$ F(S') then the (S',F') point is saved (**hit**), otherwise is rejected (**miss**). The process is repeated until the desired number of points is obtained.

To illustrate how the method works we choose an arbitrary function for which we want to produce random numbers, a Schechter function (Schechter 1976).

$$\frac{dN}{dS} = N' \left(\frac{S}{S'}\right)^{\alpha+1} \exp(-\mathrm{S/S'}), \tag{2.12}$$

where, S' is the flux which divide between the power law and exponential regime, α is the slope of the power law, and N' is a scaling factor. In this case we arbitrarily choose

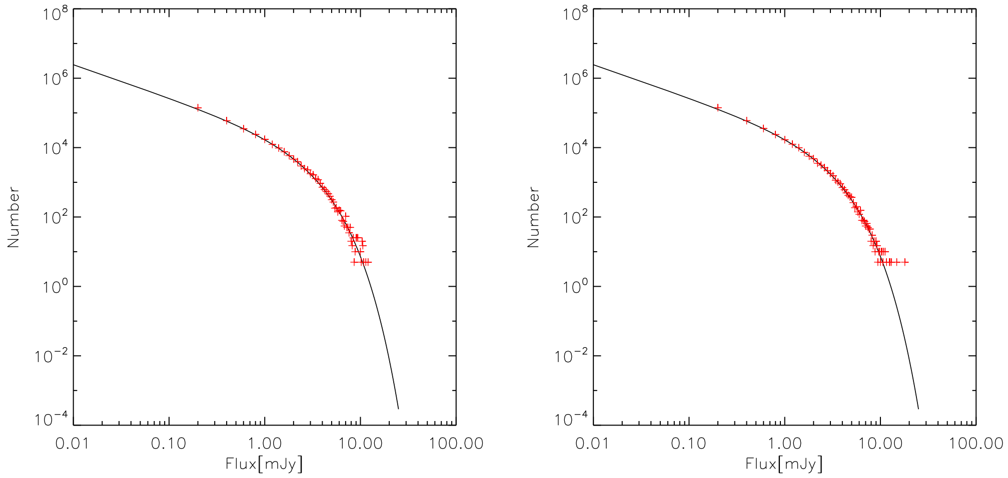

Figure 2.13: Left panel: Random numbers (red crosses) drawn from a Schechter function with parameters (N'=19600,S'=1.62,α=-1.95) using the Transformation Method. Right panel: Random numbers (red crosses) drawn from a Schechter function with parameters (N'=19600,S'=1.62,α=-1.95) using the Rejection Method.

N'=19600, S'=1.62 and α =-1.95. In Fig. 2.12 it is shown how the Rejection method works. All the blue dots are pair of numbers which are rejected (misses) and the red dots are the numbers which are saved (hits).
In Fig. 2.13 we show the random numbers obtained by using both methods. It is clear that both methods work fine, and give us the expected result. The major difference is related to the runtime of each method. For the parameters chosen in Fig. 2.13 the rejection method takes almost 2 order of magnitude longer than the transformation method.

This example is for illustrative purposes. The efficiency of the Rejection method depends largely on the chosen parameters and the way the script is written. Independent whether we use the transformation or the rejection method, we need to decide how many sources to inject in a specific area. As the source counts are described as dN/dS, where dN is the number of galaxies in the flux range dS in a specific area (usually 1 deg$^-$2), we integrate this function from some low flux limit to infinity (or to a maximum flux). From here we obtain how many random numbers are going to be needed in our simulations.

2.6.3 Applying the P(D) analysis

Once the source count model with which the simulated population will be modeled is decided, point sources with the corresponding PSF profile, are randomly injected into a noise map. For the noise map, we use jackknife maps as explained in Sect. 2.4. All the simulations are large-scale filtered and beam-smoothed, i.e., the same procedure as it was used for the real map, as can be seen in Fig. 2.14.

Let's assume that the source count model is described by two parameters, i.e., N and S. Maps are simulated over a grid in the parameter space (N,S), whose flux density distributions are compared to that of the real COSMOS map. This is shown in Fig. 2.15, where we compare the histogram of the real map against a grid. Each cell of the grid is an *average* histogram, H, which has been created averaging n histograms, h, with the same parameters (see Fig. 2.16).

$$H_{N_J S_K} = \frac{1}{n} \sum_{i=1}^{n} h^{i}_{N_J S_K}, \tag{2.13}$$

where N_J and S_K are the free parameters. We want to know which combination of them is the one that describes best the histogram of the real data, hence, for each pair of parameters we compare the simulated averaged histogram to that of the real COSMOS map, computing the χ^2 as shown in Eq. 2.14

$$\chi^2 = \sum_{i=1}^{n_{bins}} \left(\frac{m_i - Y_i}{\sqrt{Y_i + \sigma^2_{MC_i}}} \right)^2, \tag{2.14}$$

where $\mathrm{m_i}$ is the number of pixels of the real map in the ith flux density bin; Y_i is the average number of pixels of the model in the ith flux density bin. The denominator is the error of the ith flux density bin of the real map data and the simulations added in quadrature. $\sigma^2_{MC_i}$ is

$$\sigma^2_{MC_i} = \frac{\sum_{i=1}^{n} y_i}{n^2}, \tag{2.15}$$

where y_i is the number of pixels of the model in the ith flux density bin. We calculate the χ^2 for all the possible (N,S) pairs, and select the pair that minimize it as our best fit, i.e., (N_{BEST}, S_{BEST}).

Once the best fit parameters are identified, we have to assess the errors on both parameters. Given that the bin fluxes are not independent from each other, i.e., the beam area covers several pixels, we cannot compute the errors analytically and instead we use Monte Carlo simulations to determine them. For this purpose, we produce 10000 simulations with the best fit parameters that we found with the P(D) analysis. As shown in Fig. 2.17 the histograms of each of the 10000 simulations are compared against the 'histogram grid' in the same way as we did with the real data in order to determine, through the minimization of χ^2, which one is the new best solution. In this way, we have 10000 (N,S) pairs of the new solutions, which we distribute in a 2D histogram, to determine 68.2%, 95.4%, and 99.7% confidence level regions.

The 1σ errors given for S' and $\mathrm{N}'_{\mathrm{3mJy}}$ are the marginalized 68.2% per cent confidence intervals, around the nominal value found through the minimization of the χ^2. However, given that the rms map shown in Fig. 2.3 is not uniform (as ideally should be), we use simulated noise maps, in order to illustrate and validate the method. The simulated RMS distributions are a uniform distribution, and a non uniform distribution as shown in Fig. 2.18. The sources injected in these noise maps are injected following a Schechter function written as

$$\frac{dN}{dS} = N'_{3mJy} \left(\frac{S}{3mJy} \right)^{\alpha+1} e^{\frac{-(S-3mJy)}{S'}}, \tag{2.16a}$$

$$N'_{3mJy} = N\prime \left(\frac{3mJy}{S'} \right)^{\alpha+1} e^{-3mJy/S^{prime}}, \tag{2.16b}$$

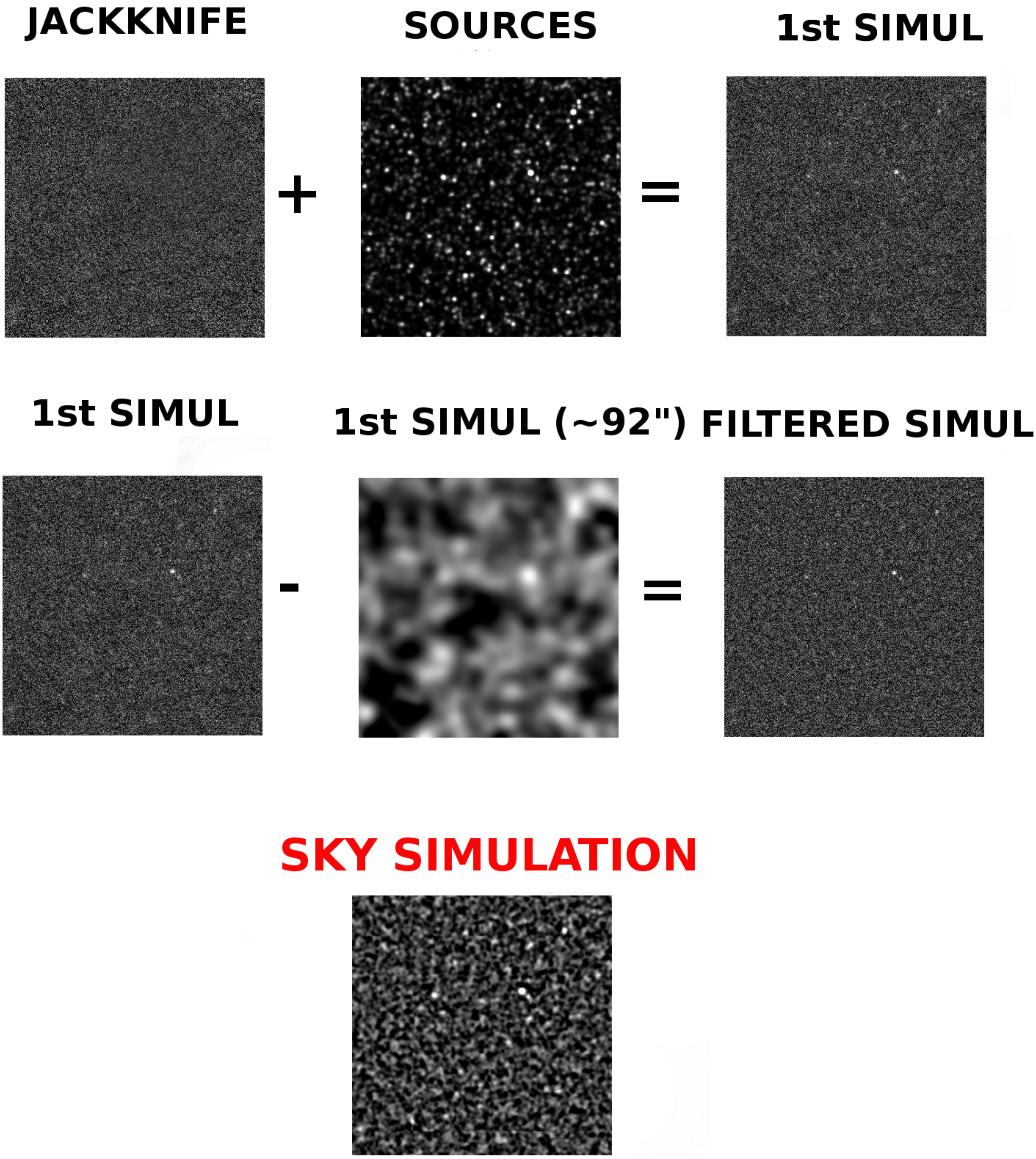

Figure 2.14: **First row**: Sources are injected in a noise map (in this case a jackknife map). **Second row**: The simulated map is smoothed to 90″ and subtracted from itself. **Third row**: Finally the resulting map is beam-smoothed in order to maximize the S/N of point sources.

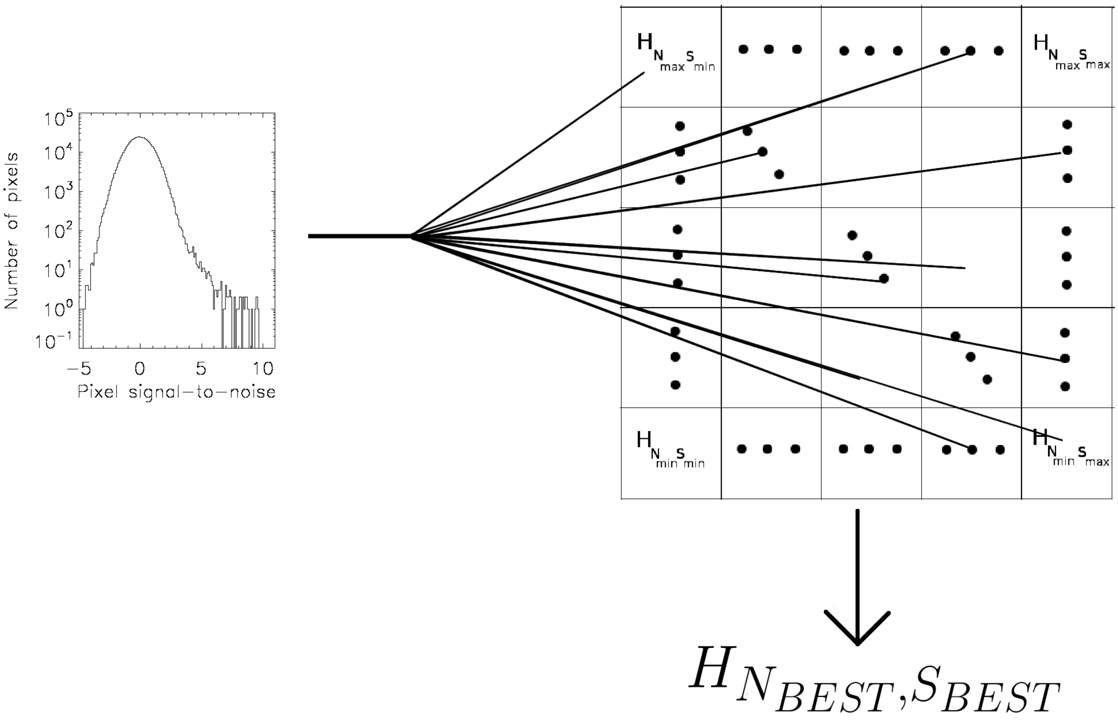

Figure 2.15: The pixel histogram of the LABOCA COSMOS map is compared against a grid of modeled histograms. For each cell of the grid we compute the χ^2 (see Eq. 2.14) between the real data and the modeled data. The model that minimizes the χ^2 is chosen as the best representation of the real data.

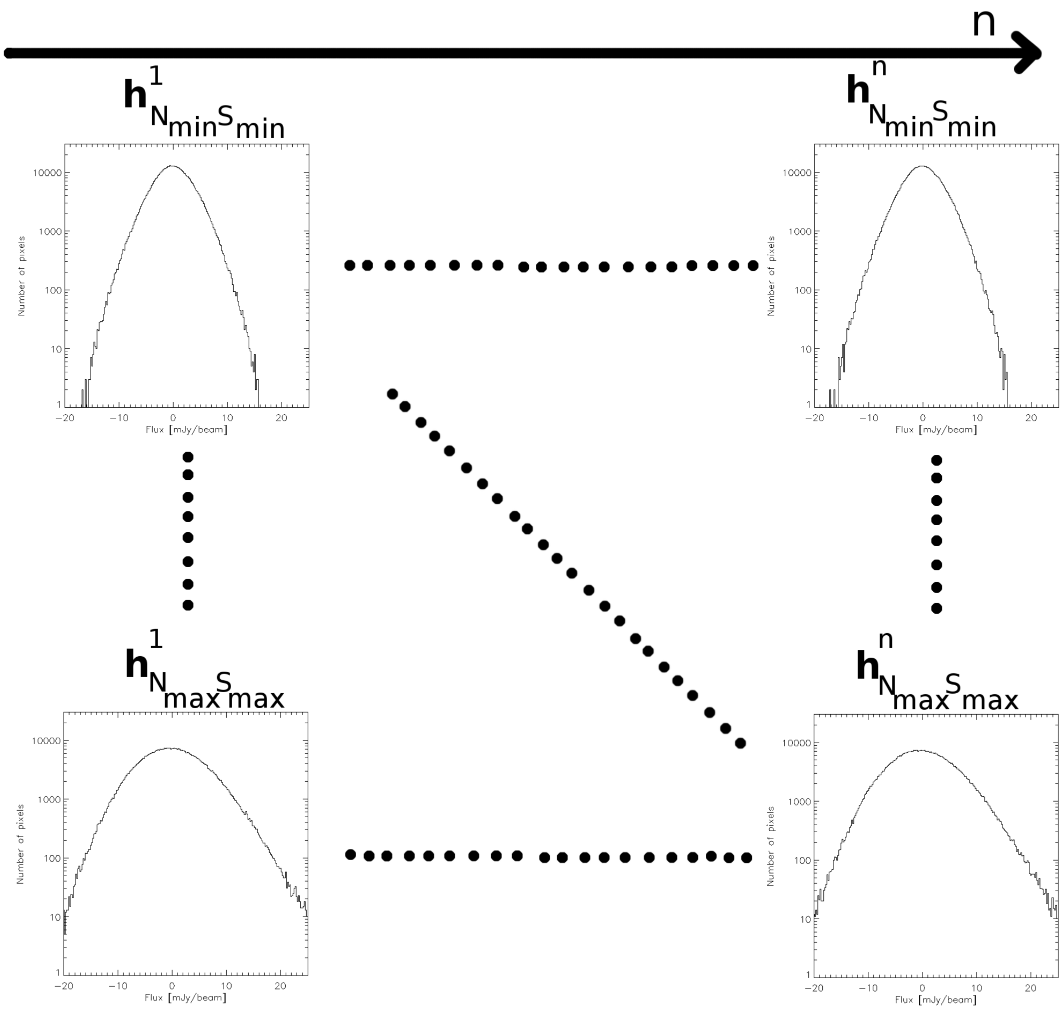

Figure 2.16: Each cell of the grid in Fig. 2.15 is composed of the average of n histograms, which have been simulated with the same parameters.

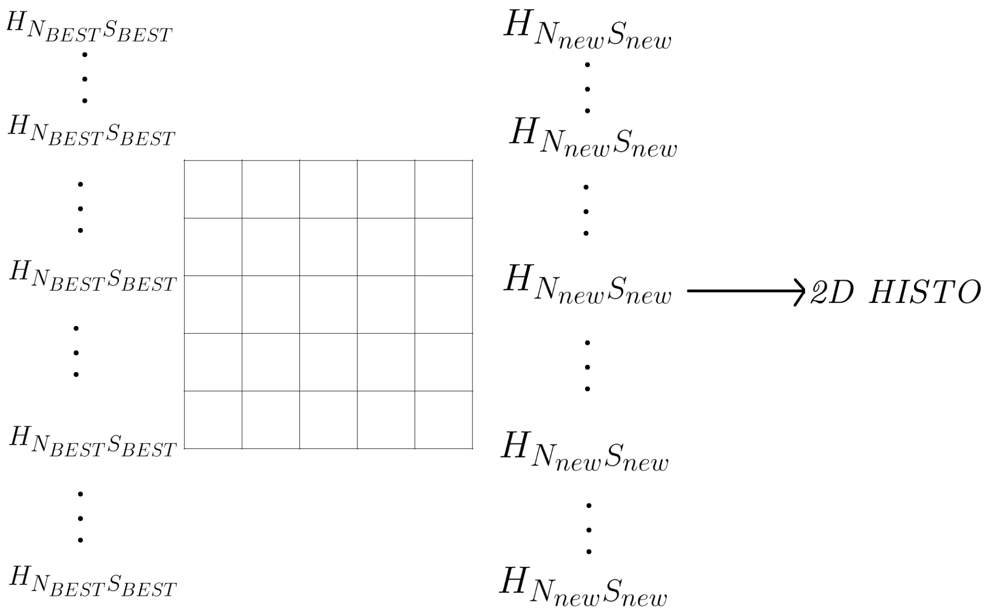

Figure 2.17: 10000 flux density histograms corresponding to simulated maps. Injected sources follow the source count model with the best fit parameters (N_{BEST}, S_{BEST}) found through the P(D) Analysis. Each histogram is compared against a grid of models (same grid as in Fig. 2.15), and the solution that minimizes the χ^2 is the new best solution. At the end of the process we have 10000 new best solutions, which are distributed in a 2D histogram. In this way we obtain the confidence level regions.

where $N'_{\rm 3mJy}$, are the differential source counts at 3 mJy, S' is the *knee* of the Schechter function, which separates the power law regime from the exponential regime; and α is the slope of the power law. The SAMPLE map, which is the simulated map that represents the *real map*, has parameters, $\alpha = -2$, $N'_{3mJy} = 1720$ deg^{-2}mJy^{-1}, and $S' = 1.3$ mJy.

Finally, the simulation is also carried out using the jackknife maps, which after validating the method with the simulated noise maps, will show what is to be expected from the analysis in the real COSMOS map.

2.6.3.1 Gaussian noise

We produce a SAMPLE map by injecting sources into a uniform noise map, i.e., constant rms (see Fig. 2.18), whose rms level is 2.1 mJy/beam. This map is large scale filtered and beam-smoothed in the same way as the LABOCA COSMOS map. We compare the SAMPLE map against a grid of simulations, which span the range 200 to 2120 in $N'_{\rm 3mJy}$ (δ = 80) and the range 0.5 to 3. in S' (δ = 0.1). The best fit is decided based on the χ^2 test. As explained above, given that the flux density bins are not uncorrelated among them we cannot compute the error analytically, and instead we produce 4000 maps with the best fit parameters. Each one is compared against the same grid that was used for the SAMPLE map, in order to obtain a new best solution from the P(D) analysis. The 4000 new best fit parameters are distributed in a 2D histogram. The χ^2 distribution of the grid where we search the best solution, and the probability distribution are shown in Fig. 2.19. It can be seen that the χ^2 reaches its minimum in a very limited area and is clear that we

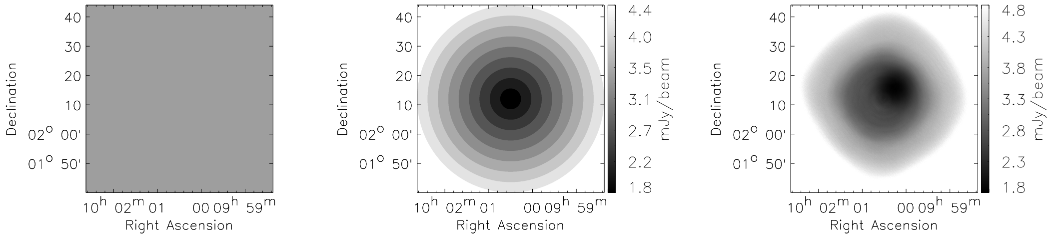

Figure 2.18: Different noise distributions used for testing the P(D) analysis method. **Left panel**: rms image used in the simulations with uniform Gaussian noise (2 mJy/beam). **Middle panel:** Concentric annuli rms map. Each annulus has a different noise level. **Right panel:** The real rms image of our LABOCA observations.

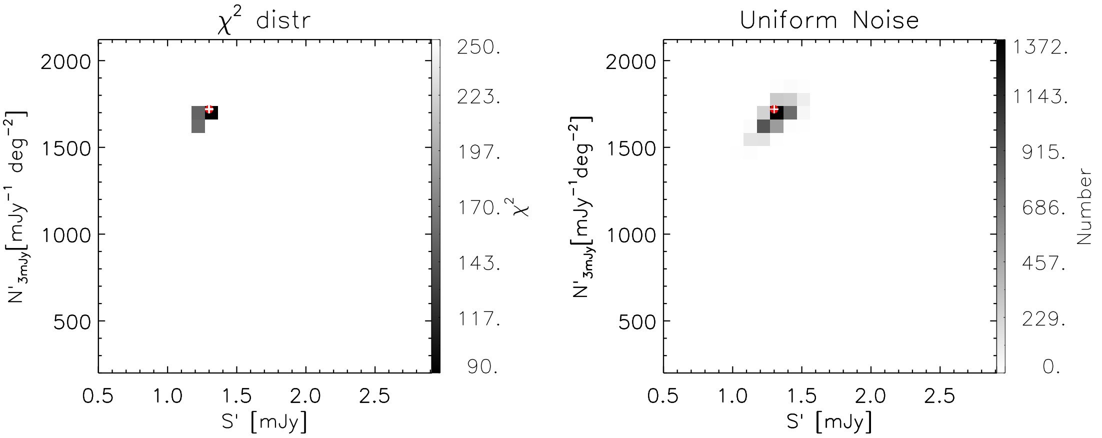

Figure 2.19: χ^2 distribution and 2D histogram for the case of sources injected into a noise map, where the noise is Gaussian distributed. Left Panel: The χ^2 values for the different pairs of parameters (N'_{3mJy},S') of the simulated maps. Black color indicates a low χ^2 value, while white color corresponds to a high χ^2 value. Right Panel: The 2D histogram of the best new solutions. The best new solutions correspond to the result returned from the P(D) analysis for 4000 simulated maps, which were simulated with the best fit parameters obtained from the χ^2 test. The white plus symbol indicates the parameters of the injected source count model, and the red dot indicates the parameters recovered via the P(D) analysis.

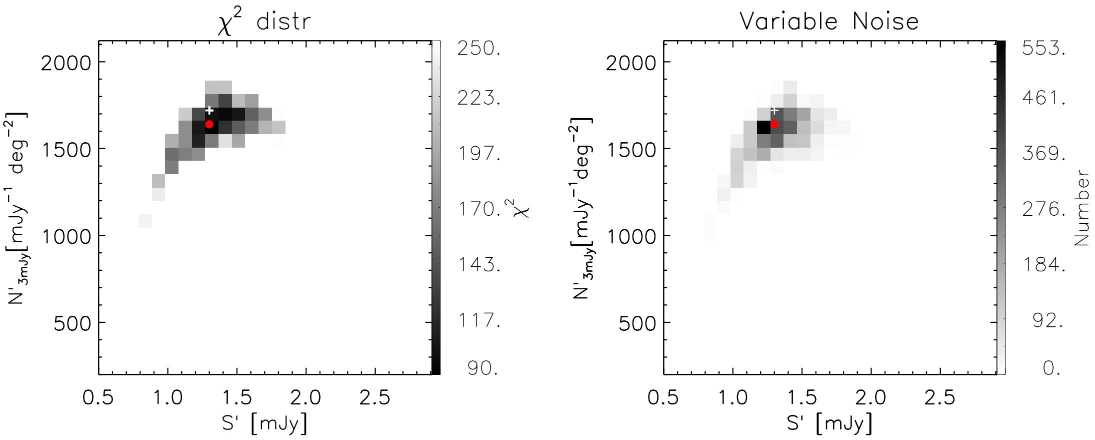

Figure 2.20: The same as Fig. 2.19 but this time the χ^2 distribution and 2D histogram are for the case of sources injected into a noise map, where the noise is variable as can be seen in the top-right panel of Fig. 2.18. The white plus symbol indicates the paramters of the injected source count model, and the red dot indicates the parameters recovered via the P(D) analysis.

recover the right answer. Indeed, we could zoom-in the parameter space, however, given that we are just illustrating how the method works and to keep the same grid that we use in the following examples we do not proceed with a zoom-in of the parameter space.

2.6.3.2 Variable Gaussian noise

As our final goal is to reproduce the number counts in the LABOCA COSMOS field map we investigate the effects of having a not uniform level across the map. To do so, the sources are injected in a noise map, where the noise increases from the center outwards. We simulate 10 different rms zones in the map, where the noise level in the inner annulus is 1.8 mJy/beam and increases in steps of 0.5 mJy/beam outwards up to 4.4 mJy/beam (see Fig. 2.18). As in the previous example we produce a SAMPLE map, using the Schechter function with the same parameters. We search, applying the P(D) analysis, the best parameters for the Schechter function, that fit best the histogram of the SAMPLE map. As can be seen in Fig. 2.20, we again recover the same input parameters as our best fit. However, this time the best solutions spread in a larger region in the parameter space.

2.6.3.3 Jackknife maps

We need to prove that the method also works in the real noise maps, which are the so-called $jackknife$ maps (see Sect. 2.4). All the analysis has been done in the same way as for the previous two examples. In Fig. 2.21 it is shown that this time we do not recover the same input parameters. However, the solution as given by the P(D) analysis even when not the same is still in excellent agreement with the one that was given originally as an input.

After all the testing showed above we get two main conclusions. The first is that the method works, as can be seen from the simulations, whether the noise is flat or varies across the map. The second conclusion is that the method does not give the right answer in the real noise map, most likely, because of the noise distribution. In the simulated

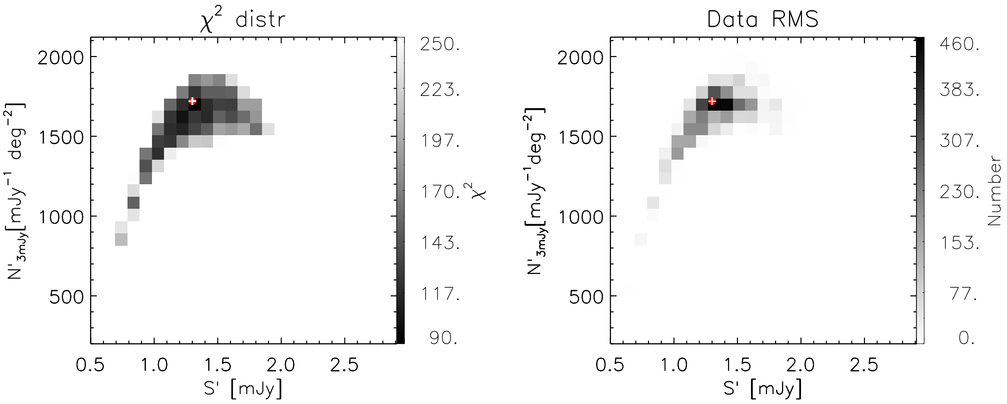

Figure 2.21: The same as Fig. 2.19, however, this time the χ^2 distribution and 2D histogram are for the case of sources injected into a noise map, where the noise is the same as in the real map as can be seen in the bottom-middle panel of Fig. 2.18. The white plus symbol indicates the paramters of the injected source count model, and the red dot indicates the parameters recovered via the P(D) analysis.

example of the variable Gaussian noise, the noise is not uniform, but is still symmetrically distributed, unlike the case of the noise in the LABOCA COSMOS map.

We also investigate the dependence of the fit as the area is decreased. In Figure 2.22 we show 4 different areas of the map, where the maximum rms level is, 4.8, 4.3, 3.8, and 3.3, respectively. It can be seen that in the case of the real noise of the LABOCA map, the obtained result from the P(D) analysis is always in excellent agreement with the parameters of the source counts model given as an input.

Since we have proven that the method works, we apply the P(D) analysis method in two real surveys, i.e., the Extended Chandra Deep Field South (ECDFS, Weiß et al. 2009), and the COSMOS field (Navarrete et al., in preparation).

2.6.3.4 LABOCA: Extended Chandra Deep Field South

We run our P(D) algorithm in the ECDFS map. This is a good consistency check that our procedure is in agreement with previous studies. This time, instead of simulating the noise, we use the jackknife maps produced in the reduction pipeline (Axel Weiß, private communication).

The source counts of the ECDFS field are derived using an area of ∼30×30 arcmin^2. For the parametrized model we use the Schechter function described in Eq. 2.12, which is more similar to the one used in Weiß et al. (2009), where instead of N$'_{3mJy}$ they use N', i.e., the differential source counts at S'. We build a grid in the parameter space that range from S'= 7 to 13.25 in steps of 0.25 and N' = 1 to 26 in steps of 1. The slope is fixed to the same value as cited by Weiß et al. (2009), i.e., α =-3.7. The results after applying the P(D) analysis, for the best fit parameters that best describe the flux density distribution of the ECDFS map are listed in Table 2.2. Moreover, in Figure 2.23 we compare the source counts obtained by Weiß et al. (2009) and in this work. It is clear that both results are in excellent agreement with each other. This result confirms that the P(D) analysis here

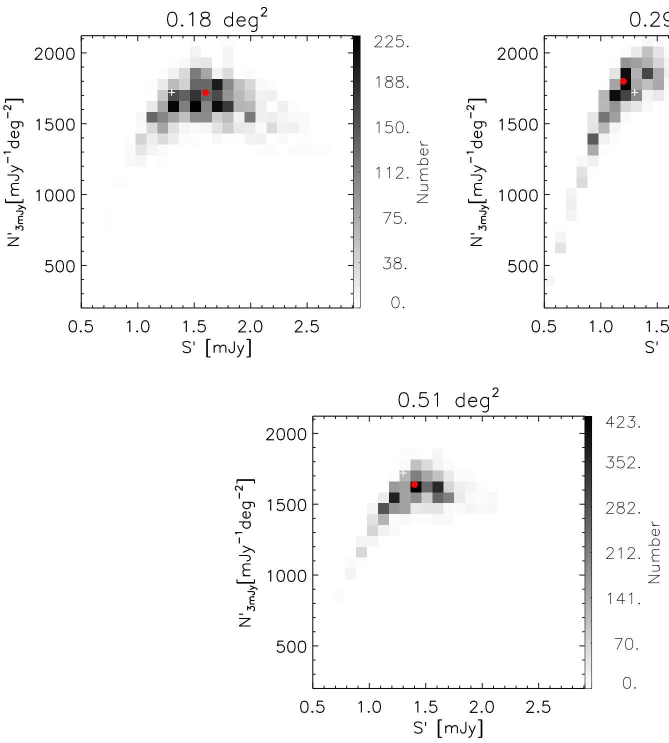

Figure 2.22: 2D histograms for the case of sources injected into a noise map, where the noise is the same as in the real map. The area considered forthe P(D) analysis decreases from left to right. In the three cases considered the P(D) analysis is a robust estimator of the original injected source count model. The white plus symbol indicates the paramters of the injected source count model, and the red dot indicates the parameters recovered via the P(D) analysis.

Figure 2.23: Comparison between the source counts for the ECDFS field, obtained by Weiß et al. (2009) (black solid line) and the one obtained in this work (red solid line). The adopted source count model is a Schechter function as defined in Eq. 2.12. The agreement between both fits is excellent and confirms that the P(D) analysis here implemented works well.

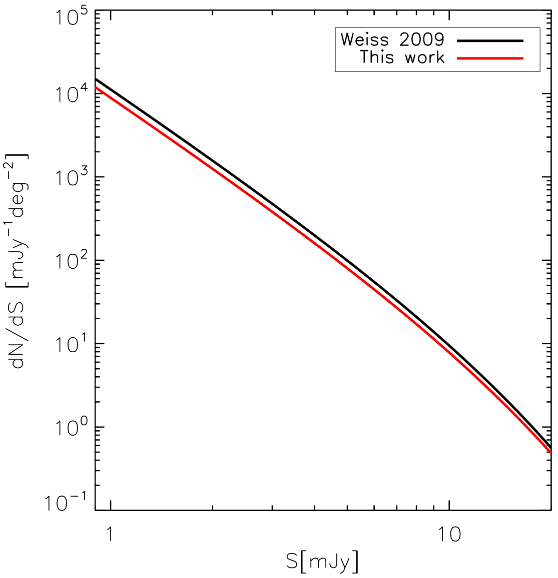

Work	S' [mJy]	N' [mJy^{-1} deg^{-2}]	α
Weiß et al. (2009)	10.5	21.5	-3.7
This work	11.	15.	-3.7

Table 2.2: Comparison of the P(D) analysis in the ECDFS

Model	$N'_{3\mathrm{mJy}}$ [mJy^{-1} deg^{-2}]	N' [mJy^{-1} deg^{-2}]	S' [mJy]	α
Eq. 2.16	570		3.55	-2.6
Eq. 2.17		79.2	5.	3.1

Table 2.3: Best fitting parameters for the differential source counts obtained with the P(D) analysis

implemented works as expected.

2.6.3.5 LABOCA: COSMOS Field

In the COSMOS field, the procedure applied is exactly the same as in the simulations and in the ECDFS field, although in this case we will study two different functional forms for the source counts model. One is the Schechter function as described by Eq. 2.16, and the second is a power law, which takes the following form:

$$\frac{dN}{dS} = N' \left(\frac{S}{S'}\right)^{-\alpha}, \tag{2.17}$$

where N′ is the normalization, α is the slope, and S′ is a fixed constant, in this case S′=5 mJy. In Table 2.3 we report the best fit parameters for the two models of the source counts obtained via the P(D) analysis. To compute the errors for each parametrized model of the number counts, the same procedure as shown for the simulations is applied. Hundred thousand simulated maps using the best fit parameters for the source counts are generated. The P(D) analysis is applied to each simulated map, and the solutions for the best fit parameters are distributed in a 2D histogram. In this way, we compute the 68.3% and 95.4% confidence levels as shown in Fig. 2.24. The histogram of the best fitting Schechter function and power law in comparison with the observations is shown in Fig. 2.25, where it can be seen that the solution found by applying the P(D) analysis and the real LABOCA COSMOS data are in good agreement with each other. In comparison with other surveys observed with SCUBA, LABOCA, SCUBA-2 (Coppin et al. 2006; Weiß et al. 2009; Casey et al. 2013), the counts derived in this work favour those studies with low source counts (see Fig. 2.26).

Casey et al. (2013) observed a smaller area, i.e., ~400 arcmin^2 of the COSMOS field at 850 μm, although to a greater depth ($\sim$ 0.8 mJy/beam). They found that that region of the COSMOS field has a deficit of the number counts compared to many literature measurements (Cowie et al. 2002; Scott & Fox 2002; Smail et al. 2002; Borys et al. 2003; Webb et al. 2003; Knudsen et al. 2008; Chen et al. 2013). However, our counts derived from a

Table 2.4: Number of sources per flux bin for different areas of the map. The different columns are: (i) **N** is the number of sources per flux bin. Each flux bin is 2 mJy wide. (ii) **err** is the Poissonian error. (iii) **C** is the completeness for the respective flux bin in the respective area.

S_{nu}^{deb} mJy	Area 1 116 arcmin^2			Area 2 340 arcmin^2			Area 3 341 arcmin^2			Area 4 752 arcmin^2			Area 5 709 arcmin^2			Area 6 415 arcmin^2		
	N	err	C	N	err	C	N	err	C	N	err	C	N	err	C	N	err	C
4	1	1.00	0.07	0	0.00	0.01	0	0.00	0.02	0	0.00	0.00	0	0.00	0.01	0	0.00	0.01
6	0	0.00	0.18	2	1.41	0.09	2	1.41	0.07	3	1.73	0.02	0	0.00	0.02	1	1.00	0.00
8	2	1.41	0.55	1	1.00	0.31	2	1.41	0.20	3	1.73	0.07	2	1.41	0.06	0	0.00	0.03
10	2	1.41	0.88	2	1.41	0.61	0	0.00	0.38	2	1.41	0.22	1	1.00	0.14	0	0.00	0.09
12	0	0.00	0.94	0	0.00	0.87	1	1.00	0.66	0	0.00	0.41	0	0.00	0.25	0	0.00	0.18
14	0	0.00	0.96	0	0.00	0.98	1	1.00	0.81	0	0.00	0.60	1	1.00	0.41	1	1.00	0.31
16	0	0.00	1.00	0	0.00	1.00	1	1.00	0.94	3	1.73	0.80	0	0.00	0.63	0	0.00	0.41
18	1	1.00	1.00	0	0.00	1.00	1	1.00	0.99	2	1.41	0.90	0	0.00	0.76	0	0.00	0.56
20	0	0.00	1.00	1	1.00	1.00	0	0.00	1.00	0	0.00	0.97	0	0.00	0.87	0	0.00	0.72
22	0	0.00	1.00	0	0.00	1.00	0	0.00	1.00	0	0.00	0.99	0	0.00	0.95	0	0.00	0.84
24	0	0.00	1.00	0	0.00	1.00	0	0.00	1.00	0	0.00	0.99	0	0.00	0.98	0	0.00	0.89
26	0	0.00	1.00	0	0.00	1.00	0	0.00	1.00	0	0.00	0.99	0	0.00	0.98	0	0.00	0.89

Table 2.5: Differential and cumulative counts for the LABOCA Field after taking into the area size and completeness values presented in Table 2.4

S_{870} mJy	N	dN/dS deg^{-2} mJy^{-1}	S_{870} mJy	N(>S) deg^{-2}
$1.68 \leq$ rms < 4.68 mJy; Area: 2698 arcmin^2				
6	8	90.0 ± 45.6	5	362.6 ± 100.9
8	10	62.4 ± 20.3	7	182.7 ± 43.4
10	7	15.4 ± 6.1	9	57.8 ± 15.1
12	1	1.3 ± 1.3	11	27.0 ± 8.9
14	3	4.5 ± 2.8	13	24.4 ± 8.5
16	4	2.4 ± 1.3	15	15.4 ± 6.5
18	4	4.4 ± 2.8	17	10.6 ± 5.9
20	1	0.9 ± 0.9	19	1.8 ± 1.8

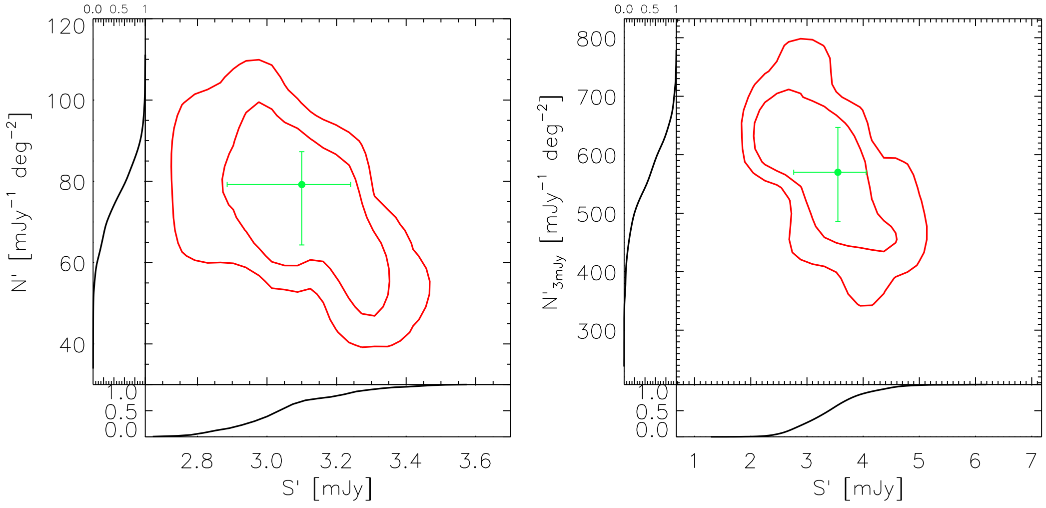

(a) (b)

Figure 2.24: **(a):** The 68.3 and 95.4 per cent confidence regions of the best-fit parameters (green dot), obtained via the P(D) analysis, for the power-law function. The rectangular boxes are the marginalized probabilities on each parameter, from here the 68.3 per cent intervals on each parameter are shown as error bars in the plot. **(b):** The same as for (a) but this time with the best-fit parameters for the Schechter function.

much larger region of the COSMOS field are in agreement with those found by Casey et al. (2013). Moreover, the LABOCA survey of the ECDFS field (Weiß et al. 2009) also shows a deficit in the number counts when comparing to previous studies, and indeed our power law fit is consistent with what was found for the ECDFS. Also, when compared to the work of Scott et al. (2008) the counts of this work are lower, however this has been found also in other works (Geach et al. 2013; Casey et al. 2013). This is justified by the fact that Scott et al. (2008) targeted an overdense region. The underdensity of the ECDFS field has been questioned by Chen et al. (2013). They observed a smaller area of the ECDFS that overlaps with the observations from LABOCA, and could not confirm the proposed underdensity of the field, based on their detections. In this work we find source counts that are consistent with what was found by Weiß et al. (2009) and Casey et al. (2013). Both works claim an underdensity in the respective fields. Weiß et al. (2009), besides using the detected sources, use the P(D) analysis to derive the source counts, which as explained in this work, is independent from the number of detected sources. From these works, it is important to notice the extension of the observed areas. While the work from Chen et al. (2013) covers $\sim$ 280 arcmin^2, Casey et al. (2013) covers $\sim$ 400 arcmin^2, Weiß et al. (2009) covers $\sim$ 900 arcmin^2, and in this work the area covered is $\sim$ 2700 arcmin^2. This means that surveys which are finding a supposed underdensity, cover larger areas than those reported previously. The large coverage makes them less prone to cosmic variance, hence more representative of the SMG population as a whole.

In Fig. 2.26 also data from surveys, which instead of mapping large contiguos blank surveys (as the one shown in this work) have chosen different observation strategies, provide us with two important constraints in the low and bright end of the SMG source counts. In the low end, most of the information is retrieved by surveys targeting galaxy clusters in order to take advantage of the gravitational lensing effect. In Knudsen et al. (2008) the

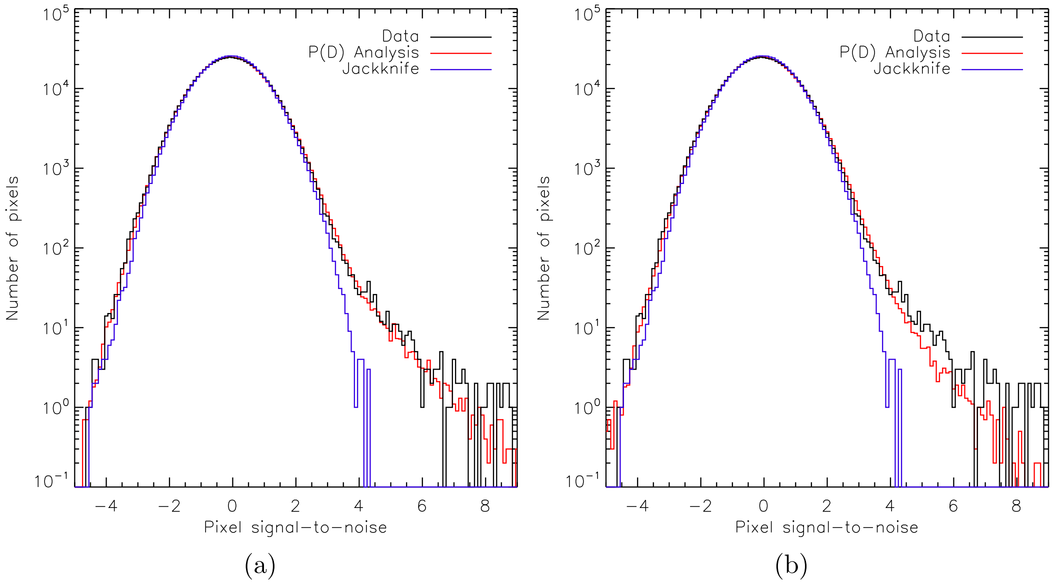

(a) (b)

Figure 2.25: **(a):** Pixel flux density distribution showing the agreement between the data and the average best-fit (power-law) model from the P(D) analysis, where the excellent agreement is clear. The blue histogram shows for reference the average histogram from the jackknife maps. **(b):** Pixel flux density distribution showing the agreement between the data and the average best-fit (Schechter) model from the P(D) analysis, where the excellent agreement is clear. The blue histogram shows for reference the average histogram from the jackknife maps.

galaxy counts below 2 mJy are studied. They target 12 galaxy clusters in order to survey faint, gravitationally lensed sources. The total area surveyed is 71.5 arcmin^2, however, when the corrections for gravitational lensing are applied, the total area surveyed corresponds to 40 arcmin^2.

The cumulative counts obtained from the P(D) analysis agree with the faint end of the source counts as observed by Knudsen et al. (2008). We notice that the LABOCA COSMOS counts at low flux levels do not have strong constraints as a result of the depth of the survey. At the bright end, submillimeter interferometric observations (Karim et al. 2013), which improve the resolution of single dish surveys by about an order of magnitude, have shown that a significant fraction of submillimeter sources brighter than 8 mJy are splitted up into multiple sources. This explains that at high fluxes, the counts of the LABOCA COSMOS map are high when compared to the counts obtained by ALMA observations of the ECDFS sources. This is also observable in the comparison between direct count estimates (Tables 2.4 and 2.5), and the result of the P(D) analysis. The direct counts method does not take into account that the flux of bright sources could arise from more than one component, and this naturally leads to an overestimate of the counts for the bright sources.

However, recently single-dish observations and interferometric observations with the Submillimeter Array (SMA), have observed much lower multiplicity than previous studies, being just compatible with the lower-end of what has been previously suggested (Smolčić et al. 2012a; Hodge et al. 2013). One reason that could help to alleviate this difference is the different beam sizes from SCUBA-2 and LABOCA (see Table 2.7). Since the LABOCA beam is larger, it is more likely that one LABOCA detection involves multiple SMGs. New millimeter interferometric observations of the COSMOS field (PI: M. Aravena) will add critical information in order to solve this discrepancy and help to understand how much this really affects the number counts.

2.7 Comparison with other millimeter surveys

The COSMOS field has been surveyed at millimeter wavelengths, with MAMBO (Bertoldi et al. 2007), AzTEC (Scott et al. 2008; Aretxaga et al. 2011), BOLOCAM (Aguirre et al. in prep; see Table 2.7 for details), and recently at 850 μm with SCUBA-2 (Casey et al. 2013). The LABOCA COSMOS map, overlayed with all the sources observed by the different surveys, is shown in Fig. 2.27. Using a circular radius of 13″.5 from the LABOCA position, i.e., within one beam, we search for counterparts of LABOCA sources in these mm-catalogs. The results are presented in Table 2.6. We find [20 or 23], [5 or 6], [5], [7], and [8 or 11] sources in common with the AzTEC/ASTE (1.1 mm), AzTEC/JCMT (1.1 mm), MAMBO/30-m (1.2 mm), BOLOCAM/CSO (1.1 mm), and SCUBA-2 COSMOS surveys, respectively. The first number inside the brackets correspond to sources detected only in the beam smoothed map, while a second number corresponds to the number of sources detected at any resolution.

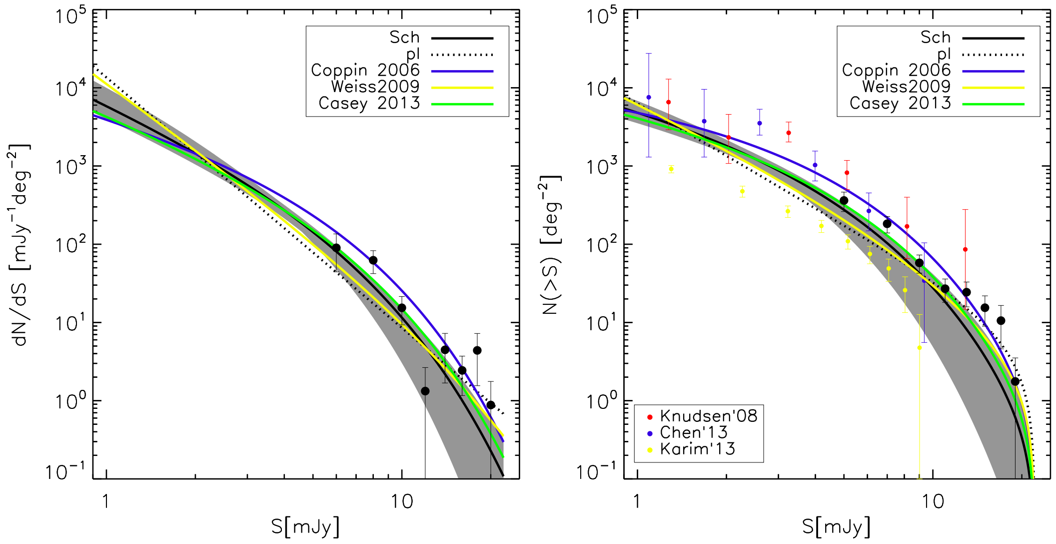

(a) (b)

Figure 2.26: Differential and cumulative source counts for the COSLA survey. **(a):** Comparison of the differential source counts from different surveys carried out at 850–870 μm. The black solid line shows the results form the P(D) analysis for the best-fitting Schechter function, whose errors are indicated by the gray shaded area. The dashed line shows the results for the power-law model, while the results from other surveys are indicated by different colors. The black dots are the number counts as obtained from the detections. **(b):** Same as **(a** but for the cumulative counts. We also add observed data point from surveys which include data for lensed SMGs (Knudsen et al. 2008; Chen et al. 2013)

In the case of the detected sources at different resolutions than 27″.6, 3 out of 4 sources which fall in the area of the SCUBA-2 survey are detected. This suggests, that the detec-

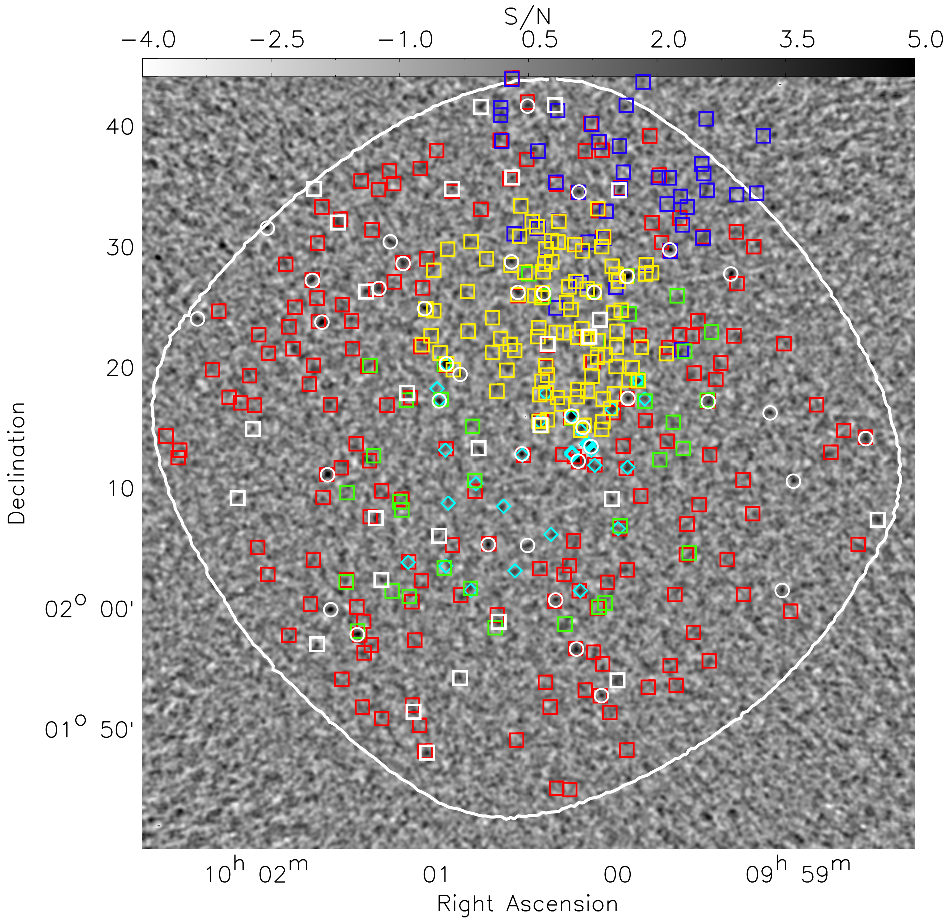

Figure 2.27: Signal-to-noise map of the LABOCA map of the COSMOS field. Red squares show the positions of the AzTEC/ASTE sources, blue squares show the positions of the AzTEC/JCMT sources, green squares show the positions of the BOLOCAM sources, cyan diamonds show the positions of the MAMBO sources, and yellow squares show the positions of the SCUBA-2 sources. The white circles correspond to our sources detected above a signal-to-noise threshold of 3.8 at a resolution of 27.″6, while the white squares correspond to sources detected above the same threshold but at other resolutions. The white contour corresponds to the 4.68 mJy/beam noise level.

tion of sources at different resolutions could be valuable in future submillimeter surveys.

The AzTEC/ASTE survey ($\mathrm{rms}_{1.1\mathrm{mm}} = 1.26$ mJy/beam) covers approximately the same area as our LABOCA observations of the COSMOS field. When considering only sources detected in the beam-smoothed map, we find $\sim$ 51% of our LABOCA sources in the AzTEC/ASTE catalog. The coincidence of the 27 sources detected at different resolutions drops to 11 %.

We convert the AzTEC 1.1 mm fluxes to 870 μm by assuming that the flux ratio between both wavelengths is given by a spectral power law index, defined as $S_{\nu_2}/S_{\nu_1} = (\nu_2/\nu_1)^{2+\beta}$, where β refers to the dust emissivity index. We expect that 27 to 69 of the AzTEC sources should be detected in our LABOCA map, depending on the chosen value of the emissivity index, i.e., β in the range 1 to 2. It seems that we could be recovering fewer sources than expected, especially if the SMG population is better described by a β value of 2.Greve et al. (2008) suggested that there is a population of submillimeter dropouts, with a flux ratio between 850 and 1200 μm in the range 0.7 to 1.7, which would explain the difference.

A population with these characteristics, would correspond to galaxies either with cold dust temperature ($T_D \lesssim 10$ K), or unusual spectral energy distributions (dust emissivity index, $\beta \sim=1$), or also could be galaxies which are at redshift greater than 4.

In fact, the SCUBA-2 COSMOS survey with its greater sensitivity is able to recover most of the 1.1 millimeter population. After translating 1.1 millimeter fluxes to 1.2 mm fluxes, in order to make a realistic comparison with the findings of Greve et al. (2008), we found that from 19 coincident sources, 9 are in the proposed range by Greve et al. (2008) and 10 above it. A proper study of this dropout population requires further investigation, however, this is beyond the scope of this work.

In Fig. 2.28 we focus on the comparison between the fluxes of common sources between SCUBA-2 and LABOCA surveys of the COSMOS field. Given that the observed frequencies are similar, an agreement between the fluxes should be expected, however, we find that LABOCA fluxes are greater than those from SCUBA-2 sources by ~20%. As shown in Fig. 2.28, the comparison between LABOCA fluxes with fluxes from surveys carried out at 1.1 millimeter are well within the expectations, if we consider that the SEDs are well represented by a modified blackbody. Given that the resolution of AzTEC on the ASTE telescope (Aretxaga et al. 2011) and LABOCA are similar, it suggests that galaxy multiplicity would be responsible of LABOCA and AzTEC sources being brighter than expected from SCUBA-2 source fluxes. In fact, high resolution interferometric observations (Smolčić et al. 2012a; Hodge et al. 2013) report that a high fraction of submillimeter sources observed with single-dish telescopes are composed of multiple galaxies. Moreover, there is evidence that the galaxy multiplicity is more common among bright sources, which is the case for the vast majority of the sources presented in this work (see Table 2.1).

2.8 Multi-wavelength counterparts of LABOCA SMGs and redshift distribution

The advantage of single dish (sub)mm observations, compared to interferometric, is a large field of view allowing to perform surveys over substantial areas in the sky. The drawback is the low angular resolution associated with such instruments making it non-trivial to find proper multi-wavelength counterparts to single-dish detected SMGs. Statistical methods, that rely on radio and IR data, which minimize the likelihood of a false association in a random sea of sources ($p-$statistics hereafter) have been developed in the past. The $p-$statistics (Downes 1986; Ivison et al. 2002, 2007; Bertoldi et al. 2007; Biggs et al. 2011; Wardlow et al. 2011; Yun et al. 2012) computes the chance probability to find a counterpart with a flux (S) greater than the counterpart candidate (in a background of randomly distributed sources) within a radius r, where we choose FWHM/2 from the millimeter source. The mean number of potential counterpart sources within a radius r away from the millimeter source and brighter than a flux S is given by

$$\mu = \pi r^2 n(S), \tag{2.18}$$

Table 2.6: Cross-Correlation of the LABOCA catalog with other millimeter surveys carried out on the COSMOS field.

COSLA	S_{870} [mJy]	AzTEC$_C$	dist [arcsec]	$S_{1100_{\rm ASTE}}$ [mJy]	AzTEC$_J$	dist [arcsec]	$S_{1100_{\rm JCMT}}$ [mJy]
1	18.13±1.59	7	10.96	$8.90^{+1.10}_{-1.10}$	——-	——	—-$^{+----}_{-----}$
2	20.97±2.02	6	4.32	$9.60^{+1.10}_{-1.00}$	——-	——	—-$^{+----}_{-----}$
3	18.81±2.59	14	6.55	$6.70^{+1.10}_{-1.10}$	095957.22+022729.3	3.85	$5.80^{+1.50}_{-1.30}$
4	18.32±2.58	12	5.47	$7.50^{+1.00}_{-1.10}$	——-	——	—-$^{+----}_{-----}$
6	15.50±2.78	3	0.42	$10.50^{+1.00}_{-1.10}$	100008.03+022612.1	2.47	$8.30^{+1.30}_{-1.30}$
8	9.34±2.02	76	1.95	$4.20^{+1.10}_{-1.10}$	——-	——	—-$^{+----}_{-----}$
9	15.54±3.31	54	10.98	$4.60^{+1.10}_{-1.10}$	——-	——	—-$^{+----}_{-----}$
10	10.00±2.19	145	10.51	$3.30^{+1.10}_{-1.20}$	——-	——	—-$^{+----}_{-----}$
11	15.04±3.48	5	2.87	$10.00^{+1.10}_{-1.10}$	095942.68+022936.0	5.17	$9.30^{+1.30}_{-1.30}$
12	13.35±3.29	——-	——	—$^{+----}_{-----}$	——-	——	—-$^{+----}_{-----}$
13	8.18±2.00	——-	——	—$^{+----}_{-----}$	——-	——	—-$^{+----}_{-----}$
15	10.18±2.92	——-	——	—$^{+----}_{-----}$	——-	——	—-$^{+----}_{-----}$
16	9.84±2.94	98	5.10	$3.80^{+1.10}_{-1.20}$	——-	——	—-$^{+----}_{-----}$
18	10.68±4.01	8	5.20	$8.70^{+1.10}_{-1.10}$	——-	——	—-$^{+----}_{-----}$
19	7.17±2.49	94	6.66	$3.90^{+1.10}_{-1.20}$	——-	——	—-$^{+----}_{-----}$
23	8.70±4.90	1	1.22	$13.00^{+1.10}_{-1.00}$	——-	——	—-$^{+----}_{-----}$
24	7.10±3.38	172	8.81	$3.00^{+1.20}_{-1.20}$	——-	——	—-$^{+----}_{-----}$
25	6.98±3.51	——-	——	—$^{+----}_{-----}$	——-	——	—-$^{+----}_{-----}$
27	7.07±4.60	10	4.75	$8.10^{+1.10}_{-1.10}$	100013.21+023428.2	2.40	$4.20^{+1.40}_{-1.30}$
30	6.47±5.13	13	7.76	$8.70^{+1.30}_{-1.40}$	——-	——	—-$^{+----}_{-----}$
31	6.58±4.47	109	4.42	$3.70^{+1.10}_{-1.10}$	——-	——	—-$^{+----}_{-----}$
32	4.64±1.98	——-	——	—$^{+----}_{-----}$	——-	——	—-$^{+----}_{-----}$
33	6.37±3.99	181	6.71	$2.90^{+1.20}_{-1.20}$	——-	——	—-$^{+----}_{-----}$
35	6.37±4.54	81	7.04	$4.10^{+1.20}_{-1.10}$	——-	——	—-$^{+----}_{-----}$
39	5.85±3.44	30	7.64	$5.50^{+1.10}_{-1.10}$	100025.23+022608.0	9.12	$1.90^{+2.00}_{-1.20}$
40	13.06±4.98	——-	——	—$^{+----}_{-----}$	095959.33+023445.8	10.43	$5.50^{+1.30}_{-1.30}$
41	9.44±5.57	17	13.12	$6.20^{+1.10}_{-1.10}$	——-	——	—-$^{+----}_{-----}$
46	7.92±5.44	154	11.72	$3.20^{+1.20}_{-1.20}$	——-	——	—-$^{+----}_{-----}$
48	6.47±3.00	38	7.95	$5.10^{+1.20}_{-1.10}$	——-	——	—-$^{+----}_{-----}$
54	5.68±2.93	——-	——	—$^{+----}_{-----}$	——-	——	—-$^{+----}_{-----}$
60	6.95±2.57	——-	——	—$^{+----}_{-----}$	——-	——	—-$^{+----}_{-----}$

COSLA	COSBO	dist [arcsec]	S_{1200} [mJy]	BOLOCAM	dist [arcsec]	$S_{1100_{\rm BOL}}$ [mJy]	SMM850.	dist [arcsec]	S_{850} [mJy]
1	1	7.16	6.20±0.90	4	9.65	5.90±1.95	4	4.78	11.09±1.56
2	3	0.15	7.45±1.10	33	8.79	3.50±1.90	5	3.33	11.49±1.62
3	——-	——	——±——	13	4.51	4.80±1.94	1	5.14	11.49±1.10
4	——-	——	——±——	——-	——	——±——	——-	——	——±——
6	——-	——	——±——	1	5.48	8.10±1.92	0	2.40	16.15±0.80
8	——-	——	——±——	——-	——	——±——	——-	——	——±——
9	——-	——	——±——	——-	——	——±——	——-	——	——±——
10	5	4.64	5.11±0.90	——-	——	——±——	——-	——	——±——
11	——-	——	——±——	——-	——	——±——	——-	——	——±——
12	——-	——	——±——	——-	——	——±——	16	7.25	7.82±1.71
13	2W	13.27	1.37±0.90	——-	——	——±——	——-	——	——±——
15	12	6.93	4.78±1.00	24	11.49	3.70±1.91	——-	——	——±——
16	——-	——	——±——	——-	——	——±——	——-	——	——±——
18	——-	——	——±——	——-	——	——±——	——-	——	——±——
19	——-	——	——±——	——-	——	——±——	——-	——	——±——
23	——-	——	——±——	——-	——	——±——	——-	——	——±——
24	——-	——	——±——	——-	——	——±——	——-	——	——±——
25	——-	——	——±——	——-	——	——±——	2	9.78	8.97±1.04
27	——-	——	——±——	——-	——	——±——	——-	——	——±——
30	——-	——	——±——	——-	——	——±——	——-	——	——±——
31	——-	——	——±——	——-	——	——±——	——-	——	——±——
32	——-	——	——±——	——-	——	——±——	53	9.76	4.70±1.47
33	——-	——	——±——	23	11.29	3.70±1.91	——-	——	——±——
35	——-	——	——±——	——-	——	——±——	——-	——	——±——
39	——-	——	——±——	8	12.79	5.50±1.92	15	8.37	5.08±1.09
40	——-	——	——±——	——-	——	——±——	——-	——	——±——
41	——-	——	——±——	——-	——	——±——	——-	——	——±——
46	——-	——	——±——	——-	——	——±——	——-	——	——±——
48	——-	——	——±——	——-	——	——±——	8	1.11	6.60±1.12
54	——-	——	——±——	——-	——	——±——	14	11.65	5.55±1.11
60	——-	——	——±——	——-	——	——±——	46	8.28	4.64±1.40

Table 2.7: Summary of other millimeter surveys on the COSMOS field.

Instrument	Telescope	λ [mm]	Area [deg^2]	Sensitivity [mJy/beam]	FWHM [arcsec]
AzTEC	ASTE	1.1	0.72	1.26	34
AzTEC	JCMT	1.1	0.15	1.2-1.4	17
MAMBO	IRAM	1.2	0.11	$\sim$1	11
BOLOCAM	CSO	1.1	0.26	1.9	31
SCUBA-2	JCMT	0.85	0.11	0.8–1.6	15
LABOCA	APEX	0.87	0.75	1.68–4.68	27.6

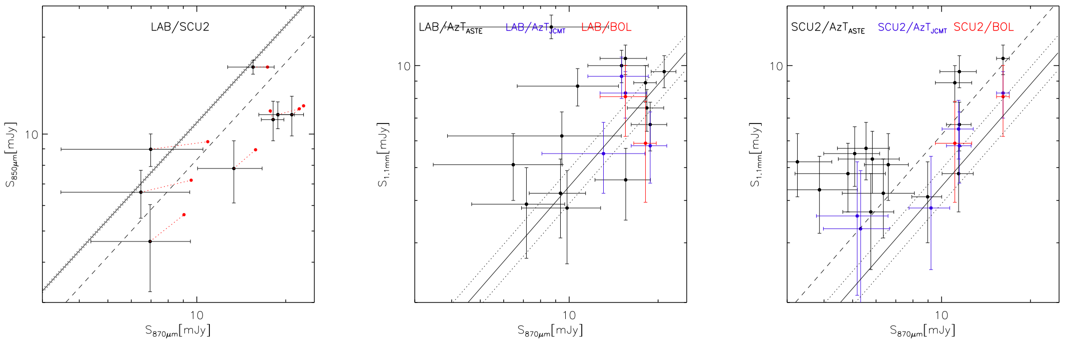

Figure 2.28: Flux (deboosted) comparison between different (sub)millimeter fluxes. **(a):** LABOCA fluxes are compared against SCUBA-2 fluxes reported in Casey et al. (2013). The solid line is the one-to-one relation, while the dashed line is in the case that LABOCA fluxes overestimate SCUBA-2 fluxes by 20%. The red dots are fluxes without applying deboosting. **(b):** The LABOCA fluxes are compared to 1.1 millimeter fluxes obtained from AzTEC (in the JCMT and in the ASTE telescopes) and BOLOCAM. The solid line is the ratio between fluxes at different frequencies, assuming a modified blackbody spectrum with a dust emissivity index β =1.5 (in the Rayleigh Jeans approximation). The dotted lines show the ratio between fluxes at both frequencies assuming different values of β, i.e., 1 or 2. **(c):** The SCUBA-2 fluxes are compared to 1.1 millimeter fluxes. As it can be seen from **(b)**, the LABOCA fluxes are in a reasonable agreement with the AzTEC fluxes

where n(S) is the local density of likely counterparts brighter than the candidate. The local density has been determined using the nearest 16 likely counterpart sources. The Poisson probability to find at least one random object is:

$$P_S = 1 - e^{-\mu} \tag{2.19}$$

A more specific calculation introduces a correction to the Poisson probability, which takes into account the fact that there is a limit in this probability. This is the extreme case (given by $P_{3\sigma}$) where one considers the faintest possible counterpart at the search radius. In this way, the corrected Poisson probability, P_C, reads:

$$P_C = 1 - e^{P_S[1+ln(P_s/P_{3\sigma})]}, \tag{2.20}$$

where $P_{3\sigma}$ is the probability to find a source brighter than the detection limit of the map within the search radius

$$P_{3\sigma} = \pi r_s^2 n_{limit}(S), \tag{2.21}$$

where r_s is the search radius (FWHM/2). We separately compute the p−statistics using the i) VLA-COSMOS radio data (Joint Large and Deep project reaching down to $\sim 12\ \mu$Jy/beam rms, see Schinnerer et al. 2007, 2010 for details), ii) Spitzer/MIPS 24 μm data down to a flux cut of 0.15 mJy (see Le Floc'h et al. 2009), and iii) IRAC data ($S_{3.6} > 1\mu$Jy; Sanders et al. 2007) fulfilling the criterion $[3.6] - [4.5] \geq 0.0$ (shown by Yun et al. 2008 to be favored by SMGs). Sources with $p \leq 0.05$ are considered as "robust" counterparts, while those with $0.05 < p < 0.2$ are considered as "tentative" counterparts. The results are presented in Table 2.8. We find that 25 out of 39 (64%) sources detected in the beam-smoothed map have at least one or more likely counterparts.

2.8.1 Redshift distribution

Extracting the photometry in > 30 bands using the latest version of the deep COSMOS multi-wavelength catalog (with UltraVista YJHK Data Release 1 data added), we compute the photometric redshifts for all of the likely counterparts, i.e., including tentative and robust counterparts, of our LABOCA SMGs. Smolčić et al. (2012a) have shown that photometric redshifts for SMGs can be accurately derived when using a library of spectral models optimized for SMGs. In this work, the photo-z were computed using the HYPERZ code (Bolzonella et al. 2000) and a set of synthetic spectral templates. We use three sets of spectral model libraries. obtained with the GALAXEV03 code (Bruzual & Charlot 2003) with different star formation histories (SFH) are used. Additionally a set of 19 spectral templates, produced with the spectrophotometric code GRASIL (Silva et al. 1998; Iglesias-Paramo et al. 2007) and optimized for SMGs by Michałowski et al. (2010). The photo-z are obtained by fitting the set of templates to the SED of a galaxy, where each template is shifted in a range of redshifts. The best redshift and template are determined via a χ^2 minimization procedure. For the extinction law, a Calzetti et al. (2000) law is applied, where the reddening spans the range A_V=0–5. The photometric redshifts, thus obtained, are tabulated in Table 2.8. Using the photometric redshifts from Table 2.8 for the LABOCA sources that are detected in the beam-smoothed map the redshift distribution of the COSLA sources is shown in Fig. 2.29, spanning the range $0.29 \leq z \geq 4.26$ with a mean value for the sample of 1.69 ± 0.18. The uncertainties on the mean are generated via bootstrapping methods. The results of this work are compared to others found in the literature (Chapman et al. 2005; Wardlow et al. 2011; Yun et al. 2012; Smolčić et al. 2012a; Casey et al. 2013). finding that they are in good agreement with them. In order to correctly interpret the redshift distribution shown in Fig. 2.29, it is important to notice that given that the search for counterparts is done at wavelengths which suffer from a positive k correction, there is a natural bias against high-redshift SMGs. For instance, in the VLA-1.4 GHz survey, SMGs with $L_{IR} \sim 10^{12}$–$10^{13}\ L_\odot$ are difficult to observe at $z \gtrsim 3$ (Murphy 2009). Also, the LABOCA-COSMOS map is not uniform (see Fig. 2.3), hence an intrinsic bias for the detection of bright sources is present. Due to the essentially flat selection function of submillimeter surveys out to z$\sim$8, and assuming that there is not a dependence of the submillimeter flux with redshift, we can interpret the redshift-distribution for the LABOCA-COSMOS survey as representative of the SMG population. From Fig. 2.29 is clear that the redshift distribution presented in this work is in good agreement with what was found for a smaller area (but deeper) of the COSMOS field (Casey et al. 2013). In general, this distribution is broader in comparison to

Table 2.8: Photometric Redshifts for COSLA sources

COSLA id	RA deg [J2000]	Dec deg [J2000]	P_C	z	dist [arcsec]
1	150.06450	2.26409	0.120	$1.32^{+0.09}_{-0.13}$	0.513
2	150.23729	2.33819	0.044	$0.71^{+0.08}_{-0.14}$	1.041
2	150.23863	2.33685	0.004	$2.81^{+0.34}_{-0.41}$	0.548
3	149.98878	2.45846	0.040	$1.07^{+0.11}_{-0.10}$	0.469
4	150.40117	2.18044	0.114	$2.23^{+0.18}_{-0.12}$	0.555
5	150.40820	2.39421	0.050	$0.29^{+0.02}_{-0.00}$	0.821
7	150.39680	1.99763	0.175	$1.61^{+0.11}_{-0.16}$	0.947
9	150.36046	1.96214	0.149	$2.88^{+0.04}_{-0.06}$	0.075
10	150.13258	2.21198	0.011	$2.11^{+0.14}_{-0.12}$	0.199
11	149.92853	2.49396	0.102	$4.26^{+0.17}_{-0.20}$	0.171
12	150.26625	2.41356	0.071	$2.44^{+0.15}_{-0.17}$	0.789
15	150.24687	2.28866	0.074	$1.91^{+0.11}_{-0.12}$	0.135
16	150.18004	2.08868	0.062	$2.82^{+0.16}_{-0.22}$	1.033
18	150.05760	1.94440	0.075	$1.88^{+0.16}_{-0.12}$	0.443
20	149.75832	2.17631	0.023	$0.48^{+0.03}_{-0.03}$	1.789
21	150.12204	2.69662	0.077	$0.63^{+0.29}_{-0.15}$	1.728
23	150.42404	2.45362	0.023	$1.44^{+0.34}_{-0.27}$	2.334
24	150.08788	2.00946	0.135	$0.50^{+0.01}_{-0.02}$	0.074
25	150.13899	2.43379	0.110	$2.36^{+0.24}_{-0.24}$	0.371
26	150.12550	2.08700	0.022	$0.82^{+0.03}_{-0.04}$	0.162
28	150.31465	2.50356	0.154	$0.78^{+0.04}_{-0.08}$	0.134
30	149.65820	2.23570	0.054	$2.64^{+0.38}_{-0.26}$	0.464
31	150.29817	2.47800	0.074	$2.49^{+0.23}_{-0.28}$	0.368
33	149.87314	2.28699	0.129	$0.44^{+0.04}_{-0.06}$	1.033
35	150.02281	1.87806	0.049	$2.60^{+0.15}_{-0.18}$	0.473
37	149.79056	2.26968	0.085	$1.06^{+0.07}_{-0.03}$	0.307
37	149.79156	2.27201	0.174	$1.10^{+0.10}_{-0.11}$	0.047

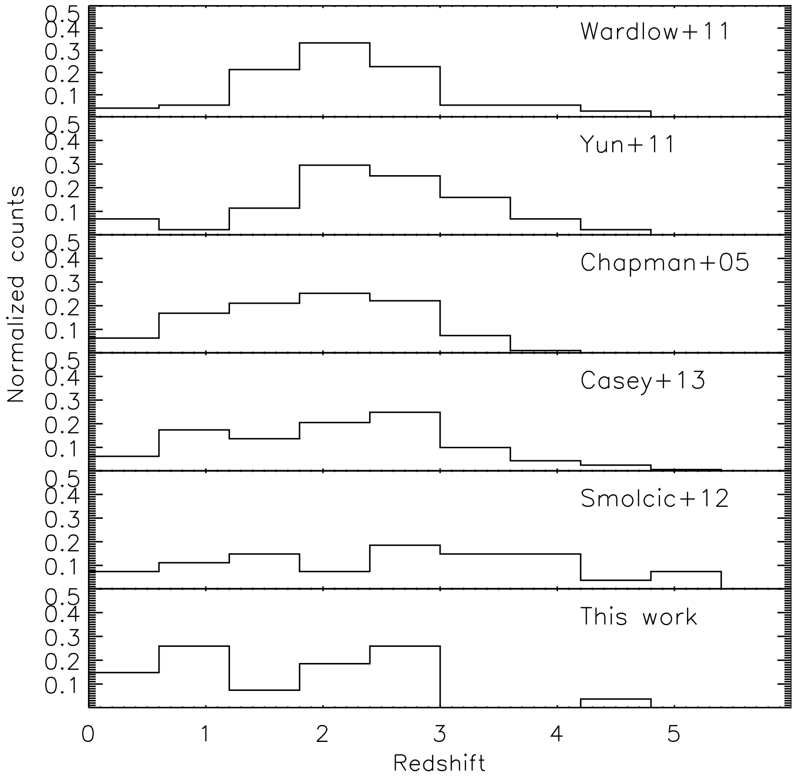

Figure 2.29: Redshift distribution of counterparts to our LABOCA-COSMOS sources with S/N > 3.8, determined via the $p-$statistics. For comparison, the different panels show results collected from the literature.

what is found by submillimeter surveys carried out in other fields. Also it has a low-z contribution, which is interestingly missed in the 1.1 mm AzTEC-GOODS-S and 870 μm LESS samples. This low redshift contribution is expected according to models of the evolution of infrared-galaxies (Béthermin et al. 2011), and could be explained by cold dust temperatures in these sources. Moreover, in a follow-up with the PdBI interferometer (see Chapter 3) of a subsample of sources from the LABOCA-COSMOS map (where the counterparts are unambiguously identified, given the significant improvement in resolution) the low-redshift contribution is confirmed. This subsample has a higher mean redshift value, $< z >= 2.6 \pm 0.4$, which is expected as the counterparts are unambiguously identified, hence the bias against high-redshift sources introduced by statistical methods is removed.

In a more detailed analysis of the redshift distribution shown in Fig. 2.30 we correlate the COSLA catalog with the sources that have been already observed with (sub)millimeter interferometers (Younger et al. 2007, 2009; Smolčić et al. 2012a). The sample is then splitted in two subsamples: (i) no having interferometric counterparts, and (ii) having interferometer counterparts. It can be easily seen that sources that have an interferometric counterpart show a distribution that does not have a strong low-z component, while the subsample without interferometric observations has most of the low-z contribution. Currently, without submillimeter interferometric observations from these galaxies is difficult to quantify how many galaxies are misclassified in the low-z part of the distribution. In this work, the statistical association of counterparts to our LABOCA sources have been shown for easier comparison with other results from the literature that relied on similar

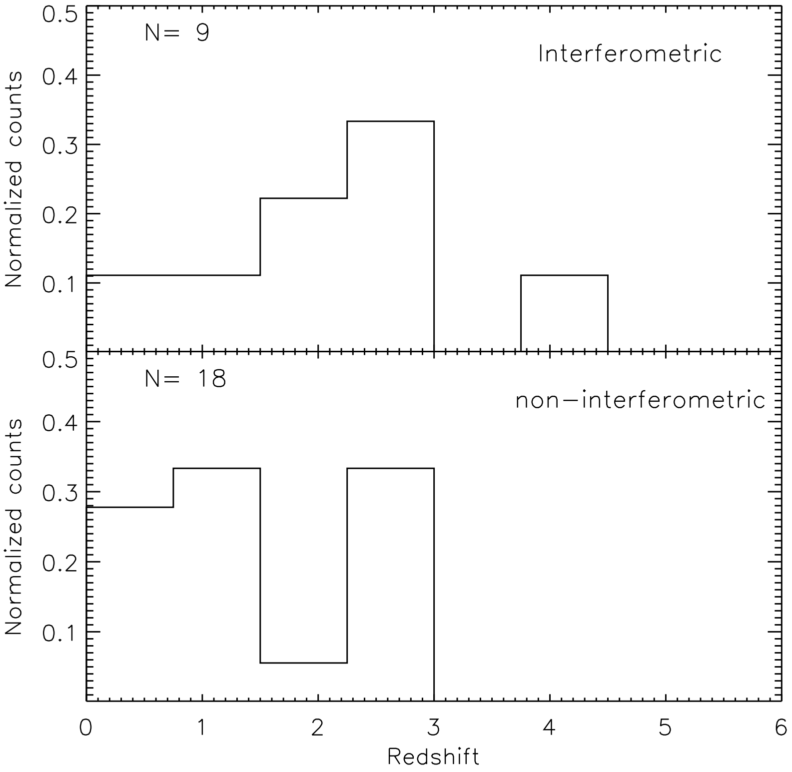

Figure 2.30: Redshift distribution of counterparts to our LABOCA-COSMOS sources with $S/N > 3.8$, determined via the $p-$statistics. **Upper panel:** Redshift distribution of COSLA sources with interferometric identified counterparts. **Lower panel:** Redshift distribution of COSLA sources without interferometric identified counterparts.

methods. These methods are biased given that generally associate counterparts to only $\sim 60\%$ of the single-dish SMGs. Moreover, recent unbiased submillimeter interferometric observations (Smolčić et al. 2012a) have suggested that about $\sim 30\%$ of these counterparts are likely to be wrong.

2.9 Summary and conclusions

In the following we summarize the main results from this work:

- We present the LABOCA survey of the COSMOS field, which is the largest continuous survey at 870 μm carried out to date. It covers an area of ~ 0.75 deg^2, reaching a depth of 1.68 mJy/beam at the center and decreasing towards the outskirts.
- Thirty nine sources have been detected above a S/N of 3.8.
- Based on simulations we quantify the reliability of the catalog, i.e., completeness, position accuracy, deboosting, and false detections.
- From the data we derive the source counts via the so-called P(D) analysis, obtaining

a solution that is in agreement with what is found for the ECDFS survey, which has also been observed with LABOCA. It is seen that the source counts obtained from the direct counts overpredict the solution found via the P(D) analysis, which is expected as direct counts do not make any consideration about sources that are blended into one source given the large beam of single dish telescopes.

- The LABOCA data is compared against data from other surveys that have mapped at (sub)mm wavelengths other areas of the COSMOS field , with BOLOCAM, AzTEC, MAMBO, and SCUBA-2. In particular, the survey carried out at 1.1 mm with AzTEC mounted on the ASTE telescope covers a similar area that is covered with LABOCA. We find that ~ 51 % of the LABOCA sources have a counterpart at 1.1 mm. This fraction reinforce the idea that there are a group of galaxies with either cold dust temperature $\mathrm{T_D} < 10K$, or unusual spectral energy distributions ($\beta \sim= 1$, or could be galaxies which are at redshift greater than 4.

3

COSLA at high angular resolution

In this Chapter follow-up observations at 1.3 mm, with the PdBI interferometer, of a previous shallower version of the COSLA catalog are presented. These observations improve the resolution around the field of the detected sources with LABOCA by a factor of ~ 18. In total 28 sources are targeted, nine SMGs remain undetected, while the remainder yields 9 highly significant (S/N > 4.5) and 17 tentative ($3 <$ S/N ≤ 4.5 with multi-wavelength source association required) detections. Combining these with other single-dish identified SMGs detected via intermediate ($\lesssim 2$") angular resolution mm-mapping in the COSMOS field we present the largest sample of this kind to-date, containing 50 sources. The comparison between secure counterparts obtained with PdBI interferometer reveals that P-statistics counterpart identification correctly associates counterparts to only $\sim 50\%$ of the parent single-dish SMG samples analyzed here. Within our samples we find that $\gtrsim 15\%$, and up to $\sim 40\%$ of single-dish identified SMGs tend to separate into multiple components when observed at intermediate angular resolution. Based on 16 interferometrically confirmed SMGs with spectroscopic redshifts, we show that photometric redshifts derived from optical to MIR photometry are as accurate for SMGs as for other galaxy populations. The redshift distribution of the SMGs with secure counterparts identified via intermediate $\lesssim 2$" resolution mm-observations, and compare this distribution to previous estimates that were based on *statistically* identified counterpart finding a broader redshift distribution with a higher abundance of low- and high-redshift SMGs. The mean redshift is higher than in previous estimates. This may add evidence to previous claims that brighter and/or mm-selected SMGs are located at higher redshifts. A surface density of $z \gtrsim 4$ SMGs ($F_{1.1\mathrm{mm}} \gtrsim 4.2$ mJy) of $\sim 34 - 54$ deg^{-1} is derived, which is significantly higher than what has been predicted by current galaxy formation models.

This work has been published in Astronomy & Astrophysics as: Smolčić, V., Aravena, M., Navarrete, F., et al. 2012, A&A, 548, A4, *Millimeter imaging of submillimeter galaxies in the COSMOS Field: redshift distribution.*

3.1 Status of research in submillimeter galaxies

3.1.1 Submillimeter galaxies

Submillimeter galaxies (SMGs; $S_{850\mu m} \gtrsim 5$ mJy) are ultra-luminous, dusty, starburst galaxies with extreme star formation rates of order 10^3 $M_\odot$ yr^{-1} (e.g. Blain 2002). They trace a phase of most intense stellar mass build-up and appear to significantly contribute to the volume-averaged cosmic star formation rate density at $z = 2 - 3$ ($\sim$ 20%; Michałowski et al. 2010). Evidence is emerging that SMGs represent the progenitors of massive elliptical galaxies (e.g. Cimatti et al. 2008; van Dokkum et al. 2008; Michałowski et al. 2010) , and their enhanced star formation properties can be intimately related to the evolution of quasi stellar objects (Sanders & Mirabel 1996; Hopkins et al. 2006; Hayward et al. 2011). Spectroscopic and photometric studies of SMGs locate them predominantly at redshifts 2-3 (e.g. Chapman et al. 2005; Wardlow et al. 2011), and only few $z > 4$ SMGs have recently been detected. Identifying the highest redshift SMGs requires time-consuming, systematic follow-up observations to properly identify them against strong lower-redshift selection biases. To date $\sim$ 10 $z > 4$ SMGs have been confirmed (Daddi et al. 2009a,b; Capak et al. 2008, 2011; Schinnerer et al. 2008; Coppin et al. 2009; Knudsen et al. 2010; Carilli et al. 2010, 2011; Riechers et al. 2010; Smolčić et al. 2011; Cox et al. 2011; Combes et al. 2012). Although the number of SMGs known remains small it appears that the abundance of SMGs at $z > 4$ is so high that it is only marginally consistent with current galaxy formation models (Baugh et al. 2005; Coppin et al. 2009; Smolčić et al. 2011). It was suggested that the high-redshift SMGs are qualitatively different from those at intermediate redshift (Wall et al. 2007) Such conclusions are premature considering that significant uncertainties have hampered the proper identification of SMGs with optical/IR sources, and thus the proper allocation of redshifts.

3.1.2 Identifying multi-wavelength counterparts to SMGs

SMGs are typically first detected with single-dish mm or sub-mm telescopes that suffer from a relatively large (10" $-$35") beam size that usually includes tens of galaxies visible in deep optical or NIR images. Numerous methods have been applied to pinpoint the proper counterparts, such as UV/IR/radio star formation indicators or the association with AGN (Ivison et al. 2005, 2007; Bertoldi et al. 2007; Biggs et al. 2011). All these probabilistic identifications introduce sample incompletness, contamination, and bias. Furthermore, SMGs may be tightly clustered and thus blended in large beam single dish observations (Younger et al. 2007, 2009). SMGs observed with interferometers at intermediate-resolution ($\sim$ 2") often do not coincide with any of the galaxies detected over the electromagnetic spectrum (Younger et al. 2009), which may be due to extreme dust extinction, or very high-redshift. To properly assess the overall properties of SMGs including their redshift distribution, it is crucial to follow up the single-dish detections with sufficiently high resolution interferometric imaging in the continuum or line emission. Before the improved sensitivities provided by the upgraded IRAM PdBI or with ALMA, interferometric follow-up has been a slow and expensive undertaking that resulted in about 50 good SMG identification s in various survey fields (Downes et al. 1999; Frayer et al. 2000; Dannerbauer et al. 2002; Downes & Solomon 2003; Genzel et al. 2003; Kneib et al. 2005; Greve et al. 2005; Tacconi et al. 2006; Sheth et al. 2004; Iono et al. 2006; Younger et al. 2007, 2009; Aravena et al. 2010a;

Ikarashi et al. 2011; Tamura et al. 2010; Hatsukade et al. 2010; Wang et al. 2011; Chen et al. 2011; Neri et al. 2003; Chapman et al. 2008; Smolčić et al. 2012b). The largest statistically significant, signal-to-noise- and flux-limited sample of interferometrically identified SMGs contains 17 sources drawn from the AzTEC/JCMT survey of 0.15□° within the COSMOS field (Younger et al. 2007, 2009). Here we present PdBI observations towards 28 SMGs drawn from the LABOCA-COSMOS 0.7□° survey (Navarrete et al., in prep.), which constitutes the yet largest interferometric follow-up of SMGs drawn from bolometer imaging surveys.

3.1.3 Determining the redshift of SMGs

The proper identification with an optical counterpart may allow the determination of the SMG redshift through optical/NIR spectroscopy. Given the ambiguity of identifications through probability considerations and the optical faintness of the counterparts, or the absence of lines in particualr redshift ranges, this has been a very difficult task. The yet largest SMG sample with spectroscopic redshifts has been established by Chapman et al. (2005), who followed-up SMG counterparts identified through deep, intermediate ($\lesssim 2$") resolution radio observations, getting redshifts for 76 of 150 targets.

Where spectroscopic redshifts cannot be measured for large samples of SMGs, deep panchromatic surveys such as COSMOS or GOODS measure photometric redshifts, which are based on χ^2 minimization fits of multi-band photometry to spectral models (e.g. Ilbert et al. 2009). With an optimized choice of spectral models and a dense multi-wavelength photometric coverage photometric redshifts reach accuracies of a few percent (e.g. Ilbert et al. 2009). Although SMGs are rare and peculiar galaxies and it is not obvious whether common photometric redshift templates can be applied to SMG counterparts, recent studies confirm that photometric redshifts can be well estimated also for SMGs, both on statistical and case-to-case basis (Daddi et al. 2009a; Wardlow et al. 2010, 2011; Yun et al. 2012; Smolčić et al. 2012b) Here we further test the photometric redshift estimates for SMGs using the yet largest "training set" of SMGs with secure spectroscopic redshifts. This allows us to derive the proper redshift distribution of an identification-unbiased, S/N-limited and nearly flux-limited sample of SMGs.

In Sec. 3.2 we describe the data used for our analysis. In Sec. 3.3 we present the PdBI observations towards 28 SMGs drawn from the LABOCA-COSMOS survey. In Sec. 3.4 we define two samples of SMGs with mm-interferometric detections in the COSMOS field. Using these in Sec. 3.5 we investigate blending of SMGs, and usually applied statistical counterpart association methods to single-dish identified SMGs. In sect. 3.6 we calibrate photometric redshifts for SMGs. In Sec. 3.7 we derive redshift distributions for our statistical samples of SMGs with unambiguously determined counterparts. We discuss and summarize our results in Sec. 3.8 and Sec. 3.9. We adopt $H_0 = 70$ km s^{-1} Mpc^{-1}, $\Omega_M = 0.3$, $\Omega_\Lambda = 0.7$, and a Chabrier (2003) initial-mass function if not stated otherwise.

3.2 Multi-wavelength data in the Cosmic Evolution Survey

3.2.1 The COSMOS project

The Cosmic Evolution Survey (COSMOS) is an imaging and spectroscopic survey of an equatorial 2□° field (Scoville et al. 2007). The field has been observed with most major space- and ground-based telescopes over nearly the full electromagnetic spectrum to high depths. Over a contiguous area of 2□° the COSMOS Project includes very deep broad-band (u*BVgrizJHK) and medium/narrow-band photometry in more than 30 bands, GALEX, deep Spitzer IRAC/MIPS, Herschel PACS/SPIRE and HST/ACS high-resolution imaging, XMM-Newton X-ray observations, 1.4 GHz and 320 MHz VLA observations, 600 and 200 MHz GMRT observations, as well as more than 25,000 optical spectra (Capak et al. 2007; Sanders et al. 2007; Scoville et al. 2007; Leauthaud et al. 2007; Koekemoer et al. 2009; Frayer et al. 2009; Hasinger et al. 2007; Zamojski et al. 2007; Taniguchi et al. 2007; Lillly et al. 2007; Lilly et al. 2009; Le Floc'h et al. 2009; McCracken et al. 2010; Trump et al. 2007; Schinnerer et al. 2004, 2007, 2010, ;Smolčić et al., in prep) The inner square degree was observed in X-rays at higher resolution and sensitivity with Chandra (Elvis et al. 2009) and at mm and submm wavelengths (Aretxaga et al. 2011; Bertoldi et al. 2007; Scott et al. 2008, ;Navarrete et al., in prep.; Aguirre et al., in prep.).

Particularly relevant for the work presented here are the deep UltraVista observations of the COSMOS field reaching 5σ (2" aperture AB magnitude) sensitivities of 24.6, 24.7, 23.9, and 23.7 in Y, J, H, and Ks, respectively (McCracken et al. 2012), as well as the VLA 1.4 GHz observations reaching an rms of 7-12 μJy/beam over the inner square degree of the COSMOS field (Schinnerer et al. 2004, 2007, 2010). We here use the updated UV-MIR COSMOS photometric catalog (Capak et al. 2007) including all the available UV-MIR photometric observations. Unpublished Herschel data exist and a joint ana lysis will be included in a future publication.

3.2.2 SMGs in the COSMOS field

The COSMOS field was mapped at mm or submm wavelengths with MAMBO at the IRAM 30m (0.11 deg^2; 1.2mm, 11" angular resolution; Bertoldi et al. 2007), BOLOCAM at the CSO (0.27 deg^2; 1.1mm; 31" angular resolution; Aguirre et al., in prep), AzTEC at the JCMT (0.15 deg^2; 1.1mm; 18" angular resolution; Scott et al. 2008), AzTEC at ASTE (0.72 deg^2; 1.1 mm; 34" angular resolution; Aretxaga et al. 2011), and LABOCA at APEX (0.7 deg^2; 870 μm; $27''$ angular resolution, Navarrete et al., in prep.). To properly determine the multi-wavelength counterparts of the SMGs identified in these surveys, numerous interferometric and spectroscopic follow-up efforts have been made (Younger et al. 2007; Younger et al. 2008; Younger et al. 2009; Capak et al. 2008; Capak et al. 2010; Schinnerer et al. 2008; Riechers et al. 2010; Aravena et al. 2010a; Smolčić et al. 2011, 2012b, , Karim et al. 2012, in prep). To date a sample of 24 interferometrically identified COSMOS SMGs has been established prior to our observations (Table 3.1). For 11 of those spectroscopic redshifts are available, either from the dedicated COSMOS optical spectroscopic follow-up using Keck II/DEIMOS (Capak et al., in prep., Karim e t al., in prep.), or from CO line observations with mm interferometers (Schinnerer et al. 2008; Riechers et al. 2010, in prep.; Baloković et al., in prep., Karim et al., in prep.).

Table 3.1: Summary of interferometrically observed COSMOS SMGs besides our work

Source	reference	LABOCA			redshift		
		source	separation ["]	$F_{870\mu\mathrm{m}}$ [mJy]	spectroscopic	photometric^{+}	mm-to-radio
AzTEC-1	(1), (2), (3)	COSLA-60		12.6 ± 3.6	4.64	$4.26^{+0.17}_{-0.20}$	–
AzTEC-2	(1), (4)	COSLA-4		14.4 ± 3.0	1.125	–	–
AzTEC-3	(1), (5)	–	–	–	5.299	$5.20^{+0.09}_{-0.21}$	–
AzTEC-4	(1)	–	–	–	–	$4.70^{+0.43}_{-1.11}$	–
AzTEC-5	(1), (6)	–	–	–	3.971	$3.05^{+0.33}_{-0.28}$	–
AzTEC-6	(1)	–	–	–	0.802	$0.82^{+0.13}_{-0.10}$	–
AzTEC-7	(1)	–	–	–	–	$2.30^{+0.10}_{-0.10}$	–
AzTEC-8	(7), (8)	COSLA-73	–	12.3 ± 3.6	3.179	$3.17^{+0.29}_{-0.22}$	–
AzTEC-9	(7)	COSLA-3	–	16.4 ± 3.3	1.357	$1.07^{+0.11}_{-0.10}$	–
AzTEC-10	(7)	–	–	–	–	$2.79^{+1.86}_{-1.29}$	–
AzTEC-11	(7)	–	–	–	1.599	$1.93^{+0.13}_{-0.18}$	–
AzTEC-11-N	(7)	–	–	–	–	$1.51^{+0.41}_{-0.92}$	–
AzTEC-11-S	(7)	–	–	–	–	–	> 2.58
AzTEC-12	(7)	–	–	–	–	$2.54^{+0.13}_{-0.33}$	–
AzTEC-13	(7)	COSLA-158	–	11.8 ± 3.9	–	–	> 3.59
AzTEC-14-E	(7)	–	–	–	–	–	> 3.03
AzTEC-14-W	(7)	–	–	–	–	$1.30^{+0.12}_{-0.36}$	–
AzTEC-15	(7)	–	–	–	–	$3.01^{+0.29}_{-0.37}$	–
AzTEC-16	(9)	–	–	–	1.505	$1.09^{+0.08}_{-0.06}$	–
J1000+0234	(10)	–	–	–	4.542	$4.45^{+0.08}_{-0.08}$	–
AzTEC/C1	(11)	COSLA-89	–	12.4 ± 3.7	–	5.6 ± 1.2	
Cosbo-1*	(12)	COSLA-1	–	13.8 ± 1.5	–	–	$3.83^{+0.68}_{-0.49}$
Cosbo-3	(8), (11)	COSLA-2	–	13.1 ± 2.6	2.490	$1.9^{+0.9}_{-0.5}$	–
Cosbo-8	(11)	–	–	–	–	3.1 ± 0.5	–
Cosbo-14	(12)	–	–	–	–	–	–

References. (1) Younger et al. (2007)
(2) Younger et al. (2009)
(3) Smolčić et al. (2011)
(4) Baloković et al., in prep
(5) Capak et al. (2010); Riechers et al. (2010)
(6) Karim et al., in prep
(7) Younger et al. (2009)
(8) Riechers et al., in prep.

(9) Sheth et al., in prep.

(10) Capak et al. (2009), Schinnerer et al. (2009)
(11) Smolčić et al., 2012.

(12) Aravena et al. (2010)

$^{+}$ Photometric redshifts drawn from the total χ^2 distribution as described in sect. 3.6 and *not* corrected for any systematic offsets

*Formally this source is not detected in optical, near- and mid-IR maps/catalogs, therefore we here use the mm-to-radio flux based redshift here, which is consistent with the photometric redshift given by Aravena et al. (2010)

The inner square degree of the COSMOS field was mapped with LABOCA at 870 μm to an rms of 1.5 mJy per 27.6" beam in the center and increase towards the edges of the map, which in total cover $\sim$ 0.7 deg^2. The final COSMOS LABOCA source catalog will be presented in Navarrete et al. (in prep.).

3.3 PdBI follow-up of LABOCA-COSMOS SMGs

3.3.1 Description of the observations with the PdBI

Our sample of 28 COSMOS LABOCA sources selected for PdBI follow-up observations (Table 3.2) was chosen with the requirement that the signal-to-noise is S/N$_{870\mu m}$ $\gtrsim$ 3.8. Eight other LABOCA-COSMOS sources had previously been observed with mm-interferometers[1] (see Table 3.1).

The SMGs in our sample were observed using the PdBI during two nights in Oct./Nov. 2007 (COSLA-10, and COSLA-19) and three nights in Oct./Nov. 2011 (the remaining 26 SMGs) in C- and D-configurations with 6 working antennas and the updated PdBI system. All observations were done in good/excellent millimeter weather conditions. During our 2007 observations we used the full 2 GHz bandwidth availabl e with the correlator at the PdBI, and the receivers were tuned to 232 GHz and 231.5 GHz for observations of COSLA-19 and COSLA-10, respectively. The total on-source time was 2.3 and 2.2 hrs for COSLA -10, and COSLA-19, respectively. Our 2011 observations were done using the WideX correlator covering a bandwidth of 3.6 GHz, with receivers tuned to 230 GHz (1.3mm). These observations were performed in snap-shot mode cycling through the 26 SMGs in each track and observing the phase/amplitude calibrator for 2.25 minutes every 19.5 min. The total on-source time reached is $\sim$ 43 minutes per source.

Sources J1055+018, J1005+066, J0923+392 were used for phase/amplitude calibration, and MWC349, J0923+392, 3C84 for flux calibration which we consider accurate within 10-20%. Calibration and editing w as done using the GILDAS CLIC package. For each source, the final *uv* data were collapsed in frequency. The final dirty maps reach an rms noise level of 0.55 mJy beam^{-1} and 0.39 mJy beam^{-1}, with FWHM beam sizes of $3.3'' \times 2.3''$ and $3.0'' \times 2.1''$ for COSLA-19 and COSLA-10, respectively, and an rms of 0.46 mJy beam^{-1} with FWHM $\sim 1.8'' \times 1.1''$ for the remaining SMGs.

3.3.2 PdBI mm-sources

We searched for point sources in the dirty 1.3 mm PdBI maps within a $\sim$ 14" radius from the phase center, which corresponds to the LABOCA map resolution of 27". Peaks with S/N > 4.5 were considered detections regardless of any multi-wavelength association. When such peaks where present in sidelobe-contaminated regions, we tested the reality of the sources by cleaning the map setting a CLEAN box around the brightest peak (see Appendix C for notes on individual sources). For peaks with $3 \lesssim$ S/N ≤ 4.5 we require an associated with an optical, near/mid-IR, or radio source within a radius of $\lesssim$ 1". Assuming

---

[1] COSLA-1, COSLA-2, COSLA-3, COSLA-4, COSLA-60, COSLA-73, COSLA-89, and COSLA-158

a Gaussian noise distribution, the S/N $>$ 4.5 requirement implies a false detection rate of $\sim$ 0.15% within a search radius of 14”. A mm source association with optical, NIR, MIR, or radio sources further decreases the probability that the source is false [2]. Given the surface densities of sources present in vario us catalogs the false match probabilities independently estimated for each band are 12% (optical), $\sim$ 2% (for each, UltraVista Y, J, H, Ks, and IRAC 3.6μm), and 0.017% (20 cm radio).

To further constrain the false match probability, we performed a source search in the same way as described above, but on the inverted, i.e. negative maps. We find only one occurrence of a $> 4.5\sigma$ (i.e. 4.8σ) peak ($\sim$ 10” away from the phase center and with no multi-wavelength counterpart) consistent with the above given false match probability expectation. We further find $\sim$ 10% of $3 \lesssim \mathrm{S/N} \leq 4.5$ peaks matched to multi-wavelength counterparts. This suggests a $\sim$ 10% false match probability for our $3 \lesssim \mathrm{S/N} \leq 4.5$ sources. Hereafter we con sider S/N $>$ 4.5 detections as significant, and those with $3 < \mathrm{S/N} \leq 4.5$ as tentative.

The identified 1.3 mm sources and their properties are summarized in Table 3.3 and comments on individual sources and their PdBI maps and multi-wavelength stamps are presented in Appendix A. Of the 28 LABOCA sources observed, 9 yielded no detection in the 1.3 mm maps (see next Section). Six of the 19 detected LABOCA sources break up into multiple sources, so that in total we identify 26 submm sources. Nine of these 26 sources have S/N $>$ 4.5, 7 have S/N between 4 and 4.5, and 10 between 3 and 4. The distribution of separations between the LABOCA source position and the corresponding PdBI source position is shown in Fig. 3.1. We find a median separation of 6.40” for all sources, a nd 5.95” for those with $\mathrm{S/N}_{870\mu\mathrm{m}} \geq 3.8$. This is consistent with the results based on artificial source tests performed on the LABOCA map. They result in a positional uncertainty fo r LABOCA sources down to $\mathrm{S/N}_{870\mu\mathrm{m}} = 3.8$ of $\sim$ 5.3” with an interquartile range of 3.1” – 9.8” (Navarrete et al., in prep.).

All detections except COSLA-6-1 and COSLA-6-2 are consistent with point-sources at our resolution. We extract their fluxes from the brightest pixel value in the dirty maps. The flux uncertainty is estimated as the rms noise level in the map. The fluxes for COSLA-6-1 and COSLA-6-2 were obtained by fitting a double Gaussian to the source. All fluxes (tabulated in Table 3.3) were corrected for the primary beam response of the PdBI dishes (assuming a Gaussian distribution with HPBW of 21”).

Scaling the observed 1.3 mm fluxes to the LABOCA 870 μm, and where available to the AzTEC 1.1 mm, or MAMBO 1.2 mm fluxes (Table 3.2), yields consistent values.[3] This is shown in Fig. 3.2 and described in more detai l for each source in Appendix C. This further strengthens the validity of our detections.

---

[2] If the source is *independent ly* detected in various bands then the final false match probability is given by the product of the individual-band false match probabilities.

[3] The fluxes were scaled assuming $S_\nu \propto \nu^{2+\beta}$ where S_ν is the flux density at frequency ν and $\beta = 1$ the dust emissivity index.

Table 3.2: LABOCA sources observed with the PdBI

LABOCA			AzTEC			MAMBO		
source name	position [J2000]	$F_{870\mu\mathrm{m}}$ [mJy]	source name	separation arc. sec.	$F_{1.1\mathrm{mm}}$ [mJy]	source name	separation arc. sec.	$F_{1.2\mathrm{mm}}$ [mJy]
COSLA-5	10 00 59.6 + 02 17 5.7	12.5 ± 2.6	–	–	–	Cosbo-12	9.9	4.78 ± 1.0
COSLA-6	10 01 23.5 + 02 26 11.1	16.0 ± 3.3	–	–	–	–	–	–
COSLA-8	10 00 25.6 + 02 15 1.7	6.9 ± 1.6	–	–	–	–	–	–
COSLA-9	10 00 14.2 + 01 56 40.5	14.4 ± 3.3	AzTEC/C8	3.8	8.7 ± 1.1	–	–	–
COSLA-10	10 00 8.6 + 02 13 9.7	6.6 ± 1.7	–	–	–	Cosbo-6	7.6	5.00 ± 0.9
COSLA-11	10 01 14.1 + 01 48 12.4	19.4 ± 4.5	–	–	–	–	–	–
COSLA-12	10 00 30.2 + 02 41 37.6	17.6 ± 4.2	–	–	–	–	–	–
COSLA-13	10 00 32.2 + 02 12 38.4	7.7 ± 1.9	AzTEC/C145	9.3	$3.3^{+1.1}_{-1.2}$	Cosbo-5	3.5	5.11 ± 0.9
COSLA-14	09 59 57.4 + 02 11 31.6	7.9 ± 2.1	AzTEC/C176	0.9	3.0 ± 1.2	Cosbo-10	8.0	5.88 ± 1.1
COSLA-16	10 00 51.4 + 02 33 35.7	14.0 ± 3.6	–	–	–	–	–	–
COSLA-17	10 01 36.4 + 02 11 2.9	12.5 ± 3.2	AzTEC/C12	6.2	$7.5^{+1.0}_{-1.1}$	–	–	–
COSLA-18	10 00 43.2 + 02 05 22.0	10.0 ± 2.6	AzTEC/C98	4.4	$3.8^{+1.1}_{-1.2}$	–	–	–
COSLA-19	10 00 7.7 + 02 11 42.7	6.7 ± 1.8	AzTEC/C34	8.9	$5.3^{+1.1}_{-1.2}$	Cosbo-4	6.4	5.55 ± 0.9
COSLA-23	10 00 10.1 + 02 13 33.3	6.4 ± 1.6	–	–	–	Cosbo-2	4.7	5.77 ± 0.9
COSLA-25	09 58 51.5 + 02 15 53.7	13.4 ± 3.8	–	–	–	–	–	–
COSLA-30	09 58 47.7 + 02 21 7.4	14.4 ± 4.2	–	–	–	–	–	–
COSLA-33	10 00 9.2 + 02 19 11.6	5.3 ± 1.8	–	–	–	–	–	–
COSLA-35	10 00 23.4 + 02 21 55.5	8.2 ± 2.2	AzTEC/C38	6.4	$5.1^{+1.2}_{-1.1}$	–	–	–
COSLA-38	10 00 12.1 + 02 14 57.2	5.8 ± 1.6	–	–	–	Cosbo-19	13.06	2.95 ± 0.9
COSLA-40	09 59 26.3 + 02 20 6.0	11.1 ± 3.4	AzTEC/C117	13.8	$3.7^{+1.1}_{-1.2}$	–	–	–
COSLA-47	10 00 33.1 + 02 26 6.9	9.0 ± 2.8	AzTEC/C80	13.4	4.1 ± 1.1	–	–	–
COSLA-48	10 00 24.7 + 02 17 42.3	6.1 ± 1.7	AzTEC/C160	10.0	3.1 ± 1.2	Cosbo-7	12.0	5.00 ± 0.9
COSLA-50	10 00 19.0 + 02 16 54.0	5.6 ± 1.6	–	–	–	–	–	–
COSLA-51	10 00 11.5 + 02 12 7.1	6.2 ± 1.7	–	–	–	–	–	–
COSLA-54	09 58 38.3 + 02 14 2.5	11.6 ± 4.1	AzTEC/C13	8.4	$8.7^{+1.3}_{-1.4}$	–	–	–
COSLA-62	10 01 53.2 + 02 20 9.5	12.5 ± 3.6	–	–	–	–	–	–
COSLA-128	10 01 38.3 + 02 23 36.1	11 ± 3.5	–	–	–	–	–	–
COSLA-161	10 00 15.6 + 02 12 36.0	5.2 ± 1.7	AzTEC/C158	15.6	$3.2^{+1.1}_{-1.2}$	Cosbo-13S	5.9	1.37 ± 0.9

Table 3.3: PdBI detections

source[‡] name	position [J2000]		$F_{1.3\mathrm{mm}}$ [mJy]	S/N	LABOCA dist. ["]	LABOCA S/N$_{870\mu\mathrm{m}}$	redshift spectroscopic	redshift photometric[+‡]	redshift mm-to-radio
COSLA-5	10 00 59.521	+02 17 02.57	2.04 ± 0.49	4.1	3.4	5.0	–	$0.85^{+0.07}_{-0.06}$	–
COSLA-6-N	10 01 23.640	+02 26 08.42	2.66 ± 0.49	5.4	3.4	4.7	–	–	$4.01^{+1.51}_{-0.83}$
COSLA-6-S	10 01 23.570	+02 26 03.62	3.08 ± 0.65	4.8	7.6	4.7	–	$0.48^{+0.19}_{-0.22}$	–
COSLA-8	10 00 25.550	+02 15 08.44	2.65 ± 0.62	4.2	6.8	4.6	–	$1.83^{+0.41}_{-1.31}$	–
COSLA-9-N	10 00 13.750	+01 56 41.54	1.69 ± 0.47	3.2	7.0	4.5	–	$2.62^{+0.60}_{-2.02}$	–
COSLA-9-S	10 00. 13.829	+01 56 38.64	1.87 ± 0.58	3.2	5.8	4.5	–	$1.90^{+0.26}_{-0.31}$	–
COSLA-11-N	10 01 14.260	+01 48 18.86	2.15 ± 0.62	3.5	6.9	4.4	–	$0.75^{+0.23}_{-0.25}$	–
COSLA-11-S	10 01 14.200	+01 48 10.31	1.43 ± 0.48	3.0	2.6	4.4	–	$3.00^{+0.14}_{-0.07}$	–
COSLA-13	10 00 31.840	+02 12 42.81	2.38 ± 0.61	3.8	7.0	4.3	2.175	$2.11^{+0.14}_{-0.12}$	–
COSLA-16-N	10 00 51.585	+02 33 33.56	1.39 ± 0.32	4.3	3.5	4.2	–	$2.16^{+0.12}_{-0.25}$	–
COSLA-16-S	10 00 51.554	+02 33 32.09	1.19 ± 0.33	3.6	4.3	4.2	–	–	$2.40^{+0.62}_{-0.51}$
COSLA-16-E	10 00 51.780	+02 33 33.58	2.26 ± 0.58	3.9	6.0	4.2	–	$1.25^{+3.03}_{-1.15}$	–
COSLA-17-S	10 01 36.772	+02 11 04.87	3.02 ± 0.57	5.3	5.9	4.2	–	$0.70^{+0.21}_{-0.22}$	–
COSLA-17-N	10 01 36.811	+02 11 09.66	3.55 ± 0.77	4.6	9.1	4.2	–	$3.37^{+0.14}_{-0.22}$	–
COSLA-18	10 00 43.190	+02 05 19.17	2.15 ± 0.48	4.5	2.8	4.2	–	$2.90^{+0.31}_{-0.43}$	–
COSLA-19	10 00 08.226	+02 11 50.677	3.17 ± 0.76	4.1	11.2	4.1	–	–	$3.98^{+1.62}_{-0.90}$
COSLA-23-N	10 00 10.161	+02 13 34.95	3.42 ± 0.47	7.3	1.9	3.9	–	$4.00^{+0.67}_{-0.90}$	–
COSLA-23-S	10 00 10.070	+02 13 26.87	3.70 ± 0.60	6.2	6.4	3.9	–	$2.58^{+1.52}_{-2.48}$	–
COSLA-33	10 00 9.580	+02 19 13.86	1.78 ± 0.58	3.1	6	3.8	–	$3.27^{+0.22}_{-0.20}$	–
COSLA-35	10 00 23.651	+02 21 55.22	2.15 ± 0.51	4.2	3.7	3.8	–	$1.91^{+1.75}_{-0.64}$	–
COSLA-38	10 00 12.590	+02 14 44.31	8.19 ± 1.85	4.4	14.8	3.7	–	$2.44^{+0.12}_{-0.11}$	–
COSLA-40	09 59 25.909	+02 19 56.40	3.41 ± 1.02	3.4	11.3	3.7	–	$1.30^{+0.09}_{-0.11}$	–
COSLA-47	10 00 33.350	+02 26 01.66	3.11 ± 0.59	5.3	6.4	3.6	–	$2.36^{+0.24}_{-0.24}$	–
COSLA-54	09 58 37.989	+02 14 08.52	3.26 ± 0.65	5.0	7.6	3.6	–	$2.64^{+0.38}_{-0.26}$	–
COSLA-128	10 01 37.990	+02 23 26.50	4.50 ± 0.94	4.8	10.7	3.1	–	$0.10^{+0.19}_{-0.00}$	–
COSLA-161	10 00 16.150	+02 12 38.27	2.54 ± 0.74	3.4	8.5	3.1	0.187	$0.19^{+0.05}_{-0.03}$	–

[‡] **Note.** S/N > 4.5 detections are marked bold-faced

[‡+] Photometric redshifts drawn from the total χ^2 distribution as described in sect. 3.6 and *not* corrected for any systematic offsets

Figure 3.1: Distribution of separations between the PdBI sources and the corresponding LABOCA-COSMOS sources.

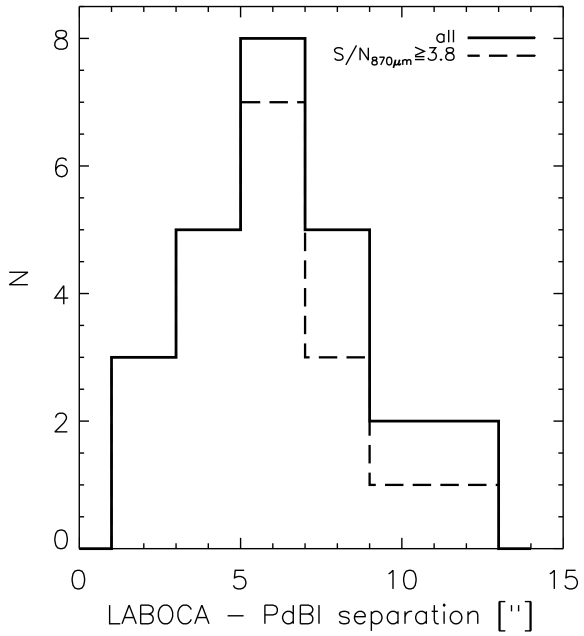

3.3.3 Non-detections

Nine LABOCA sources remain undetected within our PdBI observations. The reasons for this could be that i) the LABOCA source is fainter than our PdBI sensitivity limit ($1\sigma \sim 0.46$ mJy), ii) when observed at $\sim$ 1.5” resolution the LABOCA source breaks-up into multiple components fainter than our flux limit, or iii) the LABOCA source is spurious. To investigate this further we have made use of the COSMOS multi-wavelength data by assigning statistical counterparts to those LABOCA sources given our radio, 24 μm, and IRAC data (see Sec. 3.5.2.1 for details). For 3/9 sources we find no robust or tentative counterparts while for 6/9 we find either one or several tentative or robust counterparts (see Fig. 3.6 and Appendix C for details). For the latter sources we have then identified the maximum pixel value within a circular annulus of 1” radius in the 1.3 mm map. If multiple potential counterparts were present, we have summed up the maximum pixel values. Such derived 1.3 mm fluxes, compared to the LABOCA 870 μm fluxes are shown in Fig. 3.2. They agree well with the LABOCA fluxes suggesting that the LABOCA sources are not spurious, but single or multiple-component sources fainter than our 1.3 mm flux limit. This is also consistent with the results based on artificial source tests performed on the LABOCA map which yield that down to a S/N$_{870\mu m}$ = 3.8 5 ± 3 spurious sources are expected (Navarrete et al., in prep.).

3.3.4 Panchromatic properties of PdBI-detected LABOCA-COSMOS SMGs

Twenty-three of the 26 PdBI-detected LABOCA SMGs can be associated with multi-wavelength counterparts drawn from the deep COSMOS photometric catalog. In addition to the UV to MIR photometry from the COSMOS multi-wavelength catalog we have

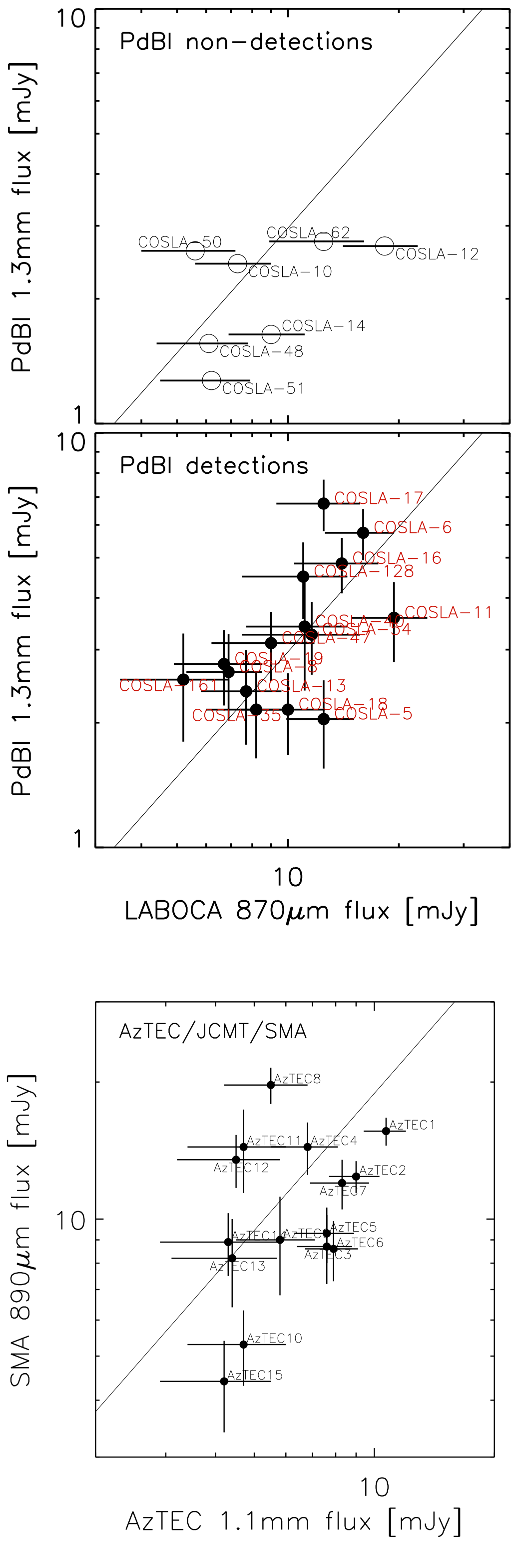

Figure 3.2: Comparison between LABOCA 870 μm and PdBI 1.3 mm fluxes for SMGs (indicated in the panel) detected (middle panel) and not detected (top panel) with the PdBI. For LABOCA sources identified as multiple PdBI sources the individual PdBI source fluxes were added, and for the LABOCA sources not detected by PdBI 1.3mm flux estimates for the most likely multi-wavelength counterparts were extracted from the PdBI maps (see Sec. 3.3.3 for details). The bottom panel shows the comparison between AzTEC 1.1 mm and SMA 890 μm fluxes (adopted from Younger et al. 2007, 2009) for AzTEC/ JCMT SMGs in our 1.1mm-selected sample. The solid line in all panels shows the flux ratios for a spectral power law index of 3.

added deep YJHK imaging from the recent UltraVista Data Release 1. Their photometry is presented in Table C.1. The COSMOS spectroscopic database (Lillly et al. 2007; Lilly et al. 2009; Trump et al. 2007) provided spectroscopic redshifts for the COSLA-13 and COSLA-161 counterparts. From the 26 SMGs identified interferometr ically only COSLA-161 was found to be associated with X-ray emission in the Chandra-COSMOS data (Elvis et al. 2009).

For each PdBI source we extracted the 1.4 GHz flux from the VLA-COSMOS Deep map (Schinnerer et al. 2010) using the AIPS task MAXFIT, and tabulate it in Table C.1. Thirteen of the 26 sourc es ($\sim$ 50% with a Poisson error of $\pm$14%) are associated with a $> 3\sigma$ radio peak, where the average rms noise level is $rms_{1.4\mathrm{GHz}} = 9$ μJy/beam. Nine sources are detected with $\mathrm{S/N}_{1.4\mathrm{GHz}} > 4$. This radio detection fraction does not depend on the significance of the PdBI-source: from those with $\mathrm{S/N} > 4.5$ we find 5 of 9 with a radio counterpart, from those with $\mathrm{S/N} \geq 5$ 3 of 6 show a radio source.

3.4 Statistical samples of SMGs in the COSMOS field identified at intermediate ($\lesssim$ 2") resolution

Our PdBI observations yielded 26 (9 significant $\mathrm{S/N} > 4.5$ and 17 tentative, $3 < \mathrm{S/N} \leq 4.5$) source detections at 1.3 mm. Combined with previous mm-interferometric detections of SMGs in the COSMOS field this adds to 50 SMGs detected with mm-interferometers. To date this is the largest interferometric SMG sample. It can be utilized, e.g., for a critical assessment of statistical co unterpart identification methods, and to measure the redshift distribution of SMGs with unambiguously determined multi-wavelength counterparts.

In the following we examine two statistically significant samples of COSMOS SMGs detected at mm-wavelengths at $\lesssim$ 2" resolution:

> **1.1mm-selected sample:** 15 SMGs drawn from the 1.1 mm AzTEC/JCMT-COSMOS survey at 18" angular resolution (AzTEC-1 to AzTEC-15; see Table 3.1) that form a ($\mathrm{S/N}_{1.1\mathrm{mm}} > 4.5$) and flux-limited ($F_{1.1\mathrm{mm}} \gtrsim 4.2$ mJy), 1.1 mm sample. All 15 SMGs were followed-up and detected with the SMA at 890 μm, yielding 17 interferometric sources (as two were found to be multiples; Younger et al. 2007, 2009). More details about the multi-wavelength photometry of the counterparts are provided in Appendix D.
>
> **870μm-selected sample**: LABOCA-COSMOS sources that were identified at 27" angular resolution and confirmed through (sub)mm-interferometry at $\lesssim$ 2" resolution (Younger et al. 2007, 2009; Aravena et al. 2010a; Smolčić et al. 2012b, , this work). Thirty six LABOCA sources were followed-up in total with the SMA, CARMA, and PdBI, and 9 resulted in no detection within the PdBI observations down to a depth of $\sim$ 0.46 mJy/beam. The remaining 27 yielded 16 significant ($\mathrm{S/N} > 4.5$) and 18 tentative ($3 < \mathrm{S/N} \leq 4.5$) interferometric (sub)mm-detections. For the less significant detections we required an association with a source seen at other wavelengths (see Table 3.3 and Table 3.1). The 1 6 *significant* detections form the least biased sample, and we hereafter refer to this subsample as the least-biased

870μm-selected sample.

The sources in the 1.1mm- and 870μm-selected samples are summarized in Table 3.1 and Table 3.4. Five SMGs belong to both samples[4] (see Table 3.1). Hereafter we will use these two samples to investigate blending, counterpart properties, and the redshift distribution of SMGs. For clarity a master table o fall interferometrically observed SMGs in the COSMOS field is given in Table 3.5.

3.5 Properties of single-dish detected SMGs when mapped at intermediate angular resolution

In this section we investigate the multiplicity of SMGs detected at intermediate ($\lesssim$ 2") angular resolution, and the statistical multi-wavelength counterpart association that is commonly applie d to single-dish detected SMGs.

3.5.1 Blending: single-dish SMGs breaking-up into multiple interferometric sources

In the 1.1mm-selected sample of the 15 AzTEC sources mapped with the SMA, AzTEC-14 clearly breaks up into two sources within the AzTEC beam when observed at ∼ 2" angular resolution (AzTEC-14-E and AzTEC-14 -W), while AzTEC-11 shows extended structure and is best fit by a double Gaussian (see Appendix D and Younger et al. 2009, for details). Thus, in the 1.1mm-selected sample only two of 15 (13% with a Poisson un certainty of 9%) single-dish sources are blended, i.e., they break up into multiple components when observed at intermediate angular resolution. The comparison between the single-dish 1.1 mm AzTEC an d the interferometric SMA 890 μm fluxes for these 15 sources, shown in the bottom panel of Fig. 3.2, suggests that although the agreement is reasonable, it is possible that some faint companions were missed thus potentially increasing the fraction of multiples in this sample.

For the 870μm-selected sample of 36 LABOCA-COSMOS SMGs followed-up and 27 out of these detected with interferometers, 6 SMGs[5] ($22\% \pm 9\%$) break up into multiple sources when observed with interferometers. This is within the statistical uncertainties of the results for the 1.1mm-selected sample. Three more LABOCA SMGs detected by PdBI[6] may also consist of multiple components (see Appendix C, Aravena et al. 2010b and Smolčić et al. 2012 for details) , and the P-statistics (see next section) suggests that at least four of the LABOCA sources not detected by our PdBI observations[7] are potential blends. This suggests a fraction of $\gtrsim 6/36 \approx 17\%$, potentially rising up to ∼ 40% of LABOCA sources blended within the single-dish beam. This is consistent with the fraction obtained if only the least-biased-870μm-selected sample is considered (see Table 3.4).

---

[4] AzTEC-1/COSLA-60, AzTEC-2/ COSLA-4, AzTEC-8/COSLA-73, AzTEC-9/COSLA-3, AzTEC-13/COSLA-158

[5] COSLA-6, COSLA-9, COSLA-11, COSLA-16, COSLA-17, COSLA-23

[6] CO SLA-3, COSLA-5, and COSLA-47

[7] COSLA-10, COSLA-12, COSLA-48, and COSLA-50

Table 3.4: Statistical samples of SMGs with $\lesssim 2''$ angular resolution mm-detections in the COSMOS field

1.1mm-selected sample	best redshift	least-biased-870μm-selected sample	best redshift
AzTEC-1	4.64^{+}	COSLA-1	$3.83^{+0.68}_{-0.49}{}^{*}$
AzTEC-2	1.125^{+}	COSLA-2	2.490^{+}
AzTEC-3	5.299^{+}	COSLA-3	1.357^{+}
AzTEC-4	$4.93^{+0.43}_{-1.11}{}^{\#}$	COSLA-4	1.125^{+}
AzTEC-5	3.971^{+}	COSLA-6-N	$4.01^{+1.51}_{-0.83}{}^{*}$
AzTEC-6	0.802^{+}	COSLA-6-S	$0.48^{+0.19}_{-0.22}$
AzTEC-7	2.30 ± 0.10	COSLA-17-S	$0.70^{+0.21}_{-0.22}$
AzTEC-8	3.179^{+}	COSLA-17-N	$3.54^{+0.14}_{-0.22}{}^{\#}$
AzTEC-9	1.357^{+}	COSLA-23-N	$4.20^{+0.67}_{-0.90}{}^{\#}$
AzTEC-10	$2.79^{+1.86}_{-1.29}$	COSLA-23-S	$2.58^{+1.52}_{-2.48}$
AzTEC-11**	1.599^{+}	COSLA-47	$2.36^{+0.24}_{-0.24}$
AzTEC-11N**	$1.51^{+0.41}_{-0.92}$	COSLA-54	$2.64^{+0.38}_{-0.26}$
AzTEC-11S**	> 2.58	COSLA-60	4.64^{+}
AzTEC-12	$2.54^{+0.13}_{-0.33}$	COSLA-73	3.179^{+}
AzTEC-13	$> 3.59^{*}$	COSLA-128	$0.10^{+0.19}_{-0.00}$
AzTEC-14-E	$> 3.03^{*}$	COSLA-158	$> 3.59^{*}$
AzTEC-14-W	$1.30^{+0.12}_{-0.36}$		
AzTEC-15	$3.17^{+0.29}_{-0.37}{}^{\#}$		

Five SMGs belong to both samples; AzTEC-1/COSLA-60, AzTEC-2/COSLA-4, AzTEC-8/COSLA-73, AzTEC-9/COSLA-3, AzTEC-13/COSLA-158

** Here we keep the nomenclature given by Younger et al. (2009). Note however that AzTEC-11-S is the northern component of the AzTEC-11 SMG, and AzTEC-11-N is its southern component (see Tab. 1 in Younger et al. 2009)

$^{+}$ spectroscopic redshift (see Table 3.1 for references)

* mm-to-radio flux ratio based redshift

$^{\#}$ photometric redshift corrected for the systematic offset of $0.04(1+z)$, see Fig. 3.8, with errors drawn from the total χ^2 distribution

Table 3.5: Master table of interferometrically observed SMGs in the COSMOS field

Source§	other names	(sub)mm-interferometry observed	detected	statistical interferometric sample
AzTEC-1$^{(1,5)}$	COSLA-60$^{(4)}$, AzTEC/C5$^{(2)}$	SMA, CARMA, PdBI	√	1.1mm, 870μm, least-biased-870μm
AzTEC-2$^{(1,5)}$	COSLA-4$^{(4)}$, AzTEC/C3$^{(2)}$	SMA, CARMA	√	1.1mm, 870μm, least-biased-870μm
AzTEC-3$^{(1,5)}$	AzTEC/C138$^{(2)}$	SMA, CARMA, PdBI	√	1.1mm
AzTEC-4$^{(1,5)}$	AzTEC/C4$^{(2)}$	SMA	√	1.1mm
AzTEC-5$^{(1,5)}$	AzTEC/C42$^{(2)}$	SMA	√	1.1mm
AzTEC-6$^{(1,5)}$	AzTEC/C106$^{(2)}$	SMA	√	1.1mm
AzTEC-7$^{(1,5)}$		SMA	√	1.1mm
AzTEC-8$^{(1,6)}$	COSLA-73$^{(4)}$, AzTEC/C2$^{(2)}$	SMA	√	1.1mm, 870μm, least-biased-870μm
AzTEC-9$^{(1,6)}$	COSLA-3$^{(4)}$, AzTEC/C14$^{(2)}$	SMA	√	1.1mm, 870μm, least-biased-870μm
AzTEC-10$^{(1,6)}$		SMA	√	1.1mm
AzTEC-11$^{(1,6)}$	AzTEC-11-N$^{(6)}$, AzTEC-11-S$^{(6)}$, AzTEC/C22$^{(2)}$	SMA	√	1.1mm
AzTEC-12$^{(1,6)}$	AzTEC/C18$^{(2)}$	SMA	√	1.1mm
AzTEC-13$^{(1,6)}$	COSLA-158$^{(4)}$	SMA	√	1.1mm, 870μm, least-biased-870μm
AzTEC-14$^{(1,6)}$	AzTEC-14-E$^{(6)}$, AzTEC-14-W$^{(6)}$	SMA	√	1.1mm
AzTEC-15$^{(1,6)}$	AzTEC/C10$^{(2)}$	SMA	√	1.1mm
AzTEC-16$^{(1,13)}$	–	CARMA	√	–
J1000+0234$^{(1,14)}$	AzTEC/C17$^{(2)}$	VLA	√	–
AzTEC/C1$^{(2,7)}$	COSLA-89$^{(4)}$	CARMA	√	870μm
Cosbo-1$^{(3,16)}$	COSLA-1$^{(4)}$, AzTEC/C7$^{(2)}$	SMA	√	870μm, least-biased-870μm
Cosbo-3$^{(3,7)}$	COSLA-2$^{(4)}$, AzTEC/C6$^{(2)}$	CARMA	√	870μm, least-biased-870μm
Cosbo-8$^{(3,7)}$	AzTEC/C118$^{(2)}$	CARMA	√	–
Cosbo-14$^{(3,16)}$		SMA	√	–
COSLA-5$^{(4,17)}$	Cosbo-12$^{(3)}$	PdBI	√	870μm
COSLA-6$^{(4,17)}$	COSLA-6-N$^{(17)}$, COSLA-6-S$^{(17)}$	PdBI	√	870μm, least-biased-870μm
COSLA-8$^{(4,17)}$		PdBI	√	870μm
COSLA-9$^{(4,17)}$	AzTEC/C8$^{(2)}$, COSLA-9-N$^{(17)}$, COSLA-9-S$^{(17)}$	PdBI	√	870μm
COSLA-10$^{(4,17)}$	Cosbo-6$^{(3)}$	PdBI	–	–
COSLA-11$^{(4,17)}$	COSLA-11-N$^{(17)}$, COSLA-11-S$^{(17)}$	PdBI	√	870μm
COSLA-12$^{(4,17)}$		PdBI	–	–
COSLA-13$^{(4,17)}$	AzTEC/C145$^{(2)}$, Cosbo-5$^{(3)}$	PdBI	√	870μm
COSLA-14$^{(4,17)}$	AzTEC/C176$^{(2)}$, Cosbo-10$^{(3)}$	PdBI	–	–
COSLA-16$^{(4,17)}$	COSLA-16-N$^{(17)}$, COSLA-16-S$^{(17)}$	PdBI	√	870μm
COSLA-17$^{(4,17)}$	AzTEC/C12$^{(2)}$, COSLA-17-N$^{(17)}$, COSLA-17-S$^{(17)}$	PdBI	√	870μm, least-biased-870μm
COSLA-18$^{(4,17)}$	AzTEC/C98$^{(2)}$	PdBI	√	870μm
COSLA-19$^{(4,17)}$	AzTEC/C34$^{(2)}$, Cosbo-4$^{(3)}$	PdBI	√	870μm
COSLA-23$^{(4,17)}$	Cosbo-2$^{(3)}$, COSLA-23-N$^{(17)}$, COSLA-23-S$^{(17)}$	PdBI	√	870μm, least-biased-870μm
COSLA-25$^{(4,17)}$		PdBI	–	–
COSLA-30$^{(4,17)}$		PdBI	–	–
COSLA-33$^{(4,17)}$		PdBI	√	870μm
COSLA-35$^{(4,17)}$	AzTEC/C38$^{(2)}$	PdBI	√	870μm
COSLA-38$^{(4,17)}$	Cosbo-19$^{(3)}$	PdBI	√	870μm
COSLA-40$^{(4,17)}$	AzTEC/C117$^{(2)}$	PdBI	√	870μm
COSLA-47$^{(4,17)}$	AzTEC/C80$^{(2)}$	PdBI	√	870μm, least-biased-870μm
COSLA-48$^{(4,17)}$	AzTEC/C160, Cosbo-7$^{(3)}$	PdBI	–	–
COSLA-50$^{(4,17)}$		PdBI	–	–
COSLA-51$^{(4,17)}$		PdBI	–	–
COSLA-54$^{(4,17)}$	AzTEC/C13$^{(2)}$	PdBI	√	870μm, least-biased-870μm
COSLA-62$^{(4,17)}$		PdBI	–	–
COSLA-128$^{(4,17)}$		PdBI	√	870μm, least-biased-870μm
COSLA-161$^{(4,17)}$	AzTEC/C158$^{(2)}$, Cosbo-13S$^{(3)}$	PdBI	√	870μm, least-biased-870μm

---

§ **References.** (1) Scott et al. (2008); (2) Aretxaga et al. (2011); (3) Bertoldi et al. (2007); (4) Navarrete et al., in prep.; (5) Younger et al. (2007); (6) Younger et al. (2009); (7) Smolčić et al. (2011); (8) Baloković et al., in prep.; (9) Capak et al. (2010); Riechers et al. (2010); (10) Karim et al., in prep.; (11) Younger et al. (2009); (12) Riechers et al., in prep.; (13) Sheth et al., in prep.; (14) Capak et al. (2009); Schinnerer et al. (2009); (15) Smolčić et al., 2012; (16) Aravena et al. (2010); (17) this work

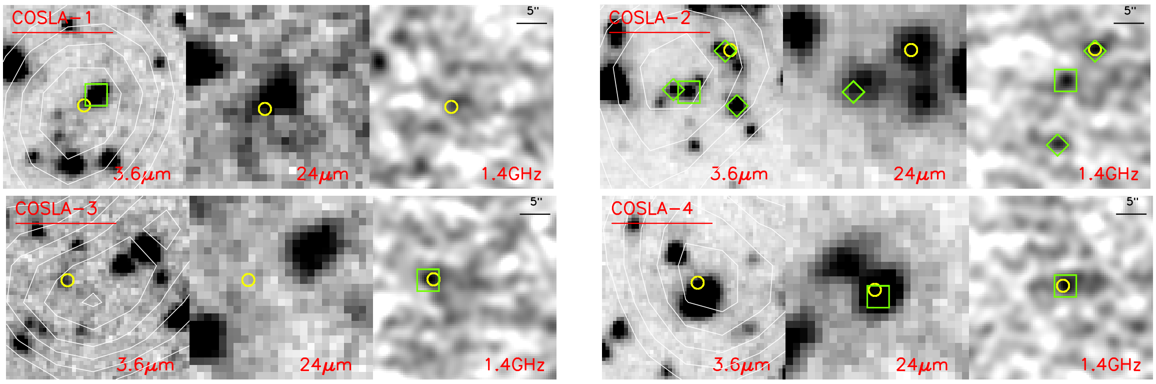

Figure 3.3: 3.6 μm, 24 μm, and 20 cm stamps (30" × 30" area) for LABOCA COSMOS sources detected by mm-interferometers at $\lesssim$ 2" resolution (see Table 3.3). The bands and sources are indicated in the panels and the names of sources detected with interferometers at S/N $>$ 4.5 are underlined. The thick yellow circle, 2" in diameter, indicates the mm-interferom eter position. Robust (square) and tentative (diamond) counterparts determined via P-statistic in each particular (3.6 μm, 24 μm, and 20 cm) band are also shown (see text for details; see al so Table 3.6). For each source LABOCA contours in 1σ steps starting at 2σ (with locally determined rms) are overlaid onto the 3.6 μm stamp.

3.5.2 Counterpart assignment methods to single-dish detected SMGs

Here we perform a statistical counterpart assignment for the SMGs detected at low angular resolution in our 1.1mm- and 870μm-selected samples, and compare them with the exact positions obtained from the interferometers.

3.5.2.1 P -statistic

The most common way to associate single-dish identified SMGs with counterparts in higher resolution maps is through the P-statistic (Downes 1986), i.e., the corrected Poisson probability that, e.g., a radio source is identified by chance in a background of randomly distributed radio/IR sources (Downes 1986; Ivison et al. 2002, 2005). For a potential radio counterpart of flux density S at distance r from the SMG position, $P_c = 1 - \exp(-P_S[1 + \ln(P_S/P_{3\sigma})])$, where $P_S = 1 - \exp(-\pi r^2 n_S)$ is the raw probability to find a source brighter than S within a distance r from the (sub-)mm source, n_S is the local density of sources brighter than the candidate, and $P_{3\sigma} = \pi r^2 n_{3\sigma}$ is the critical Poisson level, with $n_{3\sigma}$ being the source surface density above the 3σ detection level. Robust counterparts are considered those with $P_c \leq 0.05$, while tentative counterparts have $0.05 < P_c < 0.2$. The samples used to search for SMG counterparts are commonly radio, 24μm, and/or IRAC flux or color-selected (e.g., Pope et al. 2005; Biggs et al. 2011; Yun et al. 2012) and the maximum search radius is adjusted to the positional uncertainty of the SMG.

With search radii of 9", and 13.5" for the AzTEC and LABOCA SMGs, respectively, we independently computed the P-statistics for the potential radio, 24 μm, and IRAC color selected ($m_{3.6\mu\mathrm{m}} - m_{4.5\mu\mathrm{m}} \geq 0$) counterparts and display those in Tables 3.6 and 3.7, and Figs. 3.3, 3.5, and 3.7.

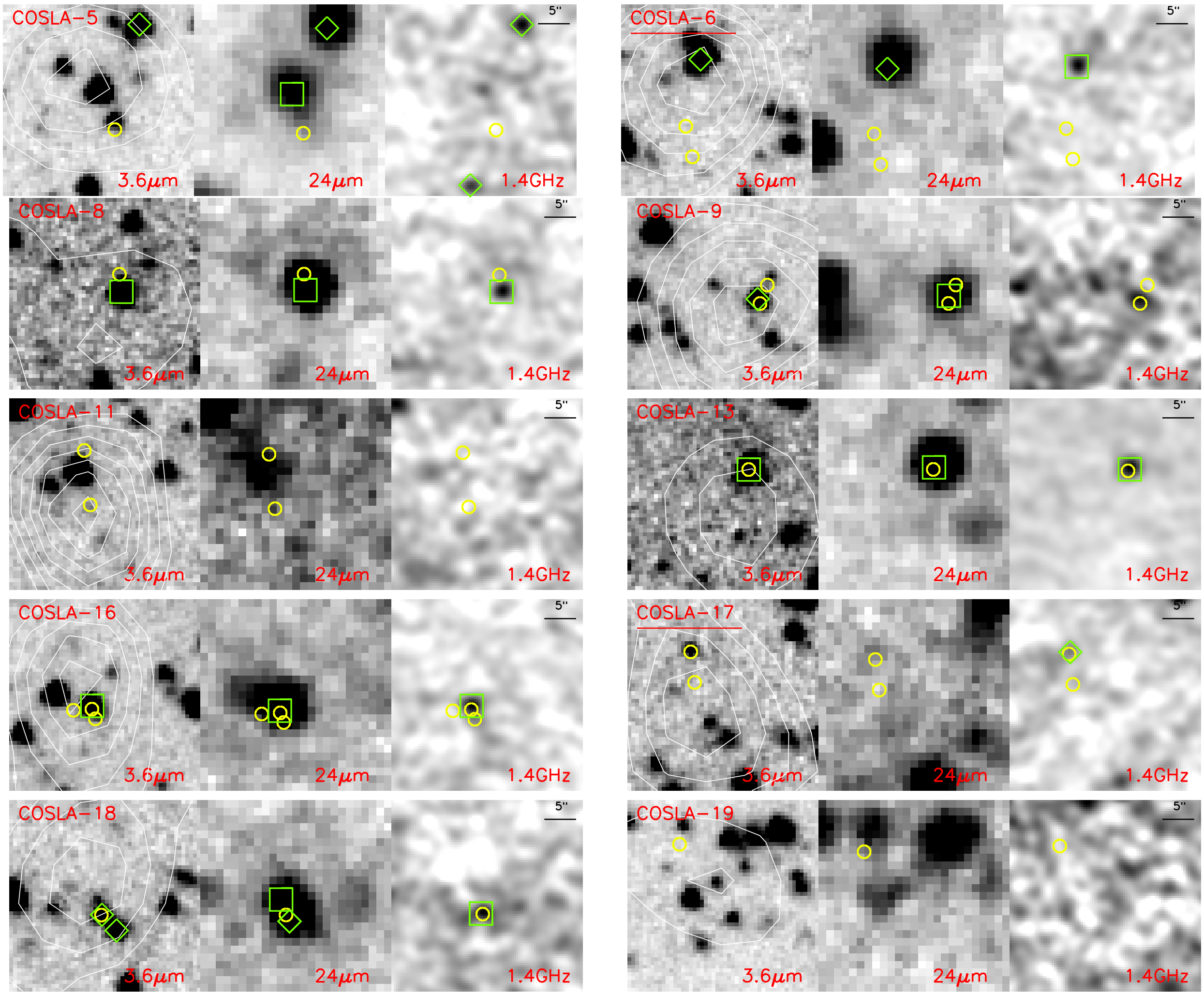

Figure 3.4: Fig. 3.3 continued.

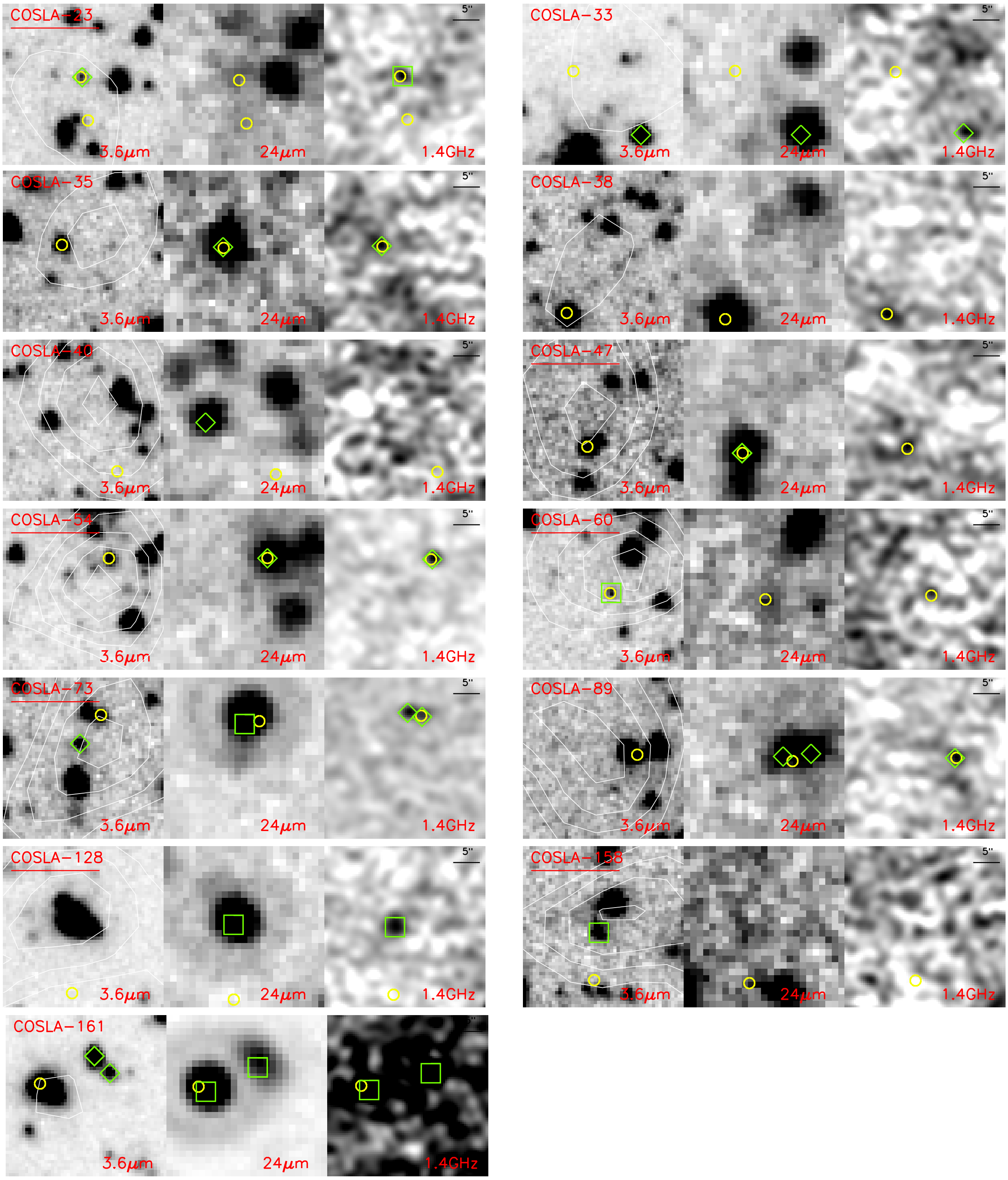

Figure 3.5: Fig. 3.3 continued.

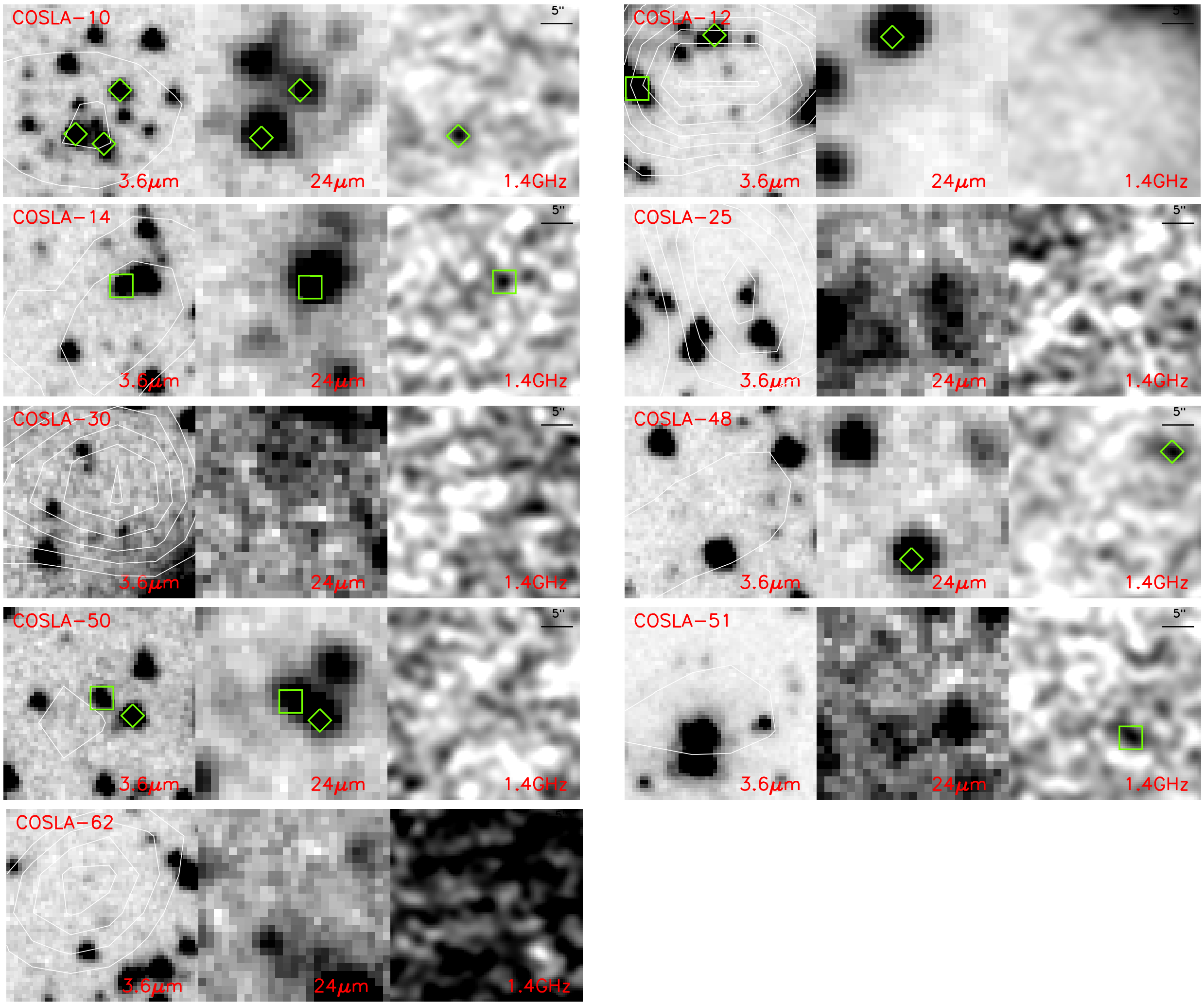

Figure 3.6: Same as Fig. 3.3 but for LABOCA sources not detected within our PdBI observations.

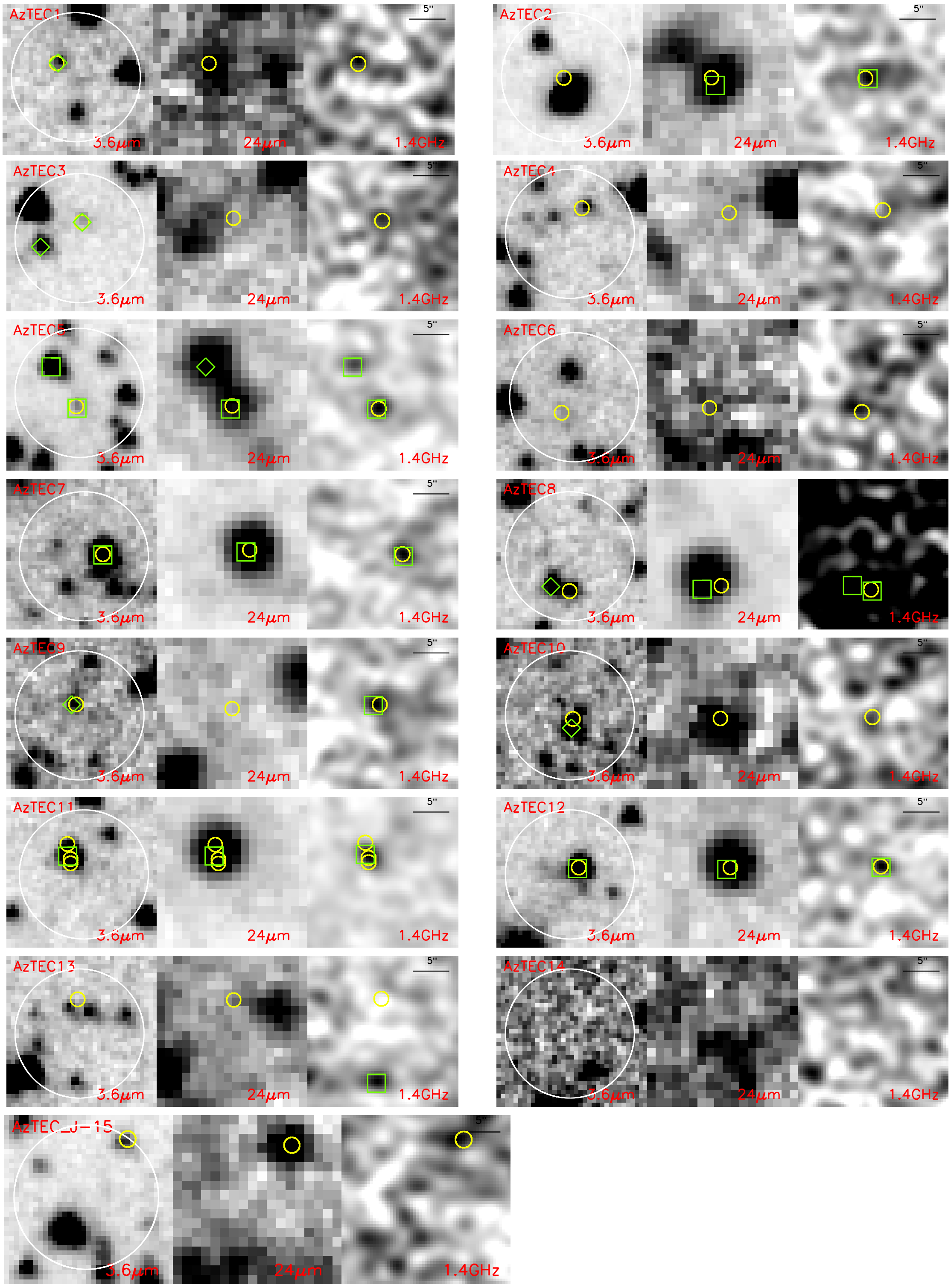

Figure 3.7: Same as Fig. 3.3, but for AzTEC/JCMT/SMA COSMOS sources in our 1.1mm-selected sample (see Table 3.1 and Table 3.7). The AzTEC/JCMT beam is indicated by the circle in the 3.6 μm stamp.

Table 3.6: LABOCA sources observed with mm-interferometers at $\lesssim 2$” resolution, and with counterparts identified via P-statistic.

name	VLA ID* COSMOSVLA*	d_{VLA} [”]	MIPS ID*	d_{MIPS} [”]	IRAC ID*	d_{IRAC} [”]	P_{VLA}	P_{MIPS}	P_{IRAC}
COSLA-1	–	–	–	–	***181505***	***0.54***	–	–	***0.005***
COSLA-2	**_J100056.94+022017.5**	**9.84**	**15949**	**9.89**	**198261**	**9.47**	**0.083**	**0.273**	**0.121**
	–	–	*13173*	*3.33*	*197942*	*1.13*	–	*0.071*	*0.005*
	–	–	15948	7.20	197682	7.45	–	0.262	0.065
	_J100057.27+022012.6	*3.12*	–	–	–	–	*0.027*	–	–
	DP_J100057.35+022002.0	7.82	–	–	197036	7.78	0.075	–	0.538
COSLA-3	***_J095957.30+022730.4***	***5.94***	–	–	***225725***	***5.70***	***0.046***	–	***0.347***
COSLA- 4	***DP_J100008.02+022612.1***	***1.00***	***9851***	***1.05***	–	–	***0.002***	–	***0.006***
COSLA-5	_J100059.24+021719.1	13.79	17275	13.53	187234	13.60	0.105	0.091	0.084
	–	–	*17272*	*1.80*	–	–	–	–	*0.006*
	_J100059.78+021653.9	13.25	–	–	185375	13.49	0.167	–	0.277
COSLA-6	*_J100123.52+022618.1*	*6.46*	*16498*	*6.68*	*221331*	*6.85*	*0.045*	*0.110*	*0.073*
COSLA-8	*_J100025.52+021505.8*	*2.54*	*11883*	*2.47*	*178641*	*2.51*	*0.012*	*0.010*	*0.024*
COSLA-9	–	–	***15193***	***5.71***	***109636***	***5.33***	–	***0.045***	***0.087***
COSLA-13	***_J100031.82+021243.1***	***5.84***	***11821***	***5.77***	***169468***	***5.49***	***0.023***	***0.030***	***0.046***
COSLA-16	***_J100051.58+023334.3***	***2.63***	***6490***	***2.86***	***248076***	***2.67***	***0.010***	***0.018***	***0.029***
COSLA-17	**_J100136.80+021109.9**	**8.64**	–	–	**163233**	**8.80**	**0.127**	–	**0.532**
COSLA-18	***_J100043.20+020519.2***	***2.84***	***11637***	***1.31***	***142009***	***2.81***	bf*0.024*	***0.013***	***0.055***
	–	–	11636	3.82	141453	5.57	–	0.060	0.185
COSLA-23	***_J100010.12+021334.9***	***1.65***	–	–	***172879***	***1.63***	***0.016***	–	***0.104***
COSLA-33	_J100008.73+021902.4	11.45	9597	11.55	193342	11.73	0.108	0.155	0.058
COSLA-35	**_J100023.65+022155.3**	**4.16**	**1749**	**4.15**	**204426**	**4.06**	**0.070**	**0.062**	**0.211**
COSLA-40	–	–	11997	6.65	197365	6.12	–	0.127	0.242
COSLA-47	–	–	**9849**	**6.20**	**219900**	**6.13**	–	**0.094**	**0.249**
COSLA-54	***_J095837.96+021408.5***	***7.91***	***9392***	***7.72***	***175095***	***7.88***	***0.052***	***0.160***	***0.250***
COSLA-60	–	–	–	–	***233568***	***1.65***	–	–	***0.043***
COSLA-73	***_J095959.33+023440.8***	***8.62***	***17463***	***7.55***	***252264***	***8.78***	***0.0 78***	***0.031***	***0.429***
	_J095959.50+023441.5	*8.64*	*17463*	*7.55*	*252508*	*8.71*	*0.057*	*0.031*	*0.364*
	–	–	–	–	251986	2.73	–	–	0.128
COSLA-89	**_J100141.77+022713.0**	**5.96**	**16255**	**4.65**	–	–	**0.113**	–	**0.068**
	–	–	16256	9.84	–	–	–	0.189	–
COSLA-128	*DP_J100137.96+022339.1*	*1.68*	*16495*	*2.52*	–	–	*0.005*	–	*0.008*
COSLA-158	–	–	–	–	*247857*	*1.31*	–	–	*0.036*
COSLA-161	_J100015.28+021240.6	*6.53*	*17233*	*6.43*	*169172*	*6.27*	*0.017*	*0.029*	*0.190*
	_J100016.05+021237.4	***7.08***	***17235***	***7.16***	–	–	***0.017***	–	***0.010***

Notes. Robust statistical P-counterparts ($p \leq 0.05$) are marked italic, tentative P-counterparts ($0.05 \leq p \leq 0.2$) are shown in regular font, while counterparts identified via mm-interferometry are marked bold-faced.

*The radio, MIPS/24μm and IRAC catalogs are available at `http://irsa.ipac.caltech.edu/data/COSMOS/tables/`

Table 3.7: AzTEC/JCMT/SMA SMGs with identified robust/tentative counterparts based on the P-statistics.

name	VLA ID* COSMOSVLA*	$d_{\rm VLA}$ ["]	MIPS ID*	$d_{\rm MIPS}$ ["]	IRAC ID*	$d_{\rm IRAC}$ ["]	$P_{\rm VLA}$	$P_{\rm MIPS}$	$P_{\rm IRAC}$
AzTEC-1	–	–	–	–	**233568**	**3.39**	–	–	**0.095**
AzTEC-2	***DP_J100008.02+022612.1***	***0.12***	***9851***	***1.06***	–	–	***0.000***	–	***0.006***
AzTEC-3	– –	– –	– –	– –	**254678** 254530	**2.30** 5.71	– –	– –	**0.119** 0.093
AzTEC- 5	***_J100019.77+023204.3*** *_J100019.99+023210.1*	***1.75*** *5.64*	***10042*** *10043*	***2.12*** *5.70*	***242438*** *242872*	***1.86*** *5.44*	***0.004*** *0.039*	***0.036*** *0.070*	***0.036*** *0.022*
AzTEC-7	***_J100018.05+024830.2***	***3.02***	***15453***	***2.36***	***304354***	***2.90***	***0.006***	***0.006***	***0.011***
AzTEC-8	***_J095959.33+023440.8*** *_J095959.50+023441.5*	***5.00*** *5.03*	***17463*** *17463*	***6.07*** *6.07*	***252264*** *252508*	***4.82*** *5.01*	***0.027*** *0.021*	***0.019*** *0.019*	***0.210*** *0.178*
AzTEC-9	***_J095957.30+022730.4***	***1.73***	–	–	***225725***	***1.63***	***0.006***	–	***0.068***
AzTEC- 10	–	–	–	–	**274390**	**1.59**	–	–	**0.064**
AzTEC- 11	***_J100008.93+024010.7***	***3.42***	***6883***	***3.49***	***272725***	***3.31***	***0.021***	bf*0.019*	***0.034***
AzTEC- 12	***_J100035.29+024353.2***	***1.55***	***2586***	***1.07***	***286894***	***1.38***	***0.005***	bf*0.004*	***0.008***
AzTEC- 13	*_J095937.10+023308.4*	*7.03*	–	–	–	–	*0.035*	–	–

Notes. Robust statistical P-counterparts ($p \leq 0.05$) are marked italic, tentative P-counterparts ($0.05 \leq p \leq 0.2$) are shown in regular font, while counterparts identified via mm-interferometry are marked bold-faced.)

* The radio, MIPS/24μm and IRAC catalogs are available at `http://irsa.ipac.caltech.edu/data/COSMOS/tables/`

3.5.2.2 Radio counterparts

In our 1.1mm-selected sample 9/15 (60%) SMGs have radio sources (drawn from the Joint Deep and Large radio catalogs with $rms \sim 7-12$ μJy/beam; Schinnerer et al. 2007, 2010) within the AzTEC beam. This fraction is consistent with that found in (sub)mm-surveys (e.g. Chapman et al. 2005) Only one mm/SMA source (AzTEC-13) in this sample is not associated with a radio source present within the single-dish beam (Younger et al. 2009). Furthermore, AzTEC-5 and AzTEC-8 each have two P-robust radio sources within the AzTEC/JCMT 18" beam. In bo th cases only one radio source is associated with the SMA mm-detection.

Correlating with the Joint VLA-COSMOS Large and Deep catalogs, out of the 36 LABOCA SMGs followed-up with interferometers, 23 ($\sim$ 64%) have radio sources ($\mathrm{rms}_{1.4\mathrm{GHz}} \gtrsim 7-12$ μJy /beam) within the beam. Of these 36, 26 were detected at mm-wavelengths with interferometers (870μm-selected sample), and out of these 26, 17 (65%) show radio sources within the LABOCA beam.

Assigning counterparts to each of these LABOCA sources via P-statistic we find that (see Table 3.6, Fig. 3.3 and Fig. 3.5) in 4 cases (2 with $\mathrm{S/N}_{1.3\mathrm{mm}} > 4.5$)[8] the robust/tentative P-counterpart is not coincident with the interferometric-source. Within Poisson uncertainties this is consistent with the results from Younger et al. (2009) for the 1.1mm-selected sample.

In our 870μm-selected sample COSLA-161 has a mm-interferometric detection and two P-robust radio counterparts. Multiple P-tentative radio counterparts are found also for COSLA-2, COSLA-5, COSLA-17, and COSLA-73 (three out of these 5 are significant interferometric detections). In all cases, except for COSLA-5, one of the radio sources is associated with the inetrferometric-source.

---

[8] COSLA-5, COSLA-6, COSLA-8, COSLA-128

Table 3.8: Summary of P-statistic results compared to intermediate resolution mm-mapping

sample	radio fraction		24 μm	
	P-statistic*	correct ID	P-statistic*	correct ID
1.1mm-selected[a]	8/15 (53.3%)	7/10 (70%)	5/15 (33.3%)	5/6 (83.3%)
870μm-selected[b]	11/26 (42.3%)	7/12 (58.3%)	6/26 (23.1%)	4/6 (66.7%)

sample	$m_{3.6\mu m} - m_{4.5\mu m} \geq 0$		combined	
	P-statistic*	correct ID	P-statistic*	correct ID
1.1mm-selected[a]	5/15 (33.3%)	5/6 (83.3%)	8/15 (53.3%)	7/10 (70%)
870μm-selected[b]	10/26 (38.5%)	7/11 (63.6%)	17/26 (65.4%)	12/18 (66.7%)

*Only robust (Pc $\leq$ 0.05) counterparts are considered here

[a] Out of 15 bolometer SMGs, 2 robust statistical counterparts are found for each of sources AzTEC-5 and AzTEC-8 (see Table 3.7)

[b] Out of 26 bolometer SMGs, 2 robust statistical counterparts are found for each of sources COSLA-73 and COSLA-161 (see Table 3.6)

Combining the above results for our 870μm-selected sample we thus find 4 cases where the robust/tentative P-counterpart is not associated with the interferometric source, and 4 more ambiguous cases where fro m the multiple robust/tentative P-counterparts found for the SMG only one is confirmed by the interferometric source. Taking the 26 single-dish SMGs in the 870μm-selected sample this amounts to a fraction of 15 ± 8% for the first and latter, separately. For the 1.1mm-selected sample we find one misidentified and two ambiguous SMG counterparts assigned via P-statistic. Taking the 15 single-dish SMGs in the 1.1mm-selected sample this amounts to 7 ± 7% and 13 ± 7%, respectively.

3.5.2.3 Radio, 24 μm and IRAC counterparts

In this section we investigate the agreement between robust counterparts determined via P-statistic using radio, 24 μm, and IRAC wavelength regimes, and counterparts identified via intermediate $lesssim2$” resolution mm-mapping.

Where both radio and mid-IR data are available, potential counterparts to single-dish detected SMGs are commonly selected by searching for P-statistics robust radio and 24 μm counterparts. Where no such source can be identified, counterparts are searched for among color selected IRAC sources ($m_{3.6\mu m} - m_{4.5\mu m} \geq 0$). In Table 3.6 and Table 3.7 we list the resulting P-robust counterparts to the LABOCA and AzTEC samples. A summary of the identifications is given in Table 3.8.

In the 870μm-selected sample we find P-robust counterparts for 17 out of the 26 PdBI-identified SMGs - irrespective whether these identification are correct or not. In total we find 18 P-robust counterparts as COSLA-73 and COSLA-161 both have two P-robust counterparts associated. From the 18 statistically identified sources, 12 (66%) are correct identifications based on our PdBI detections. This fraction remains similar if we consider only the single-dish detected SMGs with mm-interferometric detections at S/N > 4.5, i.e. identified without any pri or assumptions (i.e. multi-wavelength association): 11/13 (85%) single-dish detected SMGs have P-robust counterparts, in total there are 12 P-robust counterparts (as COSLA-73 is in this sub-sample) and 7 out of these 12 (58%) match our interferometric detections. This amounts to ∼ 50% correct identifications via

P-statistic within the samples analyzed (i.e. 7/13 for the least-biased- and 12/26 for the 870μm-selected sample).

In the 1.1mm-selected sample we find P-robust counterparts for 8 of 15 (53%) SMGs with SMA detections (Table 3.7, 3.7). Since AzTEC-5 and AzTEC-8 each have two P-robust counterparts, we find 10 P-robust associations in total. Seven of the 10 (70%) are coincident with the mm-interferometric detections. The fraction remains the same if robust *and* tentative statistical counterparts are considered. Within the Poisson uncertainties this is consistent with the results for the 870μm-selected sample, i.e. only $\sim 50\%$ of the single-dish detected SMGs have correct counterparts assigned via P-statistic.

3.5.3 The biases of assigning counterparts to single-dish detected SMGs

Intensive work has been invested into optimizing techniques to determine counterparts to single-dish detected SMGs identified at low ($\sim 10 - 35$") angular resolution (e.g. Ivison et al. 2002, 2005; Pope et al. 2006; Hainline et al. 2009; Yun et al. 2008, 2012). Deep intermediate-resolution radio observations, which are less time consuming than similar mm-wave observations, but expected to trace the same physical processes (given the IR-radio correlation; (e.g. Carilli & Yun 1999; Sargent et al. 2010) have proven efficient. However, it was soon realized that radio-counterpart assignment biases samples to low-redshift (e.g. Chapman et al. 2005; Bertoldi et al. 2007). To overcome this, with the advent of deep Spitzer observations, 24 μm- and IRAC color- selected samples have been further utilized (e.g. Pope et al. 2006; Hainline et al. 2009; Yun et al. 2008). Generally, such methods identify counterparts to $\sim 60\%$ of the parent single-dish SMG sample (e.g. Chapman et al. 2005; Biggs et al. 2011; Yun et al. 2012), yet the fraction of mis-identifications in these samples is still unclear. A further source of bias in such samples is blending of SMGs within the large single-dish beams. This may potentially be a severe problem as SMGs have been shown to strongly cluster (Blain et al. 2004; Daddi et al. 2009a,b; Capak et al. 2010; Aravena et al. 2010b; Hickox et al. 2011), and are expected to often reside in close-pairs (assuggested by simulations; Hayward et al. 2011). Here we have provided detailed insight into these issues based on statistical samples.

We generated two unique (870μm- and 1.1mm-selected) SMG samples with counterparts to LABOCA/APEX and AzTEC/JCMT COSMOS SMGs identified via intermediate ($\lesssim 2$") resolution mm-mapping (see Sec. 3.4 and Table 3.4). Consistent with results from the literature we have found *statistical* counterparts for $\sim 50 - 70\%$ of the sources in these samples (see Sec. 3.5, Table 3.6 and Table 3.7). Comparing these with the intermediate ($\lesssim 2$") resolution mm-detections, we find a $\sim 70\%$ match. If there were no caveats with the intermediate-resolution mm-detections this would imply that statistical counterpart assignment methods utilizing deep radio, 24 μm and IRAC data (such as the one applied here) identify correctly counterparts to $\sim 50\%$ of the parent single-dish samples. Furthermore, it would imply that $\gtrsim 15\%$, and possibly up to $\sim 40\%$ of single-dish detected SMGs separate into multiple components, with a median separation of ~ 5", when observed at $\lesssim 2$" angular resolution. The misclassification of statistical assignment is likely intrinsic to the methods applied and also due to the break-up of single-dish SMGs into multiple components. If indeed a l arge fraction of SMGs are blended within the single dish beams (on scales < 10"), this could affect the slope of the (sub)mm counts inferred from single-dish surveys as the bright end would be overes timated, while the faint end would be underestimated (see Kovaćs et al. 2010 for a more detailed discussion). We find that radio assignment, relative to near/mid-IR wavelength regimes, is the most efficient tracer of single-dish detected SMG counterparts (see Table 3.8). Thus, as already demons trated by Lindner et al. (2011), who find that a 20 cm rms of $\sim 2.7 - 5$ μJy already identifies radio counterparts for $\sim 90\%$ of SMGs, very deep radio maps, as will be reachable with EVLA, ASKAP, MeerKAT, and SKA, will provide in the future efficient tracers of SMG counterparts. Our samples of LABOCA/APEX and AzTEC/JCMT SMGs identified via intermediate ($\lesssim$ 2") resolution mm-mapping i) are not complete, but constitute half of the parent SMG samples (see Scott et al. 2008, Navarrete et al., in prep.), and ii) are subject of their own incompletenesses and false detection rates within heterogenous data-sets (assembled from SMA, PdBI, and CARMA observations). Thus, although our analysis suggests that roughly half of single-dish detected SMGs are correctly identified via statistical methods, a more robust insight into these issues will have to await further follow-up observations of i) complete samples of single-dish detected SMGs, ii) down to higher sensitivities than the ones presented here, iii) with uniform rms over the full single-dish beam area, and iv) preferably at (at least) two separate frequencies.

3.6 Distances to SMGs

In this Section we calibrate photometric redshifts for SMGs based on a sample of 12 SMGs detected via mm-interferometry (and 4 additional high-redshift starburst galaxies) in the COSMOS field with spectroscopic redshifts spanning a broad redshift range of $z \sim 0.1-5.3$ (see Table 3.1 and Table 3.2). We optimize the photometric redshift computation, and apply it thereafter to the remainder of our SMG sample.

3.6.1 Calibration and computation of photometric redshifts for SMGs

Photometric redshifts are computed by fitting optimized spectral template libraries to the spectral energy distribution of a given galaxy, leaving redshift as a free parameter. The redshift is then determined via a χ^2 minimization procedure. The quality of the photometric redshifts will depend on the choice of the spectral library. To obtain optimal results for the population of SMGs using Hyper-z Smolčić et al. (2012b) tested three sets of spectral model libraries on a sample of eight SMGs in the COSMOS field with counterparts determined via mm-interferometry and with available spectroscopic redshifts:

2T: Only two – burst and constant star formation history – templates drawn from the Bruzual & Charlot (2003) library (and provided with Hyper-z).

6T: Six templates provided by the Hyper-z code: burst, four exponentially declining star formation histories (star formation rate $\propto e^{-t/\tau}$ where t is time, and $\tau =$ 0.31, 1, 3 and 5 Gyr) and a constant star formation history. This selection of SFH/templates is similar to the approach used by Ilbert et al. (2009) to compute stellar masses with LePhare.

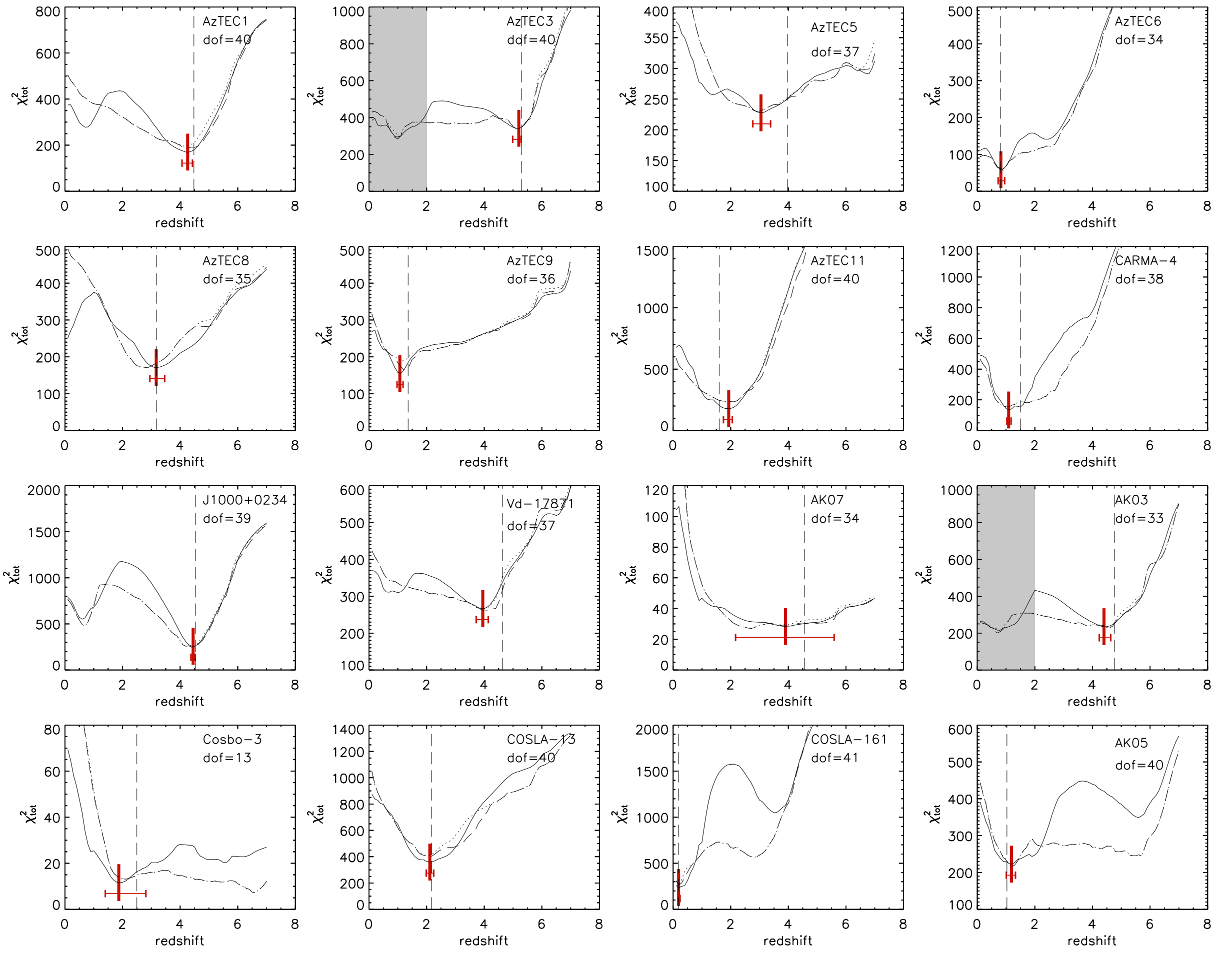

Figure 3.8: Photometric redshift total χ^2 distributions for our SMGs with spectroscopic redshifts. We show results based on various sets of spectral models (see text for details): 2T (dotted lines), 6T (dashed-lines), M (full lines). The spectroscopic redshifts are indicated by vertical dashed lines. The source names and the number of degrees of freedom (dof) in the photometric redshift χ^2 minimization are indicated in each panel. The gray -shaded areas in some of the panels indicate the redshift range ignored for the determination of the best-fit photometric redshift. The photometric redshift provided by the best model (M) and its unc ertainty was taken as the minimum χ^2 value and the 99% confidence interval, respectively, both indicated in each panel by the thick and thin red lines.

M: Spectral templates developed in GRASIL (Silva et al. 1998; Iglesias-Paramo et al. 2007) and optimized for SMGs by Michalowski et al. (2010).

They find that all three template libraries yield similar results, while the M templates result in the tightest χ^2 distributions. Here we repeat their analysis using a larger sample containing 1 2 SMGs in the COSMOS field with counterparts determined via mm-interferometry and available spectroscopic redshifts. We additionally add to this sample 4 sources (Vd-17871, AK03, AK05, AK07), selected in the same way as AzTEC-1, AzTEC-5, and J1000+0234, i.e. via criteria identifying high-redshift extreme starbursts (Lyman Break Galaxies with weak radio emission; Karim et al., in prep.). The pho tometric redshifts are computed using the entire available COSMOS photometry (> 30 bands) and the Hyper-z code with a Calzetti et al. (2000) extinction law, reddening in the range of $A_V = 0 - 5$, and allowing redshift to vary from 0 to 7.

The results are shown in Fig. 3.8, where we present the photometric redshift total χ^2 distributions for the 16 sources in our training-set. The overall match between the most probable photometric redshift (corresponding to the minimum χ^2 value) and the spectroscopic redshift is good. We emphasize that the sample used for this analysis is rather heterogeneous in respect of redshift range, detections in optical bands, blending, and AGN contribution. For example, Cosbo-3 is a blended source not detected in images at wavelengths shorter than 1 μm (see Smolčić et al. 2012., for details). Constraining its photometric redshift well (as shown in Fig. 3.8) affirms that our deblending techniques (described in detail in Smolčić et al. 2012b), as well as photometric redshift computations work well. Vd-17871 is a weak SMG (with a CO-line detection, and a continuum brightness at 1.2 mm of ~ 2.5 mJy; Karim et al., in prep.) with substantial AGN contribution iden tified in the IR (Karim et al., in prep). Even in this case our photometric redshift agrees well with the spectroscopic redshift. Note also that within our sample with spectroscopic redshifts there are no catastrophic redshift outliers.[9] For two sources (AzTEC-3 and AK03) there are two equally probable redshift peaks (i.e. $\chi^2_{\rm tot}$ minima). In both cases, however, one of those is consistent with the spectroscopic redshift. In particular , in the case of AzTEC-3 the low redshift peak can be disregarded given that the galaxy is not detected at 1.4 GHz given the depth of the VLA-COSMOS survey.

In conclusion, comparing the redshift probability distributions given the 2T, 6T, and M models, we find that the Michalowski (M) models yield optimal results (i.e. the tightest redshift probability distributions). Hence, hereafter we will adopt the Michałowski et al. (2010) spectral templates for the photometric redshift estimate for our SMGs. From the redshift probability distribution for a given source we take the most probable redshift (corresponding to that with minimum χ^2) as the photometric redshift of the SMG, and derive the 99% confidence interval from its total χ^2 distribution. The comparison between photometric and spectroscopic redshifts is quantified in Fig. 3.9 using the M template library. As already visible from Fig. 3.8 the photometric and spectroscopic redshifts are in very good agreement. We find a median of -0.02, and a standard deviation of 0.09 in the overall $(z_{\rm phot} - z_{\rm spec})/(1 + z_{\rm spec})$ distribution. However, from Fig. 3.9 it is discernible that the systematic offset is higher for higher redshifts. Fitting $z < 3$ and $z \geq 3$ ranges separately we find a median offset of 0.00, and -0.04, respectively, and a standard devi-

---

[9] The photometric redshift of AzTEC-5 shows the largest deviation from its spectroscopic redshift, but it is still with in 2σ of the $(z_{\rm phot} - z_{\rm spec})/(1 + z_{\rm spec})$ distribution (see Fig. 3.9).

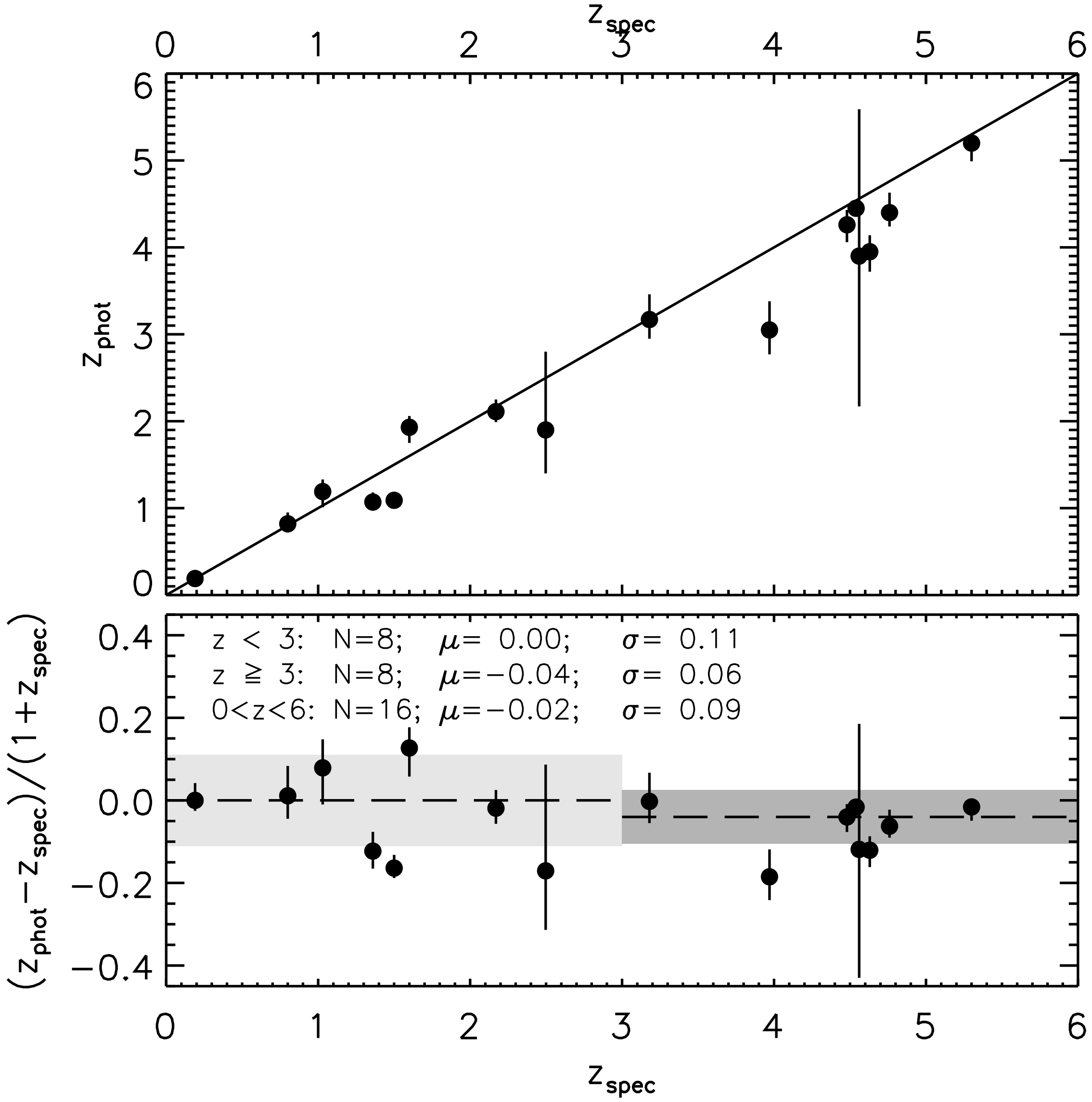

Figure 3.9: Comparison of spectroscopic and photometric redshifts for 16 starbursts in our COSMOS sample. The photometric redshifts were determined using the Michalowski spectral templates, and the shown errors are $\pm 3\sigma$ errors drawn from the χ^2 distributions of the photometric-redshift fits (see Fig. 3.8 and text for details). The median offset and standard deviation of the $\Delta z/(1+z_{\rm spec})$ distribution are indicated in the bottom panel. Note that for $z \geq 3$ we find a slight, $0.04 \cdot (1+z)$, systematic underestimate of the photometric redshifts.

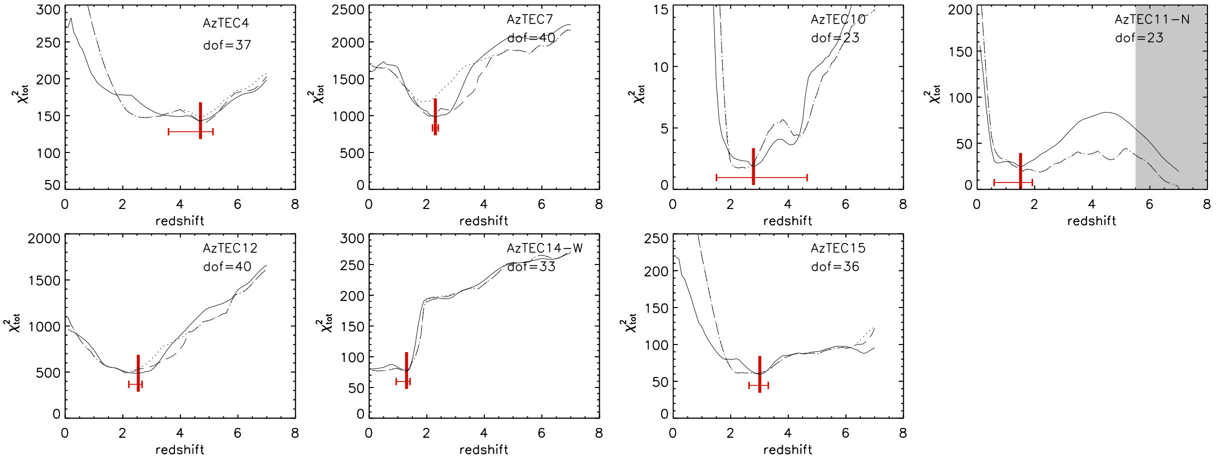

Figure 3.10: Same as Fig. 3.8, but for our AzTEC/JCMT/SMA COSMOS SMGs without spectroscopic redshifts.

ation of 0.11, and 0.06, respectively. For comparison, a similar median systematic offset (-0.023) has been found by Wardlow et al. (2011) for their full sample of LESS SMGs with statistically assigned counterparts. Yun et al. (2012) find a zero offset for GOODS-South SMGs with statistically assigned counterparts, however their results suggest a slight systematic underestimate of $z > 3$ photometric redshifts (see their Fig. 2), consistent with the results presented here. This suggests that spectral models used for photometric-redshift estimates could be better optimized for the high-redshift end. This is however beyond the scope of this paper, and here we will correct the ($z \geq 3$) photometric redshifts computed for our SMGs for this systematic offset.

Using the same approach as described above we compute photometric redshifts for all SMGs in the COSMOS field with multi-wavelength counterparts determined via mm-interferometry mapping and without spectroscopic redshifts. We present their photometric redshift total χ^2 distributions (prior to any systematic correction) in Figs. 3.10 and 3.11, and tabulate their photometric redshifts (not corrected for the systematic offset) in Table 3.1 and Table 3.3.

3.6.2 AGN considerations

As photometric redshifts are typically computed using libraries for the stellar light only, it may be argued that substantial AGN contribution to the UV-MIR SED for some SMGs may affect our photometric redshift estimate. Note however that only bright Type 1 (broad line) AGN need special treatment for photometric redshift estimates (see Salvato et al. 2009). For low-luminosity (Seyfert, Type 2) AGN, with SEDs dominated by the stellar light of a galaxy (e.g. Kauffmann et al. 2003) usual photometric redshift computations, as the one presented here, are expected to yield satisfactory results.

To address the AGN issue in our SMG sample we have utilized the X-ray data from the Chandra-COSMOS survey (Elvis et al. 2009), which provide the most direct way to identify AGN associated with the SMGs in our 1.1mm- and 870μm-selected samples.

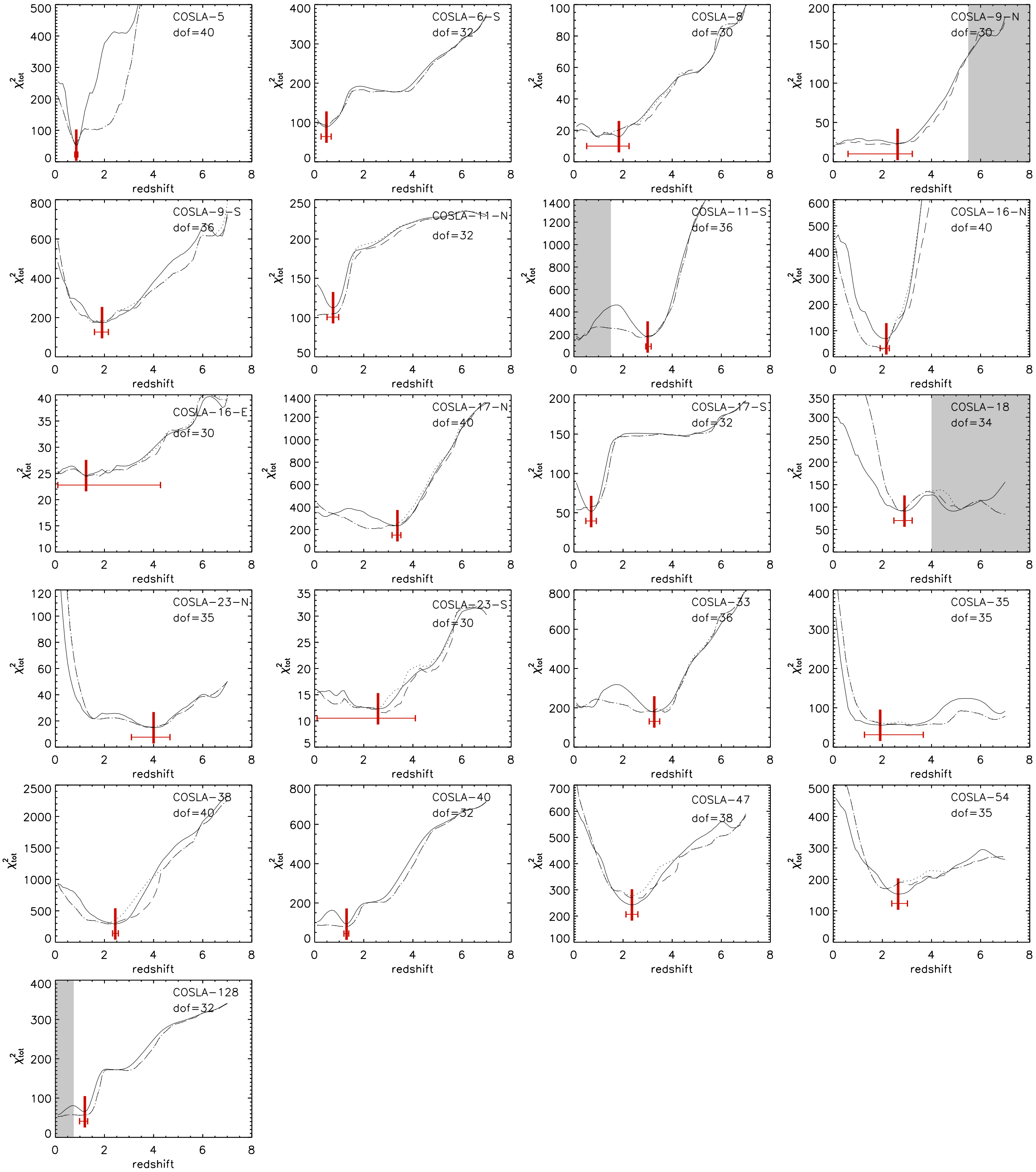

Figure 3.11: Same as Fig. 3.8, but for our LABOCA/PdBI COSMOS SMGs without spectroscopic redshifts.

Only COSLA-161, for which we find a good agreement between its photometric and spectroscopic redshifts, is found to be associated with X-ray emission (note however that given the X-ray 0.1-10 keV rest-frame luminosity of $(6.2 \pm 2.7) \times 10^{40}$ ergs s^{-1} at the source's low spectroscopic redshift, it is not clear whether the source of X-rays is star-formation or emission from the nucleus; see Appendix for more details). In order to put further constraints on the AGN properties of our SMGs, we derive the average X-ray flux in the 0.5–2 keV band using all COSMOS SMGs with interferometric positions. This is done in such a way that for each SMG we extract the X-ray counts from the 0.5–2 keV band image within a circular aperture of 1.5" in radius, and then convert this to an average X-ray flux.

For this stacking analysis we only used the so called best PSF Chandra mosaic (Elvis et al. 2009), that has a continuous coverage of the central $0.5\,\mathrm{deg}^2$ of COSMOS at 50ks depth, in order to be able to use a small extraction region and therefore reduce contamination. The background counts were estimated using the stowed Chandra background data after normalizing the background image to the average background rate in a source-free zone. After background subtraction we find a marginal detection at a 1.5σ level in the stack with $F_{0.5-2\mathrm{keV}} = (0.9 \pm 0.6) \times 10^{-17}$ erg s^{-1} cm^{-2}. For SMGs at redshifts z =2, 3, and 4, and assuming a power-law X-ray spectrum with photon index 1.8 (typical for AGN), the obtained average flux converts to average bolometric X-ray luminosities (rest-frame 0.1-10 keV) of $(7.5 \pm 5) \times 10^{41}$, $(1.9 \pm 1.3) \times 10^{42}$, and $(3.7 \pm 2.5) \times 10^{42}$ erg s^{-1} (given the marginal detection, these values should be considered as upper limits).

The inferred X-ray luminosities are typical for normal galaxies rather than strong AGN ($L_X > 10^{42}$ erg s^{-1}; e.g. Brusa et al. 2007). This rules out a major AGN contribution within our SMG sample (consistent with previous studies of SMGs; Alexander et al. 2005; Menéndez-Delmestre et al. 2009), and thus also a significant influence of AGN on the accuracy of our photometric redshift estimates. Furthermore, as demonstrated by the source Vd-17871 (see previous Section and Karim et al., in prep.) buried AGN only obvious in the IR SED do not appear to affect the method. This is consistent with the results from Wardlow et al. (2011) who have found that the accuracy of photometric redshifts is not affected for SMGs showing an IR (8 μm) excess likely due to an AGN component.

3.7 Redshift distribution of SMGs in the COSMOS field

In this section we present the redshift distributions for our 1.1mm- and 870μm-selected samples. To derive the redshift distributions, we take spectroscopic redshifts if available, and otherwise photometric redshifts based on Michałowski et al. (2010) spectral templates, and corrected for the sy stematic offset as discussed in the previous Section (see Table 3.4).

3.7.1 Redshift distribution of AzTEC/JCMT SMGs with mm-interferometric positions

Our 1.1mm-selected sample contains 17[10] SMGs with accurate positions from 890 μm interferometric observations at intermediate resolution ($\sim$ 2") with the SMA (Younger

---

[10] when AzTEC-11 is treated as two separate sources; see Appendix D for details.

et al. 2007, 2009). Spectroscopic redshifts, based on optical (DEIMOS) and/or CO (CARMA/PdBI) spectroscopic observations, are available for 7 out of 17 AzTEC/JCMT/ SMA SMGs (see Table 3.1). For 7 of the remaining sources we use photometric redshifts, derived as described in sect. 3.6 . Three sources (AzTEC-11S, AzTEC-13 and AzTEC-14E) cannot be associated with multi-wavelength counterparts in our deep COSMOS images. Thus, for these we use the mm-to-radio flux ratio based redshifts, often utilized for the derivation of distances to SMGs (Carilli & Yun 1999, 2000). Consistent with the faintness at optical, IR, and radio wavelengths the mm-to-radio flux based redshifts suggest $z \gtrsim 3$ (see Table 3.4) for all three sources when the PdBI 1.3 mm fluxes and an Arp 220 template are used (following Aravena et al. 2010a). The redshifts for AzTEC/JCMT COSMOS SMGs are summarized in Table 3.4.

The redshift distribution for the 17 AzTEC/JCMT SMGs mapped by SMA is shown in the left panel of Fig. 3.12. Given that for three sources we only have lower redshift limits, we compute the mean redshift using the statistical package ASURV which relies on survival analysis, and takes upper/lower limits properly into account (assuming that sources with limiting values follow the same distribution as the ones well constrained). We infer a mean redshift of 3.06 ± 0.37 for the AzTEC/JCMT/SMA sources. We note that treating the source AzTEC-11 as a single source yields a mean redshift of 3.00 ± 0.38.

3.7.2 Redshift distribution of LABOCA-COSMOS SMGs with mm-interferometric positions

Unlike the 1.1mm-selected sample, the 870μm-selected one is not strictly limited in flux or signal-to-noise. This is because a fraction of $\mathrm{S/N}_{870\mu\mathrm{m}} \gtrsim 3.8$ LABOCA-COSMOS SMGs have not been detected by our PdBI observations at 1.3 mm. The least biased sample that can be constructed from these detections is a sample of the LABOCA-COSMOS sources detected with interferometers at mm-wavelengths, but without prior assumptions, such as e.g. multi-wavelength counterpart associations (as described in Sec. 3.3, we required that our $\mathrm{S/N}_{1.3\mathrm{mm}} \leq 4.5$ PdBI sources had to be confirmed by independent multi-wavelength detections). This yields 16 sources (9 PdBI detected with $\mathrm{S/N} > 4.5$, and 7 detected with SMA or CARMA[11]) in our least-biased 870μm-selected sample, listed in Table 3.4. It is hard to assess the completeness of this sample. However, if i) our detection rate of the LABOCA sources can be considered random i.e. devoid of any redshift -biases, and ii) the properties of the non-detected LABOCA sources are similar to those of the detected ones, then one can assume that this subsample reflects the distribution of the parent LABOCA SMG sample within the same flux limits. Furthermore, note that the 9 LABOCA/PdBI sources detected with $\mathrm{S/N}_{1.3\mathrm{mm}} > 4.5$ within our least-biased 870μm-selected sample can be regarded as a 1.3 mm flux-limited sample ($F_{1.3\mathrm{mm}} \gtrsim 2.1$ mJy; given that we reached an rms of ~ 0.46 mJy in our PdBI maps). Hence, if the redshift distribution of the least-biased 870μm-selected sample is consistent with that of the PdBI sub-sample, we can assume that this reflects the distribution of SMGs with $F_{1.3\mathrm{mm}} \gtrsim 2.1$ mJy.

---

[11] Out of the total of 8 LABOCA-COSMOS sources detected by CARMA or SMA (see Table 3.1), only 7 were detected without priors (AzTEC/C1, $z_{\mathrm{phot}} = 5.6 \pm 1.2$ was detected at 3.2σ with the CARMA interferometer, and verified by a coincident 4.4σ radio source; Smolčić et al. 2012).

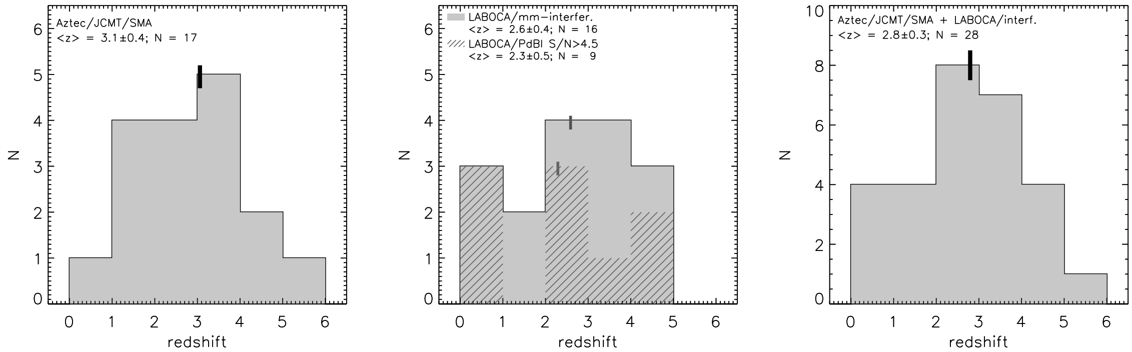

Figure 3.12: Redshift distribution of our 1.1mm-selected sample (top panel), 870μm-selected sample (middle panel), and the two samples combined (with sources present in both samples counted only once; bottom panel). In the middle panel we also show the redshift distribution of our S/N$_{1.1\mathrm{mm}} > 4.5$ PdBI-detected LABOCA sample (hatched histogram). Mean redshift values, and corresponding errors obtained using the statistical package ASURV, as well as the number of sources in each sample are indicated in each panel. Mean redshifts for every sample distribution are also indicated by the thick vertical lines .

Five out of the 16 SMGs in our least-biased 870μm-selected sample[12] have spectroscopic redshifts, for 8 we use photometric redshifts as derived in Sec. 3.6 , and for 3 we use the mm-to-radio flux based redshifts. Their redshift distribution, shown in the middle panel of Fig. 3.12, is similar to that of the PdBI subsample. Using the ASURV statistical package we infer a mean redshift of 2.59 ± 0.36, and 2.29 ± 0.48 for the least-biased 870μm-selected sample, and the PdBI S/N$_{1.3\mathrm{mm}} > 4.5$ subsample, respectively.

Given the faintness of the counterpart of COSLA-17-S its photometric redshift ($0.7^{+0.21}_{-0.22}$) is rather poorly constrained, and discrepant compared to the mm-to-radio based one ($\gtrsim 4$). Thus it is possible that this source is at high redshift. Further mm-observations of COSLA-17-N are required to affirm the reality of this source (see Appendix C for details). Nonetheless, excluding COSLA-17 N and S from the sample, we obtain consistent mean redshifts for the least-biased 870μm-selected sample (2.65 ± 0.38) and the PdBI S/N > 4.5 subsample within (2.34 ± 0.55).

We show the redshift distribution of the joint 1.1mm-selected sample and least-biased 870μm-selected sample in the right panel of Fig. 3.12. A mean redshift of 2.80 ± 0.28[13] is found. A comparison with results from literature is given in Fig. 3.13 and discussed in detail in Sec. 3.8.

3.8 Discussion

3.8.1 The redshift distribution of SMGs

In Fig. 3.13 we compare the (normalized) redshift distribution of the AzTEC/JCMT/SMA (left panel) and LABOCA/interferometric (middle panel) COSMOS samples, and their

---

[12] COSLA-2, COSLA-3, COSLA-4, COSLA-60, COSLA-73

[13] A consistent mean redshift ($\bar{z} = 2.76 \pm 0.28$) is found if AzTEC-11 is treated as a single source.

joint distribution (right panel), with redshift distributions of SMGs derived for other surveys (Chapman et al. 2005; Wardlow et al. 2011; Yun et al. 2012). The redshift distribution derived by Chapman et al. (2005) is based on a sample of 76 SMGs drawn from various SCUBA 850 μm surveys with counterparts identified via radio sources present within the SCUBA beam, and observed with Keck I to obtain optical spectroscopic redshifts (see their Tab. 2). The distribution published by Wardlow et al. (2011) is based on 74 SMGs drawn from the LESS survey at 870 μm that could be assigned robust counterparts based on the P-statistic (using radio, 24 μm and IRAC data; Biggs et al. 2011). Wardlow et al. (2011) derived photometric redshifts for these galaxies (see their Tab. 2) accurate to $\sigma_{\Delta z/(1+z)} = 0.037$. Using the P-statistic to associate counterparts to SMGs (although using a slightly modified method to that utilized by Biggs et al. 2011). Yun et al. (2012) identified 44 (robust and tentative) counterparts to SMGs detected with AzTEC at 1.1 mm in the GOODS-S field. For 16 sources in this sample a spectroscopic redshift is used, for 21 a photometric redshift was inferred by Yun et al. (2012), and for 7 only a mm-to-radio based redshift could be derived (see their Tab. 3).

From Fig. 3.13 it is immediately obvious that the redshift distribution of the COSMOS SMGs is much broader compared to that derived from previous surveys, in which the SMG counterparts were identified statistically within the large bolometer beam. In particular, significant high-redshift ($z \gtrsim 4$) and low-redshift ($z < 2$) ends are present. In the 870μm-selected sample we find 5[14] out of 16 SMGs (i.e. $\sim 30\%$) at $z < 1.5$. While the redshifts of two of these are spectroscopically confirmed, the photometric redshifts for the other three show possible secondary (higher) redshift solutions, which are more consistent with their mm-to-radio flux based redshifts. In our 1.1mm-selected sample we find 4[15] out of 17 (23.5%) SMGs at $z < 1.5$. The redshifts for three of these are spectroscopically confirmed. Thus, in total we find roughly 20-30% of SMGs at $z < 1.5$ (see left and middle panels in Fig. 3.13). Such low redshift SMGs, interestingly missed in the 1.1 mm AzTEC-GOODS-S and 870 μm-LESS samples, are expected in models of the evolution of infrared galaxies (see e.g. Fig. 7 in Béthermin et al. 2011), and they could be explained by cold dust temperatures in these sources (e.g. Greve et al. 2006; Banerji et al. 2011) A more detailed analysis of the physical properties of these SMGs will be presented in an upcoming publication.

We find significantly more SMGs at the high-redshift end ($z \gtrsim 4$) in both our 1.1mm- and least-biased-870μm-selected samples, compared to the other surveys. As discussed in detail by Chapman et al. (2005) and Wardlow et al. (2011) this is likely due to the low-redshift bias of statistical counterpart assignment methods. Using statistical means to overcome this bias Wardlow et al. (2011) estimate that $\sim 30\%$ **(and at most** $\sim 45\%$**)** of all SMGs in their sample are at redshifts $z \gtrsim 3$. Our combined AzTEC/JCMT/SMA and LABOCA/interferometric COSMOS data yield that $\sim 50\%$ of the COSMOS SMGs with interferometrically identified counterparts are at $z \gtrsim 3$. Exploring these two samples separately, we find that $\sim 50\%$ (i.e. 9/17) of the AzTEC/JCMT/SMA SMGs, and $\sim 40\%$ (i.e. 6/16) of the LABOCA/interferometric SMGs have $z \gtrsim 3$.

It is possible that the discrepancies between the $z \gtrsim 3$ SMG fractions in these different samples are due to their different average flux densities. Namely, past studies have

---

[14] COSLA-3, COSLA-4, COSLA-6S, COSLA-17S, COSLA-128

[15] AzTEC-2, AzTEC-6, AzTEC-9, AzTEC-14W

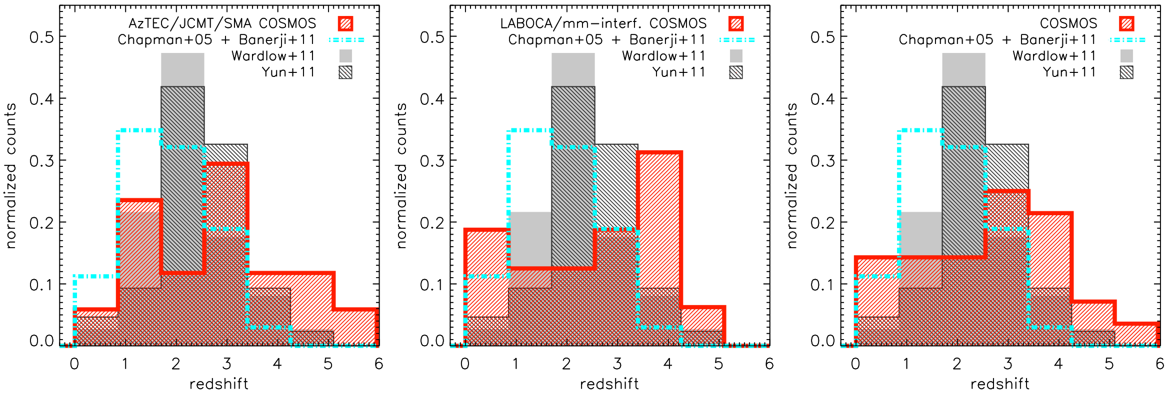

Figure 3.13: Normalized redshift distributions for SMGs drawn from various studies in the literature, indicated in the panel.

suggested the existence of a correlation between SMG brightness and redshift, in such a way that the brightest SMGs lie at the highest redshift (e.g. Ivison et al. 2002; Pope et al. 2005; Biggs et al. 2011). The LESS survey source flux limit is $F_{870\mu\mathrm{m}} > 4.4$ mJy (Biggs et al. 2011). Assuming a power-law of 3 this translates into a limit of 2.2 mJy at 1.1 mm, and 1.3 mJy at 1.3 mm. The AzTEC/JCMT/SMA COSMOS source flux limit is $F_{1.1\mathrm{mm}} > 4.2$ mJy, thus about 2 times higher, and the LABOCA/PdBI limit is $\gtrsim 2.1$ mJy, thus a factor of 1.6 higher compared to the LESS sample. Indeed, we find higher mean redshifts ($\bar{z} = 3.1 \pm 0.4$ for the 1.1mm-selected sample, and $\bar{z} = 2.6 \pm 0.4$ for the 870μm-selected sample) and thus also a higher fraction of high-redshift sources compared to the results based on the LESS survey ($\bar{z} = 2.5 \pm 0.3$). This is consistent with the suggestions from past studies that *on average* brighter SMGs are at higher redshifts. On the other hand, it has also been suggested that mm-selected samples lie on average at higher redshifts, compared to sub-mm-selected samples (e.g. Yun et al. 2012). Although our results are also consistent with this hypothesis, a more conclusive answer, disentangling these degeneracies, will have to await for deeper mm- and sub-mm selected samples with interferometric coun terparts and accurately determined redshifts.

3.8.2 High redshift SMGs

In our 1.1mm- , and 870μm-selected samples we find 9 (3 of which have radio counterparts) and 8 (4 of which have radio counterparts) $z \gtrsim 3$ SMGs. We find 5-8[16] SMGs at $z \gtrsim 4$ in our 1.1mm-selected sample, and and 3-4[17] SMGs at $z \gtrsim 4$ in our 870μm-selected sample. This corresponds to $\sim 30 - 50\%$ of the 1.1mm-selected sample, and $\sim 20\%$ of the 870μm-selected sample. As our 870μm-selected sample, is not complete, we can infer only a lower limit for the $z \gtrsim 4$ SMG surface density of $\geq 3/0.7 \approx 4$ deg^{-2}. The 1.1mm-selected sample is however nearly complete at the given 1.1 mm flux limit of $F_{1.1\mathrm{mm}} > 4.2$ mJy, and drawn from a uniform area of $0.15\Box^\circ$. Four SMGs (AzTEC-1, 3, 4, and 5) in the 1.1mm-

---

[16] AzTEC-1, AzTEC3, AzTEC-4 , AzTEC-5, J1000+0234, and possibly AzTEC-11S, AzTEC-13, and AzTEC-14E for which only lower redshift limits are available; see Table 3.1 and Table 3.4.

[17] COSLA-6-1, COSLA-23-N, COSLA-60, and possibly COSLA-158 with only a lower-redshift limit; see Table 3.4.

selected sample are found to be at $z \gtrsim 4$ (three of those have spectroscopic redshifts; see Table 3.4). J1000+0234, with a 1.1 mm flux of 4.8 ± 1.5 mJy (i.e. $\sim 3\sigma$ and thus not included in our 1.1mm-selected sample), is also spectroscopically confirmed to be at $z > 4$ (Capak et al. 2008; Schinnerer et al. 2008). Furthermore, only lower redshift limits are available for AzTEC-11S, 13 and 14E. Thus, these three SMGs may possibly also lie at $z \gtrsim 4$. Hence, these 5-8 $z \gtrsim 4$ SMGs with $F_{1.1\mathrm{mm}} > 4.2$ mJy in the $0.15\Box^\circ$ field yield a surface density in the range of $\sim 34 \pm 14$ deg^{-1} to $\sim 54 \pm 18$ deg^{-1} (Poisson errors). Both values are substantially higher than what is expected in cosmological models (Baugh et al. 2005; Swinbank et al. 2008, see also Coppin et al. 2009, 2010), even if the AzTEC/JCMT-COSMOS field were affected by cosmic variance of to a factor of 3 overdensity, as suggested by Austermann et al. (2009).

Based on the galaxy formation model of Baugh et al. (2005; top-heavy IMF; Λ cold dark matter cosmology) a surface density of ~ 7 deg^{-1} for $z > 4$ SMGs with 850 μm fluxes brighter than 5 mJy is expected (see also Swinbank et al. 2008; Coppin et al. 2009). As the AzTEC/JCMT/SMA 4.2 mJy flux limit at 1.1 mm translates to about a factor of two higher flux (i.e. 9.6 mJy) at 850 μJy, the models would predict an even lower surface density at this flux threshold.

In the GOODS-N field to date four $z > 4$ SMGs were found (Daddi et al. 2009a,b; Carilli et al. 2011). Given the 10×16.5 arcmin^2 area (but with a highly non uniform rms in the SCUBA map w ith average $1\sigma = 3.4$ mJy; Pope et al. 2005) this implies a surface density of $\gtrsim 87$ deg^{-2}, an order of magnitude higher than predicted by the models. The GOODS-N $z > 4$ SMGs are howev er associated with a protocluster at $z \sim 4.05$ which increases the surface density value. The COSMOS $z > 4$ SMGs were selected from a larger field, and although an overall overdensity of bright SMGs was found in the AzTEC/JCMT-COSMOS field (Austermann et al. 2009), the $z > 4$ SMGs do not seem to be associated with each other (Capak 2009; Capak et al. 2010; Schinnerer et al. 2009; Riechers et al. 2010; Smolčić et al. 2011). We still find significantly more $z > 4$ SMGs than current models predict. If the AzTEC/JCMT COSMOS SMGs are representative of the overall SMG population ($F_{1.1\mathrm{mm}} > 4.2$ mJy), then our results imply that current semi-analytic models underpredict the number of high-redshift starbursts.

3.9 Summary

We presented PdBI continuum observations at 1.3 mm with ~ 1.5" angular resolution and an rms noise level of ~ 0.46 mJy/beam towards 28 SMGs selected from the (single-dish) LABOCA-COSMOS survey of 27" angular resolution. Nine SMGs remain undetected, while the remainder yields 9 highly significant (S/N > 4.5) and 17 tentative ($3 <$ S/N ≤ 4.5 with multi-wavelength source association required) detections. Combining these with other single-dish identified SMGs detected via intermediate ($\lesssim 2$") angular resolution mm-mapping in the COSMOS field we present the largest sample of this kind to-date, containing 50 sources. Based on 16 interferometrically confirmed SMGs with spectroscopic redshifts, we show that photometric redshifts derived from optical to MIR photometry are as accurate for SMGs as for other galaxy populations. We derived photometric redshifts for those SMGs in our sample which lack spectroscopic redshifts.

We distinguish two statistical samples within the total sample of 50 COSMOS SMGs detected at $\lesssim 2$" angular resolution at mm-wavelengths: i) a 1.1mm-selected sample, forming a significance- ($\mathrm{S/N}_{1.1\mathrm{mm}} > 4.5$) and flux- limited ($F_{1.1\mathrm{mm}} > 4.2$ mJy) sample containing 17 SMGs with interferometric positions drawn from the AzTEC/JCMT 0.15□° COSMOS survey, and ii) a 870μm-selected sample, containing 27 single-dish SMGs drawn from the LABOCA 0.7□° COSMOS survey and detected with various (CARMA, SMA, PdBI) mm-interferometers at intermediate angular resolution.

Within our samples we find that $\gtrsim 15\%$, and up to $\sim 40\%$ of single-dish identified SMGs tend to separate into multiple components when observed at intermediate angular resolution.

The common P-statistics counterpart identification correctly associates counterparts to $\sim 50\%$ of the parent single-dish SMG samples analyzed here.

We derive the redshift distribution of the SMGs with secure counterparts identified via intermediate $\lesssim 2$" resolution mm-observations, and compare this distribution to previous estimates that were based on *statistically* identified counterparts. We find a broader redshift distribution with a higher abundance of low- and high-redshift SMGs. The mean redshift is higher than in previous estimates. This may add evidence to previous claims that brighter and/or mm-selected SMGs are located at higher redshifts.

We derive a surface density of $z \gtrsim 4$ SMGs ($F_{1.1\mathrm{mm}} \gtrsim 4.2$ mJy) of $\sim 34 - 54$ deg^{-1}, which is significantly higher than what has been predicted by current galaxy formation models.

4

Stacking method: unveiling signal from the noise

Stacking is a technique to obtain insights into the average properties of certain astronomical source populations. This is an especially powerful technique that allows to get insight into the average properties of sources (which have been observed at other wavelengths) beyond the noise level in the images. Building on previous work (Navarrete Master's thesis) various stacking techniques are explored and compared, including most recently developed methods.

More specifically, the aim of this chapter is to identify strengths and weaknesses of three different stacking methods, i.e., Weighted Mean Stack (WMS), Median, and the Global Deblending technique (GD).

It is shown that at low resolution, where effects due to blending and clustering of sources are expected to be stronger, the Global Deblending technique, is the most reliable. In the most extreme case here presented, where a map with high clustering and high density of sources is analyzed, it is found that at high signal-to-noise the weighted mean stack can largely overpredicts the real average signal by many factors while the global deblending indicator shows to be a reliable indicator in those extreme conditions.

4.1 Basic description of the stacking technique

The basics of the technique are explained in this first part of the chapter.

In order to reach better sensitivities astronomers usually take series of short exposures of the same object at different times, in the following referred to as *scans*. After many *scans* are observed they are weighted, i.e., averaged taking into account the noise level of each scan.

Mathematically this is described as follows. Suppose we measure fluxes, F_i, at different *scans* i in the map, and each of these fluxes have an associated error, σ_i. The average of the fluxes will be

$$F = \frac{F_1 + F_2 + F_3 + ... + F_N}{N} \tag{4.1}$$

and this average will have an error

$$\begin{aligned} \sigma_F^2 &= \sum_{i=1}^{N} \left(\frac{\partial F}{\partial F_i}\right)^2 \sigma_i^2 \\ &= \sum_{i=1}^{N} \left(\frac{1}{N}\right)^2 \sigma_i^2 \end{aligned} \tag{4.2}$$

In case of uniform noise across all *scans*, i.e, $\sigma_1 = \sigma_2 = \sigma_3 = ... = \sigma_N = \sigma$, Eq. 4.2 simplifies to

$$\begin{aligned} \sigma_F^2 &= \frac{N\sigma}{N^2} \\ \sigma_F &= \frac{\sigma}{\sqrt{N}} \end{aligned} \tag{4.3}$$

Analog to it, in a map with uniform noise level, extracting cutouts centered at different positions on the mapwe can weight mean all the cutouts. The final cutout will have a reduced noise level according to Eq. 4.3 This means that as more and more cutouts drawn from one image are stacked, the noise level will drop proportional to $1/\sqrt{N}$. We stress that this is valid because we are assuming that the noise of the different cutouts is uncorrelated among them, otherwise all the equations previously shown should include covariance terms, which in the extreme case where all the cutouts are completely correlated, i.e., averaging the same image N times, the noise does not drop at all but stays the same. An example of stacking is shown in the following.

Fig. 4.1 shows an example, where we have simulated 81 different *scans*, each one with the same source at the center, which has a Gaussian profile of width W peaking at $\mathrm{S_{peak}}$. The noise of each stamp is Gaussian noise with a standard deviation of σ. The units for the example have been arbitrarily chosen. By averaging the different stamps, we get an average image, where the central pixel is detected with a signal-to-noise ratio ~11.(central image in Fig. 4.1).

Next, instead of simulating 81 different scans, we simulate an entire map of $N_{\rm pixel}$ pixels per side. We inject gaussian noise with a noise level of σ, and on top of it we inject 81 sources at random positions with a Gaussian profile of width W that peaks at $\mathrm{S_{peak}} = 1.25\sigma$. This map is shown in Fig. 4.2, where grey circles are overlayed at the source positions. We show cutouts around each source position in 4.3. As expected, no individual sources are visible given the noise level chosen, however, we should be able to extract their average flux via stacking, i.e., weigh averaging cutouts from the map centered at our input sources. In the central panel of Fig. 4.3 we detect the average contribution of the 81 sources injected in the map. The key factor to get this average emission is, likewise in the example where we take many *scans* of the same object, that the noise at each position is independent from the other positions, therefore, the noise will average down and we will be able to detect a signal in the final image.

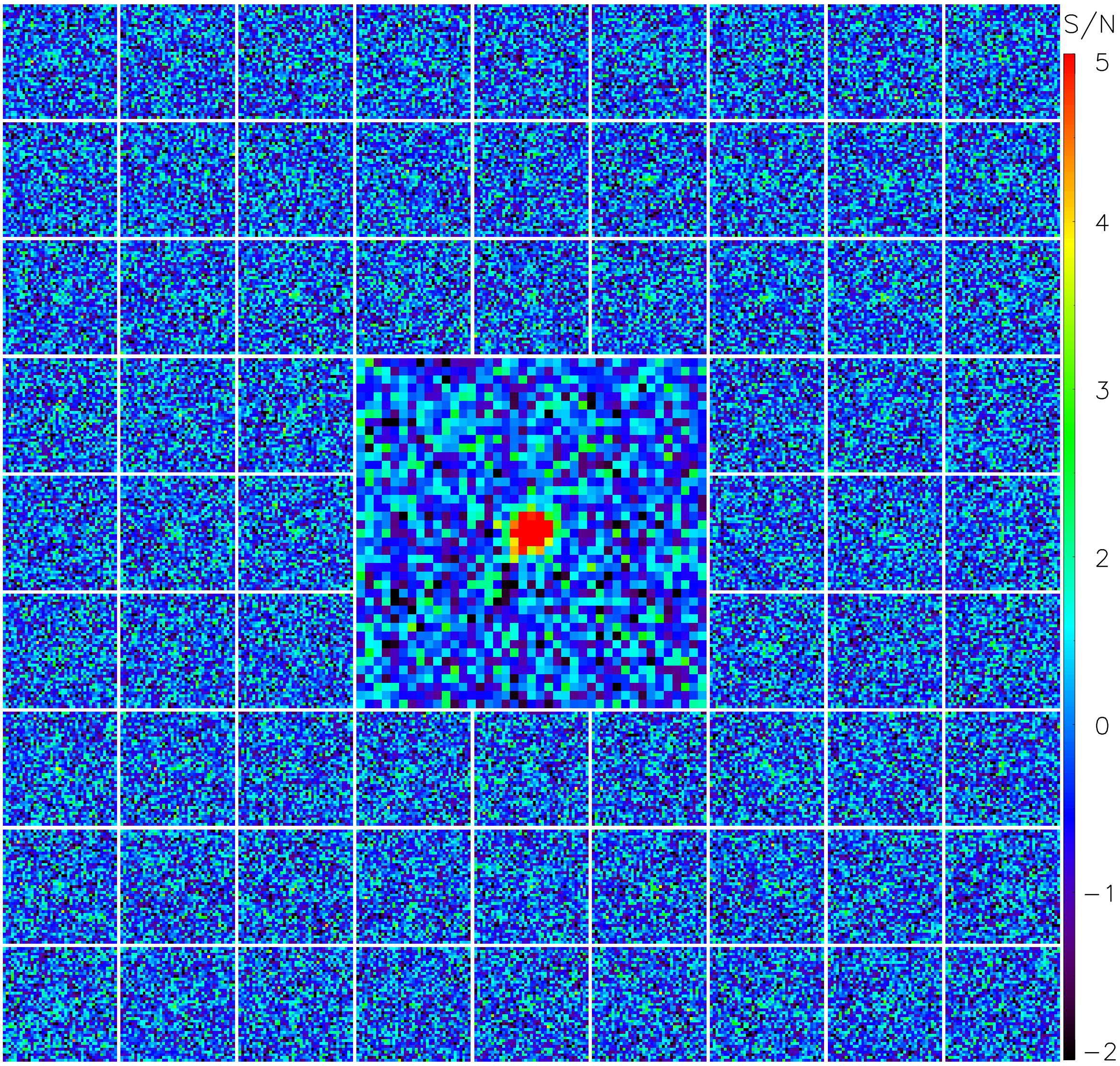

Figure 4.1: Individual *scans* of the same source (small panels). In each single *scan*, the source is not detected given that its faint signal. However, when the images are stacked (central panel), the noise level decreases and the source becomes detected with a signal-to-noise ratio ∼11, which can be seen in the central panel.

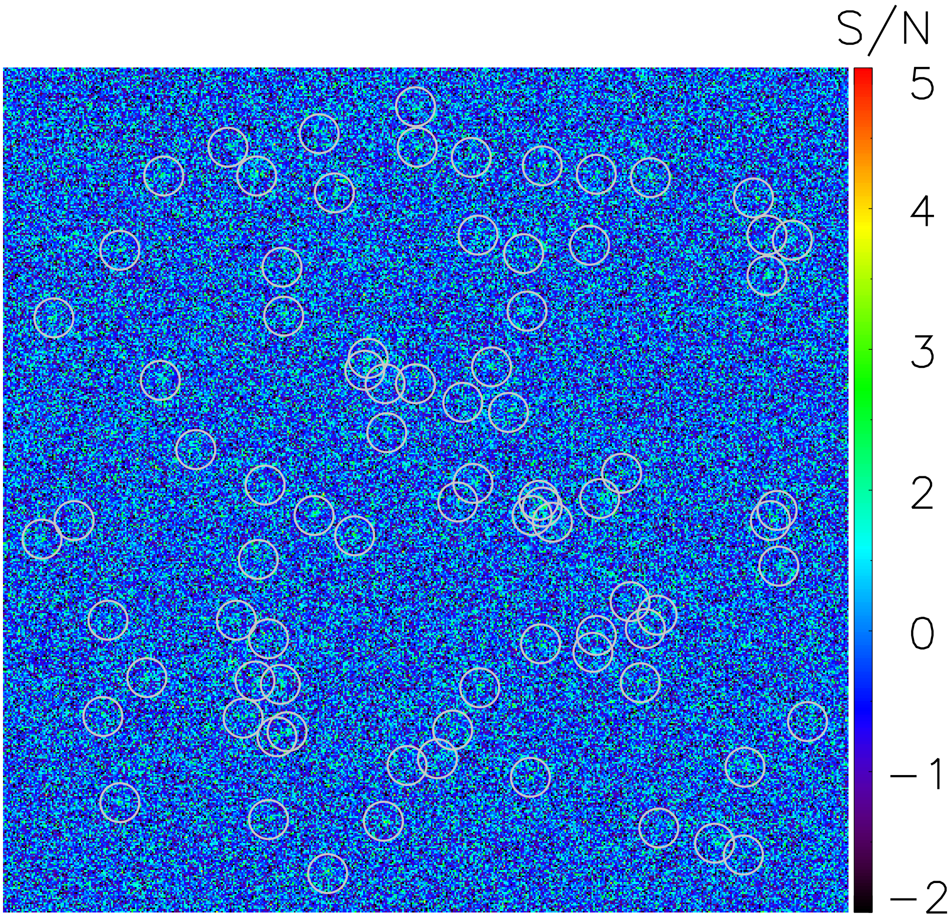

Figure 4.2: Simulation of a survey map, where there are no detections. Sources with a signal of S_{peak} are injected into the map. The source positions are indicated with grey circles.

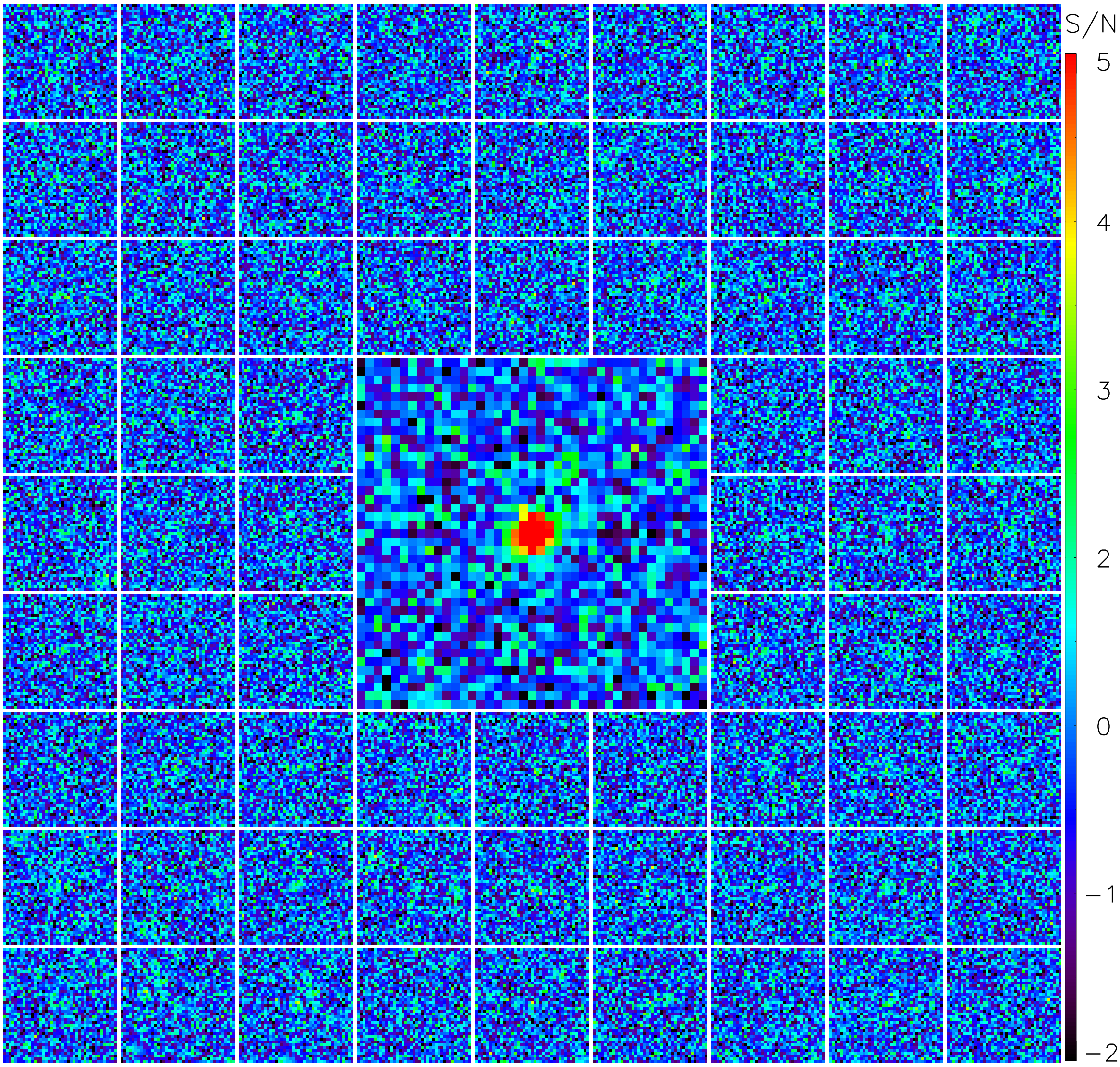

Figure 4.3: Surrounding the central stacked image, we show the cutouts around the positions indicated with grey circles in Fig. 4.2. The detected emission, shown in the central panel, has a signal-to-noise ratio ∼ 10

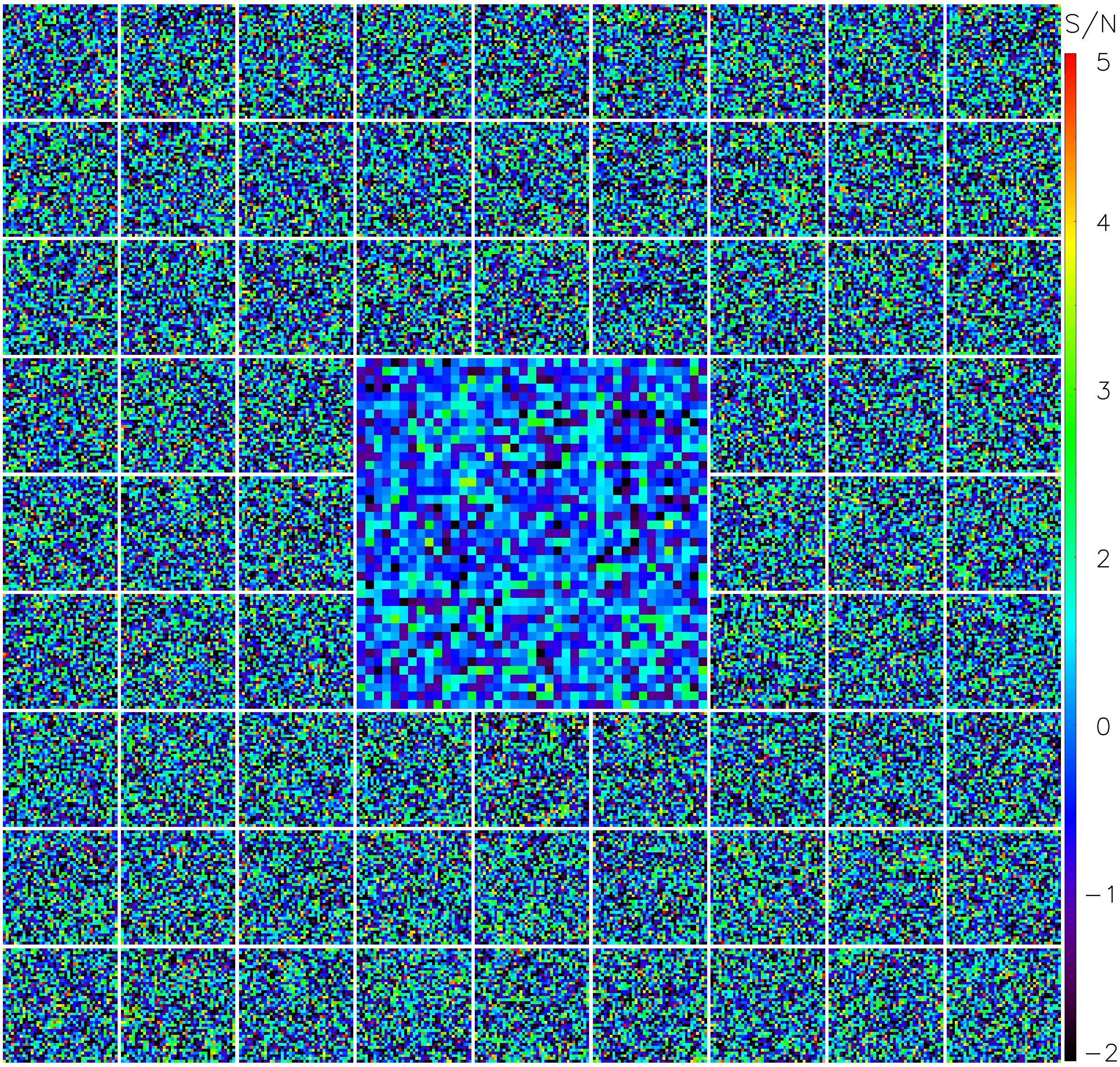

Figure 4.4: Same as Fig. 4.3, but this time the stamps correspond to random positions in the map shown in Fig. 4.2. In the central image, there is no significant detection. This shows that the detection in Fig. 4.3 is rather unlikely to be a spurious detection.

In order to ensure that the recovered signal is not spurious, we stack random positions shown in Fig. 4.4, which results in a non-detection as seen in the central panel.

Stacking is attractive as it allows to study the average properties of known galaxy samples, e.g, red objects, AGNs, star-forming galaxies, Lyman-break galaxies, galaxy clusters, etc., which remain undetected in a given passband.

4.2 Stacking technique: different methods to apply it.

In order to obtain reliable average properties from astronomical sources, different stacking techniques have been developed in the past. These are described in the following.

4.2.1 Weighted mean stacking

Weighted Mean Stacking (WMS) is the most intuitive stacking method to apply. As shown in the previous section, we cut stamps at the source positions that we are interested in. Then, for each stamp, $\mathrm{S_i}$ we consider the value of pixel j, $\mathrm{p_{i,j}}$, and its respective weight, $w_{\mathrm{i,j}}$. We weight stack them according to

$$< S >= \frac{\sum_{i=1}^{N} w_{i,j} p_{i,j}}{\sum_{i=1}^{N} w_{i,j}}, \tag{4.4}$$

where N refers to the numbers of stamps to be stacked. The $w_{i,j}$ corresponds to the inverse square of the pixel noise, i.e., $1/\ \sigma_{i,j}^2$, which is the value that maximizes the signal-to-noise ratio. This value is obtained from the weight image[1]. One option in order to build a weight image, in case is not available as an output from the image reduction process, is by getting a measure of the local noise in the vicinity of pixel $\mathrm{p_{i,j}}$ and assign that value to pixel $\mathrm{p_{i,j}}$ in the built weight image.

The noise of the stacked image can be computed in two ways. On one hand, one can compute analytically the propagation error for Eq. 4.4 given by

$$< \sigma >= \frac{1}{\sum_{i=1}^{N} w_{i,j}}, \tag{4.5}$$

On the other hand one can compute the standard deviation of the stacked image, being careful about not taking bright pixels into account. This is done by sigma clipping the pixel flux density distribution of the image, which is an iterative process. In a first iteration the standard deviation, σ, of the image is calculated and all the pixels above a threshold, e.g., 3σ, are removed. The procedure is repeated until no more pixels over the threshold are detected.

---

[1] A weight image, has the same dimensions as the signal image. Each pixel is the weight of the respective pixel in the signal map. It can be obtained for bolometer maps as explained in Sect. 2.3 or for interferometer data by using the RMSD2 task in AIPS.

4.2.2 Median stacking

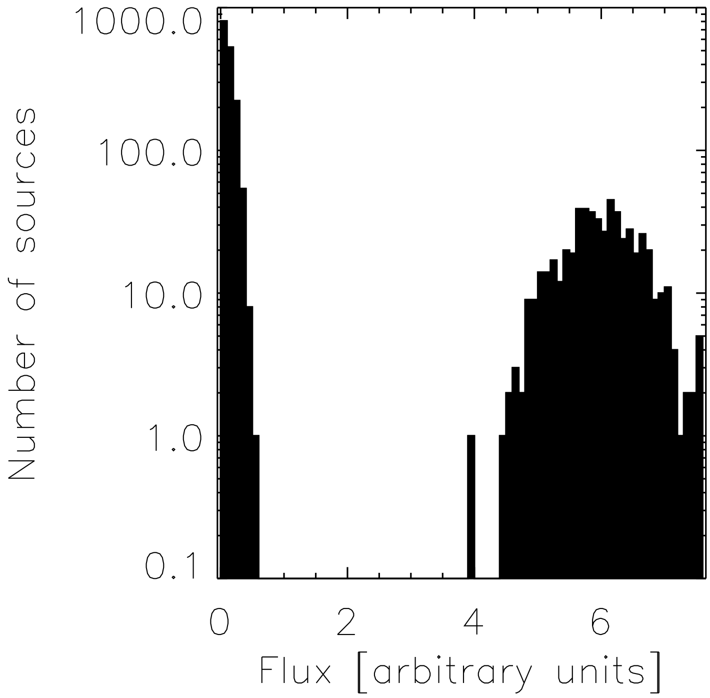

Figure 4.5: Source flux distribution used in the image. There are two different populations. One is faint and contain most of the galaxies; the other population is bright but less populated.

Median Stacking is similar to weighted mean stack, with the difference that instead of computing the weighted mean of a set of pixels, we compute the median. In presence of complex flux distributions of the underlying population to be stacked, i.e., multiple components or strong-tailed distributions, the weighted mean stacking could strongly bias the conclusions of the average population to be studied. For these complex distributions the median is generally more representative of the typical value of the whole population. As argued in White et al. (2007) median stacking is more insensitive to outlier sources as compared to the mean stacking.

This is important at some wavelengths. For instance, in radio, we want to avoid radio loud AGNs to dominate the stacking signal (Ivison et al. 2010).We analyze the median stacking with simulated maps, where we inject sources at random positions. The flux distribution of the sources is bimodal as can be seen in Fig. 4.5. One source population has a large number of members, i.e. 75%, with faint fluxes, while the remaining population has bright fluxes compared to the faint one. As expected the mean is largely affected by the bright component. In fact, the mean of the combined distribution is ∼10× larger than its median, however, the median is more representative of the bulk of the distribution.

As in (White et al. 2007) we study the median stacking flux density as a function of the noise level in the image. With this aim, we vary the noise level of the map where the

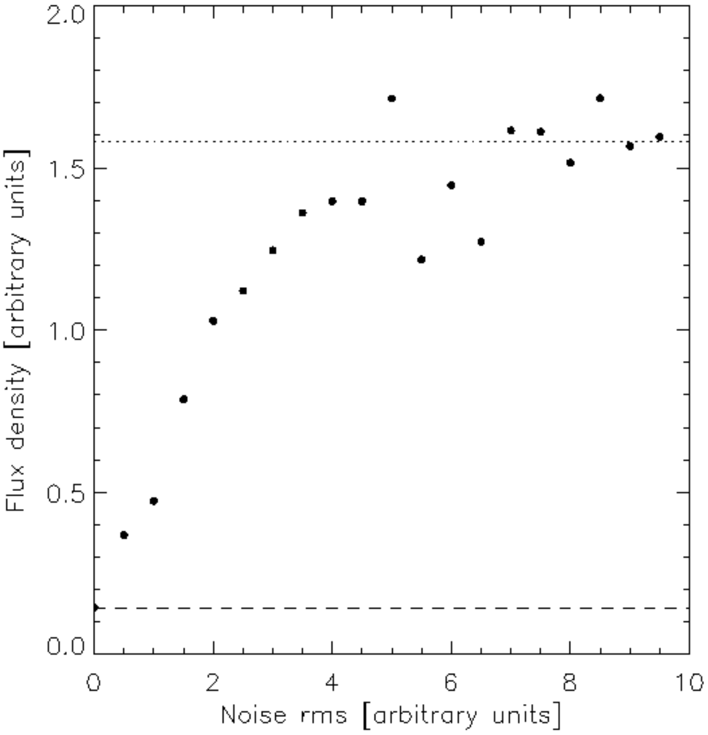

Figure 4.6: Median stacking value as a function of the noise level. The dotted line is the mean value of the distribution $\langle Flux \rangle = 1.31$ and the dashed line is the median value median(Flux)= 0.092.

sources are injected from low to high values, i.e., up to ∼70 times the median value of the distribution.As already shown by White et al. (2007), we can see in Fig. 4.6 how median stacking values vary from values close to the median of the combined distribution at low noise level, to values close to the mean of the combined distribution at high noise level. From the analysis we draw two conclusions. One is that in the presence of a population with a prominent bright-end tail, which is largely above the noise level of the image, the median will return a value more representative of the bulk of the population. The second conclusion is that in a non-detected population, which is aimed to be stacked, the median will return values similar to the mean, independent of the shape of the underlying luminosity function.

The median and WMS techniques, besides the differences in the stacking values could also differ in the noise estimates as discussed in the following. In general, for a population with a Gaussian distribution in flux, the mean is the most efficient estimate, as no other estimate will have a smaller variance (see Page 211 Kenney & Keeping 1966).

The distribution of the median of different samples with a given frequency distribution, $f(x)$, can be calculated under certain assumptions, when the number of elements, i.e. source fluxes, of the sample is high enough. Let the number of the elements in the sample be 2n+1 ($x_1 < x_2 < x_3 < ... < x_{2n} < x_{2n+1}$), so that the median is the value $\tilde{x}_0 = x_{n+1}$.

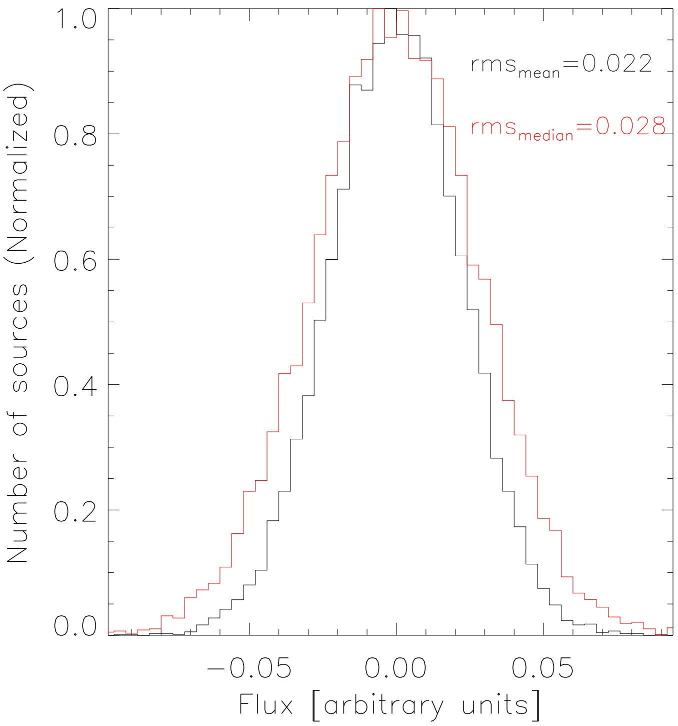

Figure 4.7: The distribution of the mean and the median of 10000 different samples. Each sample is Gaussian distributed and contains 2n+1 elements, where n=1000. The black and red histograms represent the mean and median, respectively. As expected by theory the median distribution is broader than the mean distribution (Eq. 4.9).

Defining $\tilde{x}_0$ as the population median, i.e.

$$\int_{\infty}^{\tilde{x}_0} f(x)\,dx = \frac{1}{2} \tag{4.6}$$

then it can be proven that for large values of n, the distribution of the median of a number of samples is approximately Gaussian distributed with mean $\tilde{x}_0$ and variance $1/(8nf^2(\tilde{x}_0))$ (Pag. 369 Cramér 1971), where $f(\tilde{x}_0)$ is the parent distribution function evaluated at $\tilde{x}_0$) .

If the parent population is Gaussian, then

$$f(x) = \frac{1}{\sigma\sqrt{2\pi}} e^{-(x-\mu)^2/2\sigma^2}, \tag{4.7}$$

where μ is the mean of the population, in our case $\mu = \tilde{x}_0$.

Hence, we have $f(\tilde{x}_0) = 1/(\sigma\sqrt{2\pi})$, so the variance of the median is:

$$Var(\tilde{x}) = \frac{1}{8nf^2(\tilde{x}_0)} = \frac{\pi\sigma^2}{4n} \tag{4.8}$$

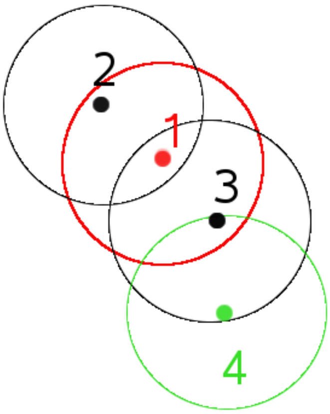

Figure 4.8: A representation of the blending problem to be solved when stacking sources in a low resolution map (circles represent the beam size). The observed flux from source 1 is affected directly by flux coming from source 2 and 3. However, the flux of source 3 has also some contribution from source 4, which means that source 1 has some indirect contribution from source 4. In order to recover the real flux of source 1 various techniques have been developed (described in the text).

Now we can compare Eq. (4.8) with the variance of the distribution of the mean of the samples, Var($\bar{x}$), which is $\sigma^2/(2n+1)$. This ratio, referred to as the efficiency is

$$\frac{Var(\bar{x})}{Var(\tilde{x})} = \frac{2}{\pi} = 0.636 \tag{4.9}$$

The square root of the efficiency gives us the difference in signal-to-noise ratio when using both estimates, hence, the noise obtained with the median estimator is a factor $\sqrt{\frac{\pi}{2}}$ ~1.25 greater than what it is obtained with the mean estimator. Besides the theoretical derivation, we show this numerically. We have simulated ten thousand samples, each sample containing 2n+1 elements, where n=1000. These elements have been distributed following a Gaussian distribution with a standard deviation value of 1 and a mean value of 0. For each sample we compute the mean and the median and plot their distributions in Fig. 4.7. As expected the rms for the distribution of the medians is a factor 25% greater than the rms for the distribution of the means.

4.2.3 Global deblending technique

If the catalog of sources to be stacked was originally observed at a similar resolution that the map where the stacking is carried out, the blending of sources is not a fundamental problem. However, when the resolution of the map where the stacking is carried out is much coarser, the presence of two or more catalog positions within a single beam has to be taken into account when computing the stacking flux density values. For instance, if two sources observed at a different wavelength at higher resolution fall in the same pixel in the low resolution map, that pixel would be considered twice , hence biasing the stacking result.

If two or more sources reside within the same beam as shown in Fig. 4.8 and we want to extract the intrinsic flux of source 1 we need to take into account the contributions from other sources in the field.A first approach is to consider only sources within a beam of some source. In that case , in Fig. 4.8, we would only consider the contributions from sources 2, and 3 to source 1, this is the approach used by Webb et al. (2004). An extension of this technique has been done by Greve et al. (2010) who additionally required to assess the contribution from source 4 to source 3 (neighbor's neighbor approach) and so on iteratively until there are no more sources within a beamwidth. This will result in an improved estimate of the stacking value, although individual intrinsic fluxes could be incorrect, since in the real map only one of the confused sources may be the dominant contributor to the observed flux. In this thesis we investigate a recent approach introduced by Kurczynski & Gawiser (2010) who provide evidence for a factor 3 rms improvement as compared to earlier deblending stacking algorithms. The description of the method is shown below (for more detailed information we refer the reader to Kurczynski & Gawiser (2010).

In general in a catalog there is a subsample of sources that we are interested in get insight of their average properties, which is referred to as target sources, while the rest of the source positions is referred to as non-target sources. Let's assume a catalog with R target positions, and F non-target positions. We define the total number of sources contained in the catalog as Λ=R+F. The conceptual difference between this method and previous methods, is that it is assumed that the intrinsic fluxes of target sources are all the same, and the intrinsic fluxes of non-target sources are also all the same. This is a fair assumption as the tradeoff of any stacking technique is to resign the knowledge about individual sources in favor of getting insight into general properties of selected populations as a whole. In the following, target and non-target positions will be identified by subindexes 0 and 1, respectively. The measured flux at the target position, j, $f_{0\mathrm{j}}$, in the presence of noise, $n_{0\mathrm{j}}$ will be related to the intrinsic flux of target sources, I_0, and the intrinsic flux of non-target sources, I_1, by

$$n_{0j} + \sum_{k=0}^{\Lambda-1} \delta_{k0}\alpha_{kj}I_0 + \sum_{k=0}^{\Lambda-1} \delta_{k1}\alpha_{kj}I_1 = f_{0j}, \tag{4.10}$$

where δ_{k0} =1 if source k is a stacking target and δ_{k0} =0 if it is a non-target; δ_{k1} =1 if source k is a non-target and δ_{k1} =0 if it is a stacking target; f_{0j} is the measured flux at the target position. α_{kj} are the Gaussian beamwidth factors $\alpha_{ij} = e^{-r_{ij}^2/2\sigma^2}$, where r_{kj} corresponds to the distance between sources at position k and j. In this way the flux contribution from a target source at position k to a source at position j will be $\alpha_{kj}\mathrm{I}_0$ Likewise, we will have for the measured fluxes at the non-target positions.

$$n_{1j} + \sum_{k=0}^{\Lambda-1} \delta_{k0}\alpha_{kj}I_0 + \sum_{k=0}^{\Lambda-1} \delta_{k1}\alpha_{kj}I_1 = f_{1j}, \tag{4.11}$$

where f_{1j} is the flux measured at a non-target position. Next, we sum Eq. 4.10 over all the target positions and Eq. 4.10 over all non-target positions

$$\sum_{j=0}^{R-1} n_{0j} + \sum_{j=0}^{R-1}\sum_{k=0}^{\Lambda-1} \delta_{k0}\alpha_{kj}I_0 + \sum_{j=0}^{R-1}\sum_{k=0}^{\Lambda-1} \delta_{k1}\alpha_{kj}I_1 = \sum_{j=0}^{R-1} f_{0j}, \tag{4.12}$$

$$\sum_{j=0}^{F-1} n_{1j} + \sum_{j=0}^{F-1}\sum_{k=0}^{\Lambda-1} \delta_{k0}\alpha_{kj}I_0 + \sum_{j=0}^{F-1}\sum_{k=0}^{\Lambda-1} \delta_{k1}\alpha_{kj}I_1 = \sum_{j=0}^{F-1} f_{1j} \tag{4.13}$$

where, if the sample to be stacked is large enough, such that the sum of independent Gaussian noise terms tends to zero, we are left with a 2 × 2 systems of equations, where we have to solve for two unknowns, i.e., I_0 and I_1

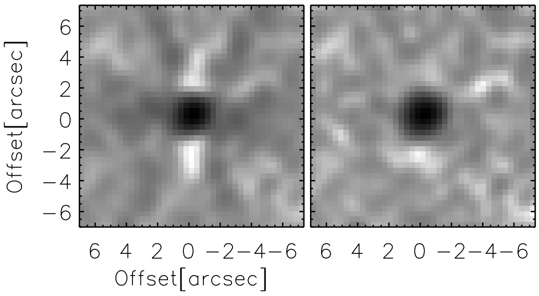

Figure 4.9: Stacking of sBzK sources at 1.4 GHz. Left panel: After stacking the positions, an average flux density signal is recovered. Given that after stacking the noise level is decreased, the dirty beam pattern shows up. Right Panel: Same as the left panel, but this time, the image has been cleaned, using the *MIRIAD* tasks, *clean* and *restore*

This 2 ×2 system can be easily extended to a 3 × 3 system (if we are interested in two target populations). In general, if N-1 target populations are defined we have to solve a N × N system.

We introduce a slight modification to this algorithm, where instead of assuming a Gaussian profile for the source flux as described by the α factors, we use the point spread function (PSF) of the image[2]. In the specific case of the LABOCA COSMOS map, the resulting PSF after the imaging process is the result of the imaging process, i.e., subtracting the large scale structure and beam smoothing the original map (see Appendix A)

In the next two sections we discuss the specific methods that will be used for the maps to be analyzed in the upcoming Chapter.

4.3 Radio interferometer stacking

Given the high resolution of the radio interferometric data that we use in this work, which is comparable to what is achievable with optical telescopes, i.e., $1\overset{''}{.}5$ with the *Very Large Array* (VLA) at 1.4 GHz in the A configuration, the problem of blended sources is not an issue.

However, stacking interferometric data impose its own challenges. It can be carried out on the image plane, as it has been done for the majority of studies in the past (White et al. 2007; Carilli et al. 2008; Dunne et al. 2009; Garn & Alexander 2009; Karim et al. 2011; Ivison et al. 2010), or it can be carried out in the *uv* plane (Lindroos & Knudsen 2013).

Here, we use the median stacking technique, which is applied on the image plane. This stacking technique is chosen since it should avoid radio AGNs from dominating the stacking signal. For the calculation of the fluxes we have to take care of two things. On one hand we will recover the dirty beam pattern and on the other hand, sources that are located towards the edge of the primary beam will suffer from the band width smearing (BWS) effect, which makes look a point source as an extended source. In Fig. 4.9 we show the stacking of sBzK sources in the VLA-COSMOS map at 1.4 GHz (Schinnerer et al. 2007), where in the left panel the dirty beam pattern can be clearly identified. We use the MIRIAD reduction software (Sault et al. 1995) to produce a clean image with the *clean* and *restore* tasks, which can be observed on the right panel of Fig. 4.9.

---

[2] We point out, that we found differences of up to 30 % in the stacked fluxes, by using the Gaussian approximation, instead of the real PSF

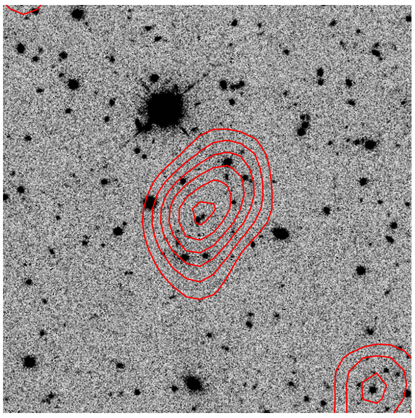

Figure 4.10: A COSLA galaxy (red contour levels) from the catalog presented in Chapter 2, superimposed on top of a K_S band image. At 2.2 μm a large number of galaxies covers the area corresponding to one galaxy at 870μm.

Finally, we compute the flux of the stacked *source* fitting a 2D Gaussian to it.

4.4 Stacking in submillimeter (or low angular resolution) maps

The single dish (sub)millimeter surveys usually have a low angular resolution, i.e., 10″-30″. In Fig. 4.10 we overlay the contours of a COSLA source on top of the K_S band image (1 to 1.5 arcsec resolution) of the corresponding region. A significant amount of sources in the K_S band image are coincident with the position of the submillimeter point source, therefore the observed flux of the COSLA source could be associated to a single or to multiple sources. In the latter case, sources are not necessarily physically related.

The multiple source contribution could be due either to a large number of sources (translating into a high density of sources per beam) present in the catalog to be stacked or to the clustering of sources.

According to Marsden et al. (2009) the density does not have an effect on the results obtained with the weighted mean stack. This interpretation only requires that the sources in the catalog are randomly distributed, therefore the density of sources should not affect the stacking result. However, the inclusion of clustering cannot be handled with this formalism.

In order to get an idea of the level of clustering we follow the approach described by Marsden et al. (2009). A large number of circles, with a specified diameter, are randomly placed in the LABOCA map. The ratio between the variance and the mean of the number of sources within the circular regions gives us an idea of the level of clustering at the corresponding diameter scale. For a random, Poisson distributed catalog, this ratio would be unity at all scales. We show this with an example carried out in the LABOCA map. For the calculation we have chosen 500 random positions in the map, which are used as the origin of the circles. We have defined the regions with circles that span sizes from 3″ to 2′ in steps of 3″. In Fig. 4.11 we show the ratio of the variance over the mean as a function of the region size for different galaxy populations, which are described in Chapter 5. The analysis is carried out at different magnitude limits for the catalogs, which are indicated by different color lines in Fig. 4.11. The clustering, at the scale of the LABOCA beam,

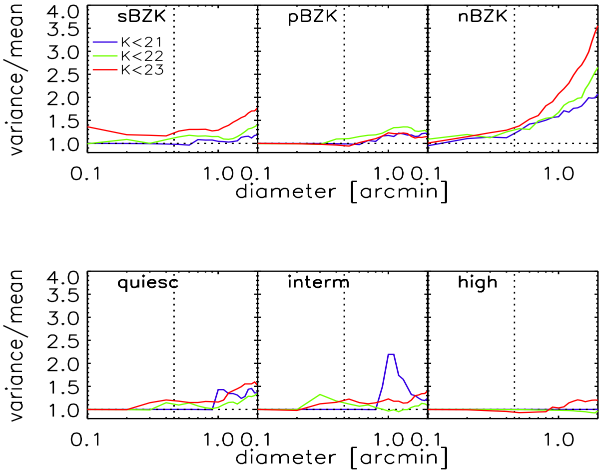

Figure 4.11: Clustering for the different populations to be stacked in the next chapter; i.e., sBzK, pBzK, nBzK, quiescent, intermediate, and high activity galaxies,shown as the ratio of variance over mean plotted against the diameter of the circle used to calculate the variance and mean of the number of sources. To calculate the clustering we place 500 circles randomly distributed over the map. We measure the variance/mean ratio for circles with diameter varying from $3''$ to $2'$. The vertical dashed line corresponds to the LABOCA beam size. In general, at the LABOCA beam size, i.e., $27\farcs6$, we observe a significant clustering level, when including galaxies down to K_S=23 (red line).

i.e., $27\farcs6$, is already significant at some of the populations, especially when we set K_S =23 as our magnitude limit (magnitude up to which our catalog is complete).

In the following we will evaluate to what degree the clustering of sources affect the weighted mean and global deblending stacking techniques. This is done in the context of the LABOCA COSMOS dataset, however, all the conclusions here obtained are easily extendable to any other low angular resolution map.

4.4.1 Comparing *WMS* and *Global Deblending* techniques

We produce simulations similar to the ones described in Sect. 2.5.2, where instead of injecting sources following a specific luminosity function, we inject sources with fluxes drawn from a random distribution. The number of sources injected in the map is arbitrarily chosen in order to simulate low density and high density environments. We show the results in Fig. 4.12, where for the test A we have injected in the map 50 target sources and 100 non-target, while for the test B we have injected 1000 target sources and 2000 non-target sources. For each test we have run 10 simulations in order to determine the errors. It can be seen that in the low density case, both methods give practically the same results. However, when the source density increases, the weighted mean stack technique overpredicts the real value by $\sim 21 \pm 4\%$. Not only the average values are larger in the weighted mean stack, also the errors are larger when compared to the ones obtained with the *Global Deblending* technique.

4.4.2 The impact of source clustering for different stacking estimators

In Sec. 4.4.1 we have compared the behavior of the *WMS* and *Global Deblending* techniques, in simulated maps, where the sources were randomly distributed. However, as we already mentioned at the beginning of this section we have some evidence that the populations we want to stack could be clustered (see Fig. 4.11). For this reason, we use simulations to test if the level of clustering affects the stacking results, and if so, how to quantify the introduced bias.

The strategy in order to understand this effect consists in simulate cases with a stronger clustering than any of the populations to be stacked. If one of the methods, i.e., WMS or Global Deblending, is barely biased by clustering then it can be used in the stacking analysis presented in the upcoming chapter without further corrections. However, if no method gives unbiased stacking results in presence of clustering, it would be necessary to reproduce the clustering level of each population and quantify the bias using simulations.

In order to simulate clustered populations with a clustering level stronger than the real populations, we first need to determine the clustering of the real populations. For this reason, we calculate the two-point angular correlation function of the populations shown in Fig. 4.11.

We measure the two-point angular correlation function using data and random catalogs with the estimator proposed by Landy & Szalay (1993),

$$w\left(\theta\right)=\frac{\left[DD\left(\theta\right)-2DR\left(\theta\right)+RR\left(\theta\right)\right]}{RR\left(\theta\right)}, \tag{4.14}$$

where DD(θ) is the number of pairs in the data catalog separated by an angle $\theta+\delta\theta$, DR (θ) correspond to the number of pairs between the data and the random catalog separated by an angle $\theta+\delta\theta$, and RR(θ) is the number of pairs in the random catalog separated by an angle $\theta+\delta\theta$.

We calculate the clustering for a region of the COSMOS field, which covers ~ 1050 arcmin^2, except for the small population of the so-called pBzK galaxies, where we have used the same area that was used for the source detection in Chapter 2, i.e., $\sim$ 2300 arcmin^2. This is shown in Fig. 4.13, where we have stacked each source population at different magnitude levels, likewise in Lin et al. (2012). We can identify that the most clustered populations are the sBzK and pBzK, while all the other populations do not show a strong clustering , at least when we selected by magnitude.

For comparison the results obtained by Lin et al. (2012) in the GOODS-North field are shown. In their study one of the populations with the strongest clustering is the sBzK population contained in the magnitude range $21.5 < \mathrm{K_S} < 22$.

4.4.2.1 Simulations

In order to understand the bias that the clustering of sources could introduce in the stacking estimators, we produce simulations. We follow the procedure described in Infante (1994), which we briefly explain here.

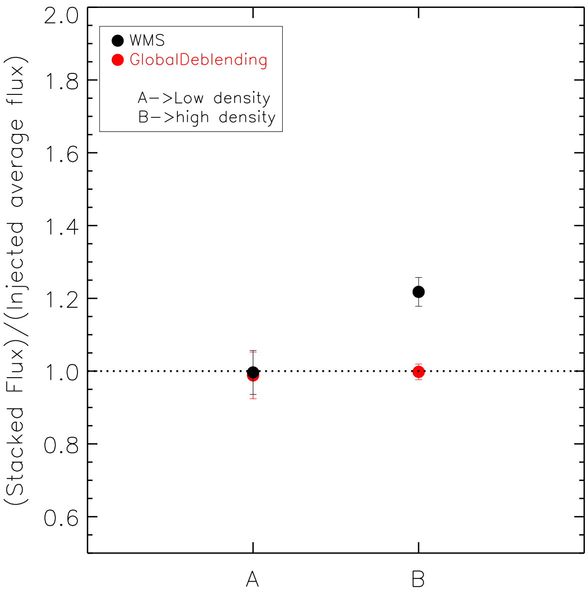

Figure 4.12: Comparison of the *WMS* (black dots) and the *Global Deblending* (red dots) Stacking techniques. The Simulation *A* contains 50 target sources, while the Simulation *B* contains 1000 target sources and 2000 non-target sources. All the sources are distributed randomly on the map. We compare the ratio of the stacked density flux over the injected average flux of the target sources. In the low density case (Simulation *A*), both methods gives similar values. However, in the high density case the *WMS* overpredicts by $\sim 21\%$ the original injected values, while the *Global Deblending* technique still returns a value close to the injected average flux.

The clustering simulation is constructed by choosing a random position. Starting from that random position we place two new sources at a certain angular distance. In the second iteration, we choose as centers those two sources and from each center we place two new sources at certain angular distance (so in the second iteration we place 4 sources in total). We do the same, until we reach the so called hierarchical level, L, which indicates how many iterations we have to do. Once we reach the limit of iterations, we choose a new random position as a center, and a new hierarchical level, and start the process again. So, this means that to build a clustered simulation following this recipe, we need to choose a bottom hierarchical level, L, ; the angular distance where the clustering tends to zero; and the ratio of the separations between two consecutive levels, θ_{l+1}/θ_l.

First, to choose L, we have to define L_{min} and L_{max}, and randomly select an L, between those two values. L is drawn from the following probability distribution,

$$p(L) = AN_L^{-\alpha}, \tag{4.15}$$

where A is a normalization factor, such that

$$\int_{L_{min}}^{L_{max}} p\,(L)\,dL = 1 \tag{4.16}$$

Given the distribution in Eq. 4.15, we normalize it so we can relate a number between 0 and 1 to L.

$$x = P\,(< L) = \frac{\int_{L_{min}}^{L} p\,(L)\,dL}{\int_{L_{min}}^{L_{max}} p\,(L)\,dL}, \tag{4.17}$$

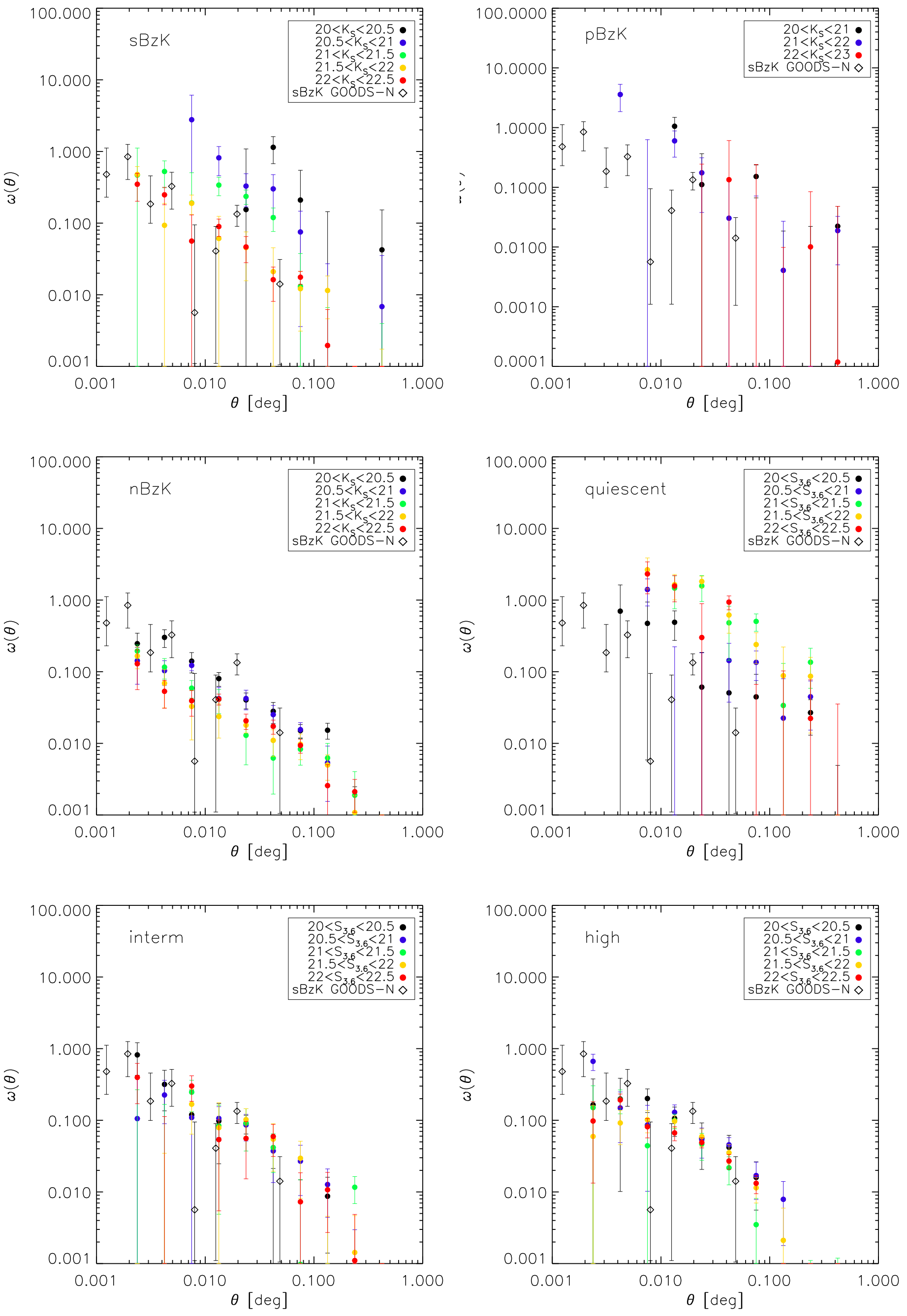

Figure 4.13: Two point angular correlation function calculated for different galaxy populations, i.e., sBzK,pBzK,nBzK,quiescent, intermediate, and high activity. (These populations will be presented in further detail in the next chapter). For each population the two point angular correlation function has been calculated following the estimator proposed by Landy & Szalay (1993) for different magnitude ranges.

Table 4.1: Clustering Simulations Parameters

Name	β	L$_{min}$	L$_{max}$	θ_1 [arcmin]	γ
Simulation1	0.6	4	6	0.1	2.3
Simulation2	0.6	6	8	0.1	2.3

and if we solve it for L, we get,

$$L = -\frac{ln\left(-N^{-\beta L_{Lmin}}x + N^{-\beta L_{Lmax}}x + 2^{\beta L_{min}}\right)}{\beta ln\left(2\right)} \tag{4.18}$$

Second, when we choose the angular distance, where the clustering tends to zero, we can choose any number, or a number based on observational constraints.

And the last thing we have to set is the ratio of the angular separations between two consecutive levels, in this case we choose a value of 2.3
The simulated images, which are presented in Fig. 4.14, were produced with the parameters shown in Table 4.1. Each map covers an area of $\sim 1400'^2$, where we have included 1000 sources (target population), which are clustered, and other 2000 sources randomly distributed (non-target population). The fluxes are randomly distributed. In 4.15 it is shown that the simulated clustering is stronger than the clustering of the populations to be studied in the next Chapter.

4.4.2.2 Applying the stacking technique in the clustering simulations

We run our stacking technique algorithm in order to compare how good the *WMS* and the *Global Deblending* stacking techniques behave under clustering conditions. The first test is done in a noiseless maps, where we inject 1000 target sources which are clustered, and 2000 non-targets sources which are randomly distributed in the map. In the second test we inject the same amount of sources but this time we inject them in a noise flat map, with a noise level of 2 mJy/beam. The average flux density of the target and non-target population vary, in such a way that for a noise level of $\sim$ 2 mJy/beam, the stacked populations would have signal-to-noise ratios of 1,2,3,4,5,10,20, and 50. So, we can study the behavior of the methods at low and high signal-to-noise ratio. The source fluxes in each simulation are randomly distributed within 20 percent of the average value. Finally in the third test, we inject the sources in a jackknife map obtained from the observation scans. The obtained results are shown in Fig. 4.16 and Fig. 4.17. From the Figures it is clear that the stronger the clustering the higher the overestimation from the *WMS* technique. In the clustering simulation 1, the *WMS* overpredicts by a factor of $\sim$ 2-3, while in the clustering simulation 2, the overprediction rises up to $\sim$ 10 times the expected value. On the other hand, the *Global Deblending* technique keeps returning flux density stacked values close to the expectations, even in the the Simulation 2, where the clustering is stronger. Furthermore, the results obtained with the *Global Deblending* technique are more stable, as can be seen from the error in Fig. 4.16 and Fig. 4.17. As expected the

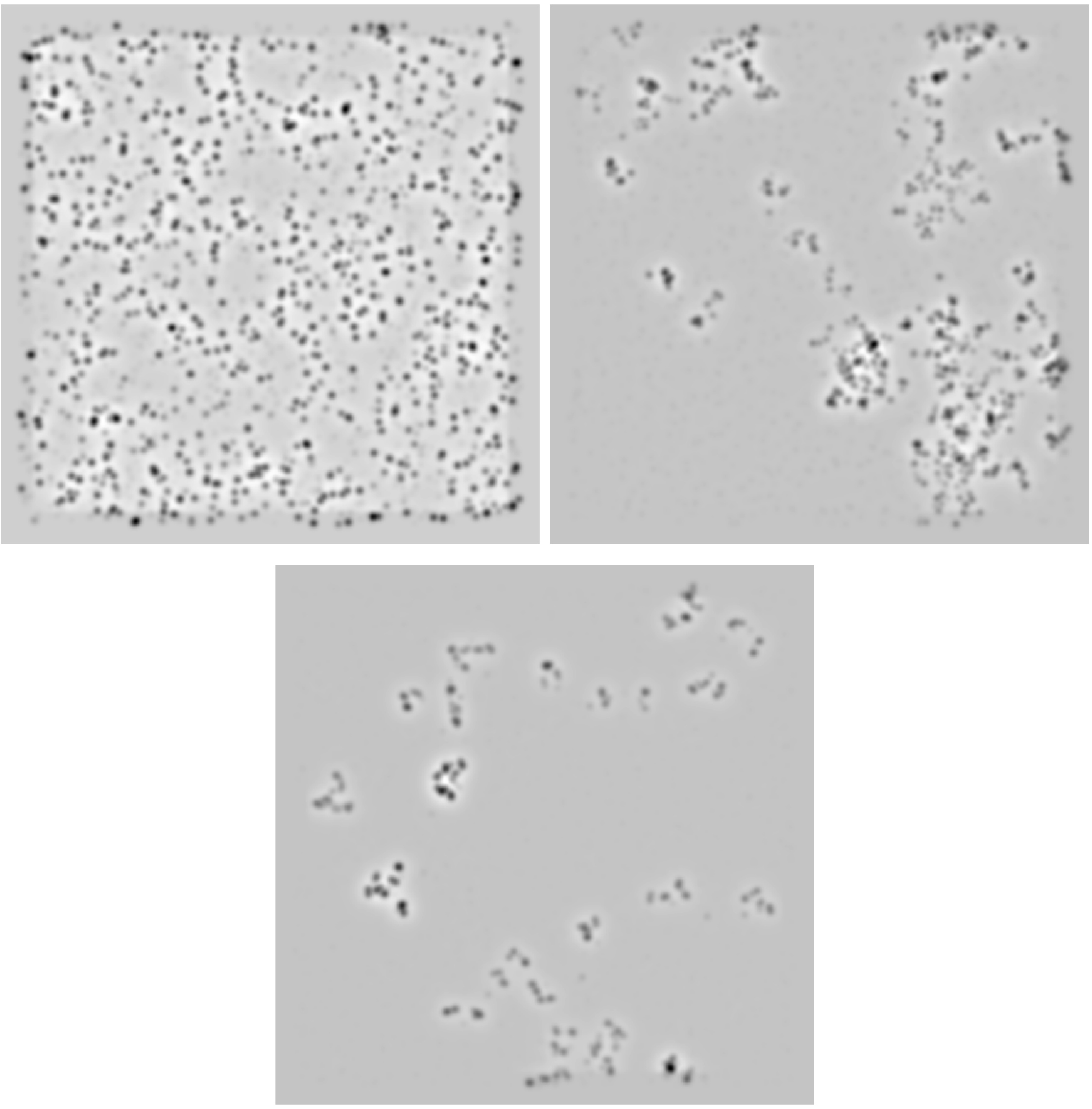

Figure 4.14: Upper left: The target and non-target populations are injected at random positions, i.e., no clustering. Upper Right: The target population is clustered with the parameters shown in Table 4.1 for Simulation 1. Bottom Middle: The target population is clustered with the parameters shown in Table 4.1 for Simulation 2. In all the three examples the injected fluxes are randomly distributed.

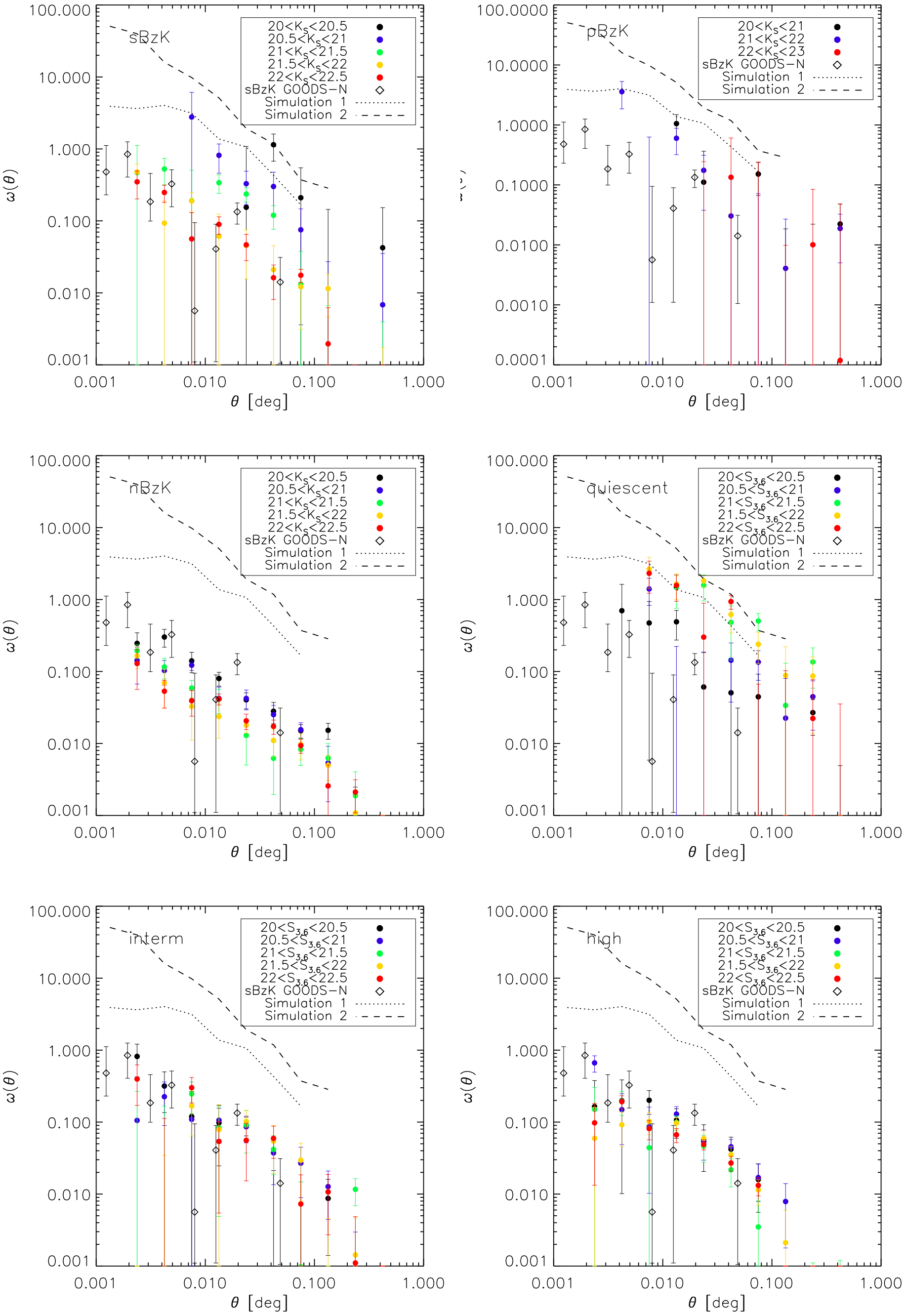

Figure 4.15: Same as Fig. 4.13, but this time we include in the plots the Simulated Clustering. It is clear that the simulations have a stronger level of clustering that any of the populations to be studied in the next Chapter.

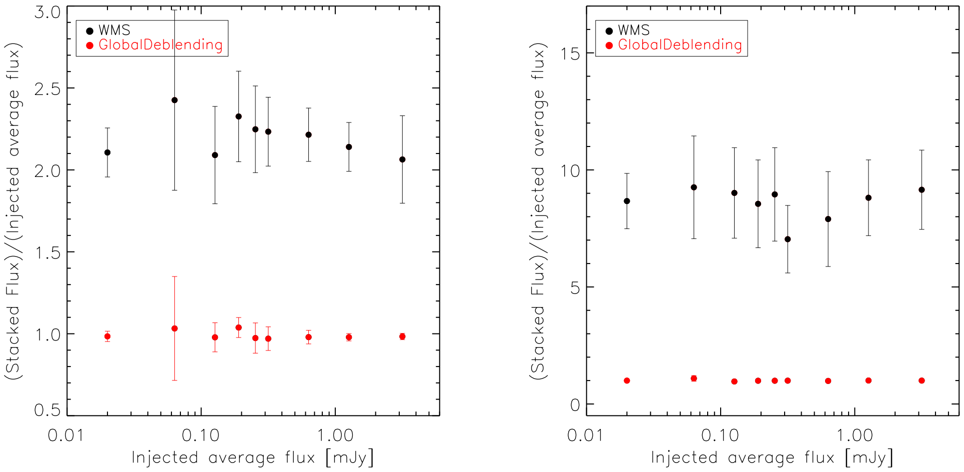

Figure 4.16: Stacking results as function of the average flux density of the sources. Left Panel: The stacking results correspond to the Clustering Simulation 1 (see Table 4.1). The sources have been injected in a map with a flat noise level of 2mJy/beam. The black dots are the results obtained with the *WMS* technique, while the red dots are the results obtained with the *Global Deblending* technique. The dots at 0.2 mJy/beam are shown for reference. They correspond to the stacking of sources injected in a noiseless map. Right Panel: Same as the left panel, but this time the stacking results correspond to the Clustering Simulation 2.

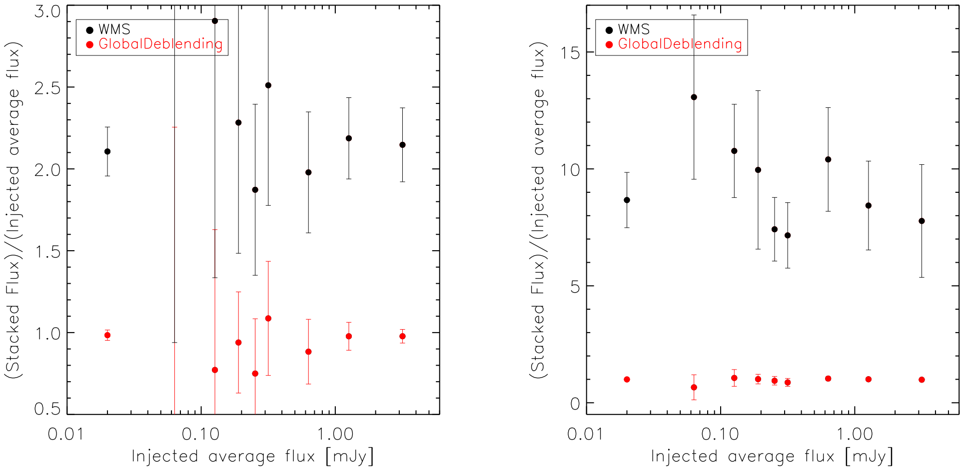

Figure 4.17: Stacking results as function of the average flux density of the sources. Left Panel: The stacking results correspond to the Clustering Simulation 1 (see Table 4.1). The sources have been injected in a jackknife map obtained from the observations. The black dots are the results obtained with the *WMS* technique, while the red dots are the results obtained with the *Global Deblending* technique. The dots at 0.2 mJy/beam are shown for reference. They correspond to the stacking of sources injected in a noiseless map. Right Panel: Same as the left panel, but this time the stacking results correspond to the Clustering Simulation 2.

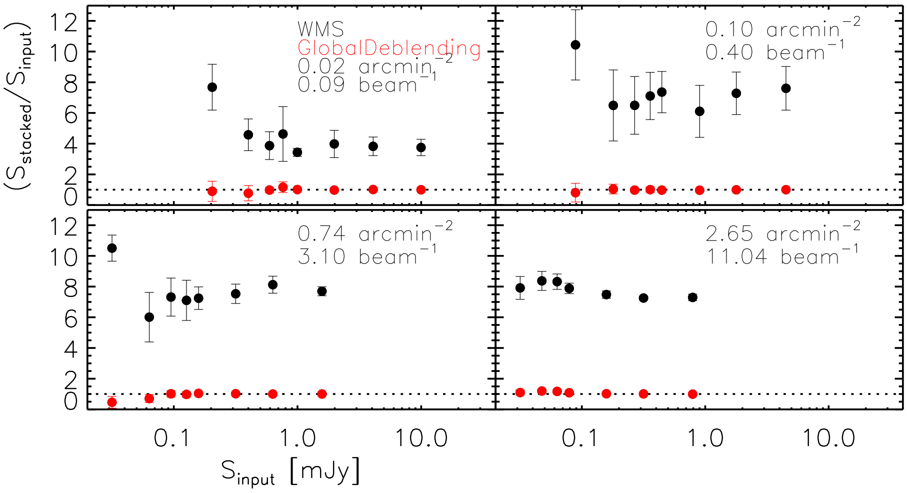

Figure 4.18: Stacking results as function of the average flux density of the sources. The sources have been injected in a jackknife map, and the clustering parameters correspond to the Simulation 2. The number of sources is increased from 100 target sources in the left upper panel to 16000 target sources in the right bottom panel. the number of non-target sources double the number of target sources. In the legend of the panels the source density is indicated. The red dots are the results obtained with the Global Deblending Technique, while black dots are the results obtained with the Weighted Mean Stacking Technique. As in previous plots, the Global Deblending returns stacked flux density values which are in excellent agreement with what is expected from the average injected flux.

errors in the flux density stacked values are larger in the case of low signal-to-noise ratio of the stacked populations.

In the next chapter we use the techniques here described to get insight of the average properties at submillimeter and radio wavelengths of different galaxy populations.

We have also computed the source density dependence of the stacking for Simulation 2, injecting sources in a jackknife map . This is shown in Fig. 4.18, where we have injected as few as 100 target (200 non-target) sources in the left upper panel, up to 16000 (32000) sources in the right bottom panel. It can be seen that the results obtained with the Global Deblending technique are in excellent agreement with what is expected from the average input fluxes.

4.5 Summary and conclusions

In the following we summarize the main results from this study:

In Chapter 4 we analyze the advantages and disadvantages of different stacking methods, i.e., Weighted Mean stacking, Median stacking, and the Global deblending technique introduced by Kurczynski & Gawiser (2010).

We focus our analysis in the Global Deblending technique as optical sources detected in the area of the LABOCA map are significantly larger in number and density compared to previous studies. Simulating maps with different levels of clustering, it is shown that while the weighted mean stacking can largely overpredicts the source input average flux, the global deblending technique is a reliable indicator. Maps are also simulated with different levels of source density, where it is shown that the global deblending technique returns output average fluxes in excellent agreement with the input ones.

- we analyze the advantages and disadvantages of different stacking methods, i.e., Weighted Mean stacking, Median stacking, and the Global deblending technique introduced by Kurczynski & Gawiser (2010).
- In maps where the clustering of the sources to be stacked is not significant, the median stacking technique returns the most representative value of the bulk of the population.
- Simulating maps with different levels of clustering, it is shown that while the weighted mean stacking can largely overpredicts the source input average flux, the global deblending technique is a reliable indicator.
- Maps are also simulated with different levels of source density, where it is shown that the global deblending technique returns output average fluxes in excellent agreement with the input ones.

5

Applying the stacking method on the LABOCA-COSMOS map

In this chapter we apply the stacking technique described in the previous chapter to the COSMOS dataset. We stack different optical color-selected populations of galaxies, which have been shown to be good discriminators between quiescent and star-forming galaxies. Unlike studying the detected sources color selected populations from optical catalogs are more representative of the bulk of the galaxy population at different redshifts. Furthermore, at the moment large samples of them are difficult to study even with state-of-the-art technology, e.g. Atacama Large Millimeter Array. The stacking is carried out in the framework of the LABOCA-COSMOS data one of the largest contiguous field observed to date at 870 μm, i.e., $\sim$0.75 deg^2. Covering such a large field implies that we stack 50000 sources, compared to 1000 or less from similar studies (Greve et al. 2010; Decarli et al. 2014). As expected, splitting the samples we find that in general the submillimeter flux density increase with redshift and stellar mass. Also star-forming galaxies at high redshift are a few times brighter than at low redshift, and no-detection is found for passive galaxies, although the latter is likely due to the small sample of passive galaxies. The stacking in the radio regime, using the VLA-COSMOS survey data at 1.4 GHz, is also carried out with the aim of analyzing the far infrared radio correlation for the different color selected populations. From the radio stacking alone it can be seen that most of the trends are similar to what is seen in the stacking at submillimeter regime, however in the radio wavelengths we recover an average signal for the pBzK galaxies. It is still unclear whether the radio emission arises from star formation activity or AGNs. Additional stacking in Herschel bands are likely the best way to further investigate this issue. Combining both datasets, i.e., submillimeter and radio, we investigate the far infrared radio correlation of the different color selected populations. We do not find evidence for a departure from what is expected. Also we separate galaxies by elliptical, spirals, and starbursts. As expected we only obtain upper limits for elliptical galaxies, while stacked signal is detected for spirals and starburst, which also do not show any evident departure from the FIRRC.

5.1 Introduction

Star formation tracers are available at different wavelengths, and among them, (sub)millimeter wavelengths have the advantage that they do not suffer from dust obscuration, furthermore they have a flat selection function over a large redshift range. The most important assumption here corresponds to accept the FIR luminosity as powered from star formation. As we already discussed, studies investigating whether the AGNs or rather starbursts (show references in Lonsdale 2006) are the origin of the FIR emission of submillimeter galaxies, tend to favor an scenario where a coeval of AGNs and starbursts is present, being the starburst the main contributor to the FIR emission.

SMGs are galaxies with enormous SFRs and very massive, i.e., $M_\star \gtrsim 10^{10} M_\odot$, however they trace only the bright end of the IR luminosity function. Star forming galaxies that dominate the star formation rate density of the Universe (SFRD) have much lower star formation rates, i.e. SFR $\lesssim 10 M_\odot$/year. Unfortunately, these galaxies are undetectable with current submillimeter surveys, where the access is mainly restricted to galaxies brighter than 4 mJy at 850 μm. The only exception being surveys targeted towards galaxy clusters, in order to take advantage of the lensing effect (Knudsen et al. 2008; Johansson et al. 2011). Large format near-infrared cameras have revealed population of moderately star-forming
In order to detect an average submillimeter signal from these galaxies, sensitivities as low as 0.1 mJy/beam at 850 μm have to be reached. With submillimeter single dish telescopes this sensitivity is not possible as the confusion noise is greater than this level. Submillimeter interferometers, e.g., ALMA, PdBI, are the natural answer to reach deeper sensitivities, however they are not suitable for large area surveys. In fact, with ALMA to cover a field of 100 arcmin^2 would take $\sim$ 500 hours to reach a sensitivity of $\sim$ 0.1 mJy. A suitable technique that helps to alleviate this problem is the stacking technique (see previous Chapter for a detailed explanation of this technique.), which at the expense of individual information for each galaxy, push down the sensitivity of the original image by doing cutouts centered on the galaxies of interest and subsequently averaging those cutouts. In this way the average properties of specific galaxy populations can be studied.

This is the motivation for stacking different color selected populations, which are more representative of the bulk of the galaxy population at different redshifts. We do this in the framework of the LABOCA-COSMOS data one of the largest contiguous field observed to date at 870 μm, i.e., $\sim 0.75\ deg^2$. Covering such a large field implies that we stack 50000 sources, compared to 1000 or less from similar studies (Greve et al. 2010; Decarli et al. 2014).

5.2 Data: maps and catalogs

Optical to Mid-Infrared
The UV-NIR photometric catalog presented by Capak et al. (2007) for the COSMOS

field presents photometry in 15 photometric bands between 0.3 and 8 μm. It contains $\sim 10^6$ sources down to a magnitude of $I_{\rm AB} < 26.5$ and covers an extension of 2 deg^2. The photometry has been extracted by using the same aperture (3 $''$) in all bands. In this paper an updated version of this catalog is used (version 1.5 April 5th 2008, hereafter COSMOS i-band catalog).

Photometric redshifts were computed by using additional intermediate and narrow bands, i.e., in total 30 photometric bands, and reach an accuracy of $\sigma_z/(1+z) \sim 0.04$ (Ilbert et al. 2010) for approximately 2×10^5 galaxies at z < 1.2 (and 0.1 accuracy for 8×10^5 galaxies; see Ilbert et al. (2010)). This remarkable photometric redshift accuracy is close to that required to investigate the Large Scale Structure (LSS), i.e., $\sigma_z/(1+z) \leq 0.02$ (Scoville et al. 2007).

In addition to this catalog, we make use of a $K_{\rm S}$ band selected catalog (McCracken et al. 2010). This catalog covers the 2 deg^2 COSMOS field, and presents photometry for the following bands: B, i^*, z$^+$, J, $K_{\rm S}$. It is 90% complete at $K_{\rm S} \sim 23$ for stars and bulges, and 70% complete for disks. Hereafter this catalog will be referred to as $K_{\rm S}$ band catalog.

The 3.6 μm catalog (Ilbert et al. 2010) was produced by using the Infrared Array Camera (IRAC) on board the *Spitzer* space telescope. The array contains 256 × 256 pixels with a field of view of 5.2 × 5.2 arcmin^2 and a resolution of $\sim 2''$. The catalog is 90% complete at 5 μJy (22.15 in AB magnitude) and 50% complete at 1 μJy (23.9 in AB magnitude). The number of sources contained in this catalog is ~200,000 (Ilbert et al. 2010).

The 24 μm selected catalog was produced by using the Multiband Imaging Photometer (MIPS) on the *Spitzer* space telescope. MIPS is an array of 128 × 128 pixels^2 with a field of view of 5.4 × 5.4 arcmin^2 and a resolution ~ 6 arcsec. The number of sources available in this catalog are 17,713 and the flux cut is 0.15 mJy. This is a shallow survey with an observation time of 16 hours, which covers the two square degrees of the COSMOS field.

(Sub)millimeter

LABOCA

The LABOCA Map and catalog were presented in Chapter 2.

The central 20 × 20 arcmin^2 (corresponding to a region with the greatest multi-wavelength coverage) of the COSMOS field were mapped at 1.2 mm. These observations were carried out with the 117 channel Max-Planck Bolometer array (MAMBO-2; Kreysa et al. 1998). The effective beam FWHM is 10.7 arcsec and the reached noise level is ~1 mJy/beam (Bertoldi et al. 2007). The catalog contains 15 sources with a significance between 4 and 7 σ and 12 with lower significance based on their association with radio sources.

Centimeter

The observations were carried out with the Very Large Array (VLA) interferometer at 1.4 GHz in A and C configurations with a final resolution of 1.5 × 1.4 arcsec^2. This is a deep map that includes data in addition to the VLA-COSMOS Large Project data (Schinnerer et al. 2007, 2010). The noise level in the final map reaches a value of ~ 7-8 μJy/beam, which is necessary to study the faint radio population. The observations match the typical resolution of ~ 1" for optical-NIR ground-based data available for the field. The catalog, (Schinnerer et al. 2007) at 1.4 GHz, corresponds to a shallower version of the VLA map mentioned above, i.e. rms ~ 10μJy/beam. It contains 3658 sources with a signal-to-noise ratio greater than 4.5. This catalog presents a statistical flux limited sample (unlike the deep catalog).

5.3 Populations to be stacked

5.3.1 BzK galaxies

The BzK color-color selection was introduced to select star-forming and old passive galaxies at $1.4 \leq z \leq 2.5$. It makes use of B, z^+ and K_{S} bands. The color difference (z-K)-(B-z) is referred to as BzK. The method was originally introduced by Daddi et al. (2004) and it has a physical motivation. The z-K_{S} color selects galaxies according to the strength of the Balmer jump at 3647Å and the 4000Å break. However, these spectral features close to each other are originated from two different galaxy environments. On one hand, the Balmer jump is characteristic of warm blue stars, which are typical in star-forming galaxies. On the other hand, the 4000Å break originates by an accumulation of absorption lines, mainly from ionized metals. This jump is stronger as the opacity increases, which is a sign of a cold and old star population. In order to discriminate between star-forming and passive galaxies, the B-z color is used. This color measures the UV slope part of the spectrum at these redshifts. A low B-z value is indicative of a star-forming galaxy, given that young star-forming galaxies have a strong presence of blue stars. In the case of old passive galaxies the spectrum is dominated by old and red stars, which produces that the color B-z rises in comparison to young galaxies.

As pointed out in McCracken et al. (2010) the Subaru B-filter used to observe the COSMOS field and the VLT B-filter used by Daddi et al. (2004) to define the BzK criteria are different, therefore to use the definition given by Daddi et al. (2004) we employ the transformation given in McCracken et al. (2010) for the (B-z) color. Defining bz = $\mathrm{B}_{J_{total}}$ - z^+_{tot} we have, in the case that bz <2.5

$$bz_{COSMOS} = bz + 0.0833 \times bz + 0.053 \tag{5.1}$$

otherwise, for objects with bz >2.5

$$bz_{COSMOS} = bz + 0.27 \tag{5.2}$$

The bz_{COSMOS} is the corrected value that we use here. Thus, the BzK selection criteria is summarized as follows:

- $(z-K)$-$(B-z) \geq$ -0.2 → Star forming galaxies at 1.4≤z≤2.5
- $(z-K)$-$(B-z) <$ -0.2 and $z-K > 2.5$ → passive galaxies at z≥1.4
- $(z-K)$-$(B-z) <$ -0.2 and $z-K < 2.5$ → galaxies at z<1.4
- $(z-K) < 0.3(B-z)$-0.5 → stars

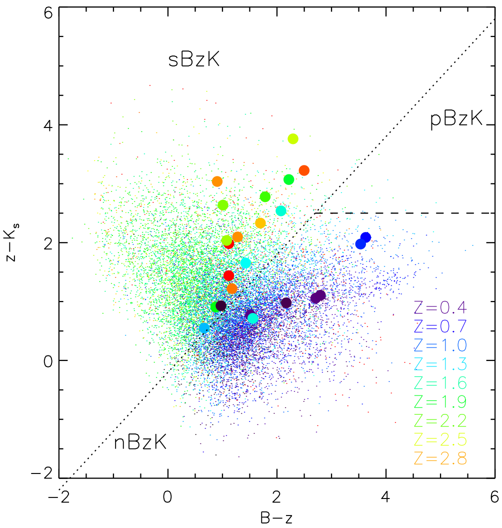

Figure 5.1: BzK color criteria (Daddi et al. 2004). BzK $>$ −0.2 (dotted line) selects star-forming galaxies at z $>$ 1.4. BzK $<$ −0.2 and z-K $>$ 2.5 (dashed line) selects old passive galaxies at z $>$ 1.4. BzK $<$ −0.2 and z-K $<$ 2.5 selects galaxies at z $<$ 1.4. Overplotted as small dots are optically selected galaxies (photometric catalog version 1.5 from Capak et al. (2007)). Big dots are submillimeter galaxies of the LABOCA COSMOS Survey presented in Chapter 2. The blue and red colors indicate low and high redshift galaxies, respectively.

This color-color criterion is shown in Fig. 5.1 for optically selected sources. Low and high redshift galaxies are shown in blue and red, respectively. The redshifts correspond to photometric redshifts (Ilbert et al. 2010). It is important to note that the BzK "star forming galaxies" could be contaminated by AGNs as a similar method has been developed to identify luminous QSOs (Sharp et al. 2002; Daddi et al. 2004). Furthermore, Type II AGN (Seyfert) also fall within this region (see Fig. 20 in Smolčić et al. 2008). It is clear that the BzK diagram is a good discriminator between low redshift and high redshift actively star forming galaxies. However, it is not such a clear identifier for passive galaxies. As argued by Reddy et al. (2005) many of these galaxies can be missed in the B-band. They propose a better method to identify these types of galaxies by using a single color such as $J - K$ or $z - K$.

Fig. 5.2 shows the BzK diagrams for optical sources in three different redshift ranges. The agglomeration around the discrimination line is clear, showing the contamination of the high redshift galaxies ($1.4 < z < 2.5$) due to low redshift galaxies at $z \simeq 1.4$. This is expected because the limit, of course, is not strict. The highest redshift range (left lower panel) shows that there are very high redshift galaxies that are coming back to the low-redshift region of the diagram, because the Balmer break is no longer falling in the relevant bands at these redshifts. An alternative possibility to select higher redshift galaxies is to shift the criterion to redder bands. Submm galaxies have a special position within this diagram. They are redder than the average in both colors B-z and z-K (Bertoldi et al. 2007). From 24 submm galaxies with identified optical counterparts 15 are placed between 1 $<$ B-z $<$ 3 and 1 $<$ B-z $<$ 4.5 (see Fig. 5.1). The radio selected sources follow a similar path in the BzK diagram like optically selected galaxies (Smolčić et al. 2008).

5.3.2 NUV - r$^+$ galaxies

This spectral classification is defined in Ilbert et al. (2010), where a set of 1500 galaxies were selected to provide an unbiased sample of galaxies, which include E/S0, early spiral, late spiral, or irregular galaxies. The selection of galaxies is based on the best-fit template (Bruzual & Charlot 2003, BC03) to the photometric data of the galaxies. From these

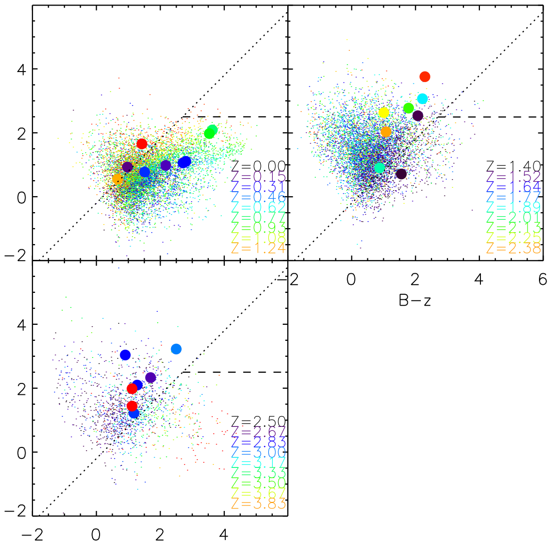

Figure 5.2: Same as Fig. 5.1 but for different redshift intervals. Right upper panel: galaxies between redshifts 0 and 1.5. Left upper panel: galaxies between redshifts 1.4 and 2.5. Left lower panel: galaxies at redshifts greater than 2.5.

templates, the intrinsic, i.e., dust unextincted, rest-frame color (NUV - r^+)$_{\rm temp}$ is used to split the sample of galaxies according to the degree of star formation activity they have. A similar criteria that can be found in the literature is M_U - M_V versus M_V-M_J, however (NUV - r^+)$_{\rm temp}$ is a better indicator of the current (light weighted average age of $\sim 10^8$ yrs) versus past star formation activity ($> 10^9$ yrs) (Arnouts et al. 2007; Martin et al. 2007). As shown in Fig. 4 of Ilbert et al. (2010) (NUV - r^+)$_{\rm temp}$ > 3.5 selects in a efficient way E/S0 galaxies, which are tagged as "quiescent galaxies". "Intermediate galaxies", which refers mainly to early spiral galaxies are selected by using $1.2 <$ (NUV - r^+)$_{\rm temp}$ $<$ 3.5. Finally, "High activity galaxies" are defined as (NUV - r^+)$_{\rm temp}$ < 1.2.

In order to apply this method, one needs to have enough photometric data, e.g., like in the COSMOS field, that allow to discriminate between different SED templates in the most accurate way. In this sense, the *BzK* classification is cheaper in terms of telescope time, as only three specific bands are needed.

Karim et al. (2011) have correlated the 3.6 μm catalog with the K band catalog of the COSMOS field, to test the agreement between the star-forming and passive populations. The conclusion from the common galaxies to both catalogs, is that both methods agree very well when separating galaxies as star-forming or passive galaxies.

5.4 870 μm stacking

5.4.1 Stacking different galaxy populations

We proceed with the stacking on the 870 μm LABOCA map of the COSMOS field (Chapter 2) of the populations described in the previous section. They have been stacked in different K_S band magnitude bins, which vary in the range $18 \leq K_S \leq 24$. Each bin contains the same number of galaxies in order to assure similar sensitivities for the different bins, hence allowing for a direct comparison. The analysis is performed over the same area that was used for the source extraction in Chapter 2, i.e., 0.75 deg^2. The results are reported in Tables 5.1 and 5.2.

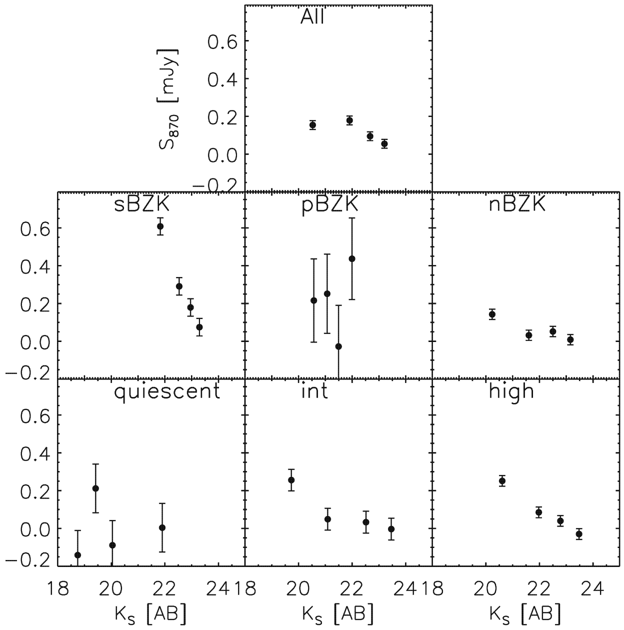

Figure 5.3: Differential stacking plot, showing the dependence of the stacked submm signal as we stack fainter galaxies in the K_S band.

We show the average density fluxes, using the Weighted Mean Stacking, and the Global Deblending Technique (Chapter 4). We report for both analysis results including and excluding pixels with a $|S/N| > 3$. In the remaining, we will report the results obtained with the Global Deblending Stacking technique without including pixels with a $|S/N| > 3$. This choice is based following the discussion in Chapter 4.

5.4.2 Dependence of the stacked signal with stellar mass and with redshift

The conclusions of the majority of the stacking studies carried out to date depend on the depth of the catalogs used for stacking. Therefore, when comparing stacking results one always has to take into account the depth of the different studies. We show in Figure 5.3 that as the stacking includes more and more faint optical galaxies there is a trend towards lower flux values (best seen in the sBzK case).

In the radio regime, at 1.4 GHz, Dunne et al. (2009) stacked BzK galaxies on the Ultra-Deep Survey (UDS, 0.62 deg^2) observing a decreasing trend when stacking fainter objects in the K_S band. Dunne et al. (2009) give an explanation for the trend based on the redshift distribution of the different populations. As the stacking is carried out in fainter K_S magnitude bins, these bins contain more objects at high redshift, which suggests that radio fluxes are decreasing less quickly with redshift compared to the K_S band fluxes.

In the case of the submillimeter regime we suggest that this trend could be related to the stellar mass of the galaxies being stacked. We show the dependence of the stacking as the stellar mass decreases in Fig. 5.4. It is clear that higher stellar mass systems have a higher contribution to the submillimeter stacked signal and that lower stellar mass systems make

Table 5.1: Stacking results on LABOCA map

All	sBzK	pBzK	nBzK
Global Deblending $S_{870\mu m}$ including detected sources			
0.15±0.02(20.53,19085, 6.61σ)	0.61±0.05(21.83,4870, 13.34σ)	0.22±0.22(20.57,227, 0.98σ)	0.14±0.03(20.24,13987, 5.24σ)
0.18±0.02(21.91,19086, 7.65σ)	0.29±0.05(22.54,4870, 6.34σ)	0.25±0.21(21.07,228, 1.20σ)	0.03±0.03(21.60,13988, 1.17σ)
0.09±0.02(22.67,19085, 4.06σ)	0.18±0.05(22.96,4870, 3.88σ)	-0.03±0.22(21.49,227, -0.13σ)	0.05±0.03(22.50,13988, 1.90σ)
0.05±0.02(23.21,19086, 2.34σ)	0.07±0.05(23.29,4871, 1.61σ)	0.44±0.22(21.99,228, 2.02σ)	0.01±0.03(23.16,13988, 0.32σ)
Global Deblending $S_{870\mu m}$ |S/N|<3			
0.14±0.02(20.53,19001, 6.16σ)	0.57±0.05(21.83,4845, 12.46σ)	0.20±0.22(20.57,225, 0.88σ)	0.13±0.03(20.24,13930, 4.82σ)
0.16±0.02(21.91,19001, 6.96σ)	0.26±0.05(22.54,4845, 5.59σ)	0.27±0.21(21.07,226, 1.30σ)	0.02±0.03(21.61,13930, 0.87σ)
0.08±0.02(22.67,19001, 3.27σ)	0.16±0.05(22.96,4845, 3.36σ)	-0.02±0.22(21.49,226, -0.11σ)	0.05±0.03(22.50,13930, 1.73σ)
0.05±0.02(23.21,19002, 2.00σ)	0.07±0.05(23.29,4846, 1.43σ)	0.37±0.22(21.99,226, 1.71σ)	0.00±0.03(23.16,13931, 0.02σ)
Weighted Mean Stack $S_{870\mu m}$ including detected sources			
0.27±0.03(20.53,19085, 7.71σ)	0.79±0.06(21.83,4870, 14.02σ)	0.45±0.24(20.57,227, 1.92σ)	0.25±0.04(20.24,13987, 5.98σ)
0.26±0.03(21.91,19086, 9.98σ)	0.34±0.06(22.54,4870, 5.59σ)	0.20±0.20(21.07,228, 1.04σ)	0.13±0.03(21.60,13988, 4.36σ)
0.16±0.03(22.67,19085, 5.16σ)	0.19±0.05(22.96,4870, 3.89σ)	0.23±0.23(21.49,227, 1.00σ)	0.11±0.03(22.50,13988, 3.57σ)
0.08±0.03(23.21,19086, 2.83σ)	0.14±0.06(23.29,4871, 2.21σ)	0.86±0.23(21.99,228, 3.78σ)	0.06±0.03(23.16,13988, 2.40σ)
Weighted Mean Stack $S_{870\mu m}$ |S/N|<3			
0.23±0.03(20.53,19001, 6.73σ)	0.69±0.05(21.83,4845, 12.57σ)	0.43±0.24(20.57,225, 1.79σ)	0.21±0.04(20.24,13930, 5.19σ)
0.21±0.03(21.91,19001, 8.51σ)	0.28±0.06(22.54,4845, 4.75σ)	0.17±0.20(21.07,226, 0.83σ)	0.10±0.03(21.61,13930, 3.57σ)
0.13±0.03(22.67,19001, 4.13σ)	0.16±0.05(22.96,4845, 3.48σ)	0.32±0.23(21.49,226, 1.36σ)	0.09±0.03(22.50,13930, 3.19σ)
0.06±0.03(23.21,19002, 2.21σ)	0.11±0.06(23.29,4846, 1.87σ)	0.54±0.22(21.99,226, 2.48σ)	0.04±0.03(23.16,13931, 1.65σ)

The units of the fluxes are mJy. The first number in parenthesis indicates median magnitude of all the sources in the respective magnitude bin. The second number corresponds to the number of stacked sources, while the third number indicates the signal-to-noise-ratio.

Table 5.2: Stacking results on LABOCA map

quiescent	intermediate	high
Global Deblending $S_{870\mu m}$ including detected sources		
-0.14±0.13(18.75,600, -1.08σ)	0.26±0.06(19.73,3102, 4.49σ)	0.25±0.03(20.61,12650, 8.85σ)
0.21±0.13(19.42,601, 1.64σ)	0.05±0.06(21.09,3103, 0.85σ)	0.09±0.03(21.98,12650, 2.98σ)
-0.09±0.13(20.04,600, -0.68σ)	0.03±0.06(22.52,3102, 0.57σ)	0.04±0.03(22.78,12650, 1.39σ)
0.00±0.13(21.90,601, 0.03σ)	-0.00±0.06(23.46,3103, -0.06σ)	-0.03±0.03(23.48,12651, -1.05σ)
Global Deblending $S_{870\mu m}$ |S/N|<3		
-0.12±0.13(18.75,597, -0.95σ)	0.24±0.06(19.73,3088, 4.12σ)	0.24±0.03(20.61,12595, 8.28σ)
0.15±0.13(19.42,597, 1.18σ)	0.05±0.06(21.09,3089, 0.88σ)	0.07±0.03(21.98,12595, 2.53σ)
-0.07±0.13(20.05,597, -0.54σ)	0.00±0.06(22.52,3089, 0.01σ)	0.02±0.03(22.78,12595, 0.82σ)
-0.04±0.13(21.92,597, -0.34σ)	-0.03±0.06(23.46,3089, -0.48σ)	-0.04±0.03(23.48,12595, -1.51σ)
Weighted Mean Stack $S_{870\mu m}$ including detected sources		
-0.16±0.14(18.75,600, -1.14σ)	0.37±0.07(19.73,3102, 5.72σ)	0.34±0.04(20.61,12650, 8.89σ)
0.23±0.13(19.42,601, 1.71σ)	0.13±0.06(21.09,3103, 2.31σ)	0.11±0.03(21.98,12650, 3.29σ)
-0.34±0.16(20.04,600, -2.11σ)	0.07±0.06(22.52,3102, 1.21σ)	0.05±0.03(22.78,12650, 1.89σ)
0.18±0.14(21.90,601, 1.25σ)	0.09±0.07(23.46,3103, 1.29σ)	-0.08±0.03(23.48,12651, -2.40σ)
Weighted Mean Stack $S_{870\mu m}$ |S/N|<3		
-0.08±0.14(18.75,597, -0.60σ)	0.32±0.07(19.73,3088, 4.81σ)	0.29±0.04(20.61,12595, 7.48σ)
0.18±0.13(19.42,597, 1.35σ)	0.11±0.06(21.09,3089, 2.00σ)	0.09±0.03(21.98,12595, 2.84σ)
-0.32±0.16(20.05,597, -1.98σ)	-0.11±0.06(22.52,3089, -1.69σ)	0.04±0.03(22.78,12595, 1.38σ)
-0.08±0.14(21.92,597, -0.54σ)	-0.08±0.07(23.46,3089, -1.20σ)	-0.09±0.03(23.48,12595, -2.68σ)

The units of the fluxes are mJy. The first number in parenthesis indicates the median magnitude of all the sources in the respective magnitude bin. The second number corresponds to the number of stacked sources, while the third number indicates the signal-to-noise-ratio.

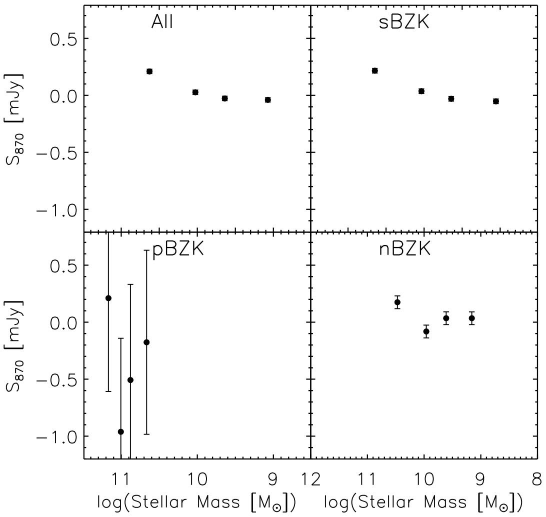

Figure 5.4: Differential stacking plot, showing the dependence of the stacked submm signal as we stack galaxies with lower stellar masses. The dashed line represent the 3σ level. In the stacking all the optical galaxies within 18 arcsec from a submillimeter source, which are listed in the LABOCA catalog, have not been taken into account. The boxes indicate the number of stacked galaxies that correspond to each point.

a minor contribution to it. To validate this explanation we show in Fig. 5.5 that fainter K_S magnitude bins contain galaxies whose stellar mass is lower than the stellar mass of brighter K_S magnitude bins.

We have not yet disentangled the redshift dependence from the stellar mass system dependence. In Figure 5.6 we plot the Stellar Mass-redshift dependence for different apparent K_S magnitude ranges (color code). The K_S luminosity is related to the stellar mass of the systems as described in Arnouts et al. (2007). In order to get an insight into the dependence on mass and redshift of the stacked signal we split the plot in different regions (each of them containing the same number of galaxies). The information of each region is shown in Table 5.3, where it is clear that the submm stacked signal increases with redshift. Furthermore, by comparing similar redshifts (regions 6 and 9) the dependence on the stellar mass is also noticed, the most massive stellar systems are the ones that are brighter at submillimeter wavelengths. This is in agreement with Hayward et al. (2011) who used a 3-D dust radiative transfer calculation on hydrodynamic simulations, and found that to produce a flux density S_{850} >3mJy a stellar mass of at least 6×10^{10} $M_\odot$ is necessary. This means that the observed trend towards lower submm fluxes which is observed in the stacked signal when using different K_S magnitude cutoffs can be explained by the stellar mass dependence described above. This does not rule out that also a different redshift dependence between the bands (K_S and 870 μm) can also be partially responsible for this slope.

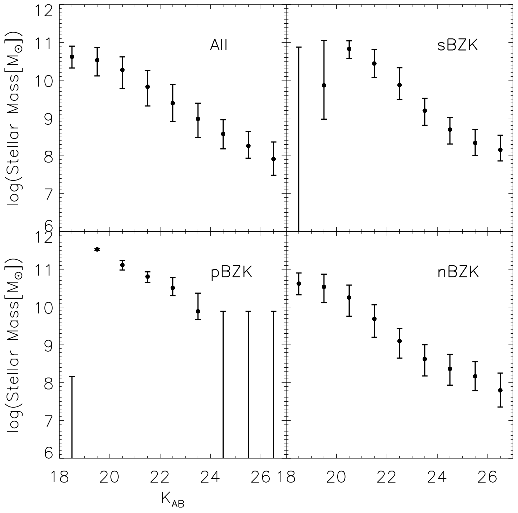

Figure 5.5: Evolution of the median Stellar Mass of the optical galaxy populations as the K_S magnitude decreases. The error bars correspond to the interquartile range of the stellar masses.

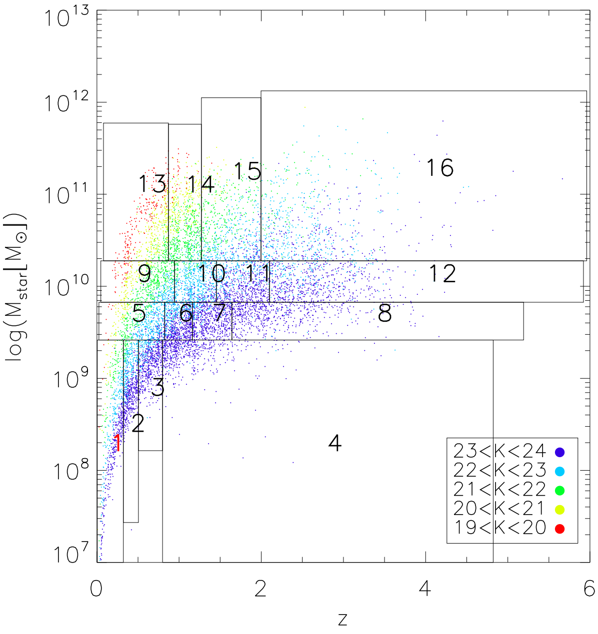

Figure 5.6: Stellar Mass-redshift dependence of the data. The color code indicates different K_S band apparent magnitude ranges. The plot is splitted in 9 different zones, each of them containing the same number of galaxies

Table 5.3: Information for the different zones in Figure 5.6

Region	Flux[mJy]	rms[mJy]	S/N[σ]	$z_{\rm med}$	Number
1	0.016	0.074	0.22	0.21	6874
2	-0.035	0.077	-0.45	0.38	6874
3	-0.062	0.079	-0.78	0.65	6874
4	-0.080	0.080	-1.00	1.01	6874
5	-0.049	0.079	-0.62	0.64	6874
6	-0.072	0.080	-0.89	0.98	6874
7	0.002	0.075	0.03	1.37	6874
8	0.037	0.072	0.51	2.06	6874
9	-0.007	0.076	-0.10	0.72	6874
10	0.021	0.074	0.29	1.18	6874
11	0.007	0.074	0.10	1.78	6874
12	0.099	0.069	1.43	2.59	6874
13	0.055	0.072	0.77	0.67	6874
14	0.125	0.066	1.869	1.06	6874
15	0.379	0.049	7.675	1.59	6874
16	0.228	0.057	3.976	2.55	6874

5.4.3 Contribution to the extragalactic infrared background light

In order to shed light on the type of galaxies that dominate the submillimeter emission we stack populations based on their color properties. Different color criteria have been developed in order to identify galaxies based on their red colors,i.e., Extreme Red Objects (EROs), Distant Red Galaxies (DRG), and BzK. In this work we focus on the BzK criterion (see Section 5.3). Also by using the color NUV-r^+, we can discern between quiescent, intermediate, and high activity galaxies (Ilbert et al. 2010).

Whether these colors are identifying star-forming galaxies or passive galaxies and their contribution to the extragalactic background light we can get insights via the stacking technique. Applying the stacking technique as pointed out in Chapter 4 to the populations described in Section 5.3 we obtain the average stacked fluxes of each population at 870 μm, which are shown in Table 5.1.

Combining this information and the surface densities of the populations, we can calculate the contribution of the different populations to the FIRB, which is shown in Figures 5.7 and 5.8. We have taken as reference values for the FIRB those published by Puget et al. (1996) and Fixsen et al. (1998), which were computed using the data from the Far Infrared Absolute Spectrometer (FIRAS) on board COBE. The contribution to the FIRB is computed in the following way:

$$\frac{S_{870\mu m} \times counts}{AreaMap}\ [\mathrm{Jy\ deg^{-2}}] \tag{5.3}$$

where $AreaMap$ corresponds to the number of beams in the map divided by the number of beams within a square degree, $S_{870\mu m}$ is the stacked flux density in Jansky, and *counts* is the number of stacked galaxies (shown in parenthesis in Table 5.1).

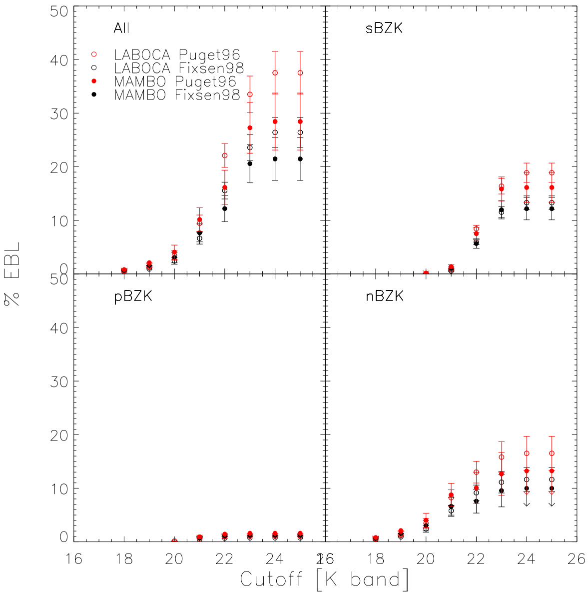

Figure 5.7: Extragalactic Background contributions as a function of the K$_S$ magnitude from galaxies in the K_S band catalog. Open dots are the contribution to the 870 μm background and for comparison we also show filled dots, which are the contributions to the 1.2 millimeter background. Black and red dots are the contributions to the FIRB based on the value for the FIRB given by Fixsen et al. (1998) and Puget et al. (1996), respectively. Upper Left Panel: Contribution from all the sources in the K$_S$ band catalog. Upper Right Panel: Contribution from sBzK galaxies. Bottom Left Panel: Contribution from pBzK galaxies. Bottom Right Panel: Contribution from nBzK galaxies.

5.4.3.1 Contribution of NIR color selected populations

We derive the contribution to the FIRB at 870 μm. For comparison we also compute the contribution at 1.2 mm, using the MAMBO data of the central 400 arcmin^2 of the COSMOS field (see Sect. 5.2) We show the results at different K_S band cutoffs (the K_S band sample is ∼70% complete up to K$_S$ ∼23). We find that taking into account all the galaxies up to K$_{AB}$ <24 we resolve 37.55% ± 3.965% of the FIRB at 870 μm and 28.43% ± 5.31% at 1.2 mm. The sBzK population contributes 18.8% ± 1.8%, while passive galaxies (pBzK) contribute <1%. The low-redshift galaxies (nBzK) contribute 16.51% ± 3.17% of the FIRB.

Comparing with other values in the literature we have to be careful, because of the different cutoff magnitudes. Takagi et al. (2007) report a contribution from the sBzK galaxies down to K$_{Vega}$ $\lesssim$ 20 of 8.3%± 3.9%, while Greve et al. (2010) reports a contribution of 3.4%±1.3%. At a similar cutoff, i.e., K$_\mathrm{S}$ < 22, we obtain 8.4%± 0.66%. If we include all the galaxies down to K$_S$ <22 the contribution is 22.09%± 2.22%, which is in agreement with the 16.5%±5.7% cited in Greve et al. (2010).

In Figure 5.7 the contribution to the FIRB at 870 μm is systematically greater than at 1.2 mm. This trend could be explained because of the smaller area covered by the survey at 1.2 mm or also by the uncertainties in the FIRB values given by Puget et al. (1996) or Fixsen et al. (1998).

Including all the galaxies in our catalog down to K$_S$ <24, without taking incompleteness into account, we recover ∼28% of the FIRB. The average flux density of these galaxies is ∼0.1 mJy. At this flux level the SMGs number counts suggest that ∼100% of the FIRB is resolved (Knudsen et al. 2008), although due to low number statistics, this number could be overestimated. However, the contributions given by Greve et al. (2010) and by this study do not resolve the total FIRB, which indicates that a large fraction of the FIRB is missed in a K_S band selected catalog, at least down to K$_{\mathrm{S}=}$23.

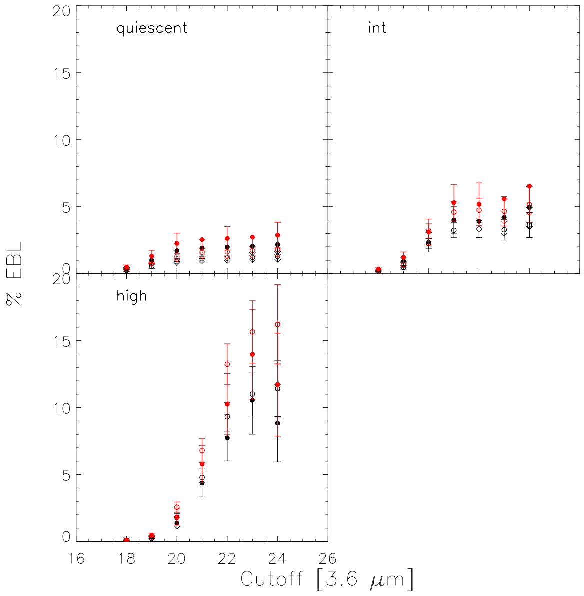

Figure 5.8: Extragalactic Background contributions as a function of the K_S magnitude from galaxies in the IRAC band catalog. Open dots are the contribution to the 870 μm background and for comparison we also show filled dots, which are the contributions to the 1.2 millimeter background. Black and red dots are the contributions to the FIRB based on the value for the FIRB given by Fixsen et al. (1998) and Puget et al. (1996), respectively. Upper Left Panel: Contribution from quiescent star forming galaxies. Upper Right Panel: Contribution from intermediate activity galaxies. Bottom Left Panel: Contribution from high activity galaxies.

5.4.3.2 Contribution of NUV$-$ r$^+$ color selected populations

In the same way as in section 5.4.3.1 we investigate different types of galaxies but this time by using the unextincted rest-frame colors (NUV-r$^+$)$_{\rm template}$ (Martin et al. 2007; Arnouts et al. 2007; Ilbert et al. 2010). Depending on the value of the color we classified the galaxies as "quiescent" ((NUV-r$^+$)$_{\rm template}$ > 3.5); "intermediate activity" ($1.2 <$ (NUV-r$^+$)$_{\rm template}$ < 3.5); "high activity" ((NUV-r$^+$)$_{\rm template}$ < 1.2).

To our knowledge there so far has been no study of the stacking of these populations at 870 μm or at 1.2 mm, so comparison with other studies is not possible and we limit ourselves to report the results of this work. The contribution at 870 μm of the quiescent galaxies is not greater than 1.81%, while intermediate activity galaxies contribute 5.15%± 1.33%. The greatest contribution as expected is coming from high-activity galaxies which contribute 16.21%±2.95%. In Figure 5.8 the contribution of the different populations at both wavelengths, i.e., 870 μm and 1.2 mm, are shown. We are able to recover $\sim 37\%$ of the FIRB at 870 μm. This is clear evidence that still a large fraction of the CIB is missed in galaxies which are fainter than $\rm K_S = 23$. The nature of these galaxies is puzzling. On one hand they could be intrinsic faint submillimeter galaxies, that at the same time are faint in the $K_{\rm S}$ band. If this is the case we should expect a large number of undetected sources in order to account for the total budget of the CIB. On the other hand, we could be missing sources which are at high redshift. In fact, using a representative submillimeter galaxy SED, we can compute the behavior of the average $K_{\rm S}$ band value as a function of the submillimeter flux and redshift. This can be seen in Fig. 5.9, where we have used the averaged SED of a sample of submillimeter galaxies computed by Michałowski et al. (2010). We scale the SED to three different 870 μm fluxes, i.e., 0.2, 2, and 8 mJy. The $K_{\rm S}$ band catalog we use here is 70% complete down to $\rm K_S = 23$, which is shown as an horizontal dot-dashed line for reference in Fig. 5.9. Galaxies with an 870 μm flux close to the average that we find for all the $K_{\rm S}$ band selected galaxies, i.e., have a $K_{\rm S}$ band magnitude fainter than 23 already at $z \sim 1$, which means that we miss a large fraction of faint submillimeter galaxies at redshifts greater than 1. On the other hand, high redshift bright submillimeter galaxies, are fainter than our $K_{\rm S}$ band threshold at $z \sim 4$, which means that we could potentially miss the contribution to the CIB of bright submillimeter galaxies at high redshift. A last scenario corresponds to highly dust obscured objects, which are not necessarily at high redshift, but where the emission in the $K_{\rm S}$ band is strongly affected by the presence of dust. This scenario is supported by observations of submillimeter galaxies themselves, where many of them do not have a counterpart or are very faint in the $\rm K_S$ band (Weiß et al. 2009; Smolčić et al. 2012a; Walter et al. 2012). The results here obtained agree with the recent findings of Viero et al. (2013), who using a deeper K band catalog (K ¡ 24) (Lawrence et al. 2007; Warren et al. 2007) in the UKIRT Deep Sky Survey (UKIDSS), find that up to 70% (40%) of the CIB at 500μm (1100 μm) can be resolved.

5.4.4 Assessing physical quantities from the 870 μm flux

In order to assess physical quantities from the 870 μm flux as the infrared luminosity ($L_{\rm IR}$) and the star formation rate (SFR) it is required to make some assumptions about the source's SED, initial mass function, etc.

For instance, to calculate the luminosity at 870 μm a K correction factor is needed. This factor transforms the flux observed at some frequency into the flux in the rest frame of the source being observed. We calculate the luminosity by using Eq. (5.4)

$$L_\nu^K = \frac{4\pi d_{lum}^2}{1+z} K S_\nu^{obs}, \tag{5.4}$$

where $d_{\rm lum}$ is the luminosity distance, in meters, to the source; z is the redshift; and K is the correction factor, which is explained in the following.

We define K as the ratio between the flux in the rest frame and the flux in the observed frame, i.e., K=$S_\nu^{\rm K}/S_\nu^{\rm obs}$. In the ideal case where the SED of a galaxy has been observed at many wavelengths, this factor could be calculated with the data from the same galaxy. However, this is not the case in our study, so we assume that a SMG can be well represented by a local ULIRG like M82. We use the template of M82 given by Polletta et al. (2007). The K correction factor as a function of redshift at the LABOCA frequency, i.e., 345 GHz, is shown in Fig. 5.10. Once, we have calculated the K correction factor we can compute quantities such as the infrared luminosity, which corresponds to the luminosity of the galaxy between 8 to 1000 μm in the rest frame (see Fig. 5.11), and the star formation rate. Next, we make the assumption that a SMG can be reasonably well represented by a modified blackbody as described in Eq. (5.5)

$$L_\nu \propto B_\nu \left(T_{\rm d}\right) \nu^\beta, \tag{5.5}$$

where $T_{\rm d}$ is the dust temperature, β the emissivity index, and B_ν the Planck function at frequency ν and temperature $T_{\rm d}$. For β we use a value of 1.5 and for $T_{\rm d}$ we use a value of 30 K, typical for SMGs (Magnelli et al. 2012).

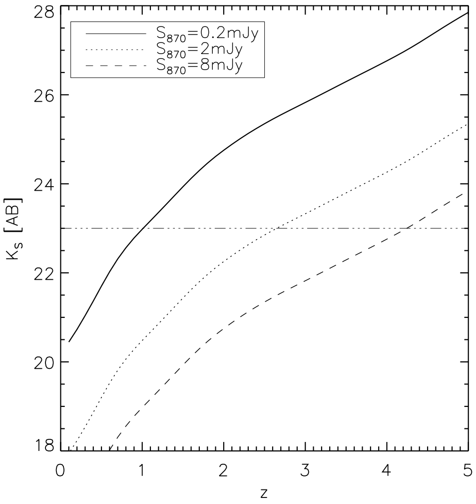

Figure 5.9: K_S band magnitude as a function of redshift for a galaxy with an average submillimeter SED (Michałowski et al. 2010). The solid line is the SED scaled to a 870 μm flux of 0.2 mJy, which is representative for the average flux of all the galaxies with a magnitude down to $K_S = 23$. The dotted line is for the SED scaled to 2 mJy, and the dashed line is for a bright submillimeter galaxy with a flux of 8 mJy. The dot-dashed horizontal line is at $K_S = 23$ the magnitude down to which our catalog is complete.

5.4.5 Stacking in redshift bins

We study the evolution of the stacked density flux of the different color criteria population as a function of redshift. Given that the K_S band catalog does not have redshift information, we correlate it with the i band catalog to assign photometric redshifts to the sources. For color selected population from the IRAC catalog we use the available photometric redshift of the catalog itself.

The different galaxy populations have been splitted in three different redshift bins to assure getting significant stacked flux density signal at least in some of the bins. Each bin has exactly the same number of galaxies in order to reach the same sensitivity in the different bins, allowing direct comparison among them. In addition we also split by magnitude, thus, we show bright magnitude samples which are complete (The K_S band catalog is 70% complete down to K_S =23) and faint samples which are not complete.

The general observed trend is a brighter 870 μm stacked signal as the redshift increases. This is in agreement with similar studies (Greve et al. 2010). The stacked fluxes have been converted to star formation rates by scaling a modified blackbody spectral energy distribution (SED), i.e. $S_\nu \propto \nu^\beta B(\nu, T_\mathrm{d})$ with $\beta = 1.5$ and $T_\mathrm{d} = 30$K, to the 870 μm flux point (see Fig. 5.10). Integrating the SED from 8 to 1000 μm we obtain the infrared luminosity (L_IR), and we convert it to SFR by using SFR[$M_\odot$yr^{-1}]$= 1.73 \times 10^{-10} L_\mathrm{IR}[L_\odot]$ (Kennicutt, Jr. 1998), which assumes a Salpeter initial mass function (IMF) (Salpeter 1955).

The redshift evolution of the 870 μm stacked signal is shown in Figures 5.12 and 5.13. The average 345 GHz signal from galaxies down to $K_S \leq 22$ in the brightest bin (blue line, note that the magnitude range is comparable to Greve et al. (2010)) , shows an evolution in redshift from <0.13 mJy to 0.44 mJy ($L_\mathrm{IR} < 0.15 \times 10^{11}$ to 1.37×10^{11} $L_\odot$ and SFR < 3 to 19 $M_\odot$/yr). These numbers are in agreement with Greve et al. (2010) who because of greater sensitivity could split their sample in a larger number of redshift bins. There, the flux is roughly constant in the low redshift bins ($\sim$ 0.1-0.2 mJy) and increases to $\sim$ 0.4 mJy at $z \sim$1.7.

The signal strength decreases as we stack the fainter magnitude bins, this trend is ex-

Figure 5.10: K correction factor at 870 μm, assuming an M82 SED template. The K term is defined as K=$S_\nu^{\rm K}/S_\nu^{\rm obs}$, hence excluding the $(1+z)$ term that takes into account the extra width of the differential frequency in the observed frame (Eq. 5.4).

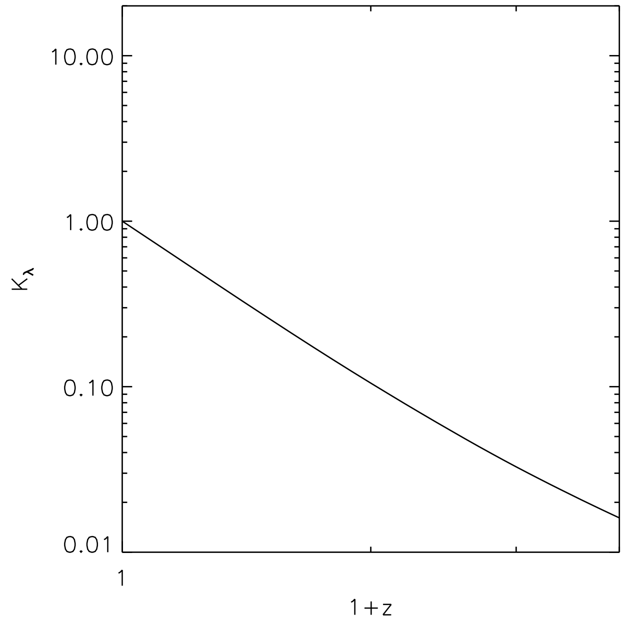

plained as we do not detect many massive stellar systems as the magnitude decrease (see Fig. 5.6). Turning to BzK selected galaxies, we find that the sBzK flux density average increases from 0.36 mJy to 0.73 mJy ($L_{\rm IR} \cong 1.27{\times}10^{11}$ to $L_{\rm IR} \cong 2.78{\times}10^{11}$ and SFR $\cong$ 22.11 to SFR $\cong 48.25\ M_\odot$/yr). In comparison, Greve et al. (2010) finds a roughly constant 870 μm signal ($\sim$ 0.4 mJy). In our case if we consider the whole data set, we find that at $z>2$ a small decrease in the submm average signal, however as already said before in this case we suffer from samples which are not complete.

The passive high redshift galaxies (pBzK) yield almost no detection except from some marginal detections at the lowest redshift bins of the whole pBzK population ($L_{\rm IR} \cong 2.02 \times 10^{11} \pm 0.64{\times}10^{11}$ L$_\odot$ and SFR $\cong 34.9\pm11.3\ M_\odot$/yr;black line) and for the brightest bin (L$_{\rm IR} \cong 4.56{\times}10^{11}\pm1.23{\times}10^{11}$ L$_\odot$ and SFR $\cong 78.9\pm21.3\ M_\odot$/yr; blue line). If we assume that the far-infrared radio correlation keeps constant as redshift increases, this is in agreement with Dunne et al. (2009) results. They find that at 1.4 GHz there is a dramatic change in the average radio emission from low redshift pBzKs in comparison with high redshift pBzKs.

For low redshift galaxies,i.e., nBzKs, the submm signal increases with redshift in all magnitude bins and again the stronger signal comes from the brightest magnitude bins. When comparing nBzKs with the high redshift star-forming galaxies (sBzK) we get a flux a factor $\sim$3 lower. This fact confirms that most of the star-formation occurs in high redshift systems. Typical SFRs for nBzKs are $\leq 10\ M_\odot$/yr and for sBzKs are $\sim$ 20–40 $M_\odot$/yr.

For the populations selected from the IRAC 3.6 μm catalog (see Fig. 5.13), the quiescent galaxies do not show any significant detection, setting an upper limit of $\sim$ 0.35 mJy; the *intermediate* galaxies contribute at the highest redshift ($z \sim 1.43$) $\sim$ 0.2 mJy with a SFR $\sim$ 12.2 $M_\odot$/yr. The major contribution is given by the brightest 3.6μm galaxies (blue line) at $z \sim 1.04$ ($\sim$0.49 mJy, SFR$\sim$25$M_\odot$/yr). The greatest contribution of *high* activity galaxies is $\sim$ 0.47 mJy at $z \sim 1.4$ which correspond to $\sim$ 28 $M_\odot$/yr). If we do not split

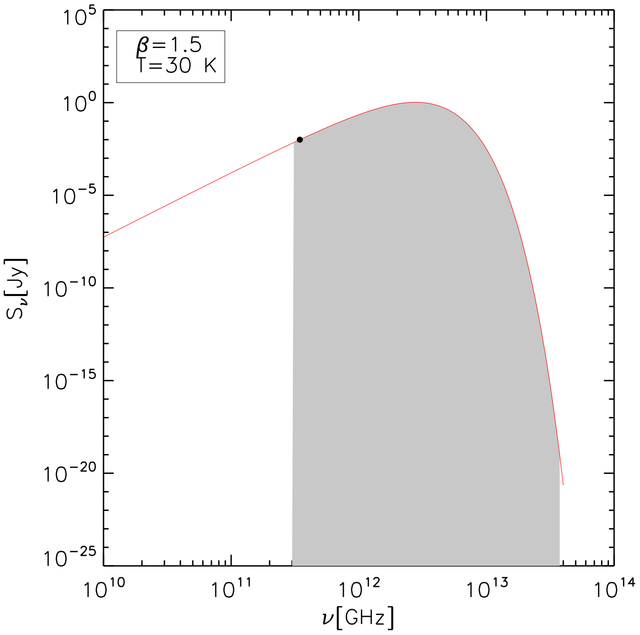

Figure 5.11: Modified blackbody SED with $\beta = 1.5$ and $T_{\mathrm{d}=30}$K. The gray filled area represent the L_{IR}, which corresponds to the integral of the SED between 8 to 1000 μm

by magnitude (dashed black line) the contribution is ~0.17 mJy at $z \sim 1.73$. The stacked density fluxes of both populations, *intermediate* and *high* activity are similar, however the *high* activity galaxies have a much greater contribution to the FIRB because of the galaxy number of this population (see Fig. 5.8). The stacked density fluxes are half way between the nBzK and sBzK galaxies. The fact that they are brighter than nBzKs can be explained as nBzK galaxies do not make distinction between low and high activity galaxies, on the other hand sBzK galaxies are placed at higher redshifts and as it was shown in Fig. 5.6 at higher redshifts galaxies have greater contributions to the submm signal. The L_{IR} and SFRs values should be taken with caution. The L_{IR} values are sensitive to the IMF and besides that the SFRs computed from the L_{IR} are sensitive to the chosen SED. Common SEDs can be on one hand modified blackbodies, which depend on the emissivity index and dust temperature ($\beta \sim 1-2$,$T_{\mathrm{d}} \sim$ 20–60K) and on the other hand typical starburst SEDs, i.e. Arp220, M82, etc. So, it is easy to have a factor 3 of difference depending on the choices of IMF and SFR as can be realized from the values cited in Greve et al. (2010).

5.5 Stacking at 1.4 GHz

5.5.1 Assessing physical quantities from the 1.4 GHz flux

In the radio wavelength regime in order to transform from the observed flux at 1.4 GHz into the rest-frame luminosity at 1.4 GHz of the observed source, we use Eq. (5.4). The K correction factor is calculated assuming that the radio spectrum is well described by a power law, i.e., $\mathrm{S}_\nu \propto \nu^\alpha$. Given that K=$\mathrm{S}_\nu^K/\mathrm{S}_\nu^{obs}$ and that $(1+z)$=$\nu_{\mathrm{rest}}/\nu_{\mathrm{obs}}$ it can be

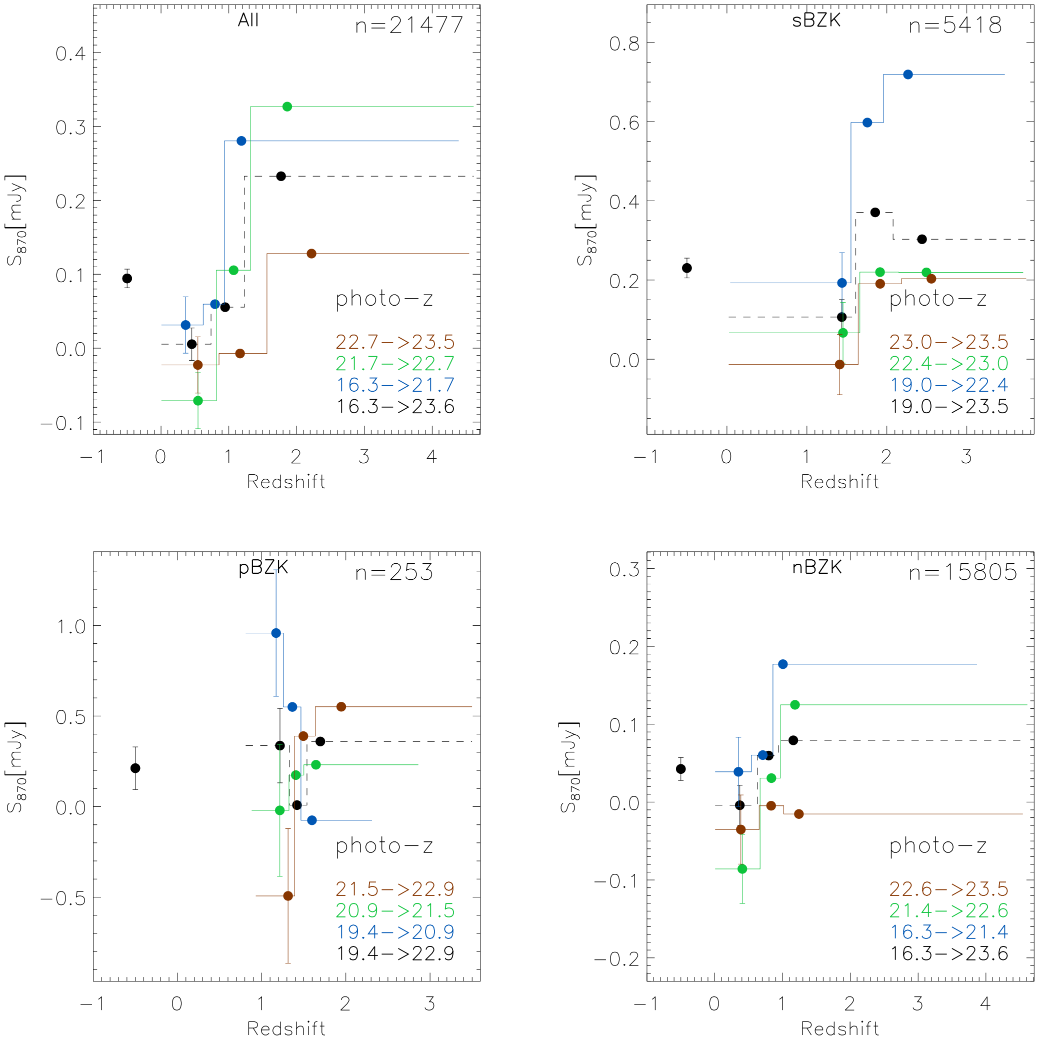

Figure 5.12: The 870 μm stacked flux density redshift evolution of different galaxy populations selected using the BzK color criteria (in the K_S band catalog). The different color solid lines show the evolution considering different magnitude bins, where each magnitude bin has the same number of galaxies. The black dashed line shows the redshift evolution of all the galaxies without slicing them according to magnitude. The black and red points at the negative redshift side show the stacked flux of all galaxies with and without available photometric redshift information, respectively. The number in the upper-right corner refers to the number of galaxies stacked in each point of the black dashed histogram, therefore each point of the solid color lines accounts for a third of this number.

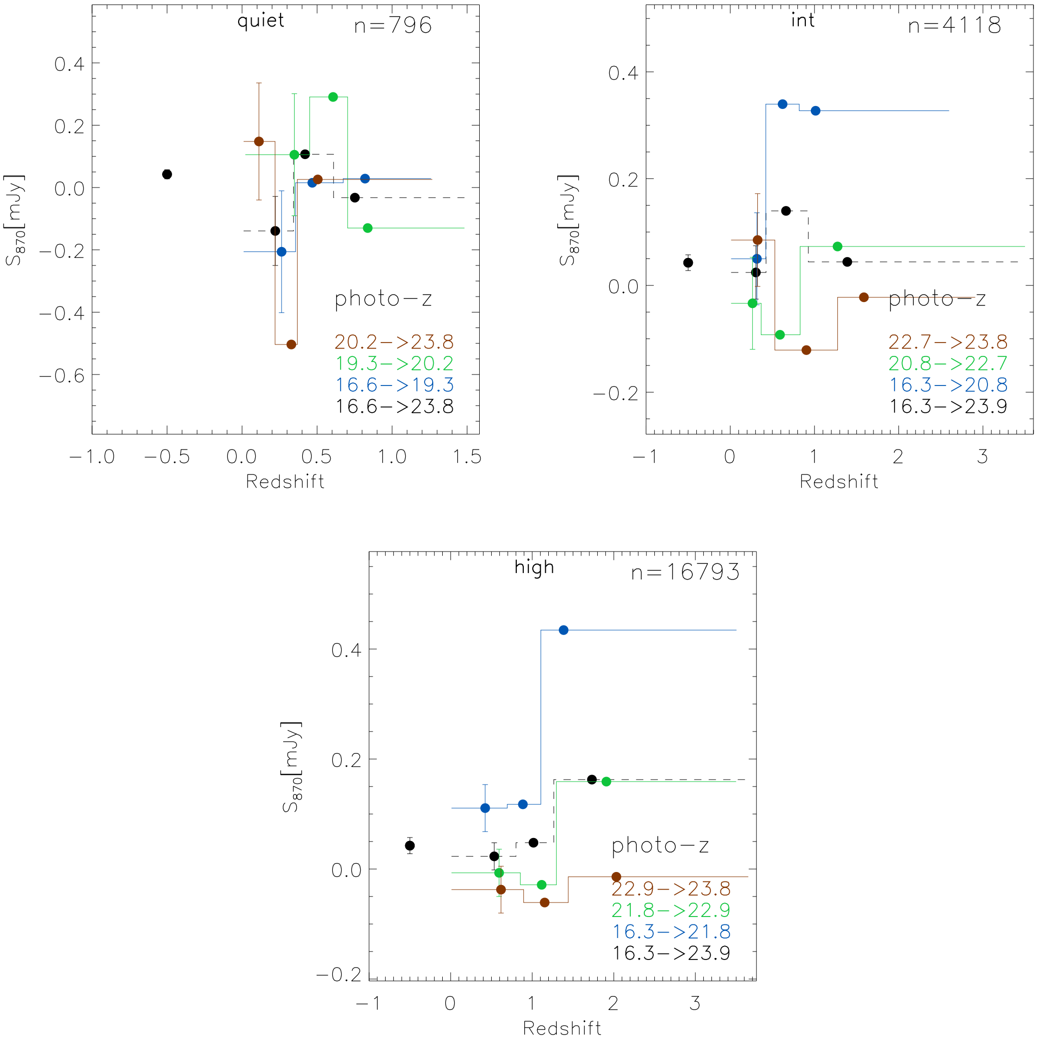

Figure 5.13: The 870 μm stacked flux density redshift evolution of different galaxy populations selected using the (NUV−r*) color (in the IRAC 3.6 μm band catalog). The lines and colors are the same as in Figure 5.12, except that at the negative redshift side there is no red point, because we have photometric redshift information for all the galaxies in the IRAC 3.6 μm catalog.

easily shown that K=$(1+z)^{-\alpha}$. The luminosity at 1.4 GHz can be calculated as

$$L_\nu^K = 4\pi d_{\text{lum}}^2 \frac{S_\nu^{\text{obs}}}{(1+z)^{(1+\alpha)}}, \tag{5.6}$$

and to have it in units of W Hz^{-1}

$$L_\nu^K = 9.523 \times 10^{12} \times 4\pi d_{\text{lum}}^2 \frac{S_\nu^{\text{obs}}}{(1+z)^{(1+\alpha)}}, \tag{5.7}$$

where z corresponds to the median redshift of the bin, D$_L$ is the luminosity distance given in Mpc, and α is the radio spectral index, which has a typical value of α ~-0.8 (Condon 1992). For the computation of the SFR, we use the calibration given by (Bell 2003)

$$\begin{aligned} \text{SFR}_{1.4\text{GHz}}(\text{M}_\odot\text{yr}^{-1}) &= 5.52 \times 10^{-22} L_{1.4\text{GHz}}, L > L_{\text{C}} \\ \text{SFR}_{1.4\text{GHz}}(\text{M}_\odot\text{yr}^{-1}) &= \frac{5.52 \times 10^{-22} L_{1.4\text{GHz}}}{0.1 + 0.9\,(L/L_C)^{0.3}}, L \leq L_{\text{C}}, \end{aligned} \tag{5.8}$$

where L_{C} =6.4×10^{21} W Hz^{-1}. This calibration is based on the infrared-radio correlation, and rests on the assumption that non-thermal radio emission tracks the SFR. It is chosen such that the radio SFR matches the infrared SFR for $L \geq L^*$ galaxies.

5.5.2 Stacking in redshift bins

As for the submm stacking, we divide the different populations by magnitude and redshift, which are stacked accordingly to the discussion of Chapter 4, i.e., using Median Stacking. The results are shown in Figs. 5.15 and 5.16. In general, analyzing the whole sample in our K_{S} band catalog, we see an increase in the radio flux density with redshift. With an average flux density rising from 4.1 μJy at $z \sim 0.46$ to 5.08 μJy at $z \sim 1.76$. If we translate it into luminosities, we see a luminosity increase from 2.64×10^{21}WHz^{-1} up to 8.19 ×10^{22}WHz^{-1} (note that error bars are included in Fig. 5.15).

Turning towards specific populations, we first analyze the BzK criterion. We find that at low-z, the pBzK galaxies have a radio luminosity (L$_{1.4GHz}$ $\cong 1.48 \times 10^{23} WHz^{-1}$) greater than that of sBzK galaxies ($L_{1.4\text{GHz}} \cong 7.36 \times 10^{22}$WHz^{-1}) in a similar z range, i.e. $z < 1.4$. In Dunne et al. (2009), stacking galaxies at 1.4 GHz in the Ultra Deep Survey, it is suggested that the low-z pBzK criterion is contaminated with star forming galaxies. Indeed, we also observe a $L_{1.4\text{GHz}}$ decrease at 1.34≤ z ≤1.62, and then finally again an increase at the highest redshift bin, reaching luminosity levels comparable to the sBzK galaxies. All of this is evidence that pBzKs galaxies are not a homogeneous population as a function of redshift. In Fig. 5.14 we show the comparison between our results and the results obtained by Dunne et al. (2009), for pBzK and sBzKs galaxies. The results here obtained confirm the $L_{1.4\text{GHz}}$ redshift evolution for both populations. Also, in the pBzK galaxies it is interesting that at high redshift the highest contribution to the $L_{1.4\text{GHz}}$ is coming from the faintest galaxies in the K_{S} band, which on average have a lower stellar mass than brighter K$_{\text{S}}$ band sources (see Fig. 5.5) at that redshift. On one hand, if this is due to star formation, it suggests that these galaxies are very efficient at producing stars. On the other hand, when star formation is not driving the bulk of this

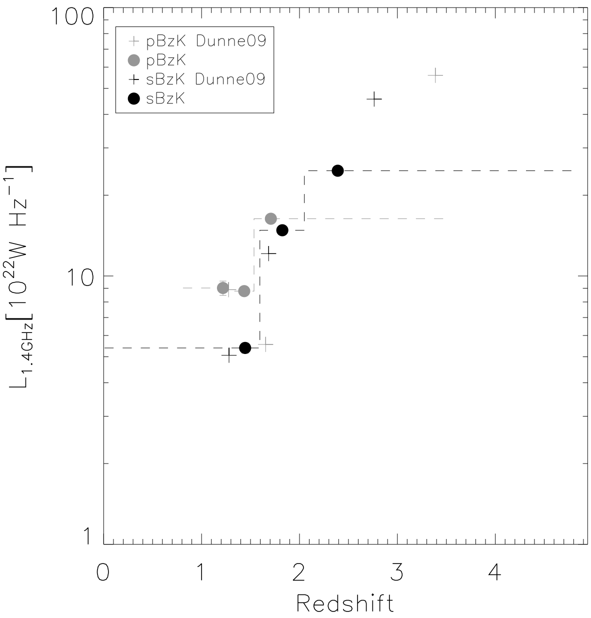

Figure 5.14: Stacked median luminosity redshift evolution for sBzK(black filled circles) and pBzK(gray filled circles) galaxies. For comparison we plot the data from Dunne et al. (2009), where black crosses are sBzK galaxies, and gray crosses are pBzK galaxies.

radio signal, it would suggest that the major contribution is due to radio quiet AGNs. Major contributions from radio quiet AGNs in the < 100 μJy regime have been predicted over the last years (Seymour et al. 2008; Smolčić et al. 2008; Padovani et al. 2009). In principle, we could disentangle which mechanism contributes the most, by stacking the galaxies at 870 μm, assuming that the submillimeter emission arises purely from star formation. However, given the low number of passive galaxies we can only set an upper limit of ~ 0.6 mJy for the 870 μm stacked flux of pBzKs. Such a signal, implies that a 3σ detection could be compared with what is obtained for sBzK galaxies, hence, we cannot draw strong conclusions on the real nature of these galaxies.

Low redshift BzKs, i.e., nBzKs, show a clear decrease of activity as the redshift decreases. Comparing them with sBzKs galaxies, nBzKs galaxies show low activity at all magnitudes and at all redshifts. For instance for the highest redshift bin of the brightest galaxies, sBzKs have $L_{1.4\mathrm{GHz}} \cong 3.23 \times 10^{23}$ W Hz^{-1}, which is ~ 7 times greater than the luminosity for the respective bin of nBzKs. This is in line with the idea that sBzK galaxies are star-forming galaxies, as can also been seen in the 870 μm stacking of previous section.

On the other hand, classifying the galaxy activity according to their unextincted rest-frame colors (NUV-r$^+$) (Sect. 5.2), we see a smooth behavior of the radio luminosities. As the activity of the galaxies increases, so does the radio luminosity. Also, all the different populations show an increase of the activity with redshift. For instance, the quiescent galaxies, on average, evolve from $L_{1.4\mathrm{GHz}} \cong 2.53 \times 10^{20}$ W Hz^{-1} at $z \sim 0.22$ up to $L_{1.4\mathrm{GHz}} \cong 1.73 \times 10^{22}$ W Hz^{-1} at $z \sim 0.75$, while the high activity galaxies evolve from $L_{1.4\mathrm{GHz}} \cong 4.23 \times 10^{21}$ W Hz^{-1} at $z \sim 0.53$ up to $L_{1.4\mathrm{GHz}} \cong 4.96 \times 10^{22}$ W Hz^{-1} at $z \sim 1.73$.

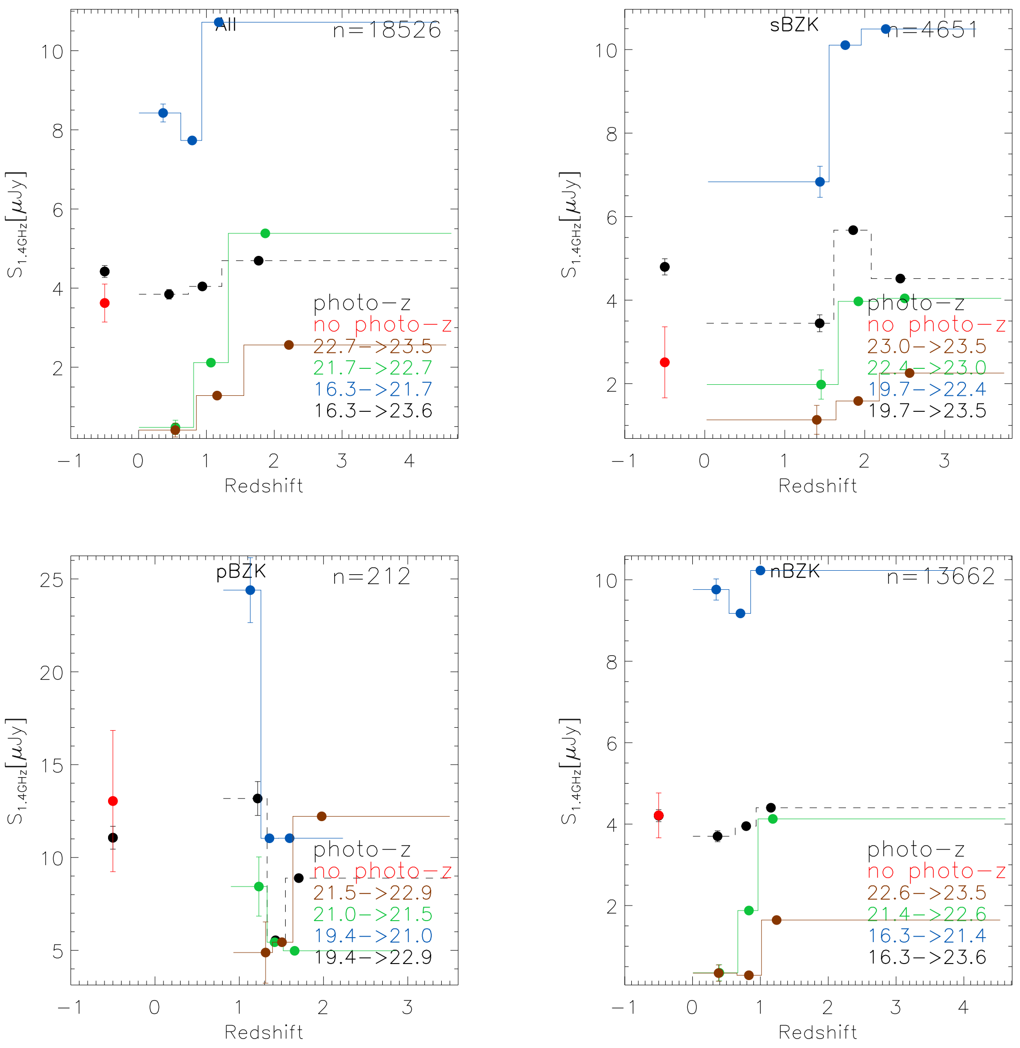

Figure 5.15: The 1.4 GHz stacked flux density redshift evolution of different galaxy populations selected using the BzK color criteria (in the K band catalog). The different color solid lines show the evolution considering different magnitude bins, where each magnitude bin has the same number of galaxies. The black dashed line shows the redshift evolution of all the galaxies without slicing them according to magnitude. The black and red points in the negative redshift side show the stacked flux of all galaxies with and without available photometric redshift information, respectively. The number in the upper-right corner refers to the number of galaxies stacked in each point of the black dashed histogram, therefore each point of the solid color lines accounts for a third of this number.

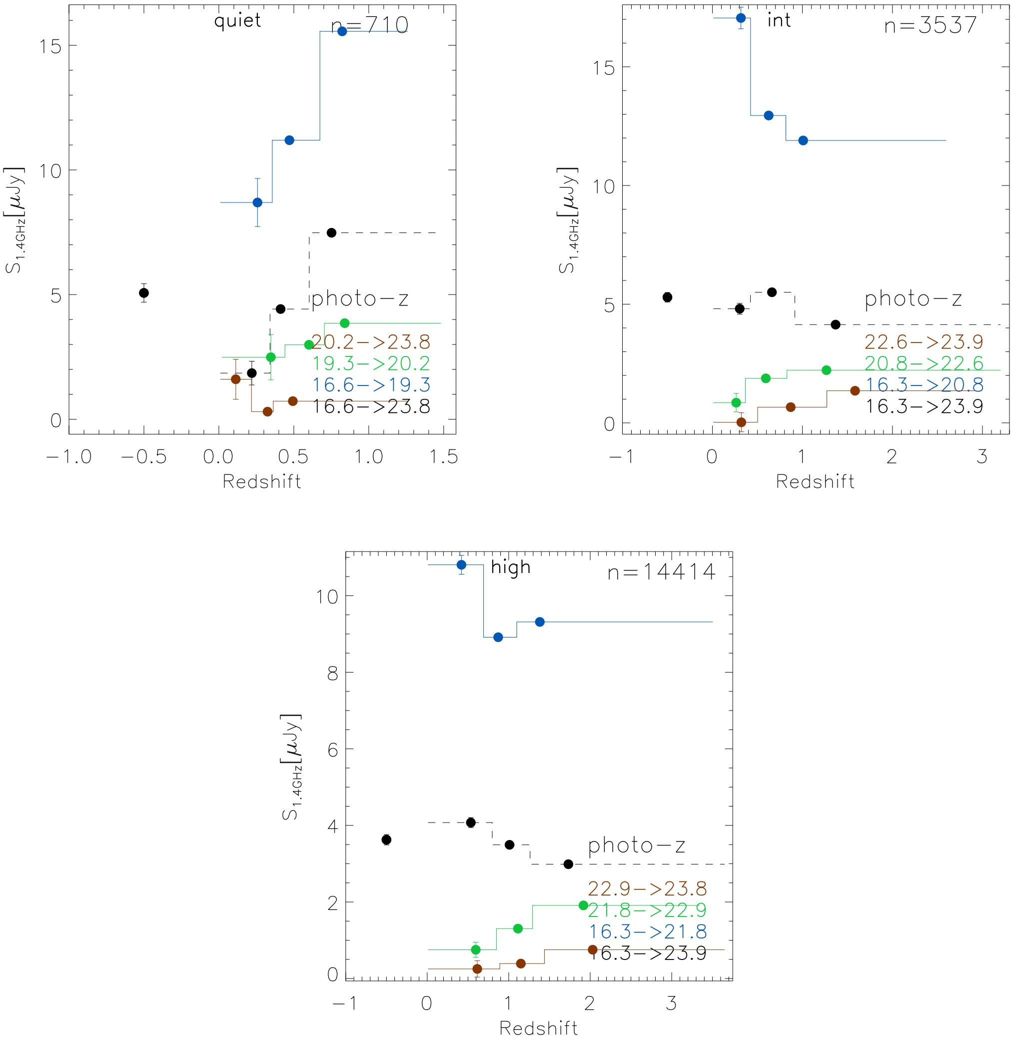

Figure 5.16: The 1.4 GHz stacked flux density redshift evolution of different galaxy populations selected using the (NUV−r*) color (in the IRAC 3.6 μm band catalog). The lines and colors are the same as in Figure 5.15, except that in the negative redshift side there is no red point, because we have redshift information for all the galaxies in the IRAC 3.6 μm catalog.

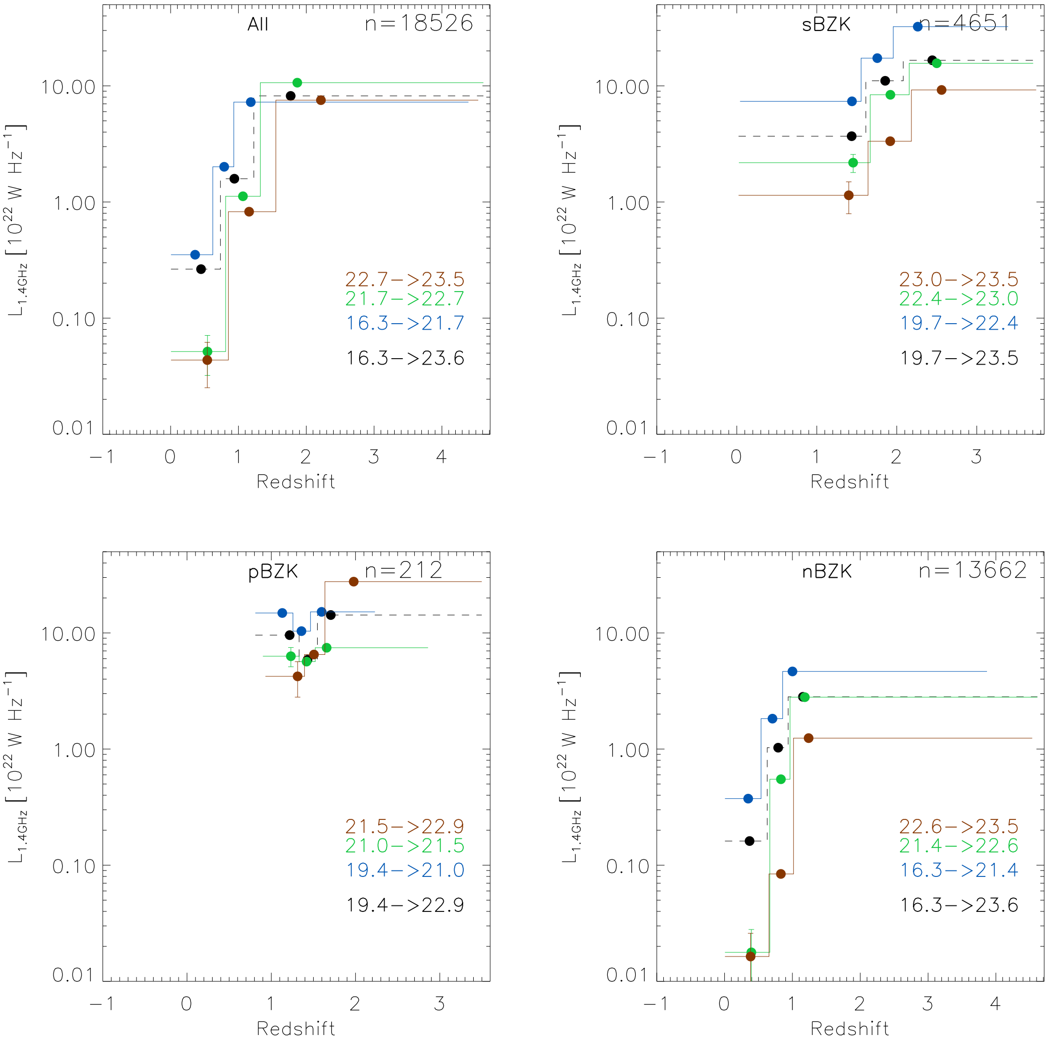

Figure 5.17: The 1.4 GHz stacked luminosity redshift evolution of different galaxy populations selected using the BzK color criteria (in the K_S band catalog). The different color solid lines show the evolution considering different magnitude bins, where each magnitude bin has the same number of galaxies. The black dashed line shows the redshift evolution of all the galaxies without slicing them according to magnitude. The black and red points in the negative redshift side show the stacked flux of all galaxies with and without available photometric redshift information, respectively. The number in the upper-right corner refers to the number of galaxies stacked in each point of the black dashed histogram, therefore each point of the solid color lines accounts for a third of this number.

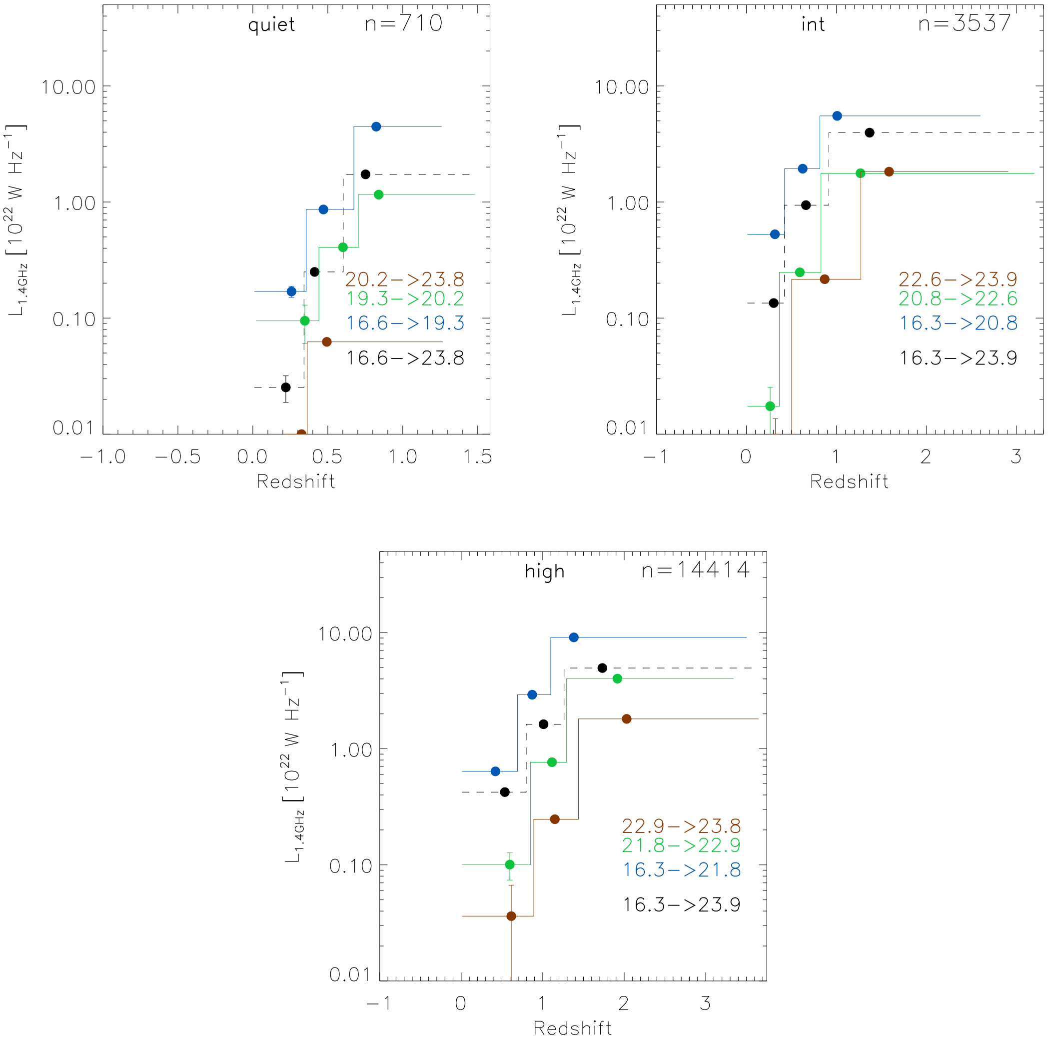

Figure 5.18: The 1.4 GHz stacked luminosity redshift evolution of different galaxy populations selected using the (NUV−r*) color (in the IRAC 3.6μm band catalog). The lines and colors are the same as in Figure 5.15, except that in the negative redshift side there is no red point, because we have redshift information for all the galaxies in the IRAC 3.6 μm catalog.

5.6 Investigating the FIR-radio correlation

Motivated by the evidence that the radio and far-infrared wavelength regime are correlated up to high redshift, i.e, $z \leq 2$ (Sargent et al. 2010; Ivison et al. 2010), we combine the 1.4 GHz and 870 μm and study if all the different populations follow the correlation as the redshift increases. Most of the studies (references) analyze this correlation via the so called q ratio, which is defined as:

$$q = log\left(\frac{L_{\rm IR}/3.75\times10^{12}}{\rm W}\right) - log\left(\frac{L_{1.4GHz}}{\rm WHz^{-1}}\right) \tag{5.9}$$

where, $L_{\rm IR}$ is the integrated luminosity from 8μm to 1000μ in the rest frame of the source. However, the derivation of $L_{\rm IR}$ from the 870 μm monochromatic flux is not trivial. As shown by Magnelli et al. (2012), although the 850 μm flux of SMGs observed in blank fields is correlated with $L_{\rm IR}$, this is not necessarily the case for fainter sources which are not observed in these surveys. As the main purpose of the stacking is to have insights on the properties of the faintest sources, for which we do not have individual detections, we prefer to study the correlation only using the observables, where no further assumptions have to be done. Carilli & Yun (2000) and Yun & Carilli (2002) have studied the far-infrared radio correlation at 850μm and 1.4 GHz, using the observed SEDs from local star-forming galaxies and show the evolution of the radio-to -submillimeter spectral index ratio as a function of redshift. For each color selected population, we build a common sample, where there are not submillimeter nor radio galaxies associated to the samples to be used. This

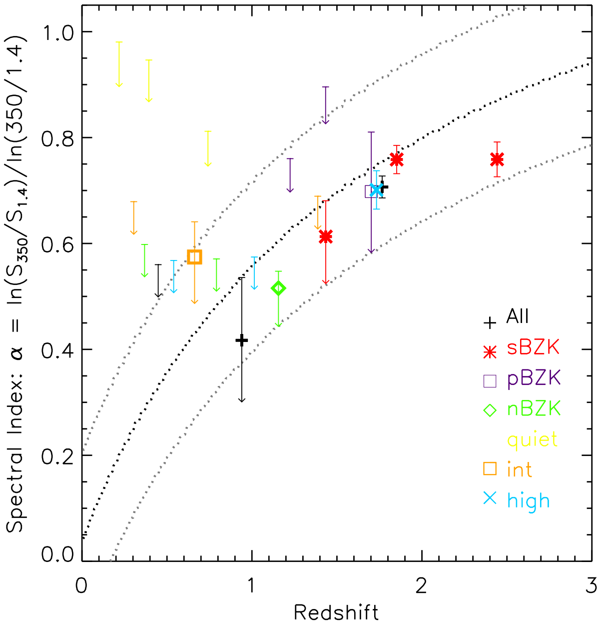

Figure 5.19: The Radio-to-Submillimeter Spectral Index as a function of redshift for color selected populations in the K band catalog. The different populations are indicated with different symbols, which are shown in the plot. All the populations show spectral indexes which are consistent with the local FIR-Radio correlation (Condon 1992)

is done in order to exclude the brightest galaxies, where it has been already shown that no evolution of the FIR-Radio correlation is expected Sargent et al. (2010). Each population is splitted in three redshift ranges as it is shown in Fig. 5.19.

Analyzing the K_S catalog, it can be seen, that the complete sample of all the galaxies with $K_S < 23$ nicely follow this correlation.

Also, galaxies defined as star-forming galaxies, i.e., sBzK, and high star formation activity, are in agreement with this correlation. For other populations, as pBzK and quiescent activity galaxies, is not possible to recover an average submillimeter signal given their low number statistics. This limit us to only report upper limits for these cases.

Given that several studies (Helou et al. 1985; Rodriguez-Martinez et al. 2006; Sandstrom et al. 2006; Roychowdhury & Chengalur 2012; Murphy 2013) have studied the correlation according to the morphology of the galaxies, we also analyze it according to the best fitted template. This information is available for the K band catalog, which is correlated with the i band catalog in order to get the photometric redshifts derived by Ilbert et al. (2010). The SED templates for Elliptical and Spiral galaxies are taken from Polletta et al. (2007) and the Starburst templates are taken from Bruzual & Charlot (2003). In Fig. 5.20 we overplot the results for the different populations and different morphologies. For elliptical galaxies we do not recover any signal but two upper limits, driven by the radio stacking detection. This is expected, as we have already seen that for pBzKs and quiescent star-forming activity galaxies we did not detect any stacked flux. On the other hand, Spiral and Starburst galaxies, where detections are available for both bands, are in agreement with the FIR-radio correlation. The populations where only upper limits are available are still consistent with the FIR-radio correlation. We do not observe any clear evidence of a departure from the FIR-radio correlation for any of the studied populations.

5.7 Summary and conclusions

In the following we summarize the main results from this study:

- We apply the stacking technique to analyze the submillimeter emission of different color selected populations: i) BzK, which separates galaxies between, high-z star forming galaxies ($sBzK$), high-z passive galaxies ($pBzK$), and low-z galaxies ($nBzK$). ii) Galaxies selected according to the (NUV - r^+)$_{\rm temp}$, which split galaxies in high, intermediate, and quiescent activity galaxies.
- Within the BzK, the sBzK have the strongest 870 μm stacked flux density, being $\sim$ 4 times more intense than the nBzK galaxies down to $K_{\rm S} < 23$.
- we split the catalog in redshift and stellar mass. It is clear that more massive galaxies tend to have the higher submm emission. Also an increasing trend of the submm emission as a function of redshift is observed, although a decrease at $z \gtrsim 2.5$ is observed. This could be indicative of a decline in star formation activity, or alternatively that the $K_{\rm S}$ band at that redshift start to sample the optical emission, hence dusty galaxies would not be detected anymore, given high opacity at optical wavelengths.

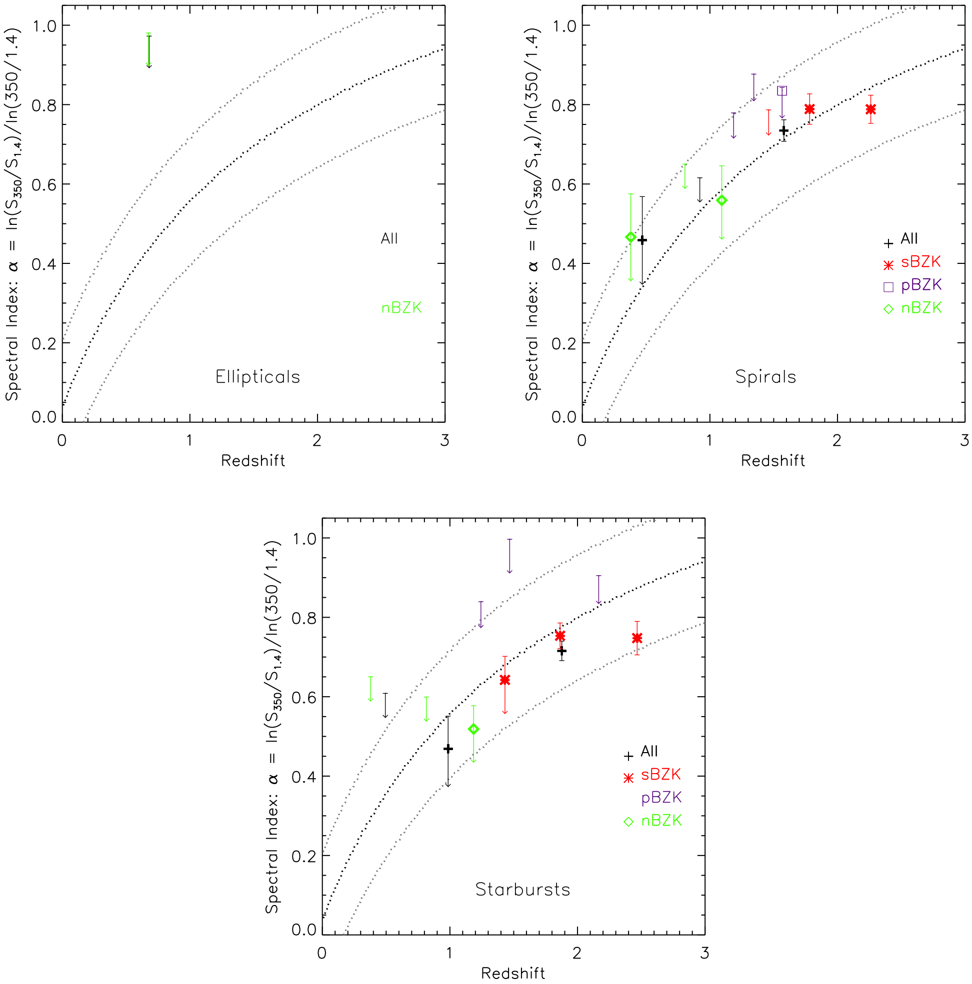

Figure 5.20: The Radio-to-Submillimeter Spectral Index for color selected populations in the K band catalog. The sample has been splitted according to their morphology,i.e., ellipticals, spirals, starbursts, which is obtained from the best SED fitting to the photometric available data. Upper left panel: The spectral index as a function of redshift for elliptical galaxies. Upper Right panel: The spectral index as a function of redshift for Spiral galaxies. Bottom Left Panel: The spectral index as a function of redshift for Starburst Galaxies. For most of the elliptical galaxies, the stacked signal is not detected neither at 870 μm nor at 1.4GHz. Spiral and Starburst galaxies show spectral indexes which are consistent with the local FIR-Radio correlation (Condon 1992)

- Analyzing the flux density stacked signal as a function of the K_S magnitude we find a strong relationship between both quantities, which is most likely due to the correlation between stellar mass and K_S magnitude.

- We also carried out the stacking in the radio regime, using the VLA-COSMOS survey data at 1.4 GHz, with the aim of analyzing the FIRRC for the different color selected populations.

  From the radio stacking alone it can be seen that most of the trends are similar to what is seen in the stacking at submillimeter regime. Typical average radio fluxes span a range from 1 to 30 μJy. The brightest population are the sBzK galaxies.

Unlike in the submillimeter regime, in the radio regime we recover an average signal for the pBzK galaxies. It is still unclear whether the radio emission arises from star formation activity or AGNs. Additional stacking in Herschel bands are likely the best way to farther investigate this issue.

- Combining both datasets, i.e., submillimeter and radio, we investigate the FIRRC of the different color selected populations. We do not find evidence for a departure from what is expected. Also we separate galaxies by elliptical, spirals, and starbursts. As expected we only obtain upper limits for elliptical galaxies, while stacked signal is detected for spirals and starburst, which also do not show any evident departure from the FIRRC.

6

Summary and outlook

In this thesis we have studied the submillimeter vision of the COSMOS field. For this, we have used the LABOCA data of the COSMOS field (COSLA).

6.1 Summary

In Chapter 2 we present the LABOCA survey of the COSMOS field, which is the largest continuous survey at 870 μm carried out to date. It covers an area of $\sim$ 0.75 deg^{-2}, reaching a depth of 1.68 mJy/beam at the center and decreasing towards the outskirts.
Thirty nine sources were detected above a S/N level of 3.8. Based on simulations we quantify the reliability of the catalog, i.e., completeness, position accuracy, deboosting, and false detections.
From the data we derive the submm source counts via the so-called P(D) analysis, obtaining a solution that is in agreement with what is found for the ECDFS survey, which has also been observed with LABOCA. It is seen that the source count model obtained from the direct counts overpredict the solution found via the P(D) analysis, which is expected as direct counts do not make any consideration about sources that are blended into one source given the large beam of single dish telescopes.
Other areas of the COSMOS field have also been mapped at (sub)mm wavelengths, with BOLOCAM, AzTEC, MAMBO, and SCUBA-2. In particular, the survey carried out at 1.1 mm with AzTEC mounted on the ASTE telescope covers a similar area that is covered with LABOCA. We find that $\sim$ 51 % of the LABOCA sources have a counterpart at 1.1 mm. This fraction reinforce the idea that there are a group of galaxies with either cold dust temperature $\mathrm{T_D} < 10K$, or unusual spectral energy distributions ($\beta \sim= 1$, or could be galaxies which are at redshift greater than 4. The flux comparison of the common sources to both surveys is in good agreement, assuming that the flux ratio between both wavelengths is given by a spectral power law index. However, comparing the common

sources with the SCUBA-2 survey, we overpredict the fluxes by $\sim 20\%$. Given that the angular resolution of the SCUBA-2 survey is $15''$ compared to $\sim 30''$ for LABOCA and AzTEC surveys, it is suggested that galaxy multiplicity would be responsible of LABOCA and AzTEC sources being brighter than expected from SCUBA-2 fluxes. In fact, high resolution interferometric observations report that a high fraction of submillimeter sources observed with single-dish telescopes are composed of multiples galaxies.

In Chapter 3 we present the results of a continuum interferometric follow-up, carried out with the PdBI interferometer at at 1.3 mm with a resolution of $\sim 1.5''$. of a subsample of 28 sources from the LABOCA-COSMOS Survey. Nineteen sources were detected at a $\gtrsim 3\sigma$ level of ≈ 1.4 mJy/beam. We combined this data to previous submillimeter interferometric data available in the COSMOS field in order to build a combined sample with a total of 50 SMGs detected at $\lesssim 2''$ angular resolution . In summary the combined sample contains: i) a 1.1 mm-selected flux-limited sample ($F_{1.1\mathrm{mm}} > 4.2$mJy, $S/N > 4.5$), which is composed of 17 sources, with interferometric positions, originally drawn from the AzTEC/JCMT 0.15 deg^2 COSMOS survey. ii) a 870 μm selected sample, containing 27 sources drawn form the LABOCA-COSMOS Survey and detected at high-resolution with various mm-interferometers, i.e., CARMA, SMA, PdBI, at intermediate angular resolution. The achieved angular resolution improved more than an order of magnitude the $27\overset{''}{.}6$ resolution obtained with LABOCA, hence allowing unambiguous detection of optical counterparts, which is of critical importance in order to build statistically complete and unbiased samples of SMGs. The main findings of this work are:

i) $\gtrsim 15\%$ and possible up to 40% of single-dish detected SMGs consist of multiple sources.

ii) $\sim 30\%$ from the sources identified, via statistical arguments, as possible counterparts of single-dish detected submillimeter sources are likely to be incorrect.

iii) In comparison with previous studies the derived redshift distribution is broader with a higher abundance of low and high-redshift SMGs. The mean redshift of the combined sample is higher than in previous estimates.

iv) We derive a surface density of $z \gtrsim 4$ SMGs of 34-54 deg^{-2}, which is significantly higher than what has been predicted by current galaxy formation models.

In Chapter 4 we analyze the advantages and disadvantages of different stacking methods, i.e., Weighted Mean stacking, Median stacking, and the Global deblending technique introduced by Kurczynski & Gawiser (2010).

We focus our analysis in the Global Deblending technique as optical sources detected in the area of the LABOCA map are significantly larger in number and density compared to previous studies. Simulating maps with different levels of clustering, it is shown that while the weighted mean stacking can largely overpredicts the source input average flux, the global deblending technique is a reliable indicator. Maps are also simulated with different levels of source density, where it is shown that the global deblending technique returns output average fluxes in excellent agreement with the input ones.

In Chapter 5 we apply the stacking technique to analyze the submillimeter emission of different color selected populations: i) BzK, which separates galaxies between, high-z star forming galaxies ($sBzK$), high-z passive galaxies ($pBzK$), and low-z galaxies ($nBzK$). ii) Galaxies selected according to the (NUV - $\mathrm{r}^{+})_{\mathrm{temp}}$, which split galaxies in high, intermediate, and quiescent activity galaxies.

Within the BzK, the sBzK have the strongest 870 μm stacked flux density, being ~ 4 times more intense than the nBzK galaxies down to $\mathrm{K_S} < 23$. Using the same threshold in the $\mathrm{K_S}$ band we split the catalog in redshift and stellar mass. It is clear that more massive galaxies tend to have the higher submm emission. Also an increasing trend of the submm emission as a function of redshift is observed, although a decrease at $z \gtrsim 2.5$ is observed. This could be indicative of a decline in star formation activity, or alternatively that the $\mathrm{K_S}$ band at that redshift start to sample the optical emission, hence dusty galaxies would not be detected anymore, given high opacity at optical wavelengths.

Analyzing the flux density stacked signal as a function of the $\mathrm{K_S}$ magnitude we find a strong relationship between both quantities, which is most likely due to the correlation between stellar mass and $\mathrm{K_S}$ magnitude. In order to study the stacked flux density as a function of redshift for the different color selected populations, we have splitted all the populations in three redshift bins (each bin containing the same amount of galaxies). In all the populations the stacked flux density increases as a function of redshift. sBzK at high-z have an average submillimeter flux of 0.73 mJy/beam, which translates into a SFR $\sim$ 40 $\mathrm{M_\odot year^{-1}}$, being the strongest emitters at 870 μm among all the color selected populations. On the other hand, pBzK are not detected at any redshift or magnitude.

We also carried out the stacking in the radio regime, using the VLA-COSMOS survey data at 1.4 GHz, with the aim of analyzing the FIRRC for the different color selected populations.

From the radio stacking alone it can be seen that most of the trends are similar to what is seen in the stacking at submillimeter regime. Typical average radio fluxes span a range from 1 to 30 μJy. The brightest population are the sBzK galaxies. Unlike in the submillimeter regime, in the radio regime we recover an average signal for the pBzK galaxies. It is still unclear whether the radio emission arises from star formation activity or AGNs. Additional stacking in Herschel bands are likely the best way to farther investigate this issue.

Combining both datasets, i.e., submillimeter and radio, we investigate the FIRRC of the different color selected populations. We do not find evidence for a departure from what is expected. Also we separate galaxies by elliptical, spirals, and starbursts. As expected we only obtain upper limits for elliptical galaxies, while stacked signal is detected for spirals and starburst, which also do not show any evident departure from the FIRRC.

6.2 Perspectives

Submillimeter surveys of large areas of the sky and follow-up submillimeter interferometric observations have been shown to be critical in order to understand the role that SMGs play in the evolution of the Universe as described throughout this thesis.

A complete characterization of the sources here shown is going to be possible by combining state-of-the-art data which is becoming available. The far-infrared part of the spectrum will be complemented by *Herschel* data in the range from 70 to 500 μm. In the millimeter part, current undergoing observations on the COSMOS field with GISMO on the IRAM 30m telescope will provide information at 2 mm. Finally, observations of the 2 deg^2 of the COSMOS field at 3 GHz, with the Jansky Very Large Array (JVLA), down to a sensitivity of 2μJy (PI: V. Smolčić), combined with previous observations at 1.4 GHz (Schinnerer et al. 2004, 2007, 2010), will allow to study the (non)evolution of the radio spectral index of SMGs, which combined with far-infrared and submillimeter data will shed light on the (non)evolution of the FIRRC for SMGs. The recently approved ALMA proposal (PI: M. Aravena) to observe 129 SMGs drawn from the AzTEC 1.1 mm sample on the COSMOS field (Aretxaga et al. 2011), with which the LABOCA survey has more than a 50% coincidence, plus the data obtained with the PdBI interferometer, will make possible to test if mm-selected and/or brighter SMGs lie at higher redshifts as has been previously suggested. Moreover, the unambiguous counterpart identification to SMGs allowed by this data, combined with LABOCA, SCUBA-2, AzTEC, and GISMO data will allow to test if mm-sources which are not recovered in submillimeter surveys (Greve et al. 2008) have very cold dust ($T_D \sim 10$ K, $\beta \sim 1$) or are placed at very high redshifts, i.e., $z > 4$.

Interferometric observations are an expensive method to identify (sub)millimeter counterparts. For this reason, the unambiguous counterpart identification combined with the LABOCA data and other (sub)mm surveys will provide us with a unique training-set, which will be critical in order to develop and improve counterpart identification methods. These are going to be of great use in future large surveys carried out with microwave kinetic inductance detectors (MKIDs), e.g., on the APEX and CCAT telescopes.

Also, some techniques developed during this thesis will be applied in other data sets.

The stacking technique is currently being applied to passive galaxies, selected with different color-criteria. For this, the stacking is being carried out on MIPS, PACS, SPIRE, LABOCA, and GISMO data. This will provide information on the contamination levels inherent to the color-criteria selection of these galaxies. Also, combining it with the stacking in radio wavelengths, it will shed light on the nature of the contaminants, e.g., star-forming galaxies or AGNs (Viero et al. 2013). The passive galaxies will be drawn from the VISTA survey of the COSMOS field, i.e. UltraVISTA. The UltraVISTA survey will be the deepest of the VISTA public surveys, and when fully complete will cover an area of 1.8 deg^2 down to $K_S \sim 24.0$, with a deeper component covering 0.75 deg^2 down to $K_S \sim 25.6$. For comparison the recent work on stacking from Viero et al. (2013) covers an area of ~ 0.8 deg^2, on the Infrared Deep Sky Survey (UKIDSS), down to $K_S \sim 24$.

The P(D) analysis applied to the LABOCA map in Chapter 2 will be applied to the GISMO data of the COSMOS field, in order to constraint the number source counts function at 2 mm.

A

Discussion of the LABOCA PSF

In this Appendix the LABOCA point spread function (PSF) is discussed.

A.1 The PSF profile of the LABOCA map

As shown in Fig. 2.3, the original LABOCA map at $19\farcs5$ resolution is large-scale filtered and beam-smoothed in order to maximize the S/N of point sources. The PSF of the LABOCA map at $19\farcs5$ resolution is almost a Gaussias as shown in Weiß et al. (2009). However, if we apply the large-scale filtering and beam-smoothing to a Gaussian of $19\farcs5$ FWHM, the resulting PSF is a Gaussian, with a peak ∼0.92 times compared to the original peak, and surrounded by a negative bowl. as shown in Fig. A.1.

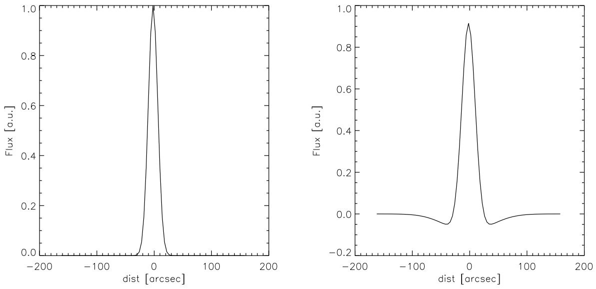

Figure A.1: Left panel: Gaussian with a FWHM of $19\farcs5$ and a peak of 1 (arbitrary units). Right panel: The Gaussian after applying the same procedure that was used for the LABOCA map, i.e., large scale filtering and beam-smoothing. The peak of the Gaussian is ∼0.92 times of the original peak.

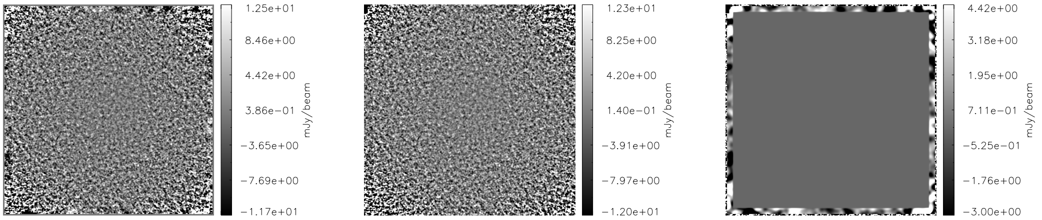

(a) (b) (c)

Figure A.2: **(a):** Simulated map that has been large-scale filtered and beam-smoothed. **(b):** Simulated map, where the sources have the same positions and fluxes as in **(a)**, but this time instead of injecting Gaussian profiles with a 19.″5 FWHM, the injected sources are modelled with the modified profile shown in Fig. A.1. **(c):** Image **(b)** is subtracted from **(a)**. The values in this residual image are about 6 order of magnitudes fainter than the scale of the real maps. We have not smoothed the borders of the image in **(a)**, which is the reason of the difference between both maps in the borders.

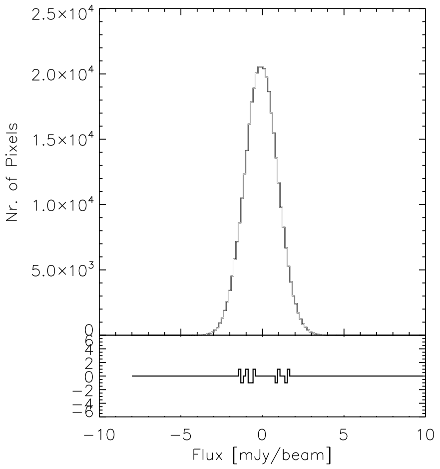

Figure A.3: Top panel: The histograms of images **(a)** and **(b)** are superimosed. Bottom Panel: The residuals after subtracting both histograms. As it can be seen, the residuals are consistent with zero.

A.2 Speeding-up the simulations

The P(D) analysis shown in Sect. 2.6 is usually a slow process. In each simulated map thousands of sources are injected, then each simulated map is large-scale filtered and beam-smoothed in order to maximize the S/N of point sources. However, this process can be speeded-up by injecting a modified point-source profile, which already include the filter out and smooth effects (Fig. A.1).

We inject this modified profile directly on top of a modified jackknife map, which has been also filtered out and smoothed. In Fig. A.2 we show the images obtained following the two procedures and the corresponding residuals after subtracting both images. The residuals are about 6 order of magnitudes fainter than the scale of the real maps, confirming that both procedures produce almost exactly the same result.

The histograms obtained with both procedures are shown in Fig. A.3, where the histogram obtained with the modified procedure is almost perfectly superimposed to the histogram of the original procedure. The similarity of both maps is also reflected in the residuals after subtracting the histograms, where the residuals are consistent with zero.

B

Multiwavelengths cutouts of the COSLA sources

In this appendix we show the multiwavelength cutouts of the LABOCA sources presented in Table 2.1. The cutouts included are: 870μm from LABOCA (at 27$''.$6 resolution), F814W filter from the ACS on-board the *HST* (i-band), the J band from the UKIRT, the 3.6μm from IRAC on-board the *Spitzer*, 24μm from MIPS on-board the *Spitzer*, and the 1.4 GHz from the VLA. Additionally, for the sources that have been identified by smoothing the LABOCA map to resolutions other than 27$''.$6, an extra cutout is added.

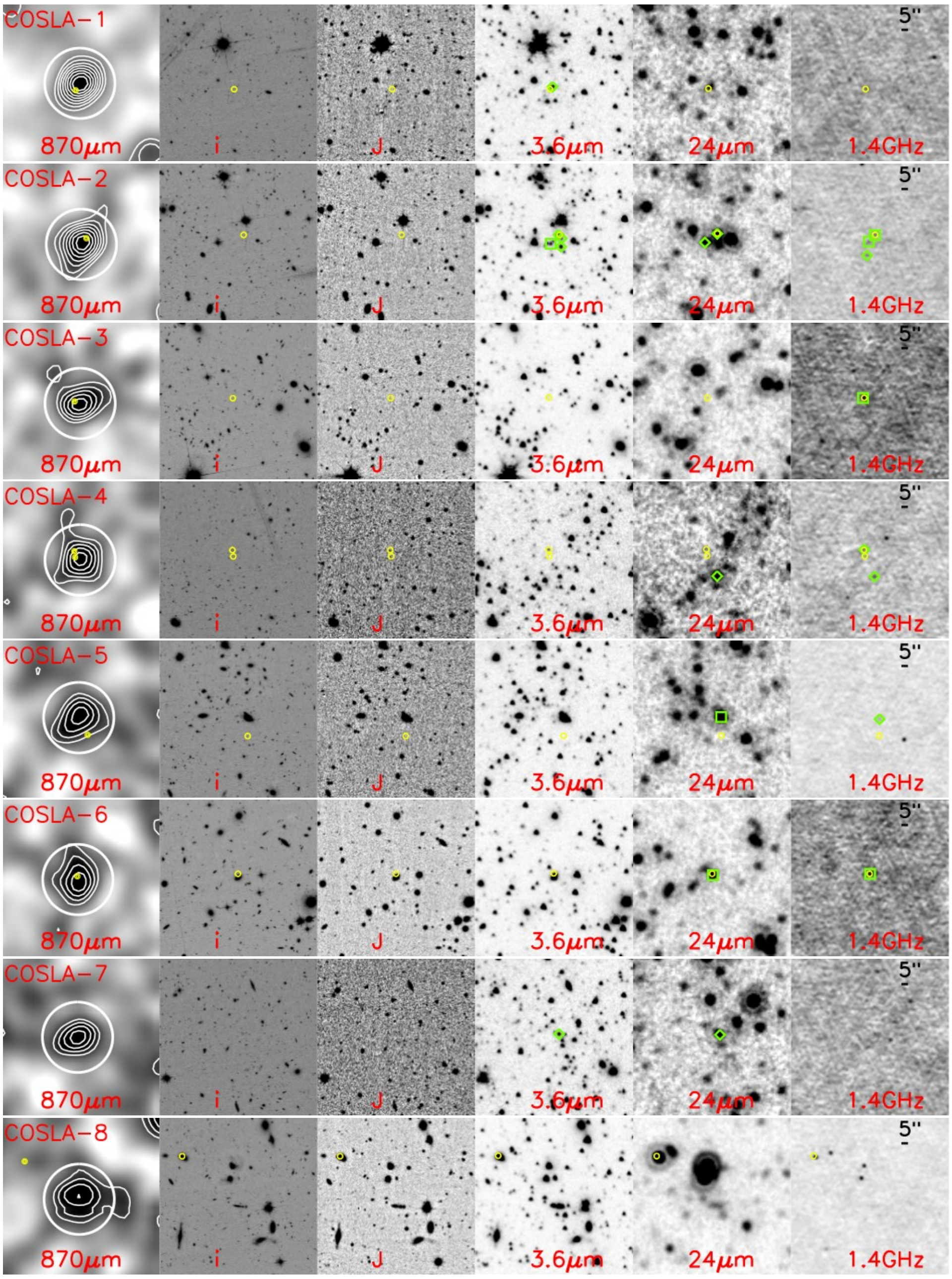

Figure B.1: Mutliwavelength cutouts of the sources presented in the COSLA catalog (see Table 2.1). In each row the wavelengths shown are: 870μm from LABOCA (at 27.″6 resolution), F814W filter from the ACS on-board the *HST* (i-band), the J band from the UKIRT, the 3.6μm from IRAC on-board the *Spitzer*, 24μm from MIPS on-board the *Spitzer*, and the 1.4 GHz from the VLA. Additionally, for the sources that have been identified by smoothing the LABOCA map to resolutions other than 27.″6, an extra cutout is added, i.e., COSLA-40 to COSLA-66. The white circle shows the beam-size of the LABOCA data. Yellow-circles show the positions detected from the PdBI follow-up (Smolčić et al. 2012a) and have a size of 2″. Green diamonds and squares show tentative and robusts counterparts, respectively, which have been identified via the p-statistics method (see Sect. 3.5.2.1 for more information about this method).

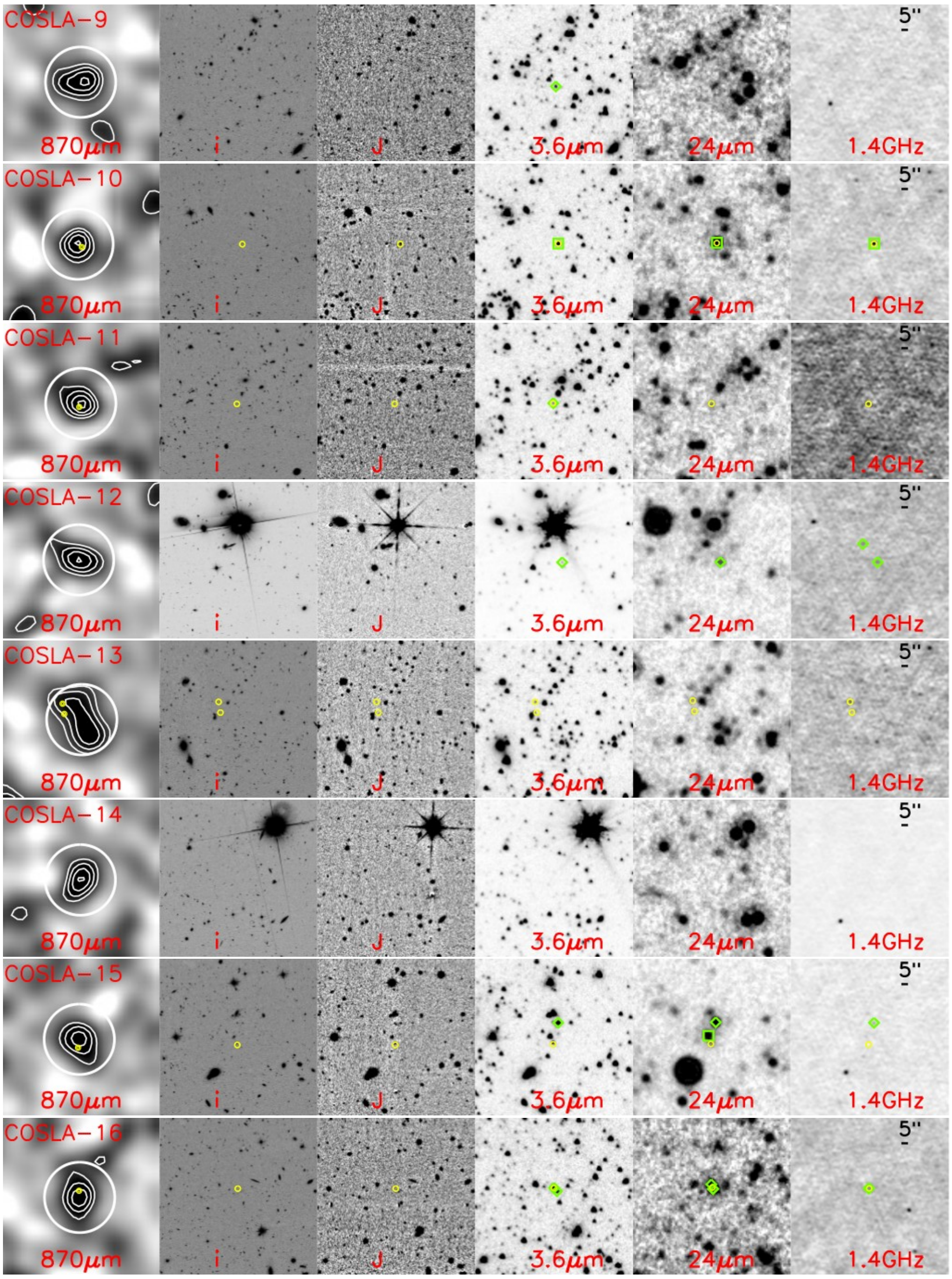

Figure B.1: Continued.

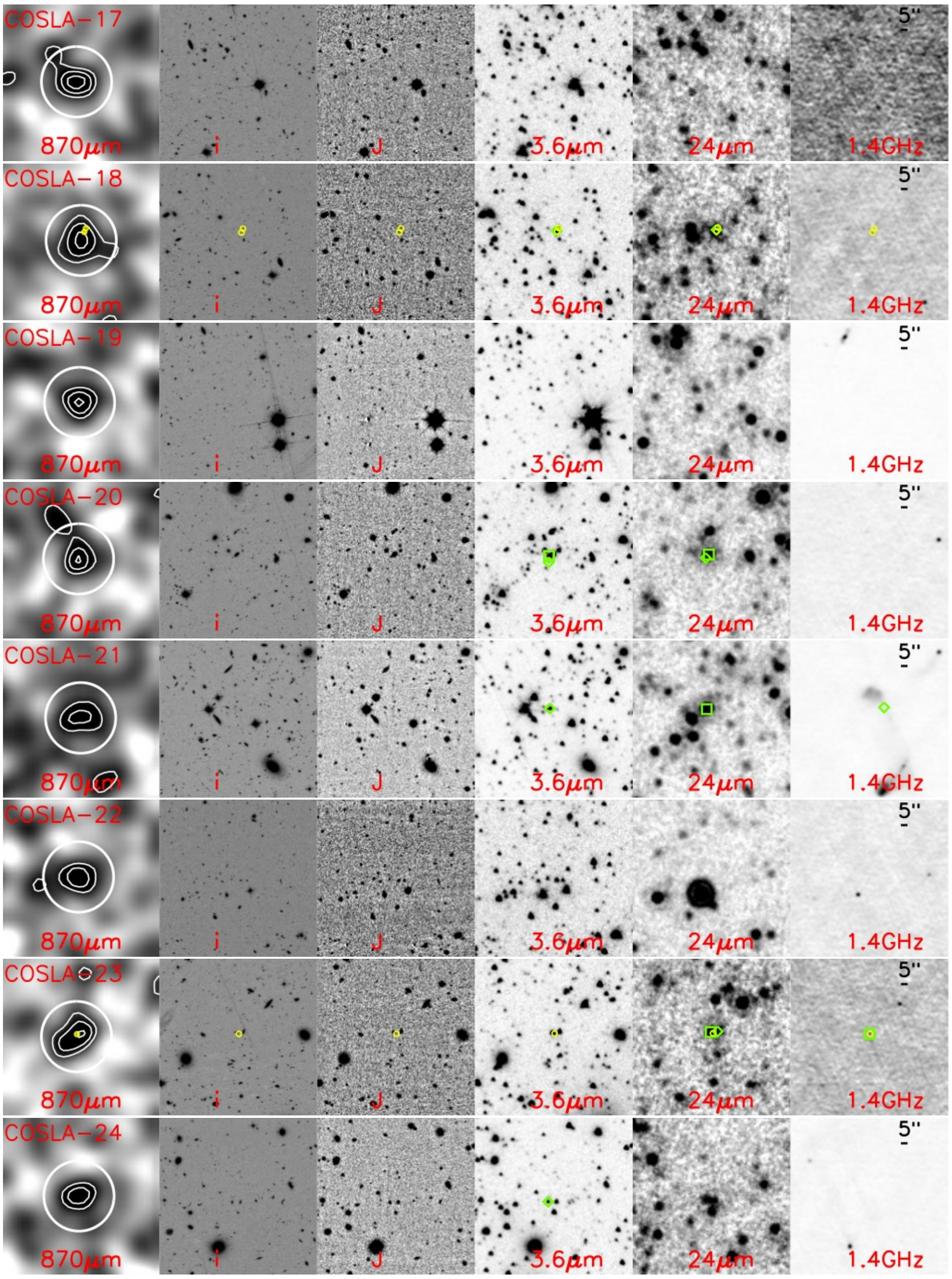

Figure B.1: Continued.

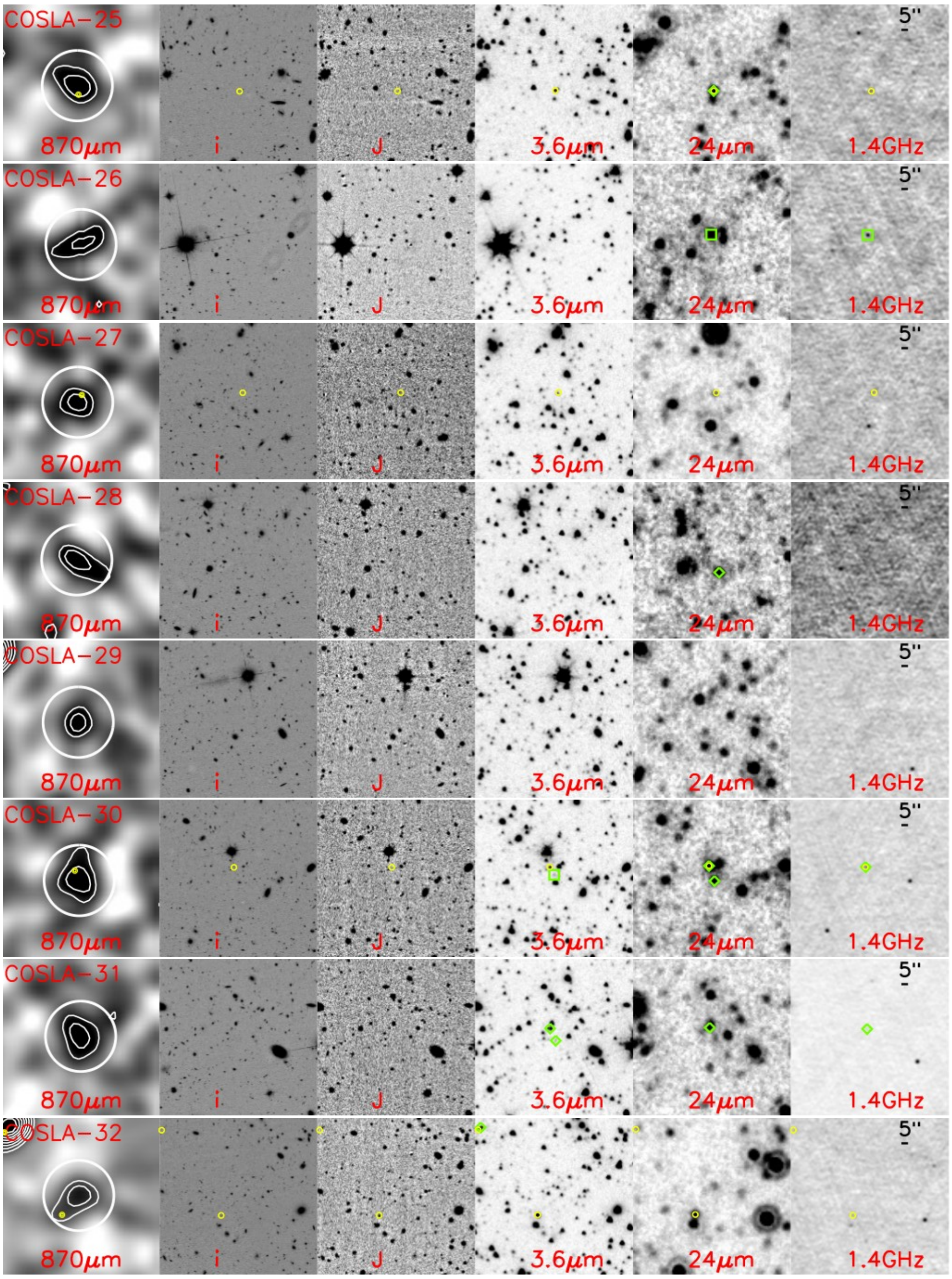

Figure B.1: Continued.

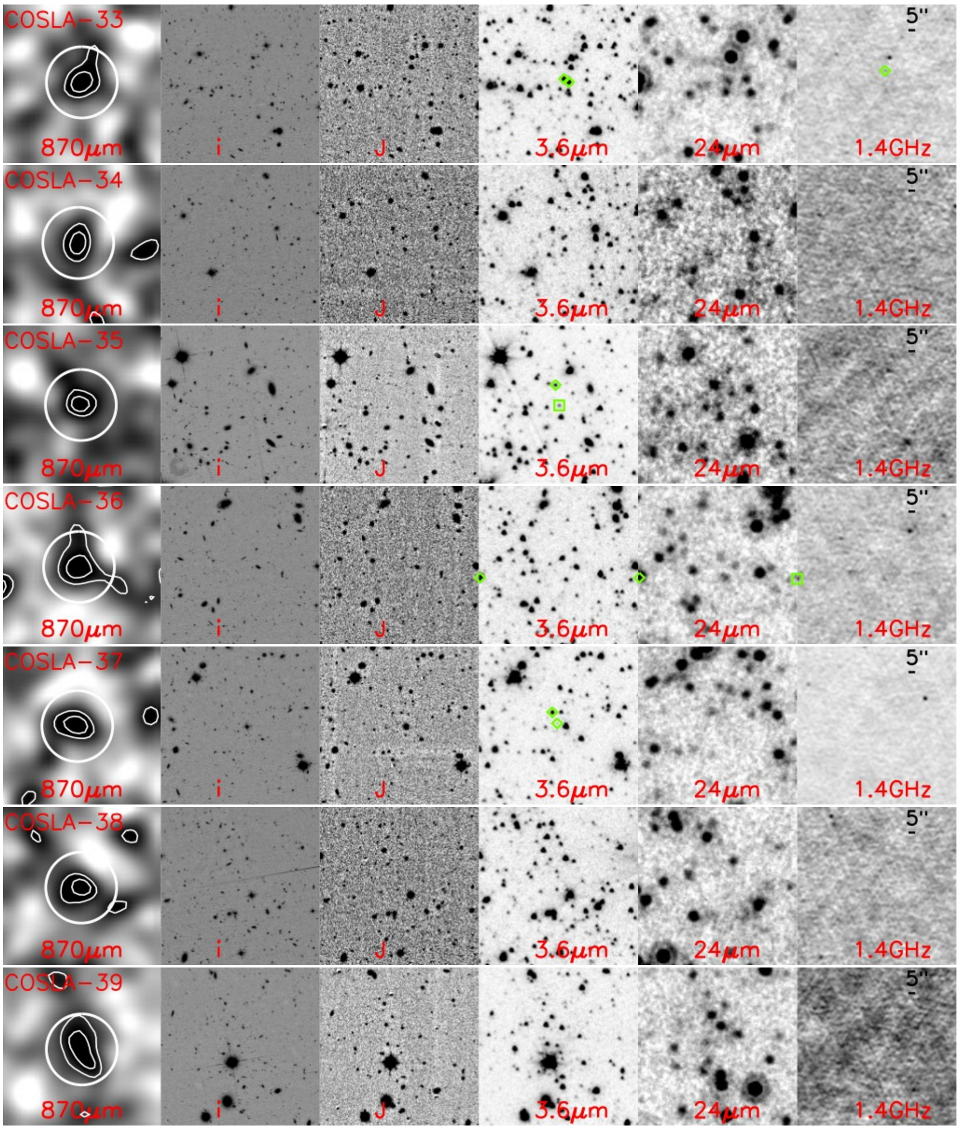

Figure B.1: Continued.

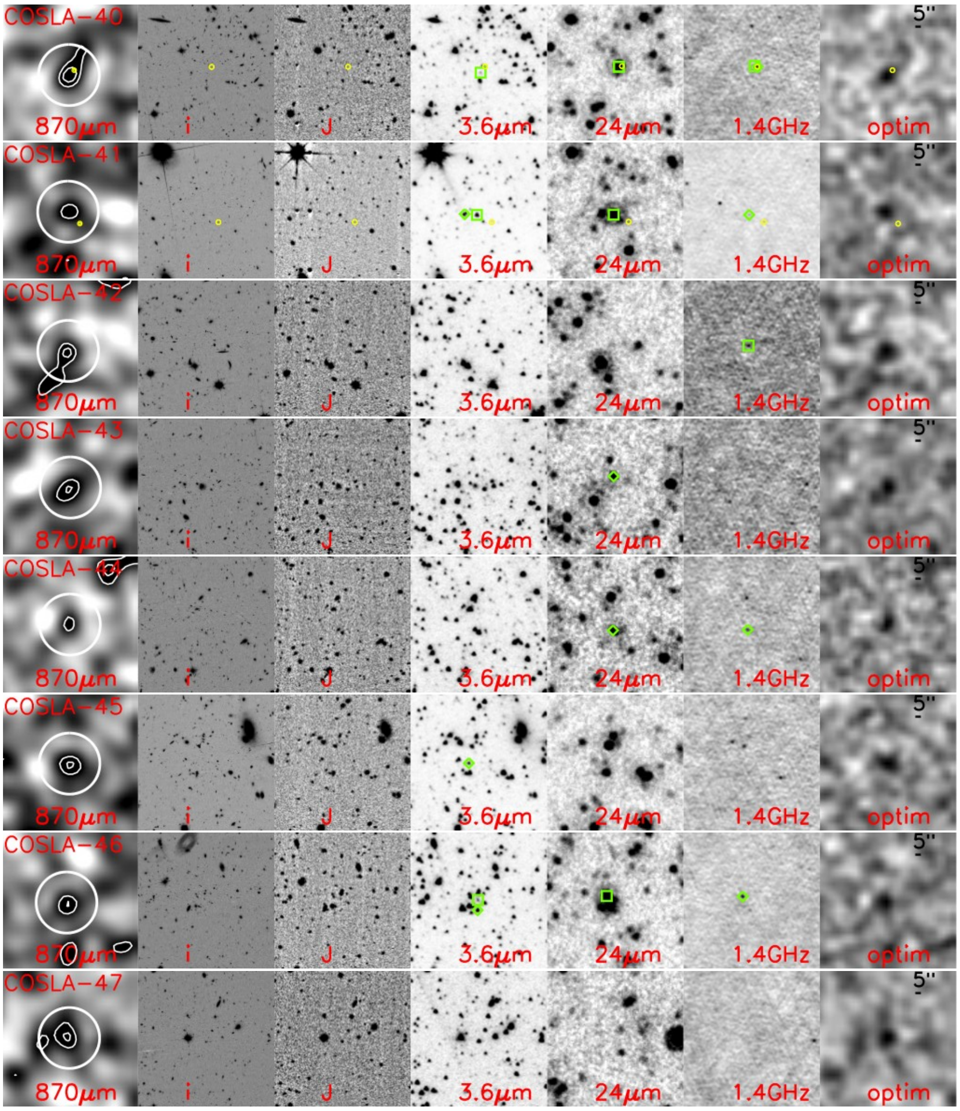

Figure B.1: Continued.

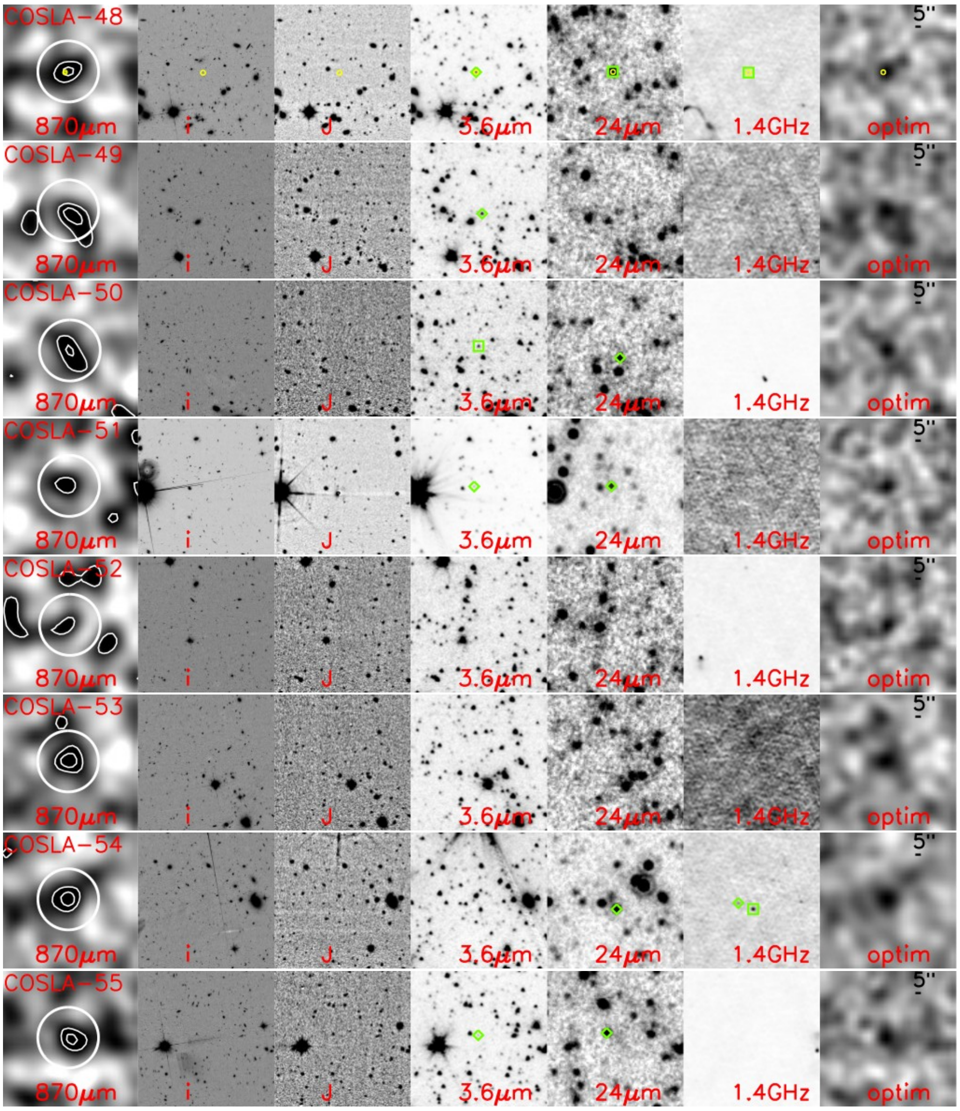

Figure B.1: Continued.

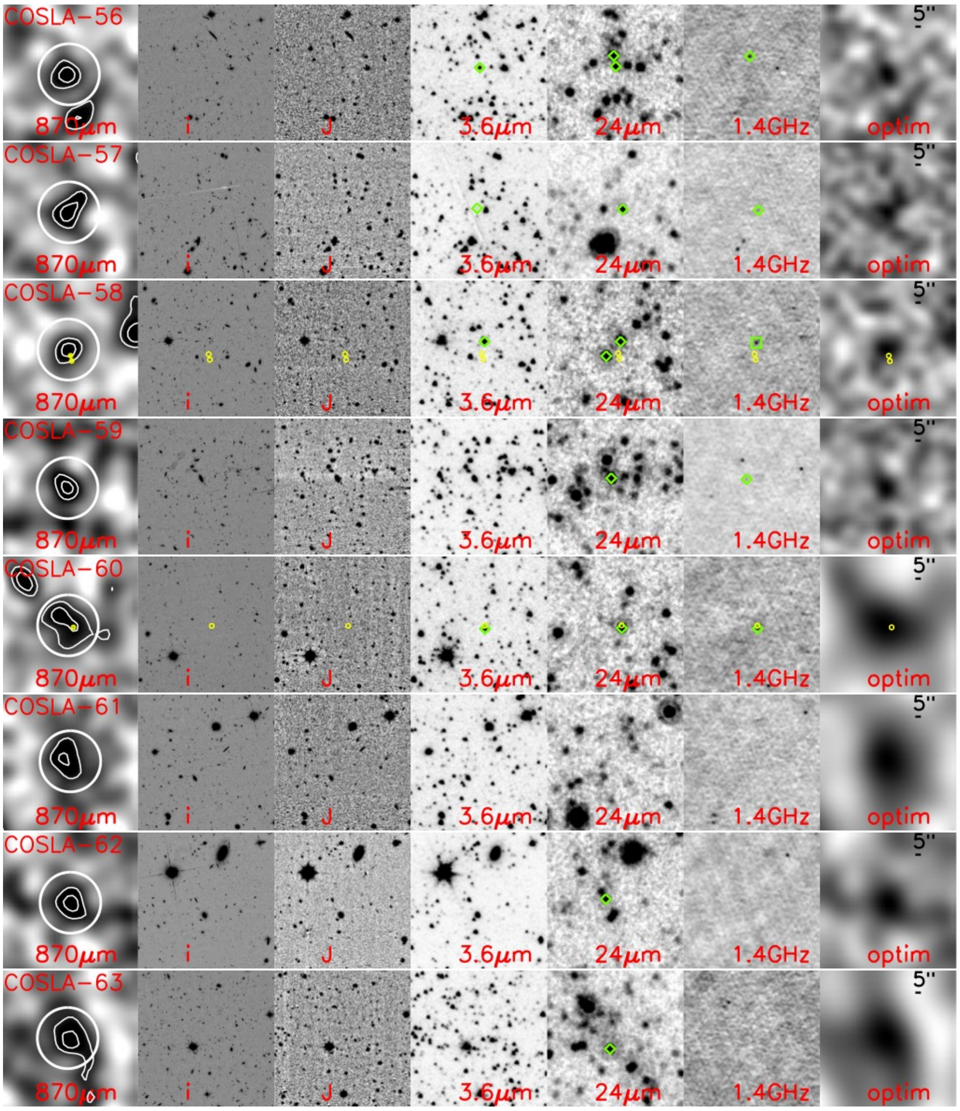

Figure B.1: Continued.

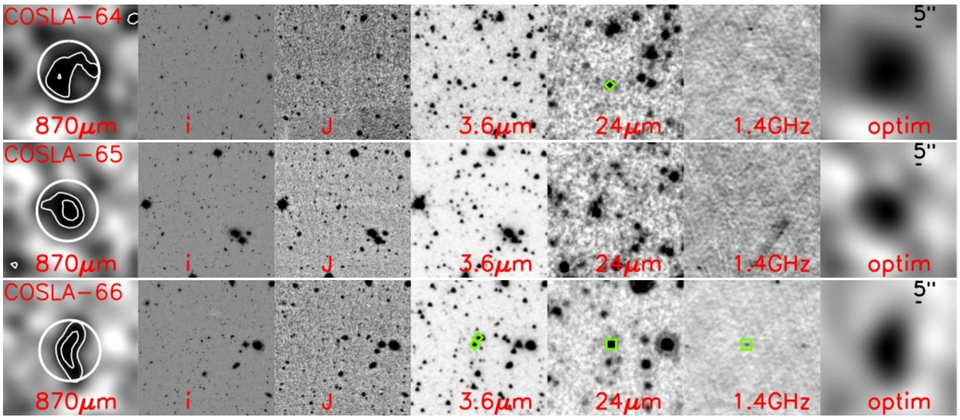

Figure B.1: Continued.

C

Notes on the LABOCA-COSMOS targets

Here we present detailed notes on individual LABOCA-COSMOS (i.e. COSLA) SMGs observed with PdBI at 1.3 mm and $\sim$ 1.5" resolution. We use a spectral index of 3, i.e. assuming $S_\nu \propto \nu^{2+\beta}$ where S_ν is the flux density at frequency ν and $\beta = 1$ the dust emissivity index, to convert fluxes from/to various (sub-)mm wavelengths (if not stated otherwise).

Cosla-5

COSLA-5 is a S/N = 4.1 detection located at $\alpha = 10\ 00\ 59.521$, $\delta = +02\ 17\ 02.57$. The PdBI-source is found at a separation of 3.4" from the LABOCA source center. The 1.3 mm flux density of the source is 2.04 ± 0.49 mJy. Scaling this to the MAMBO (1.2 mm) and LABOCA (870 μm) wavelengths we find 2.6 ± 0.6 and 6.9 ± 1.7 mJy, respectively. This is slightly lower than the extracted (and deboosted) MAMBO and LABOCA fluxes (4.78 ± 1, and 12.5 ± 2.6 mJy) and may i ndicate the presence of another mm-source, not detected in our PdBI map. Based on the rms reached in the PdBI observations, we can put a 3σ upper limit to this potential second source of 1.4 mJy.

The PdBI peak is 1.3" away from a source that is independently detected in the optical ($i^+ = 22.5$), UltraVista and IRAC bands. The photometric redshift of this source is well constrained, $z_{\rm phot} = 0.85^{+0.07}_{-0.06}$. Interestingly, at a separation of 1.1" towards the SW from the PdBI detection we find a faint source present only in the Ks band images, but not included in the catalogs (it is present in both the WIRCam and UltraVista images).

The mm-source is not associated with a radio detection suggesting a mm-to-radio flux based redshift for COSLA-5 of $z_{\rm mm/radio} \gtrsim 3.8$. Here we take the optical/IRAC/UltraVista source as the counterpart noting that given the $\sim 4\sigma$ significance of the PdBI peak, and a separation of $\gtrsim$ 1" from multi-wavelength sources further follow-up is required to confirm this source, and its redshift.

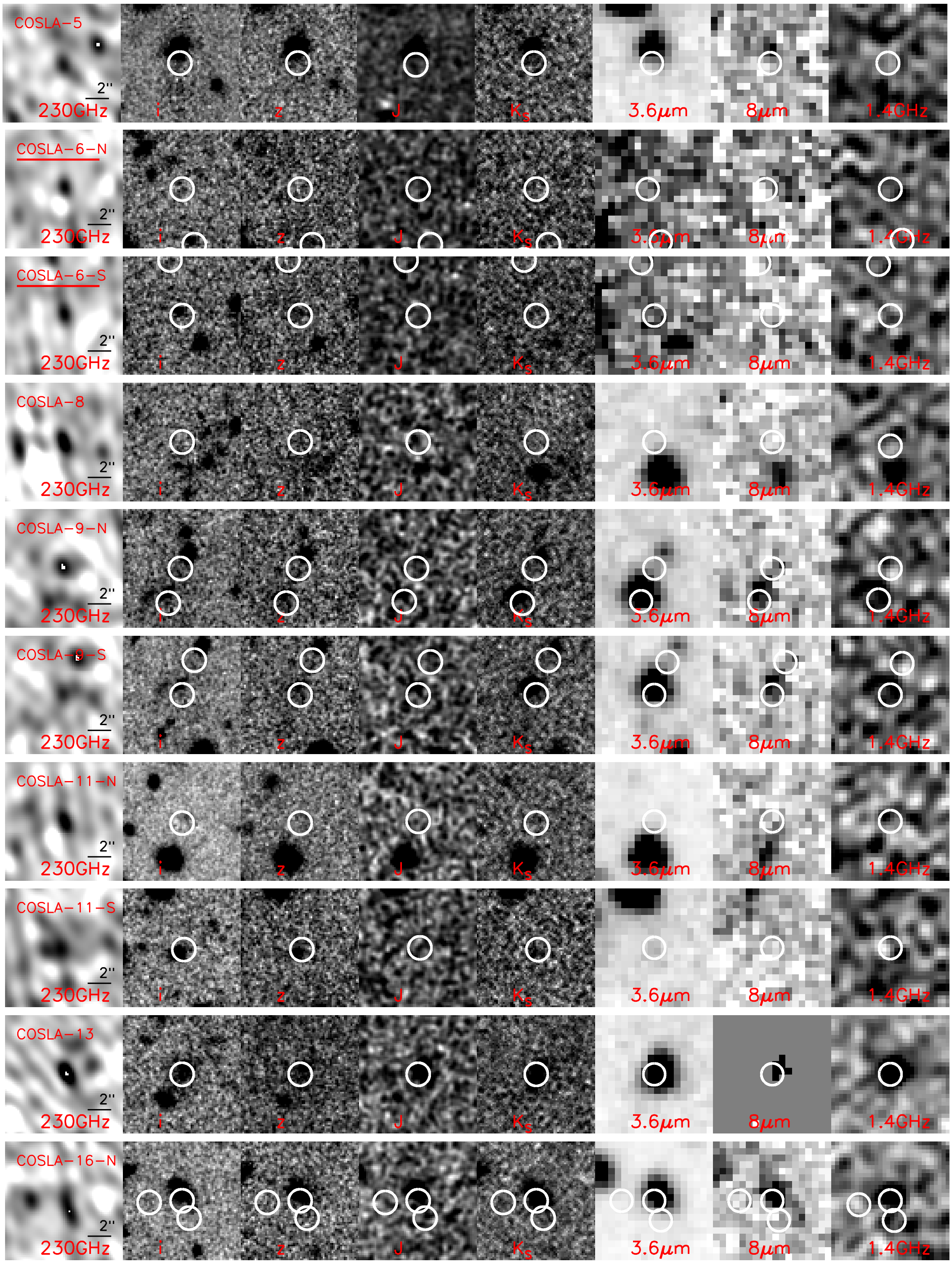

Figure C.1: Optical to radio stamps for the LABOCA-COSMOS SMGs detected by PdBI. Names of sources with S/N > 4.5 in PdBI maps are underlined.

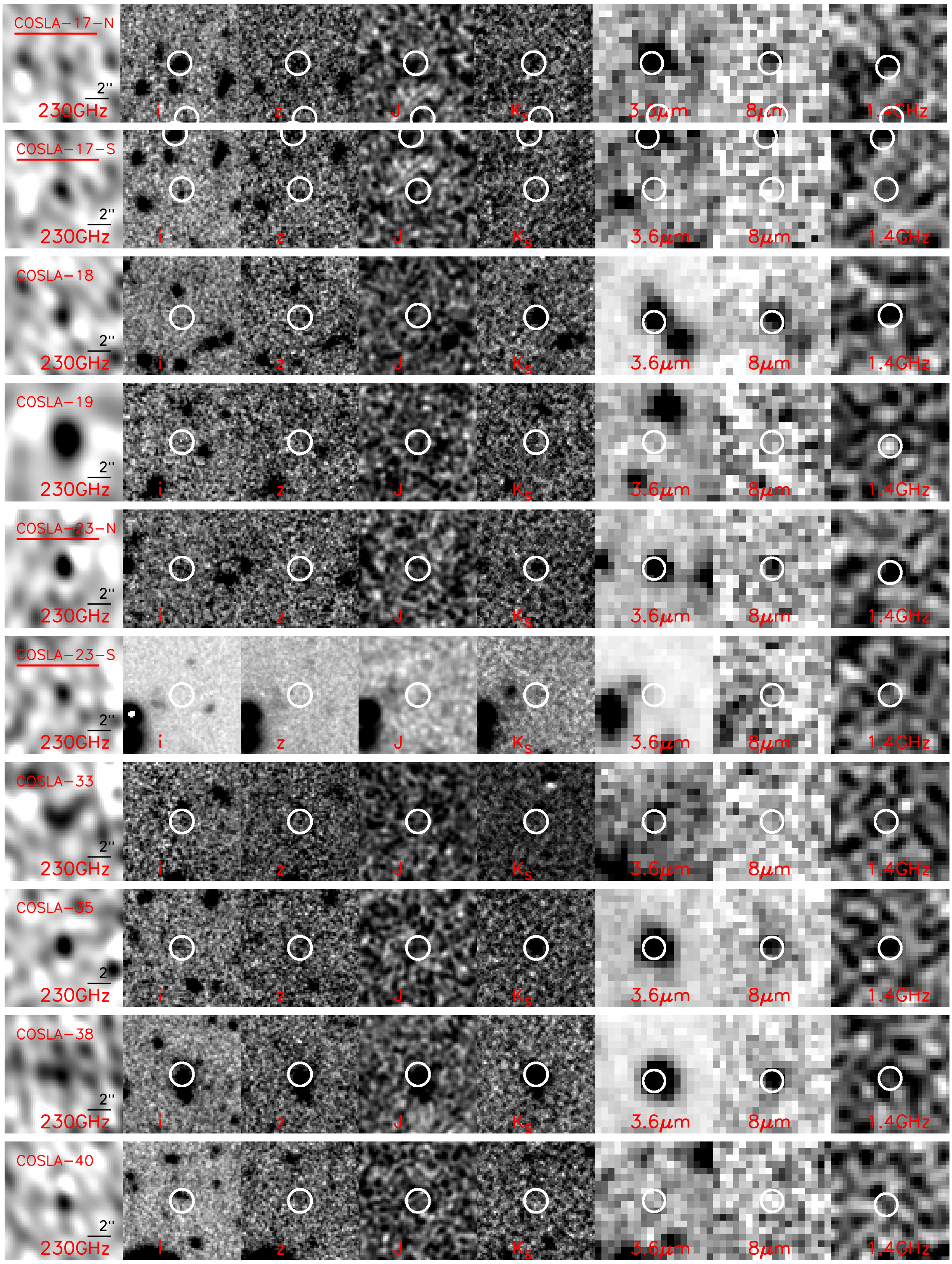

Figure C.2: Continuation of Fig. C.1

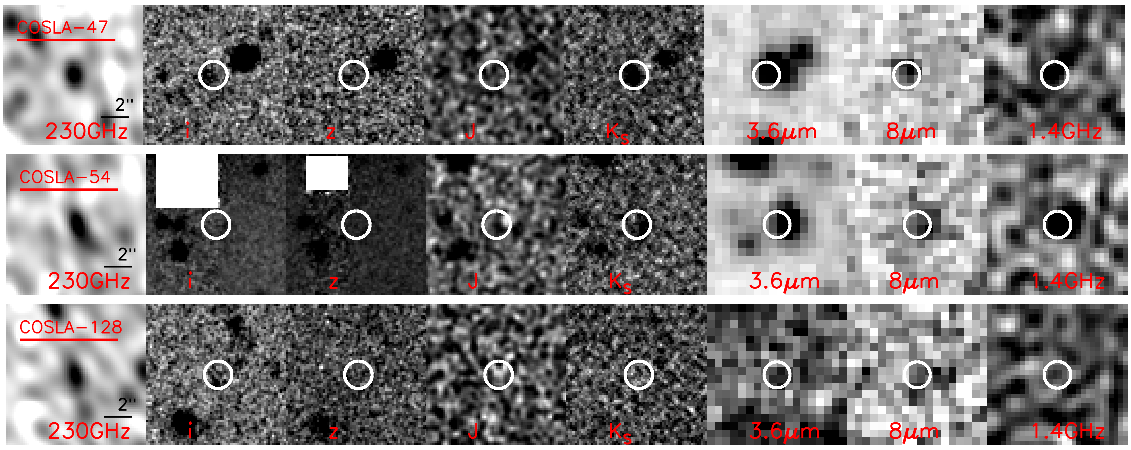

Figure C.3: Continuation of Fig. C.1

Cosla-6

Two significant (S/N > 4.5) sources are detected within the COSLA-6 PdBI map.

COSLA-6-N (S/N=5.4, α =10 01 23.64, δ =+02 26 08.42) has a 230 GHz (1.3 mm) flux density of 2.7 ± 0.5 mJy. No IRAC/UltraVista source is found nearby. The closest source is a faint optical (no UltraVista/IRAC/radio) source $2.0''$ away. Given the high significance of the mm-detection the mm-positional accuracy is $\sim$ 0.3”. Thus, it seems unlikely that this optical source is the counterpart of the mm-detection. COSLA-6-N is however coincident with a 2.1σ peak in the r adio map ($F_{1.4\mathrm{GHz}} = 19.5 \pm 9.4$ μJy). Based on this, we infer a mm-to-radio flux based redshift of $z_{\mathrm{mm-radio}} = 4.01^{+1.51}_{-0.83}$.

COSLA-6-S (S/N = 4.75, α =10 01 23.57, δ =+02 26 03.62) has a 1.3 mm flux density of 3.1 ± 0.6 mJy. It can be associated with a source detected in the optical (separation= 0.5”; $i^+ = 26.15$), but not in near- or mid-IR. It is coincident with a 3.3σ peak in the radio map ($F_{1.4\mathrm{GHz}} = 33.3 \pm 10.1$ μJy). Based on the multi-wavelength photometry, we infer a photometric redshift of $z_{\mathrm{phot}} = 0.48^{+0.19}_{-0.22}$ for this source. A second potential redshift solution (although not as likely as the first one) exists at $z \sim 4$, and it is supported by the mm-to-radio flux based redshift, $z_{\mathrm{mm/radio}} = 3.44^{+0.83}_{-0.58}$.

The combined 1.3 mm fluxes of COSLA-6-N and COSLA-6-S, scaled using a spectral index of 3, yield an expected flux density of 19.4 ± 2.7 mJy at 870 μm. This is in very good agreement with the deboosted LABOCA 870 μm flux of 16.0 ± 3.4.

Cosla-8

COSLA-8 is detected at a signal-to-noise of S/N = 4.2, and located at α = 10 00 25.55, δ = +02 15 08.44. Its 1.3 mm flux density is $F_{1.3\mathrm{mm}} = 2.65 \pm 0.62$ mJy. Using a spectral index of 3 this extrapolates to a 870 μm flux density of 8.9 ± 2.1 mJy, in good agreement

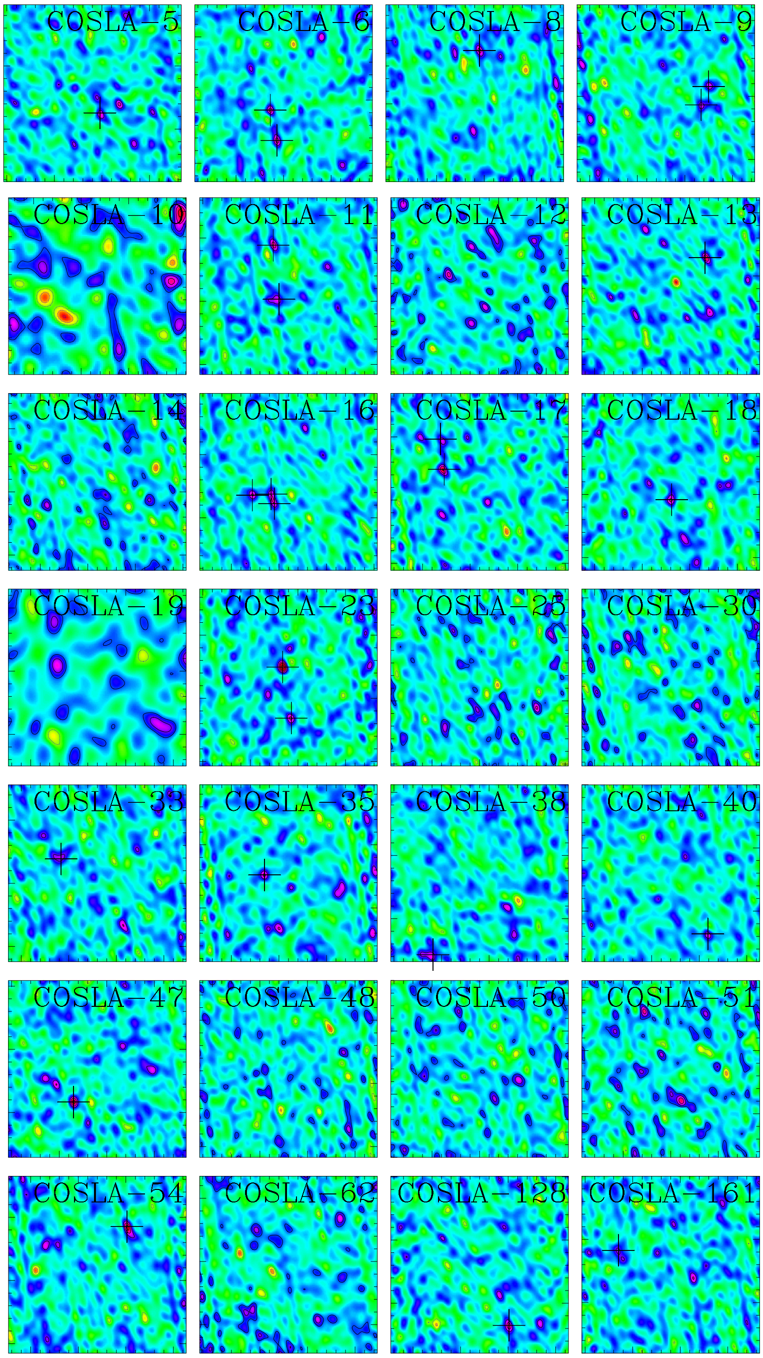

Figure C.4: Cleaned PdBI maps (color scale), 30" on the side, with $\pm 2\sigma, 3\sigma, ..$ contours overlaid. Detections (identified in the *dirty* maps, see text for details) are marked by crosses.

with the LABOCA deboosted flux of 6.9 ± 1.6 mJy. The source is located in a crowded region. A radio, IRAC, UltraVista detection is present at a separation of $\sim 3''$, however the closest source to the mm-source (separation=1.0") is detected only in the optical ($i^+ = 27.4$). A 3.3σ peak is found at the mm-position in the radio map ($F_{1.4\rm GHz} = 26.2 \pm 8.0\ \mu$Jy). The most probable photometric redshift for this source is $z\mathrm{phot} = 1.83^{+0.4}_{-1.31}$, however with a rather flat χ^2 distribution as reflected in the uncertainties.

Cosla-9

We identify two 3.2σ peaks at $\alpha = 10\ 00\ 13.83$, $\delta = +01\ 56\ 38.64$ (COSLA-9-S; 5.8" away from the LABOCA source center), and $\alpha = 10\ 00\ 13.75$, $\delta = +01\ 56\ 41.54$ (COSLA-9-N; 7" away from the LABOCA source center). COSLA-9-S can be matched to an optical/IRAC/UltraVista source ($i^+ = 24.8$, separation=0.8"), while the closest source to COSLA-9-N is detected only in the optical ($i+ = 26.1$; separation=0.4") however it is only 1.3" away from an optical/UltraVista/IRAC sour ce.

The primary beam corrected 1.3mm flux densities of COSLA-9-N and COSLA-9-S are 1.69 ± 0.47 mJy, and 1.87 ± 0.58 mJy, respectively. Added together, and scaled to the LABOCA (13.2 ± 2.1 mJy) and AzTEC (6.3 ± 1.0 mJy) frequencies yields a good match to the deboosted LABOCA (14.4 ± 3.3 mJy) and AzTEC (8.7 ± 1.1 mJy) fluxes. Given the low significance of the sources, further follow-up is required to confirm their reality.

Cosla-10

No significant source is present in the 1.3mm map. The statistical counterpart association (see Sec. 3.5.2.1 and Fig. 3.6 for details) suggests three separate potential (tentative) counterparts to this LABOCA source. The sum of the extracted 1.3 mm fluxes (taken as maximum flux within an circular area of 1" in radius centered at the statistical counterpart), corrected for the primary beam response, is 2.43 mJy. This yields a flux of 8.1 mJy when scaled to 870 μm, in very good agreement with the LABOCA flux of 7.3 ± 1.7 mJy (see Fig. 3.2). This suggests that the LABOCA source may be fainter at 1.3 mm than can be detected given our PdBI sensitivity and that it possibly breaks up into multiple components when observed at 1.5" resolution.

Cosla-11

The brightest peaks in the PdBI map are at 3.5σ (COSLA-11-N) and 3σ (COSLA-11-S).

COSLA-11-N is located at $\alpha = 10\ 01\ 14.260$, $\delta = 01\ 48\ 18.86$, and it can be associated with a faint optical detection 0.64" away ($i^+ = 27.75$). Its 1.3 mm flux density is $F_{1.3\rm mm} = 2.15 \pm 0.62$ mJy, and the source is not detected in the radio map. Based on the multi-wavelength photometry of the counterpart of COSLA-11-N, we find a photometric redshift of $z_{\rm phot} = 0.75^{+0.23}_{-0.25}$. The mm-to-radio based redshift however suggests $z_{\rm mm/radio} \gtrsim 3.6$.

COSLA-11-S ($\alpha =\ 100114.200$, $\delta =\ +014810.31$) is only 2.6" away from the center of the LABOCA source, and it coincides (separation=0.5") with independent optical and UltraVista H-band, and UltraVista J-band detections. Although fairly low S/N, the UltraVista detection increases the probability that it is a real source. Its 1.3 mm flux density is $F_{1.3\mathrm{mm}} = 1.43 \pm 0.48$ mJy. Our photometric redshift estimate yields two, almost equally probable, redshifts at $z \sim 0.2$ and $z \sim 3$. Given that the SMG is not detected in the radio map, the higher redshift solution, also consistent with the mm-to-radio flux ratio based redshift ($z_{\mathrm{mm/radio}} \gtrsim 3$), is more likely. We thus adopt the higher redshift solution for this source yielding $z_{\mathrm{photo}} = 3.00^{+0.14}_{-0.07}$ (where the errors reflect the 99% confidence interval derived using only $z > 1.5$ χ^2 values).

The combined flux densities of the two detections combined, scaled to 870 μm, yield a flux density of 12.0 ± 2.6 mJy at this wavelength. This is in good agreement with the LABOCA 870 μm flux density of 19.4 ± 4.5 mJy, and thus further affirms the reality of the sources.

Cosla-12

No significant source is present in the 1.3mm map. The statistical counterpart association (see Sec. 3.5.2.1 and Fig. 3.6 for details) suggests two separate potential (one robust and one tentative) counterparts to this LABOCA source. The sum of the extracted 1.3 mm fluxes (taken as maximum flux within an circular area of 1" in radius centered at the statistical counterpart), corrected for the primary beam response, is 2.68 mJy. Scaled to 870 μm this implies a flux o f 8.9 mJy which is lower than the LABOCA flux of 18.3 ± 4.2 mJy (see Fig. 3.2). This suggests that the LABOCA source may be fainter at 1.3 mm than can be detected given our PdBI sensitivity and/or it breaks up into multiple components when observed at 1.5" resolution.

Cosla-13

COSLA-13 is detected at a signal-to-noise ratio of S/N = 3.9 (α = 10 00 31.840, δ = +02 12 42.81). Its 1.3 mm flux density is $F_{1.3\mathrm{mm}} = 1.37 \pm 0.61$ mJy. This SMG is detected within the LABOCA (870μm), AzTEC (1.1mm), and MAMBO (1.2mm) surveys. Scaling the PdBI 1.3 mm flux to 870μm, 1.1mm, 1.2mm (using a slope of 4.6 which corresponds to the mean slope between the AzTEC/LABOCA and AzTEC/MAMBO detected fluxes) we find flux densities of 8.8 ± 3.9 mJy (870μm), 2.9 ± 1.3 mJy (1.1mm), and 2.0 ± 0.9 mJy (1.2mm). These are consistent with the AzTEC/LABOCA fluxes, and slightly lower than the MAMBO flux (note that we find consistent results when using a slope with a spectral index of 3).

The PdBI mm-source is coincident with an optical/UltraVista/IRAC/radio source (separation=0.55") with an optical spectrum at redshift $z_{\mathrm{spec}} = 2.175$.

Cosla-14

No significant source is present in the 1.3mm map. The statistical counterpart association (see Sec. 3.5.2.1 and Fig. 3.6 for details) suggests one robust statistical counterpart to this LABOCA source. The extracted 1.3 mm flux (taken as maximum flux within an circular area of 1" in radius centered at the statistical counterpart), corrected for the primary beam response, is 1.64 mJy. The scaled 870 μm flux of 5.5 mJy is fairly consistent with the LABOCA flux of 9.0 ± 2.1 mJy when scaled to 870 μm (see Fig. 3.2). This suggests that the LABOCA source may be fainter at 1.3 mm than can be detected given our PdBI sensitivity.

Cosla-16

A significant extended source is found ~ 3.5" away from the LABOCA source center. It is best fit by a double-Gaussian (using the AIPS task jmfit and fixing the width of the Gaussians), yielding two sources located at α = 10 00 51.5854, δ = +02 33 33.5648 (COSLA-16-N) and α = 10 00 51.5541, δ = +02 33 32.0948 (COSLA-16-S). The 2-Gaussian fit yields 1.3 mm flux densities of $F_{1.3\mathrm{mm}} = 1.39 \pm 0.32$ mJy (COSLA-16-N) and $F_{1.3\mathrm{mm}} = 1.19 \pm 0.33$ mJy (C OSLA-16-S).

COSLA-16-N can be associated with an optical/UltraVista/IRAC/radio source (separation = 0.79"). COSLA-16-S is not associated with a separate source in the multi-wavelength catalogs. The radio emission associated with the position of COSLA-16-N is significant ($F_{1.4\mathrm{GHz}} = 95.6 \pm 10.1$ μJy), while a 3.3σ peak, that seems to be the extension of the significant radio source, is associated with COSLA-16-S ($F_{1.4\mathrm{GHz}} = 33.3 \pm 10.1$ μJy). The multi-wavelength photometry of COSLA-16-N implies a photometric redshift of $z_{\mathrm{phot}} = 2.16^{+0.12}_{-0.25}$. The mm-to-radio based redshift inferred for COSLA-16-S is $z_{\mathrm{mm/radio}} = 2.40^{0.62}_{-0.51}$, suggesting it is associated with COSLA-16-N.

A third 3.9σ peak (COSLA-16-E) with 1.3 mm flux density of $F_{1.3\mathrm{mm}} = 2.26 \pm 0.58$ mJy is found 6" east from the LABOCA source center and it is coincident with a faint optical source (separation=0.41", $i^{+} = 29.20$). Our photometric redshift computation yields s redshift of $z_{\mathrm{phot}} = 1.25^{+3.03}_{-1.15}$, however (as also reflected in the error) the χ^2 distribution is fairly flat below $z \lesssim 4$ thus making all redshifts below $z \sim 4$ almost equally probable. The mm-to-radio flux based redsfhit suggests $z_{\mathrm{mm/radio}} \geq 3.7$.

The combined 1.3 mm flux density of the 3 identified sources, scaled to 870μm yields 16.3±2.5 mJy, in very good agreement with the deboosted LABOCA flux (14.0±3.6 mJy).

Cosla-17

Two significant S/N > 4.5 detections are found within the PdBI map.

COSLA-17-S is detected at high significance (S/N = 5.3; α = 10 01 36.772, δ = +02 11 04.87). Its 1.3 mm flux density is $F_{1.3\mathrm{mm}} = 3.0 \pm 0.6$ mJy, and it can be associated with a faint source 0.23" away with $m_{\mathrm{NB816}} = 26.2$. No IR or radio source is associated with this detection. We find a photometric redshift for this source of $z_{\mathrm{phot}} = 0.7^{+0.21}_{-0.22}$, while the mm-to-radio based redshift suggests $z_{\mathrm{mm/radio}} \gtrsim 4$.

COSLA-17-N is found at S/N=4.6 (α = 10 01 36.811, δ = +02 11 09.66) with a 1.3 mm flux density of $F_{1.3\mathrm{mm}} = 3.55 \pm 0.677$ mJy. It is perfectly coincident with an optical/UltraVista/IRAC/radio source (separation=0.09"), however it is within the side-lobe region of the brighter COSLA-17-S source. Hence further follow-up with more complete uv-coverage is required to affirm this source. We find a photometric redshift of $z_{\mathrm{phot}} = 3.37^{+0.14}_{-0.22}$, consistent wi th the mm-to-radio based redshift of $z_{\mathrm{mm/radio}} = 3.27^{+0.60}_{-0.49}$.

This SMG is detected by both LABOCA and AzTEC/ASTE surveys, and the flux ratio using these two surveys suggests a spectral index of 2.08. Using this value to scale the combined 1.3mm PdBI fluxes to 870 μm (1.1 mm) we find a flux density of 15.2 ±

2.2 mJy (9.2 ± 1.4 mJy), consistent with the deboosted LABOCA (AzTEC/ASTE) flux of 12.5 ± 3.2 mJy ($7.5^{+1.0}_{-1.1}$ mJy).

Cosla-18

COSLA-18 is detected at a signal to noise of S/N = 4.5 ($\alpha = 10\ 00\ 43.19$, $\delta = +02\ 05\ 19.17$). Its 1.3 mm flux density is $F_{1.3\mathrm{mm}} = 2.15 \pm 0.48$ mJy. Scaled to 870 μm (1.1 mm) wavelength this yields a flux density of 7.2 ± 1.6 mJy (3.5 ± 0.8 mJy), consistent with the deboosted LABOCA (AzTEC/ASTE) fluxes of 10.0 ± 2.6 mJy ($3.8^{+1.1}_{-1.2}$ mJy). The source is coincident with an optical/UltraVista/IRAC/radio source (separation=0.67"; $i^+ = 28.96$). Our photometric redshift computation yields 2 almost equally probable photometric redshifts at $z \sim 3$ and $z \sim 5$. The significant radio detection ($F_{1.4\mathrm{GHz}} = 60.1 \pm 8.9$ μJy) would argue in favor of the lower redshift solution, consistent with the mm-to-radio flux based redshift of $z_{\mathrm{mm/radio}} = 2.40^{+0.35}_{-0.34}$. Thus, here we adopt the low-redshift solution for this source, yielding $z_{\mathrm{phot}} = 2.90^{+0.31}_{-0.43}$, noting that a second solution of $z_{\mathrm{phot}} = 4.92^{+0.38}_{-0.34}$ is possible.

Cosla-19

Cosla-19 is detected at a S/N = 4.1 with a 1.3 mm flux density of 3.17 ± 0.76 mJy. Scaling this flux to 1.2 mm, 1.1 mm, and 870 μJy yields fluxes of 4.1 ± 1.0 mJy, 5.1 ± 1.2 mJy, 10.7 ± 2.6 mJy, respectively, consistent with the deduced MAMBO, AzTEC, and LABOCA fluxes of 5.55 ± 0.9 mJy, $5.3^{+1.1}_{-1.2}$ mJy, and 7.4 ± 1.8 mJy, respectively. The closest multi-wavelength source to Cosla-19 is an optical/UltraVista source 2.0" away ($i^+ = 25.66$). Such a separation makes it unlikely that this source is the counterpart of the mm-detection although given the mm-resolution and significance a ~ 0.8" positional uncertain is expected. A $2\sigma = 16.1$ μJy radio peak is associated with the PdBI mm peak yielding a mm-to-radio-flux ratio based redshift for Cosla-19 of $z_{\mathrm{mm/radio}} = 3.98^{+1.62}_{-0.90}$.

Cosla-23

Within the COSLA-23 LABOCA beam two significant (S/N > 5) sources are found in the PdBI 1.3mm map. COSLA-23-N is detected at a signal-to-noise of S/N = 7.3 at $\alpha = 10\ 00\ 10.161$, $\delta = +02\ 13\ 34.95$. It is coincident with an optical/UltraVista/IRAC/radio source (separation= 0.44"; $i^+ = 26.3$). COSLA-23-S is detected at S/N = 6.2 at $\alpha = 10\ 00\ 10.070$, $\delta = +02\ 13\ 26.87$. It can be matched to an optical/IRAC source (separation= 0.87", $i^+ = 28.49$), but it is not detected in the radio map. Based on the multi-wavelength photometry of the counterparts we find photometric redshifts of $z_{\mathrm{phot}} = 4.00^{+0.67}_{-0.90}$ (COSLA-23-N) and $z_{\mathrm{phot}} = 2.58^{+1.52}_{-2.48}$ (COSLA-23-S).

The 1.3 mm flux densities for COSLA-23-N and COSLA-23-S are 3.42 ± 0.47 mJy, and 3.70 ± 0.60 mJy, respectively. Only COSLA-23-N is within the MAMBO 11" beam, and the scaled 1.3 mm flux (4.4 ± 0.6mJy) agrees well with the COSBO-2 flux (5.77 ± 0.9 mJy).

Cosla-25

No significant source is present in the 1.3mm map. No statistical counterpart could be associated with this SMG. Therefore, it remains unclear whether the LABOCA source is spurious, breaks up into multiple components at 1.5" angular resolution, or simply is below the PdBI detection limit.

Cosla-30

No significant source is present in the 1.3mm map. No statistical counterpart could be associated with this SMG. Therefore, it remains unclear whether the LABOCA source is spurious, breaks up into multiple components at 1.5" angular resolution, or simply is below the PdBI detection limit.

Cosla-33

The most prominent feature in the PdBI map within the LABOCA beam is a 3.1σ peak 6.0" away from the LABOCA source center that can be associated with a optical/UltraVista/IRAC source ($i^+ = 25.2$, separation=0.95"). Its 1.3 mm flux density is 1.78 ± 0.58 mJy which scales to 6.02 ± 1.95 mJy at 870 μm, in good agreement with the deboosted LABOCA flux (6.8 ± 1.1 mJy). Given the low significance of the 1.3 mm source further follow-up is required to affirm its reality.

Cosla-35

COSLA-35 is detected at a signal-to-noise of S/N = 4.2 (α = 10 00 23.65, δ = +02 21 55.22). Its 1.3 mm flux density is $F_{1.3\mathrm{mm}} = 2.15 \pm 0.51$ mJy. This flux scaled to 870 μm (1.1 mm) yields a flux density of 7.3 ± 1.7 mJy (3.5 ± 0.8 mJy), consistent with the observed LABOCA (AzTEC/ASTE) fluxes of 8.2 ± 1.1 mJy ($5.1^{+1.2}_{-1.1}$ mJy). The mm-detection is coincident with an optical/UltraVista/IRAC/radio source (separation= 0.55"; $i^+ = 27.24$). We find a photometric redshift of $z_{\mathrm{phot}} = 1.91^{+1.75}_{-0.64}$.

Cosla-38

COSLA-38 is detected at a signal-to-noise ratio of S/N = 4.4 at α = 10 00 12.59, δ = +02 14 44.31, 14.8" away from the LABOCA source position (thus essentially outside the LABOCA beam; FWHM=27"). It is however only 0.67" away from the MAMBO source Cosbo-19, and coincident with a radio/UltraVista/IRAC/optical source (separation=0.23", $i^+ = 24.08$). We infer a 1.3 mm flux density of $F_{1.3\mathrm{mm}} = 8.19 \pm 1.85$ mJy, which should however be treated with caution as the correction for the primary beam response at that distance from the PdBI phase center applied to the flux is about a factor of 4. We find a photometric redshift of $z_{\mathrm{phot}} = 2.44^{+0.12}_{-0.11}$ for this SMG.

Cosla-40

COSLA-40 is detected at a signal-to-noise ratio of S/N = 3.4 (α = 09 59 25.91, δ = +02 19 56.40), 11.3" away from the LABOCA source center. Its 1.3 mm flux density is $F_{1.3\mathrm{mm}} = 3.41 \pm 1.02$ mJy. Scaling this flux to 870 μm yields a flux density of 11.5 ± 3.4 mJy, in very good agreement with the deboosted LABOCA flux ($F_{870\mu\mathrm{m}} = 11.1 \pm 3.4$ mJy). The source is coincident with an optical source (separation=0.51"; $i^+ = 25.52$), but not detected in the radio. Given the expected flux density, and the coincidence of the source with an optical detection we assume this source to be real. We find a photometric redshift of $z_{\rm phot} = 1.30^{+0.09}_{-0.11}$, but we note that χ^2 dips are also found at lower and higher redshift values, and that the mm-to-radio flux based redshift suggests $z_{\rm mm/radio} \gtrsim 4.5$.

Cosla-47

COSLA-47 is detected at α = 10 00 33.350, δ = +02 26 01.66 and a signal-to-noise ratio of S/N = 5.3, 6.4" away from the LABOCA source center. Its 1.3mm flux density is 3.11 ± 0.59 mJy, and consistent with the LABOCA/AzTEC fluxes, when scaled to these frequencies. The PdBI source is coincident (separation=0.48") with a source independently detected at optical, IR, and radio wavelengths. We find a well constrained photometric redshift of $z_{\rm phot} = 2.36^{+0.24}_{-0.24}$.

Within the LABOCA beam several more $S/N > 4$ peaks can be associated with optical/UltraVista/IRAC sources. They are however within sidelobe contaminated regions. This LABOCA SMG may be a blend of several sources, but further follow-up is required to confirm this.

Cosla-48

No significant source is present in the 1.3 mm map. The statistical counterpart association (see Sec. 3.5.2.1 and Fig. 3.6 for details) suggests two potential tentative counterparts to this LABOCA source. The sum of the extracted 1.3 mm fluxes (taken as maximum flux within an circular area of 1" in radius centered at the statistical counterpart), corrected for the primary beam response, is 1.56 mJy. This flux, scaled to 870 μm (5.2 mJy) is in very good agreement with the LABOCA flux of 6.1 ± 1.7 mJy (see Fig. 3.2). This suggests that the LABOCA source may be fainter at 1.3 mm than can be detected given our PdBI sensitivity and it breaks up into multiple components when observed at 1.5" resolution.

Cosla-50

No significant source is present in the 1.3mm map. The statistical counterpart association (see Sec. 3.5.2.1 and Fig. 3.6 for details) suggests two potential (robust and tentative) counterparts to this LABOCA source. The sum of the extracted 1.3 mm fluxes (taken as maximum flux within an circular area of 1" in radius centered at the statistical counterpart), corrected for the primary beam response, is 2.61 mJy. When scaled to 870 μm this flux (8.7 mJy) is fairly consistent with the LABOCA flux of 5.6 ± 1.6 mJy (see Fig. 3.2). This suggests that the LABOCA source may be fainter at 1.3 mm than can be detected given our PdBI sensitivity and it breaks up into multiple components when observed at 1.5" resolution.

Cosla-51

No significant source is present in the 1.3mm map. The statistical counterpart association (see Sec. 3.5.2.1 and Fig. 3.6 for details) suggests one robust potential counterpart to this LABOCA source. The extracted 1.3 mm flux (taken as maximum flux within an circular area of 1" in radius centered at the statistical counterpart), corrected for the primary beam response, is 1.27 mJy, consistent with the LABOCA flux of 6.2 ± 1.7 mJy when scaled to 870 μm (4.5 mJy; s ee Fig. 3.2). This suggests that the LABOCA source is fainter at 1.3 mm than can be detected given our PdBI sensitivity and/or it breaks up into multiple components when observed at 1.5” resolution.

Cosla-54

COSLA-54 is detected at a signal-to-noise ratio of S/N = 5.0 (α =09 58 37.99, δ = +02 14 08.52), 7.6” away from the LABOCA source center. Its 1.3 mm flux density is $F_{1.3\mathrm{mm}} = 3.26 \pm 0.65$ mJy. Scaling this flux to 870 μm (1.1 mm) yields a flux density of 11.0 ± 2.2 mJy (5.3 ± 1.1 mJy), in agreement with the deboosted LABOCA (AzTEC/ASTE) flux of 11.6 ± 4.1 mJy ($8.7^{+1.3}_{-1.4}$ mJy). The mm-detection can be associated with an optical/IRAC/radio source (separation= 0.75″; i^+=25.21). We find a photometric redshift of $z_{\mathrm{phot}} = 2.64^{+0.38}_{-0.26}$.

Cosla-62

No significant source is present in the 1.3mm map. No statistical counterpart could be associated with this SMG. Therefore, it remains unclear whether the LABOCA source is spurious, breaks up into multiple components at 1.5” angular resolution, or simply is below the PdBI detection limit.

Cosla-128

COSLA-128 is detected at a signal-to-noise ratio of S/N = 4.8 (α = 10 01 37.99, δ = +02 23 26.50). Its 1.3 mm flux density is $F_{1.3\mathrm{mm}} = 4.50 \pm 0.94$ mJy. Scaling this flux to 870 μm (1.1 mm) yields a flux density of 15.2 ± 3.2 mJy (7.3 ± 1.5 mJy), in agreement with the LABOCA (AzTEC/ASTE) flux of 11.0 ± 3.5 mJy (4.4 ± 1.1 mJy). The source is coincident with an optical detection (no MIR/radio; separation= 0.55”; i^+ = 26.57). We find a photometric redshift of $z_{\mathrm{phot}} = 0.10^{+0.19}_{-0.00}$, with secondary and tertiary possible solutions at $z \sim 1.2$, and $z \sim 3$.

Cosla-161

COSLA-161 is detected at a signal-to-noise ratio of S/N = 3.5 (α = 10 00 16.150, δ = +02 12 38.27). Its 1.3 mm flux density is $F_{1.3\mathrm{mm}} = 2.54 \pm 0.674$ mJy. Scaling this flux to 870 μm, 1.1 mm, and 1.2 mm, using a spectral index of 3, yields 10.1 ± 4.8, 4.1 ± 1.2, and 3.3 ± 0.9 mJy, respectively. This is in very good agreement with the deboosted LABOCA (10.1 ± 4.8mJy), AzTEC/ASTE (3.2 ± 1.1 mJy), and MAMBO fluxes (1.4 ± 0.9 mJy).

The SMG is coincident with an optical/IR/radio source with an available (VIMOS / IMACS) spectrum at $z_{\mathrm{spec}} = 0.187$. The source is also detected by Chandra in the X-rays, and we find a 0.5-2 keV band flux of 1.9 ± 0.8 erg s^{-1} cm^{-2}. At a redshift of 0.187 this corresponds to a bolometric X-ray luminosity (0.1-10 keV) of $(6.2 \pm 2.8) \times 10^{40}$ erg s^{-1} (assuming a power law spectral shape with photon index 1.8). Given this X-ray luminosity it is not clear whether it arises from star-formation processes or a low-power AGN.

It is interesting that a second radio source is present within the LABOCA beam ($z_{\mathrm{spec}} = 2.947$), and is not associated with mm-emission (however there is a 2.3σ peak at its position in the PdBI map).

Table C.1: Photometry table for our LABOCA SMGs with PdBI detections (magnitudes listed are total AB magnitudes corrected for galactic extinction)

Source	ID	r^+	i^+	z^+	J	H	Ks	$m_{3.6\mu m}$	$m_{4.5\mu m}$	$m_{5.8\mu m}$	$m_{8.0\mu m}$	F_{20cm} [μJy]
COSLA-5	970338	23.25 ± 0.03	22.58 ± 0.02	22.23 ± 0.02	21.69 ± 0.01	21.50 ± 0.02	21.02 ± 0.01	20.98 ± 0.01	21.23 ± 0.03	21.00 ± 0.11	21.25 ± 0.39	17.3±8.6
COSLA-6-N	–	–	–	–	–	–	–	–	–	–	–	19.4±9.4
COSLA-6-S	1201029	26.32 ± 0.19	26.24 ± 0.23	26.04 ± 0.24	–	–	–	–	–	–	–	18.6±9.3
COSLA-8	999816	28.06 ± 0.36	27.45 ± 0.25	> 26.00	–	–	–	–	–	–	–	26.2±8.0
COSLA-9N	572563	27.18 ± 0.25	26.23 ± 0.17	25.92 ± 0.17	99.00 ± 25.40	24.73 ± 0.39	24.21 ± 0.26	–	–	–	–	16.2 ± 8.1
COSLA-9S	571877	25.56 ± 0.13	24.84 ± 0.09	24.26 ± 0.08	22.71 ± 0.13	21.96 ± 0.06	21.06 ± 0.03	20.49 ± 0.01	20.23 ± 0.01	20.16 ± 0.05	20.25 ± 0.16	25.7 ± 8.4
COSLA-11-N	542814	28.18 ± 0.50	27.85 ± 0.46	26.96 ± 0.25	–	–	–	–	–	–	–	20.1±10.1
COSLA-11-S	543122	24.61 ± 0.06	24.48 ± 0.06	24.69 ± 0.08	24.95 ± 0.15	24.03 ± 0.11	23.90 ± 0.12	–	–	–	–	20.1±10.1
COSLA-13	1006169	25.14 ± 0.10	24.57 ± 0.07	24.23 ± 0.08	22.83 ± 0.03	21.97 ± 0.02	21.22 ± 0.01	20.29 ± 0.01	19.89 ± 0.01	19.36 ± 0.02	19.19 ± 0.06	11.9±7.4
COSLA-16-E	1452379	29.54 ± 0.58	29.29 ± 0.48	28.23 ± 0.25	–	–	–	–	–	–	–	20.3±10.2
COSLA-16-N	1452311	23.69 ± 0.04	23.29 ± 0.03	22.75 ± 0.03	21.94 ± 0.01	21.30 ± 0.01	20.63 ± 0.01	20.09 ± 0.01	19.84 ± 0.01	19.76 ± 0.04	20.00 ± 0.13	95.6±10.1
COSLA-16S	–	–	–	–	–	–	–	–	–	–	–	33.3 ± 10.1
COSLA-17-S	959541	28.26 ± 0.85	> 28.10	> 26.00	> 25.40	> 25.40	> 25.00	–	–	–	–	19.4±9.7
COSLA-17-N	959312	24.94 ± 0.08	24.71 ± 0.08	24.70 ± 0.08	24.33 ± 0.09	23.98 ± 0.11	23.01 ± 0.05	22.43 ± 0.04	21.93 ± 0.05	21.84 ± 0.23	21.30 ± 0.40	43.7±.2
COSLA-18	771619	29.59 ± 0.58	29.04 ± 0.49	27.70 ± 0.24	–	–	–	20.79 ± 0.01	20.38 ± 0.01	20.04 ± 0.05	20.04 ± 0.11	60.1±8.9
COSLA-19	–	–	–	–	–	–	–	–	–	–	–	16.1 ± 8.0
COSLA-23-N	1029389	28.40 ± 1.33	26.41 ± 0.30	26.15 ± 0.31	–	–	23.02 ± 0.05	22.17 ± 0.03	21.66 ± 0.04	21.64 ± 0.21	21.01 ± 0.31	53.8 ±8.8
COSLA-23-S	1029701	> 28.40	28.58 ± 0.37	30.27 ± 2.13	–	–	–	–	–	–	–	15.9 ±8.0
COSLA-33	1267015	25.35 ± 0.11	25.28 ± 0.14	25.19 ± 0.15	24.88 ± 0.41	24.30 ± 0.41	24.15 ± 0.38	23.75 ± 0.16	23.95 ± 0.35	22.42 ± 0.47	99.00 ± 22.96	17.8 ± 8.9
COSLA-35	1235579	26.58 ± 0.34	27.32 ± 0.87	25.86 ± 0.33	–	–	21.85 ± 0.03	21.07 ± 0.01	20.62 ± 0.02	20.38 ± 0.06	20.15 ± 0.15	47.2 ±8.9
COSLA-38	1026384	24.48 ± 0.06	24.17 ± 0.05	23.68 ± 0.04	22.69 ± 0.02	21.52 ± 0.01	20.86 ± 0.01	20.05 ± 0.01	19.82 ± 0.01	19.66 ± 0.04	19.97 ± 0.12	25.8 ±8.3
COSLA-40	1289293	25.74 ± 0.14	25.61 ± 0.15	25.97 ± 0.25	–	–	–	–	–	–	–	18.8 ±9.4
COSLA-47	1225491	25.69 ± 0.12	25.83 ± 0.17	25.36 ± 0.14	–	23.25 ± 0.06	22.24 ± 0.03	21.18 ± 0.02	20.79 ± 0.02	20.45 ± 0.08	20.53 ± 0.20	40.2 ±9.3
COSLA-54	1078145	26.78 ± 0.31	–	28.96 ± 2.88	–	24.11 ± 0.11	22.66 ± 0.03	21.24 ± 0.02	20.87 ± 0.02	20.39 ± 0.06	20.46 ± 0.16	121.7 ±10.7
COSLA-128	1183799	26.20 ± 0.26	26.66 ± 0.51	26.64 ± 0.60	–	–	–	–	–	–	–	18.6 ±9.3
COSLA-161	1006116	18.74 ± 0.00	18.27 ± 0.00	17.67 ± 0.00	17.23 ± 0.00	16.76 ± 0.00	16.37 ± 0.00	17.33 ± 0.00	17.40 ± 0.00	17.45 ± 0.01	15.66 ± 0.00	217.4±8.7

D

Notes on the 1.1 mm-selected Sample

Our 1.1mm-selected sample is based on the SMA follow-up of 15 brightest SMGs drawn from the 1.1 mm AzTEC/JCMT-COSMOS survey at 18" angular resolution (AzTEC-1 to AzTEC-15; see Table 3.1 ; Younger et al. 2007, 2009). Detailed notes on individual targets are given in Younger et al. (2007, 2009). Here we have extracted the multi-wavelength photometry, tabulated in Table D.1 , for the counterparts of these SMGs using the deep COSMOS multi-wavelength catalog, with UltraVista data added. The photometry in the IRAC bands had to be deblended for AzTEC-8 (see Fig. D.1), and that for AzTEC-10 had to specifically be extracted as this source was not present in the catalog (see Younger et al. 2009). The photometry extraction and deblending were performed following the procedure described in detail by Smolčić et al. (2012). Furthermore, AzTEC-11 is a peculiar source that required particular attention. Younger et al. (2009) find that the SMA detection is best fit by a double Gaussian, suggesting a multiple component (N & S) source, labeled AzTEC-11-N and AzTEC-11-S.[1] They present three positions for this SMG: i) AzTEC-11 when the SMA detection is fit using a single-Gaussian, and ii) AzTEC-11-N and AzTEC-11-S when the SMA detection is fit using a double Gaussian. AzTEC-11 is coincident with an optical/MIR/radio source with a spectroscopic redshift ($z_{\rm spec} = 1.599$). AzTEC -11-S (which is actually the northern component of the source) cannot be matched to a multi-wavelength counterpart in the deep COSMOS maps. Thus, given the rms in the 20 cm VLA-COSMOS survey we estimate a mm-to-radio based redshift of $z_{\rm mm/radio} > 2.58$. AzTEC-11-N (which is actually the southern component of the source) has an independent UltraVista and IRAC counterpart. To extract its photometry we have deblended the counterpart of AzTEC-11-N by subtracting a 2D-Gaussian from the maps at the position of the counterpart of AzTEC-11, In Fig. D.2 we show the deblended maps for AzTEC-11-N. We find a photometric redshift of $z_{\rm phot} = 1.51^{+0.41}_{-0.92}$ for this component.

---

[1] Note that the N & S labels are inverted (see Tab. 1 in Younger et al. 2009).

Table D.1: Photometry table for our 1.1mm-selected sample (magnitudes listed are total AB magnitudes corrected for galactic extinction)

Source	ID	r^+	i^+	z^+	J	H	Ks	$m_{3.6\mu m}$	$m_{4.5\mu m}$	$m_{5.8\mu m}$	$m_{8.0\mu m}$	F_{20cm} [μJy]
AzTEC-1	1485894	26.17 ± 0.16	25.20 ± 0.10	24.94 ± 0.09	25.16 ± 0.17	24.58 ± 0.19	23.46 ± 0.08	22.44 ± 0.05	22.27 ± 0.07	21.10 ± 0.14	21.04 ± 0.32	41.6±11.1
AzTEC-2*	–	–	–	–	–	–	–	–	–	–	–	47.3 ± 10.9
AzTEC-3	1447531	26.26 ± 0.19	25.01 ± 0.09	24.39 ± 0.07	23.75 ± 0.07	23.88 ± 0.11	23.73 ± 0.11	22.67 ± 0.05	22.03 ± 0.06	22.45 ± 0.43	21.35 ± 0.41	24.3±9.8
AzTEC-4	1507528	28.14 ± 0.78	26.45 ± 0.21	26.68 ± 0.32	–	–	24.07 ± 0.10	22.17 ± 0.04	21.88 ± 0.04	21.45 ± 0.19	20.80 ± 0.22	28.0±11.4
AzTEC-5	1455197	25.90 ± 0.20	25.25 ± 0.15	24.97 ± 0.16	–	–	22.90 ± 0.07	21.69 ± 0.02	21.27 ± 0.03	20.94 ± 0.10	20.48 ± 0.18	92.5±10.8
AzTEC-6	1708424	25.62 ± 0.11	25.16 ± 0.10	24.54 ± 0.07	25.57 ± 0.24	–	–	–	–	–	–	29.0±11.6
AzTEC-7	1899647	24.26 ± 0.07	23.84 ± 0.06	23.33 ± 0.05	21.83 ± 0.03	21.15 ± 0.03	20.55 ± 0.02	19.79 ± 0.01	19.52 ± 0.01	19.31 ± 0.03	19.51 ± 0.09	103.4±18.7
AzTEC-8	1473458	26.25 ± 0.13	25.90 ± 0.14	26.00 ± 0.17	–	–	23.67 ± 0.07	21.73 ± 0.03	21.22 ± 0.03	20.46 ± 0.07	20.06 ± 0.14	88.8±10.6
AzTEC-9	1271178	26.29 ± 0.20	25.34 ± 0.12	25.01 ± 0.11	–	–	–	22.92 ± 0.07	22.65 ± 0.10	>23.82	22.59 ± 1.27	53.5±9.52
AzTEC-10	–	–	–	–	–	–	23.47±0.10	21.76±0.048	21.21±0.038	20.80±0.063	20.81±0.15	26.5±11.6
AzTEC-11	1704741	23.70 ± 0.04	23.22 ± 0.03	22.87 ± 0.03	22.10 ± 0.01	21.62 ± 0.01	21.28 ± 0.01	20.22 ± 0.01	19.84 ± 0.01	19.64 ± 0.04	19.85 ± 0.11	139.4±12.7
AzTEC-11N	–	–	–	–	22.97 ± 0.20	22.45±0.20	21.78±0.20	21.25±0.30	20.96±0.11	20.86±0.11	20.88±0.18	120.8±12.6
AzTEC-11S	–	–	–	–	–	–	–	–	–	–	–	25.9 ± 13.0
AzTEC-12	1671195	24.63 ± 0.07	24.19 ± 0.06	23.90 ± 0.06	23.07 ± 0.04	21.66 ± 0.02	21.24 ± 0.02	20.27 ± 0.01	19.95 ± 0.01	19.47 ± 0.03	19.52 ± 0.08	104.2±13.8
AzTEC-13	–	–	–	–	–	–	–	–	–	–	–	20.2 ± 10.1
AzTEC-14W	1484311	26.09 ± 0.21	25.70 ± 0.19	26.64 ± 0.53	–	–	–	–	–	–	–	18.9±9.4
AzTEC-14E	–	–	–	–	–	–	–	–	–	–	–	19.4 ± 9.7
AzTEC-15	1473978	27.53 ± 0.32	27.36 ± 0.36	26.53 ± 0.23	–	24.43 ± 0.09	23.66 ± 0.05	21.77 ± 0.03	21.20 ± 0.03	21.05 ± 0.12	20.33 ± 0.17	19.5±9.7

---

[*] AzTEC-2, at a spectroscopic redshift of 1.125 (Baloković et al., in prep), is heavily blended by a bright, extended foreground galaxy.

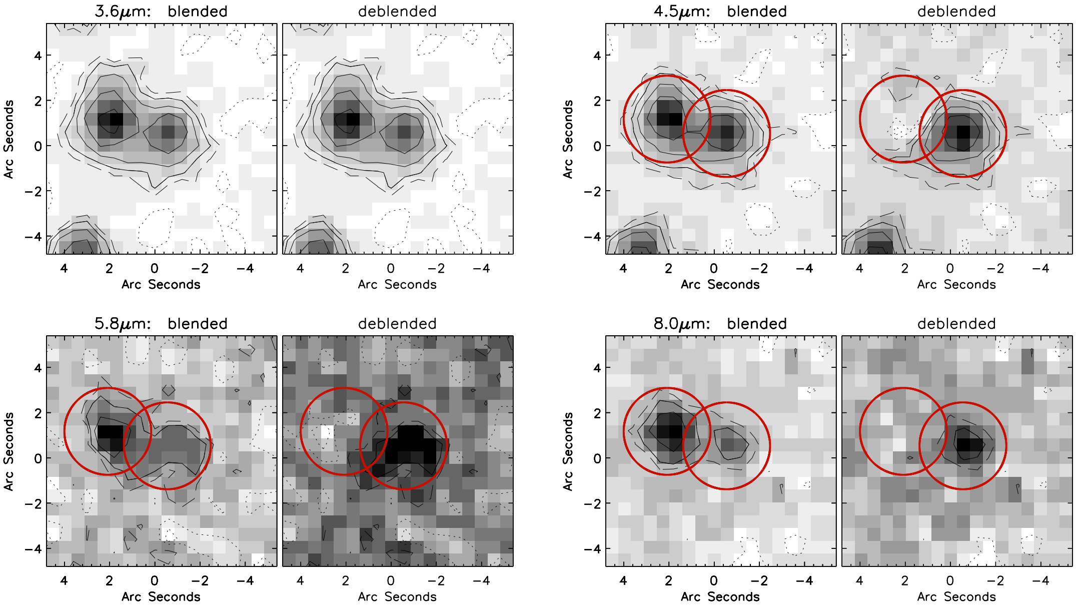

Figure D.1: Deblending of AzTEC-8 in Spitzer/IRAC bands.

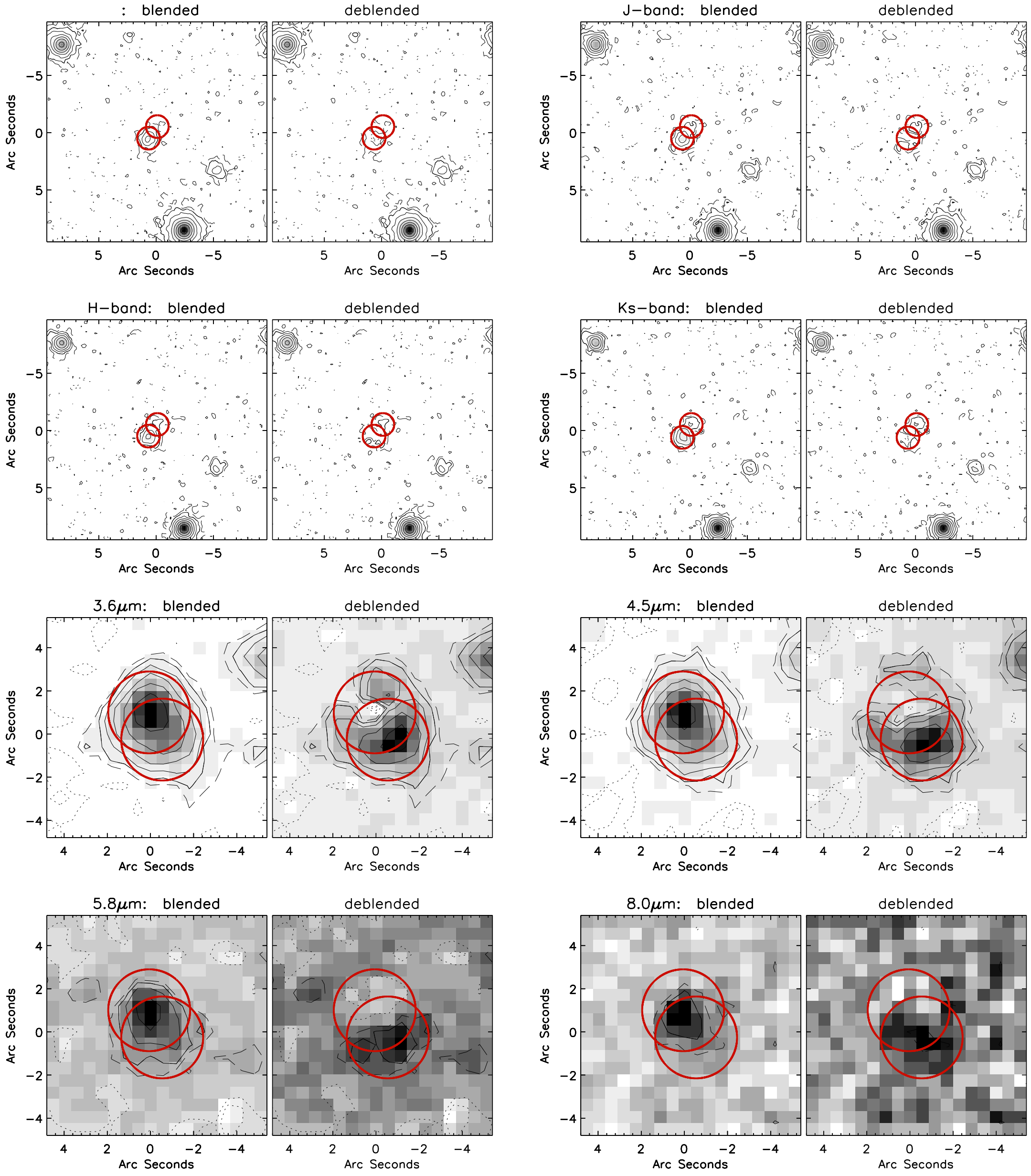

Figure D.2: Deblending of AzTEC-11-N in UltraVista YJHK and Spitzer/IRAC bands.

References

Adelberger, K. L. & Steidel, C. C. 2000, ApJ, 544, 218

Alaghband-Zadeh, S., Chapman, S. C., Swinbank, A. M., et al. 2012, MNRAS, 424, 2232

Alexander, D. M., Bauer, F. E., Chapman, S. C., et al. 2005, ApJ, 632, 736

Aravena, M., Bertoldi, F., Carilli, C., et al. 2010a, ApJ, 708, L36

Aravena, M., Younger, J. D., Fazio, G. G., et al. 2010b, ApJ, 719, L15

Aretxaga, I., Wilson, G. W., Aguilar, E., et al. 2011, MNRAS, 415, 3831

Arnouts, S., Walcher, C. J., Le Fèvre, O., et al. 2007, A&A, 476, 137

Austermann, J. E., Aretxaga, I., Hughes, D. H., et al. 2009, MNRAS, 393, 1573

Banerji, M., Chapman, S. C., Smail, I., et al. 2011, MNRAS, 418, 1071

Baugh, C. M., Lacey, C. G., Frenk, C. S., et al. 2005, MNRAS, 356, 1191

Bell, E. F. 2003, ApJ, 586, 794

Bertin, E. & Arnouts, S. 1996, A&AS, 117, 393

Bertoldi, F., Carilli, C., Aravena, M., et al. 2007, ApJS, 172, 132

Beswick, R. J., Muxlow, T. W. B., Thrall, H., Richards, A. M. S., & Garrington, S. T. 2008, MNRAS, 385, 1143

Béthermin, M., Dole, H., Lagache, G., Le Borgne, D., & Penin, A. 2011, A&A, 529, A4

Biggs, A. D., Ivison, R. J., Ibar, E., et al. 2011, MNRAS, 413, 2314

Blain, A. 2002, Phys. Rep., 369, 111

Blain, A. W., Chapman, S. C., Smail, I., & Ivison, R. 2004, ApJ, 611, 725

Bolzonella, Â., Miralles, Â.-M., & Pelló, Â. 2000, A&A

Borys, C., Chapman, S., Halpern, M., & Scott, D. 2003, MNRAS, 344, 385

Bothwell, M. S., Chapman, S. C., Tacconi, L., et al. 2010, MNRAS, 405, 17

Bothwell, M. S., Smail, I., Chapman, S. C., et al. 2013, MNRAS, 429, 3047

Bourne, N., Dunne, L., Ivison, R. J., et al. 2011, MNRAS, 410, 1155

Boyle, B. J., Cornwell, T. J., Middelberg, E., et al. 2007, MNRAS, 376, 1182

Brusa, M., Zamorani, G., Comastri, A., et al. 2007, ApJS, 172, 353

Bruzual, G. & Charlot, S. 2003, MNRAS, 344, 1000

Calzetti, D., Armus, L. E. E., Bohlin, R. C., Kinney, A. L., & Storchi-bergmann, T. 2000, ApJ, 20, 682

Capak, P., Aussel, H., Ajiki, M., et al. 2007, ApJS, 172, 99

Capak, P., Carilli, C. L., Lee, N., et al. 2008, ApJ, 681, L53

Capak, P. L. 2009, in American Astronomical Society Meeting Abstracts, Vol. 214, American Astronomical Society Meeting Abstracts 214, 200.06

Capak, P. L., Riechers, D., Scoville, N. Z., et al. 2011, Nature, 470, 233

Capak, P. L., Scoville, N. Z., Sanders, D. B., et al. 2010, in Bulletin of the American Astronomical Society, Vol. 42, American Astronomical Society Meeting Abstracts 215, 410.05

Carilli, C. L., Daddi, E., Riechers, D., et al. 2010, ApJ, 714, 1407

Carilli, C. L., Hodge, J., Walter, F., et al. 2011, ApJ, 739, L33

Carilli, C. L., Lee, N., Capak, P., et al. 2008, ApJ, 689, 883

Carilli, C. L. & Yun, M. S. 1999, ApJ, 513, L13

Carilli, C. L. & Yun, M. S. 2000, ApJ, 530, 618

Casey, C. M., Chen, C.-C., Cowie, L. L., et al. 2013, MNRAS, 436, 1919

Chabrier, G. 2003, ApJ, 586, L133

Chapman, S. C., Blain, A., Ibata, R., et al. 2009, ApJ, 691, 560

Chapman, S. C., Blain, a. W., Smail, I., & Ivison, R. J. 2005, ApJ, 622, 772

Chapman, S. C., Neri, R., Bertoldi, F., et al. 2008, ApJ, 689, 889

Chary, R.-R. & Pope, A. 2010, ArXiv e-prints

Chen, C.-C., Cowie, L. L., Barger, A. J., et al. 2013, ApJ, 776, 131

Chen, C.-C., Cowie, L. L., Wang, W.-H., Barger, A. J., & Williams, J. P. 2011, ApJ, 733, 64

Cimatti, A., Cassata, P., Pozzetti, L., et al. 2008, A&A, 482, 21

Combes, F., Rex, M., Rawle, T. D., et al. 2012, A&A, 538, L4

Condon, J. J. 1992, ARA&A, 30, 575

Coppin, K., Chapin, E. L., Mortier, a. M. J., et al. 2006, MNRAS, 372, 1621

Coppin, K. E. K., Smail, I., Alexander, D. M., et al. 2009, MNRAS, 395, 1905

Cora, S. A. 2006, MNRAS, 368, 1540

Cowie, L. L., Barger, A. J., & Kneib, J.-P. 2002, AJ, 123, 2197

Cox, P., Krips, M., Neri, R., et al. 2011, ApJ, 740, 63

Cramér , H. 1971, Mathematical Methods of Statistics (Princeton University Press)

Daddi, E., Cimatti, a., Renzini, a., et al. 2004, ApJ, 617, 746

Daddi, E., Dannerbauer, H., Krips, M., et al. 2009a, ApJ, 695, L176

Daddi, E., Dannerbauer, H., Stern, D., et al. 2009b, ApJ, 694, 1517

Dannerbauer, H., Lehnert, M. D., Lutz, D., et al. 2002, ApJ, 573, 473

Davé, R., Finlator, K., Oppenheimer, B. D., et al. 2010, MNRAS, 404, 1355

Decarli, R., Smail, I., Walter, F., et al. 2014, ApJ, 780, 115

Devlin, M. J., Ade, P. a. R., Aretxaga, I., et al. 2009, Nature, 458, 737

Downes, A. 1986, MNRAS, 218, 31

Downes, D., Neri, R., Greve, A., et al. 1999, A&A, 347, 809

Downes, D. & Solomon, P. M. 2003, ApJ, 582, 37

Dunne, L., Ivison, R. J., Maddox, S., et al. 2009, MNRAS, 394, 3

Dwek, E., Arendt, R., Hauser, M., et al. 1998, ApJ, 508, 106

Elvis, M., Civano, F., Vignali, C., et al. 2009, ApJS, 184, 158

Engel, H., Tacconi, L. J., Davies, R. I., et al. 2010, ApJ, 724, 233

Fabian, A. C. 1999, MNRAS, 308, L39

Fakhouri, O., Ma, C.-P., & Boylan-Kolchin, M. 2010, MNRAS, 406, 2267

Fixsen, D. J., Dwek, E., Mather, J. C., Bennett, C. L., & Shafer, R. A. 1998, ApJ, 508, 123

Frayer, D. T., Sanders, D. B., Surace, J. a., et al. 2009, AJ, 138, 1261

Frayer, D. T., Smail, I., Ivison, R. J., & Scoville, N. Z. 2000, AJ, 120, 1668

Frenk, C. S., Colberg, J. M., Couchman, H. M. P., et al. 2000, ArXiv Astrophysics e-prints

Fu, H., Cooray, A., Feruglio, C., et al. 2013, Nature, 498, 338

Garn, T. & Alexander, P. 2009, MNRAS, 394, 105

Geach, J. E., Chapin, E. L., Coppin, K. E. K., et al. 2013, MNRAS, 432, 53

Genzel, R., Baker, A. J., Tacconi, L. J., et al. 2003, ApJ, 584, 633

Greve, T. R., Bertoldi, F., Smail, I., et al. 2005, MNRAS, 359, 1165

Greve, T. R., Ivison, R. J., Bertoldi, F., et al. 2004, MNRAS, 354, 779

Greve, T. R., Pope, A., Scott, D., et al. 2008, MNRAS, 389, 1489

Greve, T. R., Weiβ, A., Walter, F., et al. 2010, ApJ, 719, 483

Güsten, R., Nyman, L. A., Schilke, P., et al. 2006, A&A, 16, L13

Hainline, L. J., Blain, A. W., Smail, I., et al. 2011, ApJ, 740, 96

Hainline, L. J., Blain, A. W., Smail, I., et al. 2009, ApJ, 699, 1610

Hasinger, G., Cappelluti, N., Brunner, H., et al. 2007, ApJS, 172, 29

Hatsukade, B., Iono, D., Akiyama, T., et al. 2010, ApJ, 711, 974

Hayward, C. C., Jonsson, P., Kereš, D., et al. 2012, MNRAS, 424, 951

Hayward, C. C., Kereš, D., Jonsson, P., et al. 2011, ApJ, 743, 159

Helou, G. & Bicay, M. D. 1993, ApJ, 415, 93

Helou, G., Soifer, B. T., & Rowan-Robinson, M. 1985, ApJ, 298, L7

Hickox, R. C., Myers, A. D., Brodwin, M., et al. 2011, ApJ, 731, 117

Hickox, R. C., Wardlow, J. L., Smail, I., et al. 2012, MNRAS, 421, no

Hodge, J. A., Karim, A., Smail, I., et al. 2013, ApJ, 768, 91

Hogg, D. W. & Turner, E. L. 1998, Publ. Astron. Soc. Pacific, 110, 727

Hopkins, P. F., Somerville, R. S., Hernquist, L., et al. 2006, ApJ, 652, 864

Hopkins, P. F., Younger, J. D., Hayward, C. C., Narayanan, D., & Hernquist, L. 2010, MNRAS, 402, 1693

Hughes, D., Serjeant, S., Dunlop, J., et al. 1998, Nature, 394, 19

Iglesias-Paramo, J., Buat, V., Hernandez-Fernandez, J., et al. 2007, ApJ, 670, 279

Ikarashi, S., Kohno, K., Aguirre, J. E., et al. 2011, MNRAS, 415, 3081

Ilbert, O., Capak, P., Salvato, M., et al. 2009, ApJ, 690, 1236

Ilbert, O., Salvato, M., Le Floc'h, E., et al. 2010, ApJ, 709, 644

Infante, L. 1994, Astron. Astrophys. (ISSN 0004-6361), 282, 353

Iono, D., Peck, A. B., Pope, A., et al. 2006, ApJ, 640, L1

Ivison, R. J., Alexander, D. M., Biggs, A. D., et al. 2010, MNRAS, 402, 245

Ivison, R. J., Greve, T. R., Dunlop, J. S., et al. 2007, MNRAS, 380, 199

Ivison, R. J., Greve, T. R., Smail, I., et al. 2002, MNRAS, 337, 1

Ivison, R. J., Smail, I., Dunlop, J. S., et al. 2005, MNRAS, 364, 1025

Johansson, D., Sigurdarson, H., & Horellou, C. 2011, A&A, 527, A117

Johnson, H. L. 1966, ARA&A, 4, 193

Johnson, S. P., Wilson, G. W., Wang, Q. D., et al. 2013, MNRAS, 431, 662

Jonsson, P. 2006, MNRAS, 372, 2

Karim, A., Schinnerer, E., Mart´ınez-Sansigre, A., et al. 2011, ApJ, 730, 61

Karim, A., Swinbank, A. M., Hodge, J. A., et al. 2013, MNRAS, 432, 2

Kauffmann, G., Heckman, T. M., Tremonti, C., et al. 2003, MNRAS, 346, 1055

Kenney , J. F. & Keeping, E. S. 1966, Mathematics of Statistics (D. VAN NOSTRAND COMPANY)

Kennicutt, Jr., R. C. 1998, ApJ, 498, 541

Kneib, J.-P., Neri, R., Smail, I., et al. 2005, A&A, 434, 819

Knudsen, K. K., Kneib, J.-P., Richard, J., Petitpas, G., & Egami, E. 2010, ApJ, 709, 210

Knudsen, K. K., van der Werf, P. P., & Kneib, J.-P. 2008, MNRAS, 384, 1611

Koekemoer, A. M., Barker, E., Bergeron, L. E., et al. 2009, AAS

Kovacs, A., Chapman, S. C., Dowell, C. D., et al. 2006, ApJ, 650, 592

Kroupa, P. 2001, MNRAS, 322, 231

Kurczynski, P. & Gawiser, E. 2010, AJ, 139, 1592

Lacki, B. C., Thompson, T. A., & Quataert, E. 2010, ApJ, 717, 1

Lagache, G., Puget, J.-L., & Dole, H. 2005, ARA&A, 43, 727

Lagos, C. d. P., Cora, S. A., & Padilla, N. D. 2008, MNRAS, 388, 587

Landy, S. D. & Szalay, A. S. 1993, ApJ, 412, 64

Lawrence, A., Warren, S. J., Almaini, O., et al. 2007, MNRAS, 379, 1599

Le Floc'h, E., Aussel, H., Ilbert, O., et al. 2009, ApJ, 703, 222

Leauthaud, A., Massey, R., Kneib, J.-P., et al. 2007, ApJS, 219

Lillly, S. J., Le Fèvre, O., Renzini, A., et al. 2007, ApJS, 172, 70

Lilly, S. J., Le Brun, V., Maier, C., et al. 2009, ApJS, 184, 218

Lin, L., Dickinson, M., Jian, H.-Y., et al. 2012, ApJ, 756, 71

Lin, Y.-T., Mohr, J. J., & Stanford, S. A. 2003, ApJ, 591, 749

Lindner, R. R., Baker, a. J., Omont, a., et al. 2011, ApJ, 737, 83

Lindroos, L. & Knudsen, K. K. 2013, Proc. Int. Astron. Union, 8, 94

Lipari, S., Terlevich, R., Diaz, R. J., et al. 2003, MNRAS, 340, 289

Low, F. J. 1965, ApJ, 142, 1287

Magnelli, B., Lutz, D., Santini, P., et al. 2012, A&A, 539, A155

Maloney, P. R., Glenn, J., Aguirre, J. E., et al. 2005, ApJ, 635, 1044

Marsden, G., Ade, P. A. R., Bock, J. J., et al. 2009, ApJ, 707, 1729

Martin, D. C., Wyder, T. K., Schiminovich, D., et al. 2007, ApJS, 173, 342

McCracken, H. J., Capak, P., Salvato, M., et al. 2010, ApJ, 708, 202

McCracken, H. J., Milvang-Jensen, B., Dunlop, J., et al. 2012, A&A, 544, A156

Menéndez-Delmestre, K., Blain, A. W., Smail, I., et al. 2009, ApJ, 699, 667

Michałowski, M., Hjorth, J., & Watson, D. 2010, A&A, 514, A67

Muñoz Arancibia, A. M., Navarrete, F. P., Padilla, N. D., et al. 2015, MNRAS, 446, 2291

Murphy, E. J. 2009, ApJ, 706, 482

Murphy, E. J. 2013, ApJ, 777, 58

Neri, R., Genzel, R., Ivison, R. J., et al. 2003, ApJ, 597, L113

Niklas, S. & Beck, R. 1997, A&A, 320, 54

Padovani, P., Mainieri, V., Tozzi, P., et al. 2009, ApJ, 694, 235

Penner, K., Pope, A., Chapin, E. L., et al. 2011, MNRAS, 410, 2749

Polletta, M., Tajer, M., Maraschi, L., et al. 2007, ApJ, 663, 81

Pope, A., Borys, C., Scott, D., et al. 2005, MNRAS, 358, 149

Pope, A., Scott, D., Dickinson, M., et al. 2006, MNRAS, 370, 1185

Puget, J.-L., Abergel, A., Bernard, J.-P., et al. 1996, A&A

Reddy, N. A., Erb, D. K., Steidel, C. C., et al. 2005, ApJ, 633, 748

Rees, M. J., Silk, J. I., Werner, M. W., & Wickramasinghe, N. C. 1969, Nature, 223, 788

Riechers, D. A., Capak, P. L., Carilli, C. L., et al. 2010, ApJ, 720, L131

Rieke, G. H. & Lebofsky, M. J. 1979, ARA&A, 17, 477

Rodriguez-Martinez, M. I., Allen, R. J., Wiklind, T., & Loinard, L. 2006, 2007 AAS/AAPT Jt. Meet., 38

Roychowdhury, S. & Chengalur, J. N. 2012, Mon. Not. R. Astron. Soc. Lett., 423, L127

Salpeter, E. E. 1955, ApJ, 121, 161

Salvato, M., Hasinger, G., Ilbert, O., et al. 2009, ApJ, 690, 1250

Sanders, D. B. 1999, Astrophys. Space Sci., 266, 18

Sanders, D. B. & Mirabel, I. F. 1996, ARA&A, 34, 749

Sanders, D. B., Salvato, M., Aussel, H., et al. 2007, ApJS, 172, 86

Sanders, D. B., Soifer, B. T., Elias, J. H., et al. 1988, ApJ, 325, 74

Sandstrom, K. M., Bolatto, A., Leroy, A., et al. 2006, in Bulletin of the American Astronomical Society, Vol. 38, American Astronomical Society Meeting Abstracts, 178.07

Sargent, M. T., Schinnerer, E., Murphy, E., et al. 2010, ApJS, 186, 341

Sault, R. J., Teuben, P. J., & Wright, M. C. H. 1995, Astron. Data Anal. Softw. Syst. IV, 77

Schechter, P. 1976, ApJ, 203, 297

Schinnerer, E., Capak, P., Carilli, C. L., Scoville, N. Z., & COSMOS Collaboration. 2009, in American Astronomical Society Meeting Abstracts, Vol. 214, American Astronomical Society Meeting Abstracts 214, 200.08

Schinnerer, E., Carilli, C. L., Bondi, M., et al. 2007, ApJS, 172, 46

Schinnerer, E., Carilli, C. L., Capak, P., et al. 2008, ApJ, 689, L5

Schinnerer, E., Carilli, C. L., Scoville, N. Z., et al. 2004, AJ, 128, 1974

Schinnerer, E., Sargent, M. T., Bondi, M., et al. 2010, ApJS, 188, 384

Schuller, F. 2012, in Millimeter, ed. W. S. Holland, Vol. 8452

Scott, K. S., Austermann, J. E., Perera, T. a., et al. 2008, MNRAS, 385, 2225

Scott, K. S., Yun, M. S., Wilson, G. W., et al. 2010, MNRAS, 2278, no

Scott, S. E. & Fox, M. 2002, MNRAS, 331, 817

Scoville, N., Aussel, H., Brusa, M., et al. 2007, ApJS, 172, 1

Seymour, N., Dwelly, T., Moss, D., et al. 2008, MNRAS, 386, 1695

Sharp, R. G., Sabbey, C. N., Vivas, A. K., et al. 2002, MNRAS, 337, 1153

Sheth, K., Blain, A. W., Kneib, J.-P., et al. 2004, ApJ, 614, L5

Silva, L., Granato, G. L., Bressan, A., & Danese, L. 1998, ApJ, 509, 103

Simpson, J. M., Swinbank, A. M., Smail, I., et al. 2014, Atrophys. J., 788, 125

Siringo, G., Kreysa, E., Kovács, a., et al. 2009, A&A, 497, 945

Smail, I., Ivison, R. J., Blain, A. W., & Kneib, J.-P. 2002, MNRAS, 331, 495

Smolčić, V., Aravena, M., Navarrete, F., et al. 2012a, A&A, 548, A4

Smolčić, V., Capak, P., Ilbert, O., et al. 2011, ApJ, 731, L27

Smolčić, V., Navarrete, F., Aravena, M., et al. 2012b, ApJS, 200, 10

Smolčić, V., Schinnerer, E., Scodeggio, M., et al. 2008, ApJS, 177, 14

Steidel, C. C., Adelberger, K. L., Giavalisco, M., Dickinson, M., & Pettini, M. 1999, ApJ, 519, 1

Swinbank, A. M., Lacey, C. G., Smail, I., et al. 2008, MNRAS, 391, 420

Swinbank, A. M., Smail, I., Chapman, S. C., et al. 2010, MNRAS, 405, 12

Tacconi, L. J., Genzel, R., Smail, I., et al. 2008, ApJ, 680, 246

Tacconi, L. J., Neri, R., Chapman, S. C., et al. 2006, ApJ, 640, 228

Takagi, T., Mortier, A. M. J., Shimasaku, K., et al. 2007, MNRAS, 381, 1154

Tamura, Y., Iono, D., Wilner, D. J., et al. 2010, ApJ, 724, 1270

Taniguchi, Y., Scoville, N., Murayama, T., et al. 2007, ApJS, 172, 9

Targett, T. A., Dunlop, J. S., Cirasuolo, M., et al. 2013, MNRAS, 432, 2012

Tecce, T. E., Cora, S. A., Tissera, P. B., Abadi, M. G., & Lagos, C. d. P. 2010, MNRAS, 408, 2008

Telesco, C. M. & Harper, D. A. 1977, BAAS, 9

Toft, S., Smolčić, V., Magnelli, B., et al. 2014, ApJ, 782, 68

Trump, J. R., Impey, C. D., McCarthy, P. J., et al. 2007, ApJS, 172, 383

van der Kruit, P. C. 1973, A&A, 29, 263

van Dokkum, P. G., Franx, M., Kriek, M., et al. 2008, ApJ, 677, L5

Viero, M. P., Moncelsi, L., Quadri, R. F., et al. 2013, ApJ, 779, 32

Voelk, Â. 1989, Astron. Astrophys. (ISSN 0004-6361), 218, 67

Wall, J. V., Pope, A., & Scott, D. 2007, MNRAS, 383, 435

Walter, F., Decarli, R., Carilli, C., et al. 2012, Nature, 486, 233

Wang, S. X., Brandt, W. N., Luo, B., et al. 2013, ApJ, 778, 179

Wang, W.-H., Cowie, L. L., Barger, A. J., & Williams, J. P. 2011, ApJ, 726, L18

Wardlow, J. L., Smail, I., Coppin, K. E. K., et al. 2011, MNRAS, 415, 1479

Wardlow, J. L., Smail, I., Wilson, G. W., et al. 2010, MNRAS, 401, 2299

Warren, S. J., Hambly, N. C., Dye, S., et al. 2007, MNRAS, 375, 213

Webb, T. M., Eales, S., Foucaud, S., et al. 2003, ApJ, 582, 6

Webb, T. M. A., Brodwin, M., Eales, S., & Lilly, S. J. 2004, ApJ, 605, 645

Weiß, A., De Breuck, C., Marrone, D. P., et al. 2013, ApJ, 767, 88

Weiß, a., Kovács, A., Coppin, K., et al. 2009, ApJ, 707, 1201

White, R. L., Helfand, D. J., Becker, R. H., Glikman, E., & de Vries, W. 2007, ApJ, 654, 99

Wiklind, T., Conselice, C. J., Dahlen, T., et al. 2014, 51

Younger, J. D., Fazio, G. G., Huang, J., et al. 2007, ApJ, 671, 1531

Younger, J. D., Fazio, G. G., Huang, J.-S., et al. 2009, ApJ, 704, 803

Younger, J. D., Fazio, G. G., Wilner, D. J., et al. 2008, ApJ, 688, 59

Yun, M. S., Aretxaga, I., Ashby, M. L. N., et al. 2008, MNRAS, 389, 333

Yun, M. S. & Carilli, C. L. 2002, ApJ, 568, 88

Yun, M. S., Scott, K. S., Guo, Y., et al. 2012, MNRAS, 420, 957

Zamojski, M. A., Schiminovich, D., Rich, R. M., et al. 2007, ApJ, 172, 468

Acknowledgements

I feel like there are many persons whom I should say thanks. As probably most of the PhD students in the world, my experience had a lot of contrasts. For every special moment (positive and negative) I have faces to remember.

I would especially thanks to my family, for the incredible support I have had from them. “Muchas gracias, no creo que pueda expresar fácilmente el incre´ıble apoyo que han sido. No saben como aprecié cada una de sus visitas y también cada una de las veces que los pude visitar. Quiero que sepan que soy consciente de las condiciones priviligiadas que he tenido, las cuales se esforzaron en darme durante toda mi etapa de estudiante.”

I would also like to give special thanks to Frank Bertoldi, who allowed me to carry out my research in his group at AIfA. He has given me a lot of support so I could continue with my PhD to the end.

I would also want to thanks Prof. Karl Menten who has been always very kind to me. I am also very grateful as he always let me continue working in the offices of the MPIfR, where I had all my data.

A really big thanks go to Prof. Vernesa Smolčić, from who I learnt a lot. She trusted in me and gave me big responsibilities in her projects, which was actually a lot of fun for me.

I am also in debt with many of my colleagues and also with friends outside from the institute who where there to make me feel like at home. The fact of knowing so many people with so many different backgrounds certainly has enriched my vision of the world. Thanks Laura, Arturo, Esteban, Denise (both the Chilean and the German), Miriam, Miguel, Luisa, Jürgen, Brenda, Fujun, Luis, Juan, Carlitos, Rebeca, Carlos Carosko, Ewan, Christof, Jorge, Ramiro, Rosy. Also to Rosa who is the one that has been always there during this last period of my PhD.

Also, and I would not like to sound too egocentric here, I would like to thanks myself because I continued moving forward although sometimes I felt like I was moving nowhere. It is very tempting to say ’this is the end’, but when one keep trying inevitably one finds out how far from the end one really was.

Felipe Navarrete
Bonn, 2014